

Department of Mathematics and Statistics

A New Approach for Modelling Insolation from the Space Perspective

Sofya Prakhova

**This thesis is presented for the Degree of
Doctor of Philosophy
of
Curtin University**

April 2014

Declaration

To the best of my knowledge and belief this thesis contains no material previously published by any other person except where due acknowledgment has been made. This thesis contains no material which has been accepted for the award of any other higher degree or diploma in any university.

A handwritten signature in blue ink, appearing to be 'J. G. A.', written in a cursive style.

23.04.2014

Abstract

The area of climate modelling is very topical nowadays. There are many organisations all over the world who are concerned about the continued rise of average global temperature and the impact this has on our lives. The main one is probably the Intergovernmental Panel on Climate Change, which publishes reports regularly with the last one being released just at the end of last year. Indeed, the negative impacts of climate change will affect the life of every creature and some of the outcomes may be irreversible. There are many research studies currently being conducted in order to predict future climate changes and to find ways to avoid or at least to mitigate the negative effects.

The most powerful tools for investigating future climate changes are global climate simulation models, the development of which started about half of the century ago. These models are being developed at the different institutions all over the world and they incorporate many different components, starting from the simplest energy balance models and ending up with the most comprehensive general circulation models. The vast majority of these models are the result of teams of researchers working together for many years. As we will show, many of the models emphasize different aspects of climate modelling, but all their contributions are important. It is only by joint effort and cooperation around the world that the solutions to negative effects of climate change can be found.

A recent development in climate research is recognition that space activity such as solar flares, cosmic rays, gamma ray bursts and so on can have a significant impact on various Earth-based systems. In this thesis, a new approach for modelling insolation within climate models is proposed. In contrast to existing methods, the new approach takes the space point of view. In the future, this allows for the explicit incorporation of more general space activity into the modelling. This is not possible with the current insolation models where the earth's point of view is used. Also, the existing methods of modelling space activity do not incorporate these activities directly. Instead, most of them formulate a likely impact on various chemical species in the atmosphere and incorporate this into a more general climate model.

The new approach has then been incorporated into an existing global climate model. Apart from yielding more accurate estimates of insolation, this has also allowed simulating the seasonal variations of insolation within this model.

In Chapter 1, a literature review is presented. Firstly, the current available approaches for modelling insolation are reviewed. Then the two main existing classes of climate models - the General Circulation Models (GCMs) and the Earth System Models of Intermediate Complexity (EMICs) - are described. After that, a comprehensive description of main stages of development of these models is given. Furthermore, we describe the main challenges faced by their developers and outline the results predicted by these models. For each new type of development, we give an example of a model which incorporates this. Finally, the aim of this thesis is formulated.

In the second chapter, a detailed description of the new proposed insolation model is provided. The choice of coordinate plane where the calculations were performed is explained and the main equations are formulated. The method of computing the incoming radiation is described in detail. Also, the illumination areas for different latitudinal belts in the Northern and Southern Hemispheres are presented. Furthermore, an approximation technique which was used for the computation is introduced. At the end of the chapter, the computational results produced by the model are presented. They include the amount of insolation for each latitudinal belt throughout the year and also a comparison of the annual values of insolation with satellite data obtained from NASA (National Aeronautics and Space Administration). The obtained results indicate a very good agreement in modelling the annual distribution of insolation for the equatorial and middle latitude regions, and slightly less for the polar regions. The average accuracy of the model is 97%.

In the third Chapter, the details of incorporation of the new insolation model into the Earth System Model of Intermediate Complexity C-GOLDSTEIN are provided. First it is shown that replacing the original annual averages for insolation with those from the new insolation model still yields reasonable results. Also included is the description of a curve fitting procedure which was first applied to the results for each latitudinal belt. We then explain how the obtained curves are incorporated into the model code and how the seasonal simulations of insolation were performed. At the end of the chapter, the results of simulations are presented. The modification has increased

the average accuracy of modelling the insolation within this model by 2%. In addition, realistic monthly temperature distributions have been obtained.

In summary, a new approach for modelling insolation from the space perspective is proposed in this thesis. This is shown to yield accurate results when compared to satellite data and also to perform well when is used within a global climate model. This provides a good basis for an explicit incorporation of the impact of other space activity into climate modelling in the future.

Publications and Conference Presentations

- S. Prakhova, V. Rehbock and I. Suleimanov, “*Novel Insolation Model for Climate Prediction*” at Mathematics for Planet Earth, Jul 10, 2013, Melbourne.
- S. Prakhova, V. Rehbock and I. Suleimanov, “*Incorporating of Solar Activity Variations into the Global Climate Model*” at Engineering Mathematics and Applications, Dec 3, 2013, Brisbane.
- S. Prakhova, I. Suleimanov and V. Rehbock, “*A New Approach for Modelling Insolation from the Space Perspective*”, Applied Mathematical Sciences, vol. 8 n. 60, pp. 2951-2964, 2014.

Acknowledgement

I would like to thank Lou Caccetta for providing me with the scholarship and an opportunity to undertake PhD studies.

I am very grateful to Igor Suleimanov from Ufa State Petroleum Technological University in Russia. I am grateful for his ongoing support, encouragement, his bright ideas for developing the model, a very high level of professionalism and deep knowledge. This project would not have been possible without his contribution. I am grateful to him that he believed in me when no one else did.

And of course I wish to thank my supervisor, Volker Rehbock, who is supporting me in all my endeavours. I know that it was not an easy decision for him to agree to supervise the project in the area which is different to his, but I'm happy that he did agree. I am grateful for his tolerance, patience, and his constant willingness to understand. I am also grateful for his help, not only with my studies, but with other aspects of life as well, and for giving me a chance.

List of Figures

Figure 2.1 Coordinate systems and radiation vector (annual cycle)	34
Figure 2.2 The coordinates of the centre of the ellipses	35
Figure 2.3 The projection of a latitudinal belt in X1OZ1 coordinate plane.....	36
Figure 2.4 The projection of a latitudinal belt in Y1OZ1 coordinate plane.....	37
Figure 2.5 The projection of a latitudinal belt in X1OY1 coordinate plane	37
Figure 2.6 The direction of the radiation vector from the Earth's point of view and the surface orientation	38
Figure 2.7 The illumination area for a positively-oriented surface and for a negatively-oriented surface for the latitudinal belt	39
Figure 2.8 The determination of illumination areas for different latitudinal belts.....	40
Figure 2.9 Illumination areas for 0°-10°N latitudinal belt for $\alpha=10^\circ$, $\alpha=40^\circ$ and $\alpha=60^\circ$ (a-c)	43
Figure 2.10 Illumination areas for 10°-20°N latitudinal belt for $\alpha=20^\circ$, $\alpha=40^\circ$ and $\alpha=60^\circ$ (a-c)	44
Figure 2.11 Illumination areas for 20°-30°N latitudinal belt for $\alpha=20^\circ$, $\alpha=40^\circ$ and $\alpha=60^\circ$ (a-c)	45
Figure 2.12 Illumination areas for 30°-40°N latitudinal belt for $\alpha=20^\circ$, $\alpha=40^\circ$ and $\alpha=60^\circ$ (a-c)	46
Figure 2.13 Illumination areas for 40°-50°N latitudinal belt for $\alpha=20^\circ$, $\alpha=40^\circ$ and $\alpha=60^\circ$ (a-c)	47
Figure 2.14 Illumination areas for 50°-60°N latitudinal belt for $\alpha=20^\circ$, $\alpha=40^\circ$ and $\alpha=60^\circ$ (a-c)	48
Figure 2.15 Illumination areas for 60°-70°N latitudinal belt for $\alpha=20^\circ$, $\alpha=40^\circ$ and $\alpha=60^\circ$ (a-c)	49
Figure 2.16 Illumination areas for 70°-80°N latitudinal belt for $\alpha=20^\circ$, $\alpha=40^\circ$ and $\alpha=60^\circ$ (a-c)	50
Figure 2.17 Illumination areas for 80°-90°N latitudinal belt for $\alpha=20^\circ$, $\alpha=40^\circ$ and $\alpha=60^\circ$ (a-c)	51
Figure 2.18 Illumination areas for 30°-40°S latitudinal belt for $\alpha=20^\circ$, $\alpha=40^\circ$ and $\alpha=60^\circ$ (a-c)	53
Figure 2.19 Illumination areas for 40°-50°S latitudinal belt for $\alpha=20^\circ$, $\alpha=40^\circ$ and $\alpha=60^\circ$ (a-c)	54
Figure 2.20 Illumination areas for 70°-80°S latitudinal belt for $\alpha=20^\circ$, $\alpha=40^\circ$ and $\alpha=60^\circ$ (a-c)	55
Figure 2.21 Illumination areas for 80°-90°S latitudinal belt for $\alpha=20^\circ$, $\alpha=40^\circ$ and $\alpha=60^\circ$ (a-c)	56
Figure 2.22 The area of integration for the $0 - \beta$ illumination area	58
Figure 2.23 The area of integration for the $\beta - \varepsilon$ illumination areas.....	61
Figure 2.24 The area of integration for the $\varepsilon - (\pi/2 - \varepsilon)$ Type I illumination areas	62
Figure 2.25 The area of integration for the $\varepsilon - (\pi/2 - \varepsilon)$ Type II illumination areas ...	64
Figure 2.26 The area of integration for the $\varepsilon - (\pi/2 - \varepsilon)$ Type III illumination areas..	64
Figure 2.27 The area of integration for the $(\pi/2 - \varepsilon) - \pi/2$ Type I illumination area ..	66

Figure 2.28 The area of integration for the $(\pi/2 - \varepsilon) - \pi/2$ Type II illumination area.	66
Figure 2.29 The areas of integration for the C_2 - D_2 symmetrical illumination area ...	68
Figure 2.30 The areas of integration for the D_2 - C_2 symmetrical illumination area....	70
Figure 2.31 The areas of integration for the polar symmetrical Type I illumination area	71
Figure 2.32 The areas of integration for the polar symmetrical Type II illumination area	71
Figure 2.33 The areas of integration for the polar symmetrical Type III illumination area	72
Figure 2.34 The areas of integration for the polar symmetrical Type IV illumination area	72
Figure 2.35 The approximation of the $0 - \beta$ illumination area	75
Figure 2.36 The approximation of the β - ε illumination area	76
Figure 2.37 The approximation of the $\varepsilon - (\pi/2 - \varepsilon)$ Type I illumination area	77
Figure 2.38 The approximation of the $\varepsilon - (\pi/2 - \varepsilon)$ Type II illumination area.....	79
Figure 2.39 The approximation of the $\varepsilon - (\pi/2 - \varepsilon)$ Type III illumination area.....	79
Figure 2.40 The approximation of the $(\pi/2 - \varepsilon) - \pi/2$ Type I illumination area.....	81
Figure 2.41 The approximation of the C_2 - D_2 symmetrical illumination area	82
Figure 2.42 The approximation of the D_2 - C_2 symmetrical illumination area	83
Figure 2.43 The approximation of the polar symmetrical Type I illumination area..	85
Figure 2.44 The approximation of the polar symmetrical Type II illumination area	86
Figure 2.45 The approximation of the polar symmetrical Type IV illumination area	87
Figure 2.46 The projection of latitudinal belt in YOZ plane (a) and XOY plane (b) ..	88
Figure 2.47 The amount of radiation received by odd latitudinal belts in the Northern Hemisphere	90
Figure 2.48 The amount of radiation received by even latitudinal belts in the Northern Hemisphere	90
Figure 2.49 The amount of radiation received by odd latitudinal belts in the Southern Hemisphere	91
Figure 2.50 The amount of radiation received by even latitudinal belts in the Southern Hemisphere	91
Figure 3.1 The annual mean temperature distribution	94
Figure 3.2 Curve fitting for 0° - 10° N latitudinal belt	99
Figure 3.3 Curve fitting for 10° - 20° N latitudinal belt	100
Figure 3.4 Curve fitting for 20° - 30° N latitudinal belt	100
Figure 3.5 Curve fitting for 30° - 40° N latitudinal belt	101
Figure 3.6 Curve fitting for 40° - 50° N latitudinal belt	101
Figure 3.7 Curve fitting for 50° - 60° N latitudinal belt	102
Figure 3.8 Curve fitting for 60° - 70° N latitudinal belt	102
Figure 3.9 Curve fitting for 70° - 80° N latitudinal belt	103
Figure 3.10 Curve fitting for 80° - 90° N latitudinal belt	103
Figure 3.11 Curve fitting for 0° - 10° S latitudinal belt	108
Figure 3.12 Curve fitting for 10° - 20° S latitudinal belt	108

Figure 3.13 Curve fitting for 20°-30°S latitudinal belt	109
Figure 3.14 Curve fitting for 30°-40°S latitudinal belt	109
Figure 3.15 Curve fitting for 40°-50°S latitudinal belt	110
Figure 3.16 Curve fitting for 50°-60°S latitudinal belt	110
Figure 3.17 Curve fitting for 60°-70°S latitudinal belt	111
Figure 3.18 Curve fitting for 70°-80°S latitudinal belt	111
Figure 3.19 Curve fitting for 80°-90°S latitudinal belt	112
Figure 3.20 Temperature distribution for December	114
Figure 3.21 Temperature distribution for January	114
Figure 3.22 Temperature distribution for February	115
Figure 3.23 Temperature distribution for March	115
Figure 3.24 Temperature distribution for April	116
Figure 3.25 Temperature distribution for May	116
Figure 3.26 Temperature distribution for June	117
Figure 3.27 Temperature distribution for July	117
Figure 3.28 Temperature distribution for August	118
Figure 3.29 Temperature distribution for September.....	118
Figure 3.30 Temperature distribution for October	119
Figure 3.31 Temperature distribution for November.....	119

List of Tables

Table 2.1 The illumination areas for 0° - 50° latitudinal belts for the period of time from the winter solstice to the vernal equinox	41
Table 2.2 The illumination areas for 50° - 90° latitudinal belts for the period of time from the winter solstice to the vernal equinox	41
Table 2.3 The limits of integration for the $0 - \beta$ illumination area.....	59
Table 2.4 The limits of integration for the $\beta - \varepsilon$ and $\varepsilon - (\pi/2 - \varepsilon)$ Type I illumination areas.....	63
Table 2.5 The limits of integration for the $\varepsilon - (\pi/2 - \varepsilon)$ Type II illumination area	65
Table 2.6 The limits of integration for the $\varepsilon - (\pi/2 - \varepsilon)$ Type III illumination area	65
Table 2.7 The limits of integration for the $(\pi/2 - \varepsilon) - \pi/2$ Type I illumination area ...	67
Table 2.8 The limits of integration for the $(\pi/2 - \varepsilon) - \pi/2$ Type II illumination area..	67
Table 2.9 The limits of integration for C_2 - D_2 symmetrical illumination area	69
Table 2.10 The limits of integration for D_2 - C_2 symmetrical illumination area.....	70
Table 2.11 The limits of integration for the polar symmetrical Type I illumination area	73
Table 2.12 The limits of integration for the polar symmetrical Type II illumination area	73
Table 2.13 The limits of integration for the polar symmetrical Type III illumination area	73
Table 2.14 The limits of integration for the polar symmetrical Type IV illumination area	74
Table 2.15 The updated limits of integration for $0 - \beta$ illumination area	75
Table 2.16 The updated limits of integration for $\beta - \varepsilon$ and $\varepsilon - (\pi/2 - \varepsilon)$ Type I illumination areas	78
Table 2.17 The updated limits of integration for the $\varepsilon - (\pi/2 - \varepsilon)$ Type II illumination area	80
Table 2.18 The updated limits of integration for the $\varepsilon - (\pi/2 - \varepsilon)$ Type III illumination area	80
Table 2.19 The updated limits of integration for the $(\pi/2 - \varepsilon) - \pi/2$ Type I illumination area	81
Table 2.20 The updated limits of integration for C_2 - D_2 symmetrical illumination area	82
Table 2.21 The updated limits of integration for D_2 - C_2 symmetrical illumination area	84
Table 2.22 The updated limits of integration for the polar symmetrical Type I illumination area.....	85
Table 2.23 The updated limits of integration for the polar symmetrical Type II illumination area.....	86
Table 2.24 The updated limits of integration for the polar symmetrical Type IV illumination area.....	87
Table 2.25 Calculations of the insolation for the whole year period for the Northern and Southern Hemispheres.....	89

Table 2.26 Comparison of the obtained results with satellite data	92
Table 3.1 The comparison of the results of initial and proposed insolation models..	95
Table 3.2 The coefficients of the straight lines ($C_{1,i}$, $C_{2,i}$, $D_{1,i}$, $D_{2,i}$, E_i).....	104
Table 3.3 The coefficients of the straight lines ($C_{3,i}$, $C_{4,i}$, $D_{3,i}$, $D_{4,i}$)	104
Table 3.4 The coefficients of wave functions ($A_{1,i}$, $B_{1,i}$, $\omega_{1,i}$, $\varphi_{1,i}$).....	104
Table 3.5 The coefficients of wave functions ($A_{2,i}$, $B_{2,i}$, $\omega_{2,i}$, $\varphi_{2,i}$).....	105
Table 3.6 The coefficients of wave functions ($A_{3,i}$, $B_{3,i}$, $\omega_{3,i}$, $\varphi_{3,i}$).....	105
Table 3.7 Total error estimation.....	105
Table 3.8 The results of calculations of SS_{res} , SS_{tos} and R^2 coefficient for each latitudinal belt.....	106
Table 3.9 The results of calculations of SS_{res} , SS_{tos} and R^2 coefficient for each latitudinal belt.....	112

Table of Contents

CHAPTER 1 LITERATURE REVIEW	1
1.1 Insolation Modelling	1
1.2 The development of general circulation models	4
1.2.1 The early development of general circulation models	4
1.2.2. The development in climate models during 1990-1995	10
1.2.3. The development in climate models during 1995-2000	15
1.2.4. The development in climate models during 2000-2005	20
1.2.5. The development in climate models since 2005	22
1.3. Earth System Model of Intermediate Complexity	28
1.3.1. A general description of EMICs	28
1.3.2. A description of C-GOLDSTEIN	29
1.4. The incorporation of impact of external forces on the Earth and problem formulation	31
CHAPTER 2 NOVEL INSOLATION MODEL	34
2.1. Model description.....	34
2.2. The illumination area for the Northern Hemisphere latitudinal belts	42
2.3. The illumination areas for the Southern Hemisphere latitudinal belts	52
2.4. Radiation Calculation	57
2.5. Limits of integration for the Northern Hemisphere	58
2.6. Limits of integration for the Southern Hemisphere	67
2.7. The approximation technique	74
2.7.1. The approximation of the latitudinal belts in the Northern Hemisphere.....	74
2.7.2. The approximation of the latitudinal belts in the Southern Hemisphere.....	81
2.8. The calculation of the area of the latitudinal belt	87
2.9. Computation and results.....	88
CHAPTER 3 INCORPORATION OF THE PROPOSED MODEL INTO GLOBAL CLIMATE MODEL C-GOLDSTEIN	93
3.1. The verification and comparison of the results for the annual average insolation	93
3.2. Incorporation of seasonal variations of insolation into C-GOLSTEIN.....	95
3.2.1. A curve fitting procedure for latitudinal belts in the Northern Hemisphere	96
3.2.2. A curve fitting procedure for latitudinal belts in the Southern Hemisphere	106
3.2.3. Simulating the seasonal variations of insolation within C-GOLDSTEIN.....	113

CONCLUSIONS AND FUTURE WORK.....	121
REFERENCES	124
APPENDIX 1.....	131
APPENDIX 2.....	137

Chapter 1 Literature Review

Climate modelling is a broadly developed area which is of a great interest nowadays. The modelling of insolation started long time ago, with the first work belonging to the Serbian mathematician and astronomer Milankovitch (Milankovitch, 1920). This was conducted in order to explain the long-term variations in the orbital parameters. Later on a number of different approaches were proposed. The various ways of modelling insolation are presented in Section 1.1.

The development of climate models started back in the early 1960s, when the first general circulation models containing only the atmosphere appeared (Manabe, Smagorinsky, & Strickler, 1965). But as time was progressing and the computational capacities increased, more components were developed and coupled together. The resulting comprehensive models are known as General Circulation Models (See Section 1.2). These models represent powerful tools for predicting future climate changes, as well as for understanding the climate of the past.

Parallel to them, another group of models was developing- the Earth System Models of Intermediate Complexity (See Section 1.3). These models are more simplified than the comprehensive GCMs. However, they have a number of advantages, such as their capability to be used for the forecasts up to several millennia, as well as for performing extensive sensitivity studies. The incorporation of impact of external forces on the Earth and the problem formulation are presented in Section 1.4.

1.1 Insolation Modelling

The first method of calculating daily insolation is proposed in (Milankovitch, 1920), which is indeed the first publication to present a set of formulae for this task. The method is based on spherical trigonometry applied to the astronomical coordinates on the celestial sphere for the Earth's orbital motion. The English version is available in, for example, (Milankovič, 1998). The theory was developed in order to investigate the relationship between insolation and climate on the global scale, in particular, the appearance of ice ages.

In the following calculations, φ is the latitude and δ is the solar declination. For the latitudes where there is a daily sunset and sunrise, i.e. $-\left(\frac{\pi}{2} - |\delta|\right) < \varphi < \frac{\pi}{2} - |\delta|$, the insolation for them was calculated as:

$$W_d = \frac{S}{\pi p^2} (H_0 \sin(\varphi) \sin(\delta) + \cos(\varphi) \cos(\delta) \sin(H_0)).$$

Here S is a modulated version of the solar constant due to the eccentricity of the earth's orbit, defined in terms of a , where a is the semi-major axis of the orbit. Also, ρ is the Earth-Sun distance measured in units of the semi-major axis a , H_0 is the absolute value of the hour angle at sunrise and sunset. This was calculated as:

$$\cos(H_0) = -\tan(\varphi) \tan(\delta).$$

For other latitudes where there is either a polar day or a polar night (i.e. $|\varphi| > \frac{\pi}{2} - |\delta|$) different formulae were applied. For the latitudes with no daily sunrise ($H_0=0$) the amount of insolation equals to zero, whereas for the case of no daily sunset ($H_0=\pi$) the amount of insolation was calculated as:

$$W_d = \frac{S}{p^2} \sin(\varphi) \sin(\delta).$$

However, the theory was rejected by geologists in 1955, since its prediction did not match with the past climate patterns observed from geological records available at that time.

Later, one of the first global energy balance models started to be developed. This required some representation of insolation.

In the paper (Budyko, 1969), a simple one-dimensional energy balance model had been developed. The impact of variations in radiation on the climate change was investigated. In particular, those changes which are related to glaciation were examined in great detail. Empirical formulae for outgoing radiation and for heat transport were proposed. The heat balance equation of the Earth-atmosphere system contains a gain or loss of heat as a result of the atmosphere and hydrosphere circulation, planetary albedo, the outgoing radiation and the incoming radiation at the top of the atmosphere. For the insolation the annual mean tabulated values for each latitudinal belt were used. An empirical formula for the temperature in terms of the amount of radiation received was also derived in the research.

Another analysis (W. D. Sellers, 1969) was conducted independently at the same time. Here a simple energy balance model has also been developed. Average annual mean values for each latitudinal belt were used for determining the incident solar radiation

similar to (Budyko, 1969). The impact of water vapour, carbon dioxide, dust and clouds on terrestrial radiation was specified by introducing certain empirical coefficients.

The paper also aimed to investigate how the decreases or increases in the solar constant would affect the ice caps.

A different approach for modelling the incoming radiation was used later on by (North, 1975). In his paper, an energy balance model similar to the one in (Budyko, 1969) has been considered. However, the heat transport was represented in thermal diffusion form, and a number of additional boundary conditions have been specified for the energy balance equation, such as no heat transport at the poles etc. Also, the insolation formulation was different. Here the mean annual distribution of incoming radiation was approximated by using the second order Legendre polynomial of the form:

$$S(x) \cong 1 + S_2 P_2(x),$$

where $S(x)$ is the mean annual distribution of radiation reaching the top of the atmosphere, x is the sine of latitude, $S_2 = -0.477$, and $P_2(x) = \frac{1}{2}(3x^2 - 1)$ is the second Legendre polynomial (North, Cahalan, & Coakley, 1981). With this approximation $S(x)$ is a parabola in x and has a zero derivative at the equator.

In the paper by (North & Coakley Jr, 1979), the seasonal distribution of insolation was modelled. This was done on a basis of the previous approximation for the mean annual models. Again, a Legendre polynomial expansion has been used for the representation of seasonal changes of insolation:

$$S(x, t) \approx 1 + S_1 \cos(2\pi t) P_1(x) + (S_2 + S_{22} \cos(4\pi t)) P_2(x),$$

where t is time, $S_1 = -0.796$, $S_2 = -0.477$, $S_{22} = 0.147$, $P_1(x)$ and $P_2(x)$ are the first and the second order Legendre polynomials, respectively.

In the last two approaches mentioned above the coefficients of the Legendre polynomials were obtained from the computations of (Milankovitch, 1920), which was given attention again at that time. The reason for this was an improvement in geological dating techniques and a consequently improved interpretation of the geological records.

The Milankovitch theory was revived by a number of authors, for example (Berger, 1978). The paper proposes new trigonometric formulae for calculating the long-term variations of the earth orbital elements, such as obliquity angle, precession, and the

eccentricity of the Earth. This also brought attention back to the formulae for calculating daily insolation originally proposed by (Milankovitch, 1920).

The approaches mentioned above provide quite a high accuracy and are commonly used in current GCMs and EMICs. These are described in more details in the following sections.

1.2 The development of general circulation models

The description of general circulation models is divided into a number of time periods. The development for each time period is introduced in Sections 1.2.1 -1.2.5, respectively.

1.2.1 The early development of general circulation models

The first atmospheric general circulation models which were coupled to ocean models had an idealized geography and no annual insolation cycle. The ocean component was represented by a very simple model with no oceanic heat storage and no oceanic heat transport (they are often referred as a swamp ocean models). A detailed description is provided in Section 1.2.1.1. Some models used fixed cloud cover, while in the others different computational approaches were used for determining this. The results obtained from these early models provide some indication of how an increased carbon dioxide concentration will affect the global temperature distribution. Later on the simplified distribution of the oceans and continents was replaced by more realistic ones in some of the models (See Section 1.2.1.2). This type of model was computationally fast in terms of reaching equilibrium within about 300 days. However, since the annual insolation cycle is neglected, the predictions obtained from using models of this type need to be treated with caution.

The type of ocean model used in the early era of climate model development has made the inclusion of a seasonal insolation cycle impossible. Its inclusion would have meant that the ocean is frozen at night time and in the polar latitudes (Schlesinger & Mitchell, 1987). A huge breakthrough came when a new simple mixed layer ocean component was developed and coupled to the atmospheric components. This allowed for the incorporation of the seasonal insolation cycle into the general circulation models, because the new type of ocean component permitted the ocean heat storage

and ocean heat transport by currents. The use of this kind of ocean model has also increased the sensitivity of the models to the cloudiness changes (Wilson & Mitchell, 1987). An example of the model with the seasonal cycle is presented in Section 1.2.1.3. The models further differed by their treatment of sea ice. There were two main modelling approaches available: to prescribe sea ice or to predict it. In the prescribed approach the sea surface temperature was prescribed from the climatology for the control integration. However, for increased carbon dioxide integration the sea surface temperature was determined from a succession of perturbation experiments (Schlesinger & Mitchell, 1987). The usage of this approach yields results closer to the real climatic ones. However, one of the drawbacks was the strong influence of these prescribed changes on the CO₂-induced climate. An example is introduced in Section 1.2.1.4.

For the second way of modelling sea ice, the sea surface temperature and sea ice extent were determined by the ocean or the sea ice model. This requires at least the upper ocean model to incorporate heat capacity. The details of the models calculating the sea ice prognostically are given in Section 1.2.1.5. The advantage of this approach is that the sea surface temperature and the sea ice extent can interact with the atmosphere to establish a climate equilibrium (Schlesinger & Mitchell, 1987). The disadvantage is the possibility of errors in the predicted parameters during the control simulation due to deficiencies in the atmospheric and ocean components at early stages of the model development.

Most of the models at that time were used to study the climate response to differing rates of carbon dioxide increase. Some papers (Mitchell, Senior, & Ingram, 1989) also aimed to investigate how different cloud parameterization schemes affect that response.

1.2.1.1 Idealized geography, no annual insolation cycle, swamp ocean, fixed clouds.

An example of this type of early model can be found in (Manabe & Wetherald, 1975). The authors used a highly simplified three dimensional general circulation model. For all the area below a latitude of 66.5°, the computational domain was spread into two equal parts - the ocean and the continent. The area above 66.5° was assumed to be just the continent. The ocean was simply modelled as an area of wet land or an area which

possesses an infinite source of soil moisture for evaporation. The grid resolution of the model is about 500 km.

The model contains a thermodynamic equation, a convective equation, radiation transfer and an equation for water vapour. These simple equations were solved using an energy conserving form of the finite-difference formulation in the model. The clouds and spatial distribution of ozone were determined depending on the latitude and longitude only. The mixing ratio of carbon dioxide was assumed to be constant, and the distribution of water vapour was defined from the prognostic equation. The surface temperature calculation was done under the assumption that no heat is stored at the earth's surface. The prognostic system of water vapour involved the three dimensional advection of water vapour, evaporation, vertical mixing, non-convective condensation, and an idealized moist convective argument. The form of precipitation (snow or rain) was determined at a height of about 350 m for the continents with everything below zero degrees being a snow. For the ocean the freezing point was set up at -2° .

Both the snow cover and the ice cover were separated into the permanent and the temporary types with different albedo values prescribed for each case. The albedo of the soil was assigned in terms of latitude.

1.2.1.2 Realistic geography, no annual insolation cycle, swamp ocean, fixed/computed clouds.

An example of this type of AOGCM is the Community Climate Model (CCM) developed in the National Centre for Atmospheric Research (NCAR) (USA). Its description is provided in (W. M. Washington & Meehl, 1983).

The model was run with both fixed clouds and then with computed cloud patterns. The purpose of the paper was to investigate the climate response to the different rates of carbon dioxide increase, and also how climate is affected by using two different cloud parameterization schemes. Realistic geography of the oceans and continents was used. The atmospheric component here is represented by a spectral atmospheric general circulation model. The model has a global domain and realistic geography. The latitudinal resolution of the model is 4.4° , and the longitudinal one is 7.5° . The equations of motion were written in the sigma coordinate system with the vorticity and divergence as the prognostic variables for the horizontal motion field. The wind vector was modelled on the basis of a stream function and a velocity potential. The model

also contains the continuity equation and the prognostic equation for the temperature and water vapour mixing.

The model does not include annual or diurnal cycles. The convective adjustment scheme was used for parameterizing convection and condensation. The radiative transfer was separated into a longwave and a shortwave radiation. The model also incorporates the vertical distribution of CO₂, ozone and water vapour. The mixing ratio of carbon dioxide was assumed to be constant in the atmosphere.

The cloud parameterization scheme in case of the computed clouds was obtained from (Ramanathan, Pitcher, Malone, & Blackmon, 1983). It was assumed that the upper layer clouds have an emissivity of one. The model includes two types of clouds: convective and non-convective ones, with the fractional cloud cover being 30% and 95%, respectively. The clouds were also assumed to form so as to fill a layer completely in a vertical direction. The land and sea albedo were prescribed as a function of latitude. The sea ice was assumed to be fixed.

The bulk aerodynamic parameterization was applied for the stress at the surface and the sensible and latent heat fluxes. There was assumed to be no heat conduction into the soil. The sea surface temperature remained constant during the calculation. However, the surface temperature was computed for each time step.

1.2.1.3. Realistic geography, annual insolation cycle, mixed-layer ocean, fixed clouds.

One of the first models of this kind is the Geophysical Fluid Dynamic Laboratory (GFDL) model, the details of which are introduced in (Manabe & Stouffer, 1980). The initial version of the model was primarily used for investigating the climate response to the quadrupling of the carbon dioxide in the atmosphere. The proposed model consists of three main components: an Atmospheric Model, a Heat and Water balance Model of the Continents and a Mixed Layer Ocean Model.

In the Atmospheric Model the temperature, moisture, surface pressure, vertical component of vorticity and the horizontal divergence were calculated based on the divergence equation, a thermodynamical equation, and continuity equations of moisture and mass. The prognostic equations were integrated with respect to time by using a semi-implicit method and a time-smoothing technique. Physical processes such

as water vapour condensation, snowfall and rainfall were included in the model as well.

Seasonal and latitudinal variation of insolation together with carbon dioxide, ozone, water vapour and cloud effects were considered in the model. The cloud cover and the distribution of ozone were assumed to be zonally uniform and were modelled as a function of latitude, height and also the season for the second parameter. The variations of insolation at the top of the atmosphere were approximated by the second order Legendre polynomial (North & Coakley Jr, 1979).

In the Heat and Water balance Model of the Continents the surface temperature was calculated under the assumption that no heat is stored in the soil. The net downward radiation flux was modelled as depending on surface albedo. It was prescribed as a function of latitude over the oceans, a function of latitude and snow depth for the snow regions and the geography of the continents. The soil moisture change was prescribed in terms of rainfall, evaporation, snowmelt and runoff. The snow depth change was modelled depending on snowfall, sublimation and snowmelt.

In the Mixed Layer Ocean Model the mixed ocean layer was prescribed as vertically isothermal with constant thickness. The global computational domain and realistic geography were used. Layer temperature change was modelled as a function of the rate of net heat gained by the ocean, the heat capacity of water and the thickness of the layer for ice-free regions. For the iced-covered regions the temperature was assigned to be constant at the freezing point. The horizontal heat transport was not incorporated into the model at the time. The albedo of the mixed layer ocean was calculated in terms of the latitude. The thickness of sea ice was computed in terms of the rate of snowfall, the rate of sublimation, the rate of melting sea ice and the rate of freezing sea ice. The wind stress impact on sea ice and the impact due to ocean currents were neglected.

1.2.1.4. Realistic geography, annual insolation cycle, mixed-layer ocean, fixed clouds, prescribed ice.

The paper dealing with the prescribed sea ice is (Mitchell, 1983). Here, a five level atmospheric model was used with both seasonal and diurnal cycles. Two different experiments were performed. The first one investigated the impact of increasing the carbon dioxide level, for which the prescribed present day sea surface temperature was

used. In the second experiment the present day sea surface temperature was increased by 2° and the CO₂ concentration was doubled.

All the layers of the atmosphere in the model are of an equal mass and thickness. The horizontal resolution is about 330 km and quasi-uniform over the sphere. Basic equations were solved within the model. The surface fluxes of heat and moisture were assigned as a function of the surface type and the surface stability. The model has an interactive radiation scheme, and includes soil moisture and snow variables. The important atmospheric gases such as ozone, carbon dioxide and water vapour were incorporated into the solar radiation calculation.

The soil moisture was modelled as a function of rainfall, condensation, snowmelt and evaporation. The model contains the clouds varying in terms of height and thickness and uses zonal mean cloud amounts from seasonal observations.

The surface albedo was prescribed differently for different types of surfaces. For snow-free land it was prescribed depending on the latitude. For snow-covered land and sea ice, it was modelled as a function of snow depth and temperature, respectively. The sea surface temperature and sea ice extents were obtained from a Fourier analysis of the climatological temperature data.

1.2.1.5. Realistic geography, annual insolation cycle, mixed-layer ocean, computed clouds, predicted ice.

One model of this class is The Oregon State University (OSU) model (Schlesinger & Zhao, 1989). This is also a global atmospheric general circulation model, but coupled to a 60-m deep mixed layer ocean model. The latitudinal resolution of the model is 4°, and the longitudinal one is 5°. The computation of radiation was done according to (Milankovitch, 1920). The prognostic variables of the atmosphere are the atmospheric velocity, temperature, surface pressure, water vapour, the surface temperature, snow mass, soil water and clouds. The prognostic variables of the ocean are the oceanic mixed-layer temperature and sea ice thickness, which were calculated on the basis of a thermodynamic sea ice model.

1.2.2. The development in climate models during 1990-1995

As time progressed, the AOGCMs were continuing to develop, slowly in terms of some of the components and more rapidly for others. Significant progress had been achieved for the representation of land based processes by the middle of the 1990s. The land surface components of some models of that generation started to include the multiple soil types, the representation of leaves, roots, the dependence of albedo, roughness and stomatal conductance on the type of vegetation and its canopy geometry, and carbon uptake and respiration (Gates et al., 1996). Further details are provided in Section 1.2.2.1.

For the atmospheric component of the models the resolution has been increasing continuously, which has resulted in significant improvement of surface air temperature forecasting. Generally speaking, the GCMs of that generation were able to simulate the large scale features of the current climate realistically. However, the modelling of regional features still required a lot of additional work. The representation of clouds and their seasonal variations were a major deficiency in the atmospheric models of that time.

For the ocean models the development was mainly going towards increased resolution and some success had been achieved. However, this still remained as an area which required significant future work. The main difficulties which remained were in the representation of mixing processes, the structure and strength of the western boundary currents, the simulation of the meridional heat transport, and the portrayal of convection and subduction (Gates, et al., 1996).

The atmospheric and ocean components in the models interacted through heat, momentum and fresh water fluxes. Those fluxes now started to be adjusted in some of the general circulation models. The purpose of this was to correct the errors which systematically appeared in the simulations. However, many modelling groups were still developing their models without flux adjustment and refused to give up on the idea of creating a complete model purely based on physics. The models with flux adjustment are introduced in more detail in Section 1.2.2.2.

Some success was also reached in modelling the sea ice component. In the new components the sea ice could now move freely. More details are given in Section 1.2.2.3.

Another significant improvement in the middle of the 1990s is the development and coupling of the first three-dimensional aerosol models (see Section 1.2.2.4). A big inspiration for this was the eruption of Mount Pinatubo in 1991, which erupted with significant amounts of dust and this remained in the atmosphere for a long period of time. The three-dimensional models of that time were capable of explicitly representing the spatial variability of solar radiation, the aerosol distribution, and cloudiness. Some of the models were developed in particular for modelling aerosol sulphate (Pham, Müller, Brasseur, Granier, & Megie, 1995), some for mineral dust (Tegen & Fung, 1994), and some for soot (Penner, Eddleman, & Novakov, 1993)

1.2.2.1. The models with the improved land surface component

An example of significantly improved land surface modelling is introduced in (Dickinson, Kennedy, & Henderson-Sellers, 1993). The model was developed as a component for the NCAR Model.

The model has 18 different vegetation/land cover types, such as crop/mixed farming, deciduous and needle leaf trees, desert, tundra, ice cap/glacier, evergreen shrub, mixed woodland etc. The specific land type and soil information were assigned to each model grid square. Three different parameters were defined for each land grid point: the visible solar albedo of vegetation, near-infrared albedo of vegetation, and soil albedo. A different vegetation cover was assigned to different types of land depending on the fractional ground shading and the relative areas of transpiring and non-transpiring plant surfaces. The soil information was classified and stored in different colour, texture and drainage classes. Snow albedos were assigned as a function of a spectral mix of the incident radiation/solar zenith angle, soot loading of the snow, snow depth, and grain size. The foliage temperature was calculated taking into account the energy balance requirements and consequent fluxes of heat and moisture from the foliage to the canopy air.

1.2.2.2. Models with flux adjustment

An example of a model with flux adjustment is the Canadian Climate Centre (CCC) model. Its description is provided in (McFarlane, Boer, Blanchet, & Lazare, 1992).

The model was used to perform a ten year climate simulation, which was then compared with real observations.

A spectral triangular horizontal resolution was used in the model with the latitudinal-longitudinal resolution being approximately $3.75^\circ \times 3.75^\circ$. The basic dynamic equation was specified in terms of vorticity, divergence, temperature, the logarithm of surface pressure and specific humidity. The model includes a seasonal cycle of insolation (Berger, 1978). The upward/downward shortwave fluxes were calculated for a conservative atmosphere and a first-guess absorbing atmosphere. The optical depth and single-scattering albedo were assigned depending on cloud liquid water content and ice crystal content. The longwave radiation was modelled in terms of six spectral intervals.

A convective adjustment scheme was applied on pairs of vertical levels in case of the atmosphere being conditionally unstable. A procedure for eliminating negative specific humidities (hole fitting) was used as well. The vertical fluxes of momentum, heat and moisture due to turbulent flow were defined by using the eddy diffusivity formulation in the free atmosphere. The surface fluxes were represented in terms of drag coefficients, which are the functions of the surface-layer bulk Richardson number.

In the land surface component 24 different soil/vegetation types were assigned for each grid box. The composite productivity or heat capacity in each of them was calculated depending on soil type, soil moisture and snow cover.

A simple mixed layer ocean component was used here. A simplified heat flux procedure was applied to the ocean heat flux in order to reach an agreement between the simulated surface temperature and the observed climatological values. The residual field was defined on a monthly basis calculated as the difference between the monthly mean net surface flux and the flux obtained by the change in the local heat storage of the slab as obtained from the climatological sea surface temperature field (McFarlane, et al., 1992). The residual term was applied in free-ice areas. A thermodynamic sea-ice component was used. The surface temperature of sea ice was determined depending on the surface heat balance and a heat flux from the ocean below, which was consequently assigned as a function of the constant ice thickness and the temperature gradient between the ocean and the ice. The prognostic snow mass was determined from a budget equation. A limitation was assigned to the snow mass prognostic parameter in order to keep the density in the lower part of a deep snowpack from

exceeding the sea ice density. Also, the flux at the bottom of the sea ice was adjusted at points with an excessive sea ice mass, with different values being given to the regions of permanent ice cover and the regions of just seasonal ice cover.

The results obtained by the model demonstrate that it is generally capable of reproducing the observed climatology well.

1.2.2.3. Models with the sea ice movement by currents (“free-drift” scheme)

An example of a model with a “free-drift” ice scheme is presented in (Stouffer & Manabe, 1999). The aim of that paper was to investigate the response of the ocean and atmospheric processes (such as the thermohaline circulation (THC), sea level change and air temperature change) to the CO₂ increase. Five different transient integrations were performed under five different carbon dioxide rate increases: 0.25%, 0.5%, 1%, 2% and 4%.

The proposed model contained a general circulation model of the world oceans, a general circulation model of the atmosphere and heat and water budgets of the continents.

The atmospheric component consisted of prognostic equations such as the equations of motion, thermodynamic equations, water vapour equations and surface pressure equations. These equations were constructed for a thin spherical shell by (C. T. Gordon & Stern, 1982). The surface heat budget was separated into four components: net radiation, sensible flux, latent flux and oceanic heat flux. Each flux was then zonally averaged and its change in response to a given CO₂ increase was modelled as a function of latitude separately for oceans and continents. After that all radiation flux responses were separated into a solar component and a terrestrial component for oceans and continents. The seasonal variations of insolation were taken into account (North & Coakley Jr, 1979). Other processes such as snow change, precipitation, land surface temperature change, albedo and budget of soil moisture were modelled here as well.

The oceanic component consists of a prognostic system of sea ice and a Water Mass model of the World Ocean developed by (Bryan & Lewis, 1979). The second model contains the equation of horizontal motion, a hydrostatic approximation, the continuity equation, the equation of state and the conservation equations for potential temperature and salt. In the prognostic system the sea ice can either move freely on the ocean

surface or remain slayable depending on its thickness. The thickness was determined from a thermodynamic heat balance and the ocean currents' advection.

1.2.2.4. Three-dimensional aerosol models

Models of this type are those described in (Langner & Rodhe, 1991; Penner, et al., 1993). The authors of the second paper used the MPI-Mainz MOGUNTIA model. The model has 10° by 10° resolution and has 10 layers between the surface and 100hPa. The prognostic parameters of the model are dimethyl sulphide (DMS), sulphur dioxide (SO₂) and sulphate (SO₄²⁻), the last one being considered as an aerosol. An objective analysis procedure was used to obtain mass-converting three-dimensional wind fields from the observations. The vertical transport of DMS in deep convective clouds was related to the convective precipitation by using a diagnostic cloud model. The emissions considered in the model are: anthropogenic SO₂, the SO₂ released from biomass burning and volcanoes, and the DMS released from oceans, soil and plants. The estimates of sulphur compounds resulting from volcanic emission were obtained from (Stoiber, Williams, & Huebert, 1987) The estimations of anthropogenic emission were taken from the studies of (Rotty, 1987). A temperature dependent emission function was used to estimate the emissions from soil and vegetation. An emission factor was used to calculate the emissions occurring from biomass burning. The amount of DMS emitted from the ocean contributes to the uncertainties of the modelling.

Various day-time and night-time chemical reactions of SO₂ and DMS with other elements were considered in the model. The rate of removal of the in - cloud particles and gases by precipitation was assigned to be proportional to the average rate of formation of precipitation.

This model allowed the user to obtain the distribution of DMS, SO₂, and SO₄²⁻ in the lowest model layer and to determine the regions with its highest concentration. The comparison with real observations showed an agreement within a factor of two to three for DMS, a reasonable agreement for SO₂ prediction and generally good agreement for SO₄²⁻ with the exception of a few locations. In general, the model provided good forecasting for the annual average estimates. However, the seasonal simulations still required a significant improvement due to the limitations in model formulation and emission estimates.

1.2.3. The development in climate models during 1995-2000

By the beginning of the 21st century further progress had been made in ocean model resolution. For that generation of models a coarse resolution was considered to be greater than 2°, a medium one is between 2/3° and 2°, the eddy-permitting resolution is from 1/6° to 2/3°. This factor, together with improvement in the parameterisation of sub-grid scale mixing have allowed researchers to reach significant success in modelling ocean heat transport. In addition, the results of simulating the thermohaline circulation and sea temperature have become more realistic as well. Examples of the AOGCMs with a medium-resolution ocean component and which also provide good results on ocean heat transport are NCAR1 (1.0×1.0) (W. M. Washington & Meehl, 1996), HadCM3 (1.25×1.25) (C. Gordon et al., 2000), CGCM1 (1.8×1.8) (Boer, Flato, & Ramsden, 2000), CGCM2 (1.8×1.8) (Flato & Boer, 2001). An example of an eddy-permitting model is introduced in Section 1.2.3.1.

The representation of plant physiology had also become more realistic in some of the land surface components of that time. This was a significant improvement as it permits the simulation of carbon dioxide and gas isotope fluxes. The components of this type belong to the third generation of land surface components.

The models with dynamic vegetation can be separated into two main groups: the terrestrial biogeochemical models (TBMs) and the dynamic global vegetation models (DGVMs). The TBM simulate fluxes of carbon, water and nitrogen, which are coupled within terrestrial ecosystems. Models of this class are BIOME3 (Haxeltine & Prentice, 1996), DOLY (F. I. Woodward, Smith, & Emanuel, 1995), and SiB2 (P. Sellers et al., 1996). Details of the last of these models are presented in Section 1.2.3.2.

The DGVMs further couple all the processes represented in the TBM with changes in ecosystem structure and composition. The DGVM include the representation of photosynthesis, respiration and canopy energy balance, the controls of stomatal conductance and canopy boundary-layer conductance, and the allocation of carbon and nitrogen within the plant (Cramer et al., 2001). There are many different models of this kind and they differ by the number of modelled processes and parameters such as litter fall, the trees species, vegetation dynamic completion etc. Representatives of this class of the models are SDGVM (F. Woodward, Lomas, & Betts, 1998), IBIS (Foley et al., 1996) and so on (see Section 1.2.3.3. for more details).

Another significant improvement of the AOGCMs at that time was the inclusion of the carbon cycle into the atmospheric and ocean component of the model. This contributes to many processes and also affects climate change directly. Terrestrial carbon transport is presented in the models in Section 1.2.3.3. An example of a model with ocean carbon transport is given in Section 1.2.3.4.

In the area of sea ice modelling the development was progressing very slowly at that time. The sea ice dynamics were added to the models, but this generated more errors in the wind field and surface heat fluxes, so these two processes were basically offsetting each other.

1.2.3.1. Ocean models with eddy-permitting resolution

An example of an eddy-permitting model is the model from (W. Washington et al., 2000). Here the resolution of the ocean component is $0.67^\circ \times 0.67^\circ$. The purpose of the paper was to present the results from two different experiments: a 0.5% per year carbon dioxide increase experiment to the time of carbon dioxide doubling and a 1% per year carbon dioxide increase experiment with idealized stabilization at doubling and quadrupling of carbon dioxide.

The atmospheric component is a spectral model, which has 18 vertical levels and a horizontal latitudinal-longitudinal resolution of $2.8^\circ \times 2.8^\circ$. The component is the parallel version of the NCAR CCM3. The insolation was calculated according to the method prescribed in (North & Coakley Jr, 1979). The cloud fraction and optical parameters were calculated from grid scale parameters. The long wave radiation was computed with the consideration of seven different greenhouse gases, such as CO_2 , O_3 , CH_4 , N_2O etc. A small adjustment was applied to the cloud parameters in order to reach the energy balance in case of prescribed ocean sea surface temperature.

The land surface model is a one dimensional model in which the energy, momentum and water exchanges between the atmosphere and earth's surface were modelled. It has different prescribed vegetation types, as well as hydraulic and thermal properties of twelve prescribed soil types. As previously mentioned, the resolution for the ocean component was 0.67° . However, in the equatorial regions it is increased to 0.5° . Only the mean observed annual estimate of river transport to the Arctic was used in the model. The globally averaged water flux over the ocean-ice system was set to zero. The polar runoffs were added uniformly to the ocean along the coastlines.

The model has a fully dynamic-thermodynamic sea component. The prognostic parameters of the model are ice thickness, ice concentration, velocity, snow thickness, and surface temperature of ice. The ice dynamics were represented by the elastic-viscous-plastic (EVP) ice rheology. The one-layer ice and snow thermodynamic scheme with a single ice thickness per grid point were used in the thermodynamic part. The model was run on a Cartesian grid in the two regions beyond the polar circles. The results of the ocean heat transport obtained after the model simulations were in a very good agreement with observations.

1.2.3.2. The terrestrial biogeochemical models (TBMs)

One of the models of this class is the SiB2 model described in (P. Sellers, et al., 1996). The simultaneous transfer of carbon dioxide and water vapour into and out of a plant leaf has been incorporated into the modelling by the use of a photosynthesis-conductance model. The vegetation phenology was prescribed from satellite data obtained from the NOAA (National Oceanic and Atmospheric Administration). Time series fields of the fraction of photosynthetically active radiation absorbed by the green vegetation canopy (FPAR), the total LAI (leaf index area) and the canopy greenness fraction were derived.

Also, there was an improvement in the modelling of base flows. The accuracy of computations of the underlayer exchanges within the soil profile increased as well. In addition, the representation of snow melt has been improved. In this model it was modelled in a way which prevents rapid thermal transitions in case of snow cover being low (a “patchy” snow formulation).

A number of atmospheric boundary conditions were specified, such as air temperature, vapour pressure, wind speed etc. The soil model has three levels, with the third one being a source for hydrological base flow and upward recharge of the root zone. For each vegetation type, a number of morphological, optical and physiological properties were specified. Those parameters included height of canopy top and bottom, leaf width, leaf length, mean topographic slope, leaf transmittance, the partial pressure of oxygen in the leaf interior, stomatal slope factor etc. The time varying parameters for the vegetation types are total leaf-area index, FPAR, canopy roughness length, mean canopy extinction coefficient and so on. This modelling approach allowed users to obtain much more realistic results.

The evaporation from the canopy was prescribed as evaporation of water from snow/ice or water intercepted by canopy and transpiration of soil water extracted by the root system. The evaporation from the soil surface consists of the loss from snow/ice and “puddled” water held on the soil surface and the evaporation of soil moisture from within the top soil layer.

A limitation was applied on the effective heat capacity of snow in order to allow realistic diurnal variations of the surface temperature wave. This “patchy” snowmelt treatment yields more realistic results for the surface reflectance, energy balance, temperature transitions and land surface albedo.

1.2.3.3. The Dynamic Global Vegetation Models

The IBIS model (the integrated biosphere simulator) was presented in (Foley, et al., 1996). The model included the following features: land surface processes, canopy physiology, vegetation phenology, and terrestrial carbon balance and vegetation dynamics.

The biophysical processes described were designed in a way which is convenient for the incorporation of the model into GCMs. The energy, CO₂, momentum and water fluxes between the surface, the vegetation canopies, and the atmosphere were modelled. A number of parameters were represented explicitly in the model, such as the temperature of the canopy air spaces, the specific humidity within the canopy air spaces, the temperature of the soil surface and the temperature of the vegetation canopies. For each vegetation layer a two-stream approximation of solar radiation was used. The calculations were performed separately for direct and diffusive radiation. The total evapotranspiration consisted of the canopy transpiration, evaporation of water intercepted by vegetation canopies and the evaporation from the soil surface.

The photosynthesis rate was modelled in terms of absorbed light, leaf temperature, CO₂ concentration within the leaf, and the Rubisco enzyme capacity for photosynthesis. The light-limited rate of photosynthesis was prescribed as a function of the flux density of photosynthetically active radiation absorbed by the leaf, the intrinsic quantum efficiency for carbon dioxide uptake in C₃ plants, the compensation point for gross photosynthesis, and the concentration of carbon dioxide in the intercellular air spaces of the leaf.

There are nine different plant functional types in the model, including four types of evergreen trees, three types of deciduous trees, cool grasses and warm grasses. The seasonal processes of the deciduous trees dropping their leaves and the leaves reappearing again was assigned depending on either the critical temperature threshold or the time of the year.

The competition for common light and water resource pools was modelled explicitly. The annual carbon balance was represented as a sum of hourly carbon fluxes.

1.2.3.4. Models with ocean carbon cycle

A description of a model with ocean carbon cycle is presented in (Murnane, Sarmiento, & Le Quéré, 1999). The ocean model consists of 12 levels of increasing thickness and a total depth of five thousand metres. It also contains a Solubility Model, a Potential Solubility Model, an Ocean Biogeochemistry Model, and air-sea flux of carbon dioxide. In addition, the virtual flux in a form of a linear function of the salinity restoring fluxes has been used for correcting tracer concentration within the model.

In the Potential Solubility Model the air-sea fluxes were modelled depending on the heat and water fluxes at the ocean surface. The thermal flux of CO₂ was prescribed in terms of the heat capacity of seawater, density, the modelled heat flux, the sea surface temperature, the equilibrium CO₂ concentration for a given temperature and salinity, and the buffer factor. The buffer factor is the ratio of the fractional change in carbon dioxide and the fractional change in the dissolved inorganic carbon (DIC) after equilibrium.

In the Solubility Model the carbon simulations were run until (DIC) content reaches a steady state. The heating and cooling of surface waters was considered as the main cause for the appearance of air-sea fluxes of carbon dioxide and the change in its solubility. The water (salt) fluxes, gas exchange kinetics and ocean circulation have an impact on those fluxes as well. The concentration of DIC change with time was modelled depending on the gas transfer velocity, the carbon dioxide concentration in equilibrium with atmosphere, and carbon dioxide concentration of the surface layer. The model also contained a mass balance equation for CO₂. The biological processes that increase the deep ocean concentration were neglected in the model.

The Biological Pump component was based on the phosphorus cycling. The stoichiometric ratio of organic carbon production and phosphate production was

assigned to be 120. One half of the newly produced organic carbon was put into dissolved organic carbon and the second half was put into particulate organic carbon. The CaCO_3 production and remineralisation were estimated at each time step.

The solubility pump, the biological pump and the gas exchange kinetics were examined in order to investigate their influence on the interhemispheric transport of carbon dioxide in a steady state, preindustrial ocean. However, this was complicated by the existence of a steep gradient and the change of its sign near the equator. The inputs from the rivers and sediment burial of carbon and nutrients were not taken into account.

1.2.4. The development in climate models during 2000-2005

By the middle of 2000s, significant progress had finally been achieved in the area of cloud modelling, which had remained the main source of uncertainties for quite long time. Previously the parameterization of cloud fields was used. The models current at that time started to model each particular cloud element such as the cloud particles and cloud droplets. Schemes of improved microphysics parameterization were proposed by many authors, for instance (Ivanova, Mitchell, Arnott, & Poellot, 2001). Although a big step forward had been made, many questions about the cloud representation in models still remain unanswered.

The resolution of the models and the computational power was also constantly being increased, which resulted in more successful regional forecasting as well in the improvements of large-scale forecasts obtained in earlier stages. The parameterization of many processes in the atmospheric, land surface and sea ice components had been improved. The simulations of seasonal variations have also been improved within the atmospheric components of the models.

Also, with the improvement of the AOGCMs, the flux adjustment was no longer needed and went out of use since the capabilities of that generation of model already allowed realistic climate forecasting based on the physical processes only.

Significant progress was achieved in the area of aerosol modelling. One of the factors contributing to this was also an ongoing improvement in the observation capacities, such as the satellite retrievals of the aerosol depth in the regions free of clouds etc. At that time more and more atmospheric models started to incorporate an aerosol component. Examples are the LSCE model (Schulz et al., 2006), ECHAM5-HAM

(Stier et al., 2005), UIO_CTM (Myhre et al., 2004), the GEOSCHEM model (Martin, 2004), the LOA model (Reddy et al., 2005), and the GISS model (Adams, Seinfeld, Koch, Mickley, & Jacob, 2001). The complexity, resolution and the number of vertical levels of the models had been improved as well. Some models of that era also started to include an interactive aerosol sub-component, such as MIROC-med (Hasumi & Emori, 2004) and IPSL-CM4 (O Marti et al., 2005). The second one of these is described in more detail later in this section.

Some more recent models also consider indirect effects of aerosols (the way they affect the cloud albedo and the lifetime of clouds) in addition to the direct ones (scattering and absorption).

The standard horizontal resolution for the ocean component of the models of that generation is already 1° to 2° . Continued effort was still concentrated on the development of more eddy-permitting models ($1/6^\circ$ to $2/3^\circ$), which were still limited by their very high computational costs.

There was some success in the representation of land processes as well. New techniques appeared for modelling high latitude organic soils, sub-grid scale snow parameterisation, and higher resolution river routing. The model described in (Yeh & Eltahir, 2005) had a coupled groundwater component. The representation of the soil moisture-precipitation feedback had been improved in the models of that generation as well.

New numerical approaches for solving the ice dynamic equations have been included in a number of models (Marsland, Haak, Jungclaus, Latif, & Röske, 2003). Also, new schemes including heat capacities and salinity-dependent conductivity started to be in use. However, the area of sea ice modelling was still being developed more slowly than the others.

The description of the MIROC-med model is introduced in (Hasumi & Emori, 2004). The zonal resolution of the ocean component is approximately 1.4° . The meridional resolution also started from around 1.4° at high latitudes and gradually decreased to 0.56° in the equatorial region. There were 43 vertical layers excluding the bottom boundary layer. The coast lines were prescribed from the lines which connect the velocity points. The vertical grid spaces were different for different depth levels.

The spatial resolution of the sea-ice component was $1.4^\circ \times 1.4^\circ$. The ice was represented by one vertical layer and also had one snow layer on top of it. There were two different categories of ice thickness considered: a thin ice and a thick ice.

For the land surface component the MATSIRO model was used (Takata, Emori, & Watanabe, 2003). Here the energy and water interaction between the land surface and the atmosphere were modelled. The surface flux calculation was different for the snow-free and snow-covered areas. The snow amount was prescribed as a function of snow fall, snow melt and sublimation.

The atmospheric component had a 2.8° by 2.8° horizontal resolution and 20 vertical layers with quite a fine vertical resolution near the planetary boundary level. The physical parameterization of cumulus convection, large-scale convection, radiative transfer, surface fluxes, vertical diffusion and internal gravity wave drag had been applied.

The aerosol effects on the cloud albedo and the lifetime of clouds (also sometimes referred as the first and the second aerosol indirect effects) had been taken into account. However, this had only been done for one type of cloud- the stratus water ones. In the radiation scheme of the model the aerosol microphysics and its radiative effect on cloud water, optical parameters for clouds and aerosols, and vertical cloud overlapping were prescribed.

The model also has ice clouds, five aerosol species and seven species of particulate matter. The hygroscopic growth of aerosols was assumed to be homogeneously intermingled with water. The shape of particulate matters was assumed to be spherical. The effect of the particle size on the radiative fluxes was taken into account as well. The radiative fluxes were obtained under the condition of maximum-random cloud overlap.

1.2.5. The development in climate models since 2005

Many of the current AOGCMs have now progressed to the Earth System Models (ESMs). The reason for that is the inclusion of various biogeochemical cycles into the global climate models. This is a very important step forward since having a closed biogeochemical cycle incorporated into the model allows for the computation of the carbon dioxide concentration prognostically under prescribed emission rates. The ESMs are currently the most comprehensive tools for investigating future climate changes. There are already quite a few models which have evolved to Earth System Models, including HadGEM2-ES (UK) (W. Collins et al., 2011), MIROC-ESM-CHEM (Japan) (M. Watanabe et al., 2010), MRI-ESM1 (Japan) (Adachi), and

NorESM1-ME (Norway) (Tjiputra et al., 2012). All the models outlined above have aerosols, atmospheric chemistry, land carbon and ocean biogeochemistry incorporated. However, to be considered as an ESM a model is merely required to have one of those properties.

Many ESMs nowadays use an advanced representation of marine biogeochemistry. In particular, they include nutrients, plankton, zooplankton and detritus. This type of biogeochemistry model is known as a NPZD model. Examples of models which use the improved scheme are MIROC-ESM (S. Watanabe et al., 2008) and MIROC-ESM-CHEM (M. Watanabe, et al., 2010). The NPZD model used in them is from (Schmittner, Oschlies, Giraud, Eby, & Simmons, 2005).

A recent achievement is the coupling of the land ice sheets to the global climate models (Lipscomb et al., 2013; Vizcaíno et al., 2008), which allows for the simulation of freshwater fluxes from Greenland and Antarctica and to investigate their impact on rising sea levels. The details of the model with ice sheets are presented in Section 1.2.4.1. However, only very few ESMs have these capacities so far.

Ongoing development is happening for the aerosol components of climate models. There has been success in the simulation of mass, number, size distribution and mixing state of interacting multi-component aerosol particles (e.g., (Liu et al., 2012)). Currently the representation of aerosols in the models varies significantly, including the prescribed (BCC-CSM1.1 (Xin et al., 2013), CNRM-CM5 (A Voltaire et al., 2013)), semi-interactive (FGOALS-s2, (Bao et al., 2013), GFDL-ESM2M (Dunne et al., 2013)) and interactive (CSM4 (Gent et al., 2011), CanCM4 (von Salzen et al., 2013), CSIRO-Mk3.6.0 (Rotstayn et al., 2012) aerosol types. However, the aerosol-cloud interaction still remains an active area of work.

Another recent major achievement in the development of climate models is an inclusion of the atmospheric chemistry. Nowadays a number of Earth System Models includes the prognostic equations for calculating atmospheric ozone and other chemical elements. This allows investigation of the impact of the ozone hole on climate and the effect that stratospheric dynamics has on the tropospheric circulation. Examples of this type are CanESM2 (von Salzen, et al., 2013), CESM1 (FASTCHEM) (Eyring et al., 2013), HadGEM2-CC (W. Collins, et al., 2011). A large number of climate models now also have a fully resolved stratosphere with some models reaching above the stratopause (50km). Models with a fully resolved stratosphere are CESM1(WACCM) (Hurrell et al., 2013), CMCC-CESM (Vichi et al., 2011), and

MRI-CGCM3 (Yukimoto, Adachi, & Hosaka, 2012). An example of a model incorporating atmospheric chemistry and a fully resolved stratosphere is introduced in Section 1.2.4.2.

The carbon exchange between the land and atmosphere is now incorporated into a large number of models (INM-CM4 (Volodin, Dianskii, & Gusev, 2010), GFDL-ESM2G (Dunne et al., 2012), IPSL-CM5A-LR (Dufresne et al., 2013)). This is a significant step forward since the dead organic carbon respired by the heterotrophic organisms in the soil contributes significantly to the global carbon cycle. The soil carbon was assumed to be located within the top 1m of the soil. The major soil databases were used for modelling the land carbon.

In addition to this, land use started to be considered in the land component of the models. In particular, the deforestation and the conservation of natural grasslands due to extended land use together with its impact on climate are being investigated. Several main factors need to be taken into consideration, such as the type of vegetation being removed, the type of crops being grown, whether the crops are being irrigated or not etc. The changes in the vegetation cover have many consequences, such as a change in radiative forcing due to land surface albedo change, a surface temperature change, changes in surface heat fluxes and many other effects.

The land surface models which allow the investigation of the impact of land used are JSBACH (Raddatz et al., 2007), CABLE (Abramowitz, Leuning, Clark, & Pitman, 2008), ISPA (Aurore Voldoire, 2006) etc. Those models are now starting to be coupled to global climate models.

There are currently two different ways to model crops and pasture distribution. In some global climate models such as IPSL (Olivier Marti et al., 2010) and ARPEGE (Salas-Mélia et al., 2005) information was obtained from land cover maps. In the other models such as SPEEDY (Strengers et al., 2010), CCSM (W. D. Collins et al., 2006) and ECHAM5 (Roeckner et al., 2006) it was simulated. Simulations with preindustrial vegetation maps and greenhouse gas concentrations and others with present day conditions have been performed in order to examine the effects of these changes.

1.2.5.1. The models with land ice

An EBM model coupled with ice sheets is introduced in (Vizcaíno, et al., 2008). The atmospheric component of the model is ECHAM3, which has a horizontal resolution

of about 5.6° and 19 vertical layers. The prognostic equations of the model are solved for temperature, humidity, surface pressure, cloud water, vorticity, and divergence. Solar radiation here was calculated according to the method prescribed in (Milankovitch, 1920). The horizontal resolution of the ocean component is 5.6° in two overlapping grids. There are 22 vertical layers of varying thicknesses. The thickness of the uppermost layer is 50m and then it is increasing downward to nearly 800m for the bottom of the ocean. The model incorporates a parameterization of the sub-grid-scale tracer transport due to eddies. The sea ice is represented by a simple dynamic sea ice model.

A simple biogeochemical cycle model as described in (Maier-Reimer, 1993) was used with a primitive formulation of plankton productivity. A perfect stoichiometric constancy of organic material was assumed in the model. In contrast, the complex Lund-Potsdam-Jena Dynamic Global Vegetation Model (LPI) (Sitch et al., 2003) has been used to represent the land processes. The model has ten functional plant types with different physiological, morphological, phenological, and bioclimatic properties. The feedback through canopy conductance between photosynthesis and transpiration is taken into account. The model also includes population dynamics, soil organic matter, resource competition, and tissue turnover. The terrestrial vegetation dynamic, land-atmosphere carbon, and water exchanges are all combined together in one modular framework.

A three-dimensional ice sheet model SICOPOLIS was used within the EBM. The model contains of 21 vertical levels for the ice column. The model consists of time-dependent equations for ice velocity, temperature, water content, ice sheet thickness, ice sheet extend, and age for any specific grounded ice. The equations were scaled with respect to the ratio of typical thickness to typical length. The ice was assumed to be an incompressible, heat-conducting, power-law fluid. The effective shear stress was assigned in terms of the components of the frictional stress tensor. Sliding is allowed only if the basal ice temperature is higher than pressure melting temperature. Global mean values have been assigned for the geothermal heat fluxes. The tropical regions have been excluded from the model domain.

To avoid biases in the simulations a number of corrections were used. In particular, a linear height correction was applied for near-surface temperatures, an exponential height-desertification one for the precipitation rates. In addition, an empirical formulation was used to convert seasonal precipitation rates into the seasonal

accumulation ones. If the iceberg calving and basal melting occurred due to ocean heat supply, the freshwater flux from the ice sheet is treated as ice. If the surface melting and basal melting occurred due to geothermal heat fluxes, the freshwater flux from the ice sheet is treated as liquid water.

The results obtained from the model demonstrate a smaller loss of mass than the results obtained from non-coupled studies (Alley, Clark, Huybrechts, & Joughin, 2005). The reason for this could be the fact that the current simulations were performed by using the model with relatively coarse resolution of both the atmospheric and the ice sheet components. In addition, some corrections were used and the governing equations were scaled. However, this represents one of the first attempts to couple the land ice with the Energy Balance Model. It was also concluded that the changes in ice sheet balance contribute significantly to the changes in the climate system in general and therefore more work should be done in coupling them to the EBMs and AOGCMs.

1.2.5.2. The models with atmospheric chemistry

An example of the Earth System model with atmospheric chemistry and a fully resolved stratosphere is GFDL-CM3 (Donner et al., 2011). The land component of the model includes a recently developed model for land water, energy and carbon balance. A multilayer model of snowpack above the soil, a parameterization of water table height and a frozen soil-water phase are incorporated into the land component. It also takes into account the mass and energy exchange between the lakes and both the atmosphere and the rivers. The vegetation structure, phenology and carbon dioxide are modelled according to (Shevliakova et al., 2009). The longitudinal resolution of ocean component is 1° , while the latitudinal one varies from 1° for the polar and middle-latitude regions to $1/3^\circ$ degrees at the equator. There are 50 vertical layers of different thicknesses. For a sea ice component the GFDL Sea Ice Simulator was used, which is a dynamical model with three vertical layers and five ice thickness categories. The snow layer has no heat capacity, the lower layer of the ice has a sensible capacity and the upper one has both a sensible and a latent heat capacities.

A cubed sphere grid is used in the atmospheric component of the model, with the total number of cells being 13824. The size of grid cells varies from 163 km at the six corners of the cubed sphere to 231 km near the centre of each face. There are 48

vertical levels in the model extending up to about 83 km, which is above the stratopause.

The distribution of ice and water content in stratiform clouds was determined according to the cloud fraction and condensate amount. Within each grid-scale column it was assumed that the prescribed cloud drop number is uniform. The convective clouds are internally homogeneous and replace the stratiform clouds when occur in the same layer. The size of ice particles in shallow cumulus and stratiform clouds was assigned depending on the temperature. Historical concentrations of carbon dioxide, nitrous oxide, methane and halocarbons were incorporated into modelling.

The mass distribution and the optical properties of aerosols are affected by a number of processes. These processes are: emission, chemical production (gas and aqueous-phase oxidation of SO₂ by radicals, ozone, and hydrogen peroxide), transport (advection, convection, eddy diffusion by turbulence), dry removal (gravitational settling and impaction at the surface by turbulence), and wet removal (in- and below-cloud scavenging by large-scale and convective clouds).

Tropospheric and stratospheric models are merged in the CM3 model. The tropospheric model is the one from (Horowitz et al., 2003). The model called MOZARTv.2 is a highly flexible, global three-dimensional chemical transport model. The resolution of the model is 2.8° by 2.8°. The number of vertical layers is 34 with the uppermost one being at approximately 40 km. The model contains 63 chemical species, including simple and common species such as NO₂, N, and CH₄, as well as the more complex species such as CH₃COCH₃, EO₂ (HOCH₂CH₂O₂) etc. The model also contains detailed oxidation schemes for non-methane hydrocarbons, the parameterization of dry and wet deposition, and the subgrid scale convective and boundary layer parameterization. Various sources of surface emission were considered in the model. Examples are biofuel and biomass burning, oceanic emission and so on. The stratospheric concentrations of some long-lived species (NO_x, HNO₃, N₂O₅, N₂O, and O₃) were constrained by relaxation towards their climatological values obtained from different models.

The model for the stratosphere is the UMETRAC model described in (Austin & Butchart, 2003). The model has latitudinal resolution of 2.5° and the longitudinal one of 3.75°, and 64 vertical layers. The coupled chemistry scheme of the model contains 13 advected tracers, including the parameterized long-lived species and families. All the major processes affecting the stratospheric ozone were represented explicitly. The

model produces realistic results for the annual-mean, zonally averaged ozone and also reproduces the seasonal variations of total column ozone well. However, ozone in high latitudes was slightly underestimated compared to actual observations and the bias was generally larger for the Southern Hemisphere.

1.3. Earth System Model of Intermediate Complexity

A general description of EMICs is introduced in Section 1.3.1. A description of a particular EMIC, C-GOLDSTEIN, is presented in Section 1.3.2.

1.3.1. A general description of EMICs

Parallel to the general circulation models, another class of models was developing, known as the Earth System Models of Intermediate Complexity. These models have components similar to those of the GCMs and went through a similar evolution process. However, the Earth System Models of Intermediate Complexity generally include fewer processes than their more comprehensive prototypes, and also use parameterization techniques rather than representing physical processes explicitly.

However, the EMICs are widely used in climate modelling. They are capable of performing forecasts up to several millennia, as well as being able to simulate the climate of the distant past. This is simply not possible by using the general circulation models due to their high computational costs and the large amount of memory required. The forecasts performed by the GCMs normally do not exceed a few centuries. Also, the EMICs sometimes even have additional components which the GCMs of the current generation do not yet have (for example, the land ice was incorporated into the EMICs earlier than into GCMs). In addition, the Earth System Models of Intermediate Complexity are very good tools for showing up the main trends of possible climate changes, which can later be investigated in greater detail by GCMs. The development of the EMICs started around the late 1980s, with one of the first ones being the models described in (Gallée et al., 1992) and (Harvey, 1992). The other EMICs are PUMA (Maier-Reimer, Mikolajewicz, & Hasselmann, 1993), IAP RAS (Mokhov, Eliseev, Handorf, & Petoukhov), EcBilt (Opsteegh, Haarsma, Selten, & Kattenberg, 1998), C-GOLDSTEIN (Marsh, Edwards, & Shepherd, 2002), CLIMBER-3 α (Montoya et al., 2005), IGSM2 (Sokolov et al., 2005). Remarkably, in

the middle of the 1990s, some of the Earth System Models of Intermediate complexity already had atmospheric chemistry and closed cycles included (Alcamo, 1994), whereas the GCMs started to incorporate these only recently (as detailed in Section 1.2.5.).

Some of the current EMICs incorporate ice sheets. Examples of these are CLIMBER-2 (Petoukhov et al., 2000) and LOVECLIM1.2 (Goosse et al., 2010). Some of the most recent models also incorporate the ocean sediment, such as the DCESS model (Shaffer, Olsen, & Pedersen, 2008) and the Bern3D-LPJ (Ritz, Stocker, & Joos, 2011).

The EMICs are currently being widely used in performing various climate studies together with the general circulation models.

A more detailed description of one of the EMICs, C-GOLDSTEIN (Marsh, et al., 2002) is provided in Section 1.3.2.

1.3.2. A description of C-GOLDSTEIN

C-GOLDSTEIN (Global Ocean-Linear Drag Salt and Temperature Equation INtegrator) consists of a two-dimensional atmospheric model, a three-dimensional ocean model, and simple land surface and sea ice models. Longitudinal resolution of the atmospheric component is 10° , while latitudinal resolution varies from 3° near the equator to 20° for polar regions. The model code is written in FORTRAN.

The ocean component is based on thermocline equations with an additional linear drag term in the horizontal momentum equations. The isoneutral and eddy-diffusive mixing scheme, the option of implicit time steps, spatially variable drag, and variable upstream weighting for convection are also included in the model. A condition of zero normal fluxes of heat and salt was specified at the lateral boundaries. The lower boundary fluxes of two prognostic variables (temperature and salinity) were set to zero.

The land component has no dynamical land-surface scheme and only determines the runoff of fresh water. The surface temperature was assumed to be equal to the atmospheric temperature and the evaporation is set to zero. The sea ice component contains dynamic equations which were solved for the fraction of the ocean surface covered by sea ice and the average height of sea ice. The fraction of the ocean surface was assigned depending on position. The growth of ice was calculated mainly depending on the heat flux from the atmosphere to the sea ice and the heat flux from the sea ice to the ocean. The albedo over sea ice was assigned as a linear function of

air temperature within a given range. It was assumed that the sea ice has no heat capacity and the existence of snow was neglected. The flux of fresh water into the ocean was modelled in terms of precipitation, runoff, evaporation over open water, ice melting, and ice freezing. The heat and freshwater fluxes were adjusted for the realism of results.

The atmospheric component of the model is represented by an Energy Moisture Balance Model. The prognostic parameters are air temperature and specific humidity at the surface. The model balances heat and moisture within the atmosphere. Here incoming and outgoing fluxes, sensible heat exchange with the underlying surface, latent heat release due to precipitation and horizontal transport processes were modelled. Different values of the absorption coefficient were assigned over the ocean and over the land. The net flux of longwave radiation into the atmosphere was modelled as a function of the surface and atmospheric emissivities, the temperature of the underlying surface and the Stefan-Boltzmann constant. The model does not contain a radiation scheme or clouds. The outgoing planetary longwave radiation was calculated taking the heating due to increases in carbon dioxide into account.

The incoming radiation was approximation by Legendre polynomials (North, 1975) and produces latitudinal-dependent annual average values.

The standard time step used for calculations was 0.73 days for the atmosphere and double that for the ocean. An implicit Atlantic-to-Pacific atmospheric moisture heat transport in three different geographical zones was used in the form of extra terms in the net surface freshwater flux. An additional forcing field due to perturbed freshwater forcing was set up at each ocean time step in the regions 20°-50°N and 50°-70°N.

The second order central differences method was used for solving the prognostic equations of the model in space. For solving them in time a forward difference method was used instead. A list of default parameters was given for the ocean, the atmosphere, and the sea ice variables.

Within the model both short-term and multi-millennium forecasts can be performed within a relatively short computational time. In order to obtain near present-day climate, a 2000 year experiment needs to be performed (known as SPINUP) which starts from some unrealistic conditions (such as zero mean global air temperature) and then progresses until the system comes close to equilibrium. All subsequent experiments (such as investigating an effect of rising carbon dioxide, thermohaline

circulation sensitivity experiments and so on) were performed by starting from these near equilibrium initial conditions.

1.4. The incorporation of impact of external forces on the Earth and problem formulation

From the overview of the global climate models provided one can see that several different methods of calculating insolation are used. In the comprehensive GCMs the seasonal variations of insolation are required. Thus the methods presented by (Milankovitch, 1920) or (North & Coakley Jr, 1979) are mainly used. Note that the first one is basically the only one which provides the geometry based formulae for calculating daily insolation. On the other hand, when using EMICs to perform multi-millennium forecasts where computational costs need to be kept low, annual average models are widely used, such as the one from (Budyko, 1969), or the annual mean approximation of insolation proposed by (North, 1975).

Although the current insolation models provide reasonably accurate results, they cannot incorporate the influence of external forces, which can have a big impact on our climate and which may even lead to extreme events. An example of such an event is the Carrington event in August-September 1859, which resulted in telegraph failures all over Northern America and Europe and produced visible aurorae as far south as Cuba and Hawaii. Another example is a flare which occurred in March 1989, when power was knocked out across most of the Quebec province in Canada. Recently, much attention has focused upon increasing our understanding of the Carrington event, in order to better quantify what extreme space events can do to our current technological society (Rodger, Verronen, Clilverd, Seppälä, & Turunen, 2008). Events of this magnitude can also lead to satellite breakdown, with high associated financial costs. In addition, recent predictions indicate that such extreme events will be more likely over the coming decades (Thomas, Arkenberg, Snyder, & Brock, 2011).

A number of papers have attempted to model instances of large solar flares. During solar flares, highly energized protons can ionize air molecules, which then produces fast secondary electrons (Calisto, Verronen, Rozanov, & Peter, 2012). These electrons can then dissociate the nitrogen molecule. This results in the depletion of the total

ozone column, acceleration of the zonal winds in polar jets, as well as in the cooling of surface air temperatures.

In order to investigate an effect of solar flares on the Earth, the certain increased ionization rates were assigned at different altitudes. For the flares which occurred during the satellite era, the rates were obtained from direct measurements (Jackman et al., 1995; Verronen et al., 2005). In order to simulate solar flares which occurred before the spacecraft era, the rates of ionisation were either scaled up from the known events to an estimated intensity (Thomas, Jackman, & Melott, 2007), or were taken from the ice core nitrate levels (Rodger, et al., 2008).

In some models the ionisation rates were assumed to be distributed uniformly beyond the 60° latitudinal belts (Thomas, et al., 2007). In other approaches (e.g., (Thomas, et al., 2011)), an ionisation rate scale factor averaged over longitude and dependent on latitude and time was applied. After assigning the ionisation rates in this manner, the model was run under specified conditions. The different chemical reactions which occur in the atmosphere and the transport processes are modelled. However, this approach does not take into account the orientation of the external forces (for example it would be reasonable to expect that one side of the Earth is affected more than the other), since a uniform latitudinal distribution was used.

Attention has also been paid to other forms of space activity, such as gamma-ray bursts (Thomas et al., 2005), cosmic rays (Carslaw, Harrison, & Kirkby, 2002; Usoskin & Kovaltsov, 2006) and the effect of the appearance of supernovas (Thomas, Melott, Fields, & Anthony-Twarog, 2008). However, as for the modelling of solar flares, these effects were not incorporated directly into climate models. Instead, it was mainly their likely effect on ionization rates which was modelled in a very approximate manner and then built into existing climate models.

In this thesis, we propose a space perspective of modelling insolation in contrast to the existing methods which use the earth's point of view. We aim to model incoming radiation as a flux coming from the space. This will allow for explicit incorporation of the impact of space activity on the Earth, such as solar flares, cosmic rays etc. in the future. In addition, it will allow modellers to take into account the orientation of the external forces. The derivation of the model uses the methods of vector field theory and surface integrals (see Chapter 2).

The developed model then will be incorporated into the EMIC C-GOLDSTEIN for testing. The C-COLDSTEIN model was chosen since it is open source and readily available to researchers, unlike many other global climate models. It does not have the seasonal variations of insolation in its original form. The details of the incorporation into C-GOLDSTEIN are presented in Chapter 3.

Chapter 2 Novel Insolation Model

In this chapter, we give a detailed development of a new model to calculate the insolation across latitudinal belts at any time of the year. In contrast to the existing methods which use the Earth's point of view, we model the incoming insolation from the space perspective. This will be a good basis for incorporating the impact of space activity, such as solar flares, radiation etc. In Section 2.1, we provide a general description of the model, such as describing the coordinate planes, introducing the notations used, deriving the main equations, and describing the main idea of the modelling approach. In Sections 2.2-2.3, we present the illumination areas for the Northern and the Southern Hemisphere latitudinal belts, respectively. In Section 2.4, we describe the calculation of the radiation. In Sections 2.5-2.6, we provide the limits of integration for the Northern and Southern Hemisphere, respectively. In Section 2.7, we describe an approximation technique which we applied to the boundaries of the integration region in order to facilitate computation. In Section 2.8, we describe the formulation of the area of the latitudinal belt. In Section 2.9, we describe the technique for calculating the total insolation within a latitudinal belt and present the results.

2.1. Model description

Consider Figure 2.1.

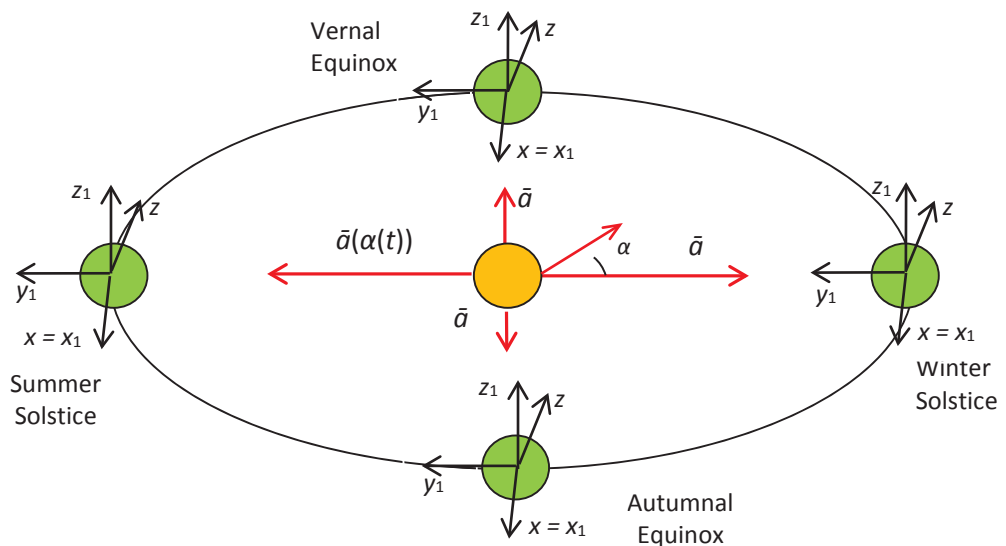


Fig. 2.1 Coordinate systems and radiation vector (annual cycle).

Here the radiation vector is $\bar{a}(\alpha(t)) = [F \sin(\alpha(t)), -F \cos(\alpha(t)), 0]$, $F = 1367 \text{ Wt/m}^2$

is the solar constant, and $\alpha(t) \in [0^\circ, 360^\circ]$ is the angle of the Earth's rotation around the Sun, where $\alpha=0$ corresponds to the winter solstice. The Earth orbit was assumed to be circular for the purpose of modelling.

The (x, y, z) coordinate axes are aligned with the equatorial plane. The OZ axis represents the Earth's axis of rotation and OY is in the Earth's equatorial plane. The (x_1, y_1, z_1) axes are aligned with the ecliptic plane and this is inclined to the equatorial plane by an obliquity angle which is $\varepsilon = 23^\circ 26'$ under present astronomical conditions. This coordinate system remains fixed as the Earth rotates around the Sun.

All the calculations are performed in the (x_1, y_1, z_1) coordinates. The reason for this choice is that the formulation of the radiation vector \bar{a} remains the same as the Earth rotates around the Sun.

The following notations were used to denote the centres of the ellipses (Figure 2.2). We should note the Earth is assumed to be exactly spherical in our formulation.

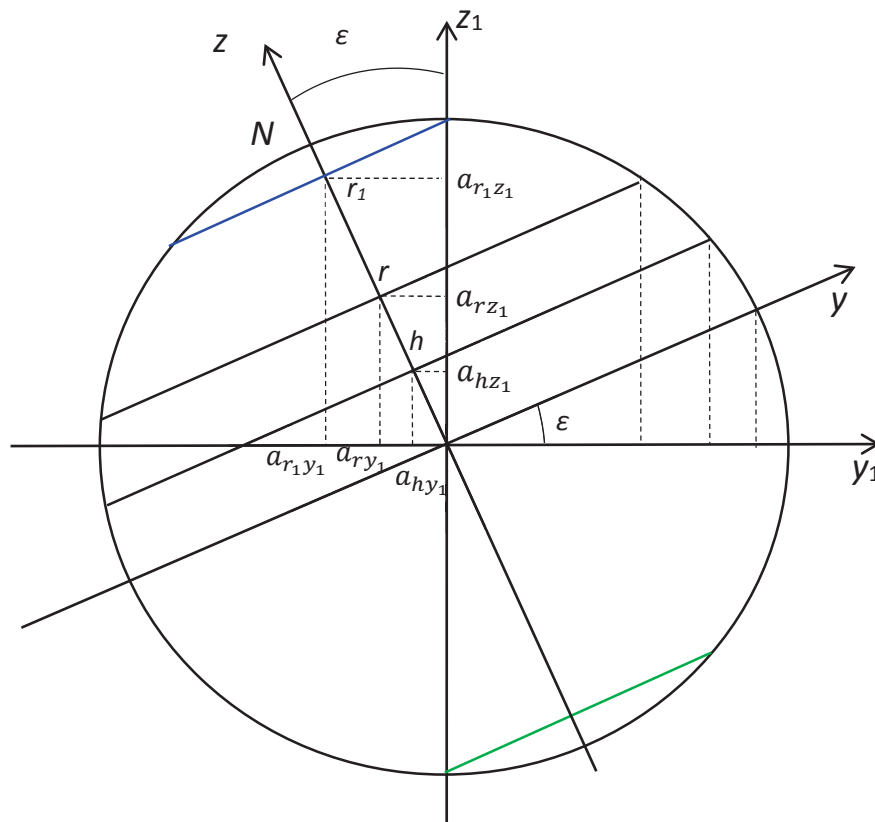


Fig. 2.2 The coordinates of the centre of the ellipses.

Here the angle ε is the obliquity angle, R is the Earth's radius, r , h and r_1 are the perpendicular distances from the equatorial plane to the upper and lower latitude limits of the belt and to the polar belt, respectively. From Figure 2.2, it can be determined

that

$$a_{r_1 z_1} = r_1 \cos(\varepsilon),$$

$$a_{r z_1} = r \cos(\varepsilon),$$

$$a_{h z_1} = h \cos(\varepsilon),$$

$$a_{r_1 y_1} = -r_1 \sin(\varepsilon),$$

$$a_{r y_1} = -r \sin(\varepsilon),$$

$$a_{h y_1} = -h \sin(\varepsilon).$$

The amount of light which is received by any particular area changes throughout the year. In the current approach it is modelled by an ellipse which changes with time since it is determined by α . An ellipse change affects the change of size of the hatched area of the latitudinal belt (see Figure 2.3).

The following projection planes were obtained (Figures 2.3-2.5).

In Figure 2.3 the black hatched area is the area receiving sunlight. The red hatched area is the area of a latitudinal belt receiving sunlight, which is referred as the illumination area from this point onwards. The equations of the ellipse, circle, lower, upper and polar latitudinal belt are presented in terms of the notations introduced above.

The projection of the latitudinal belt obtained in the X_1OZ_1 coordinate plane forms an ellipse.

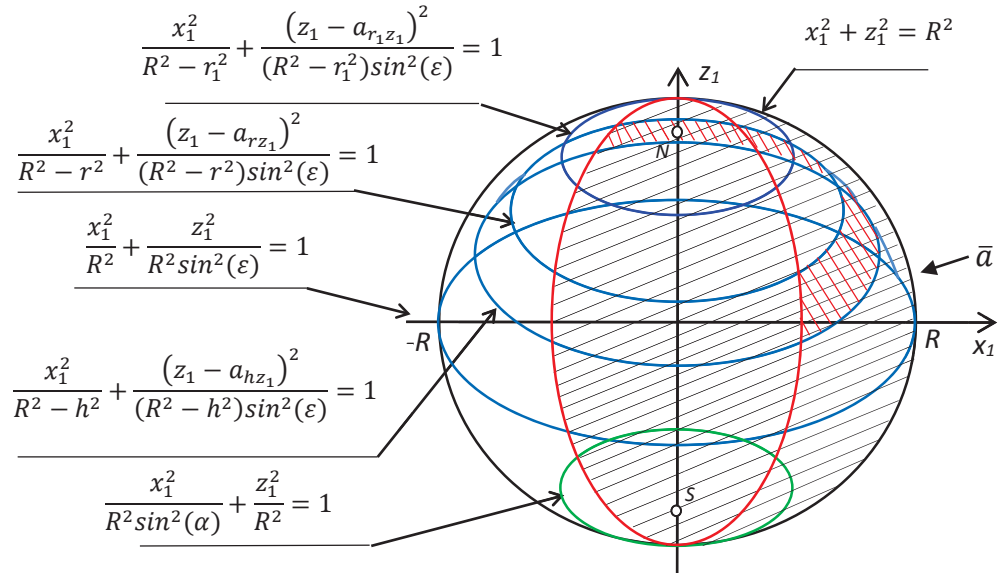


Fig. 2.3 The projection of a latitudinal belt in X_1OZ_1 coordinate plane.

The projection of the latitudinal belt obtained in the Y_1OZ_1 coordinate plane forms a nearly trapezoidal region.

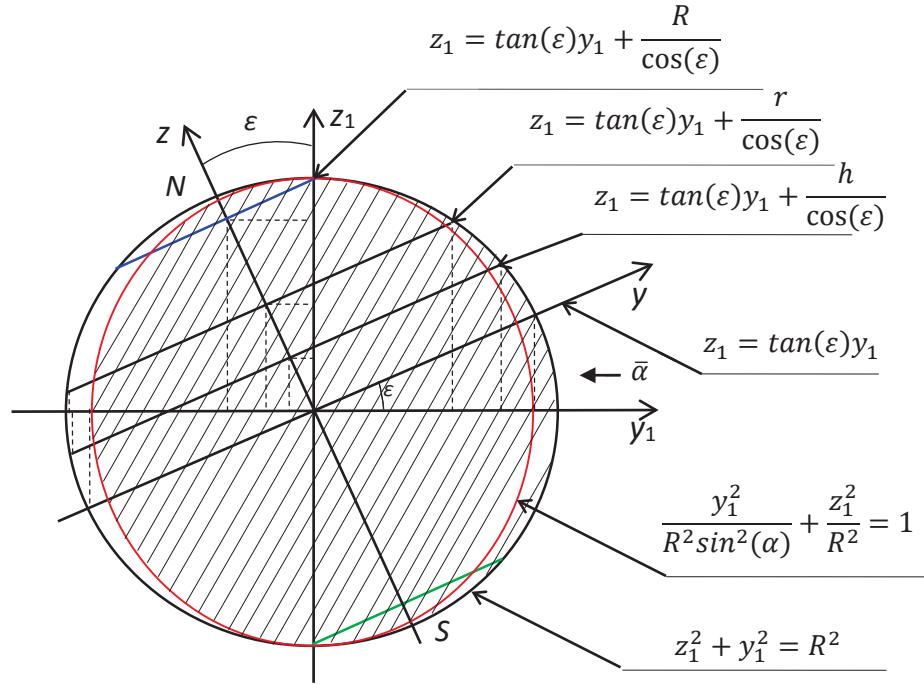


Fig. 2.4 The projection of a latitudinal belt in Y_1OZ_1 coordinate plane.

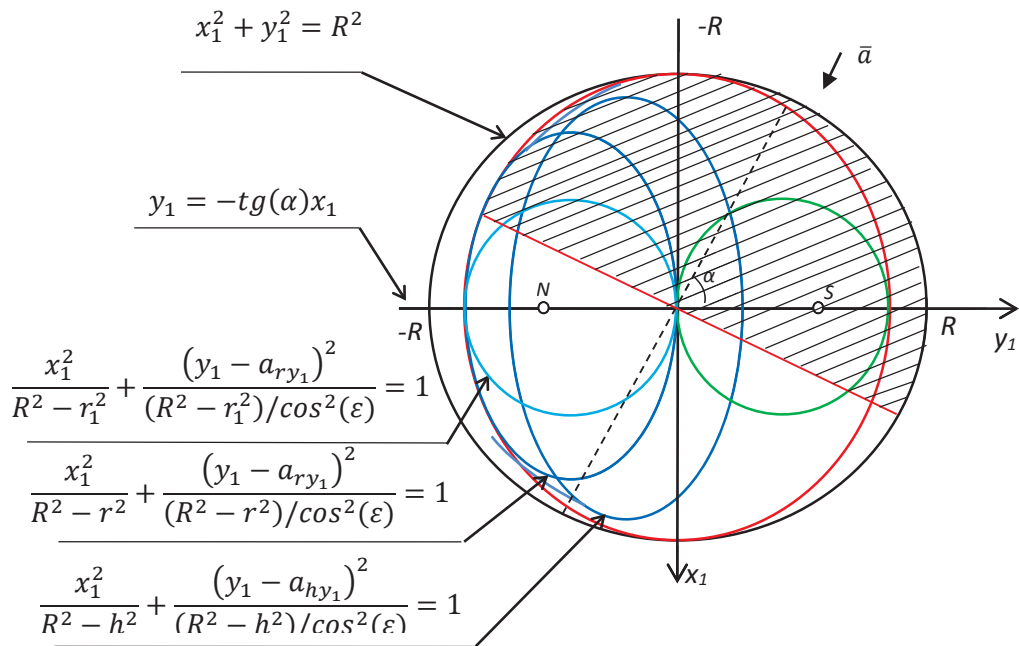


Fig. 2.5 The projection of a latitudinal belt in X_1OY_1 coordinate plane.

The projections of the latitudinal belt in the X_1OY_1 coordinate plane also form ellipses. The Y_1OZ_1 plane was chosen for projecting a latitudinal belt in the (x_1, y_1, z_1) coordinate frame. Clearly, the projections obtained in that plane are the easiest for calculations (see Figure 2.4). The ellipses obtained as the projections of the latitudinal belts in the

two other planes (Figure 2.3 and Figure 2.5) are considerably more difficult to use for computations.

In Figure 2.6, we show the direction of the radiation vector from the Earth's point of view. Here \bar{n} denotes the outward unit normal vector.

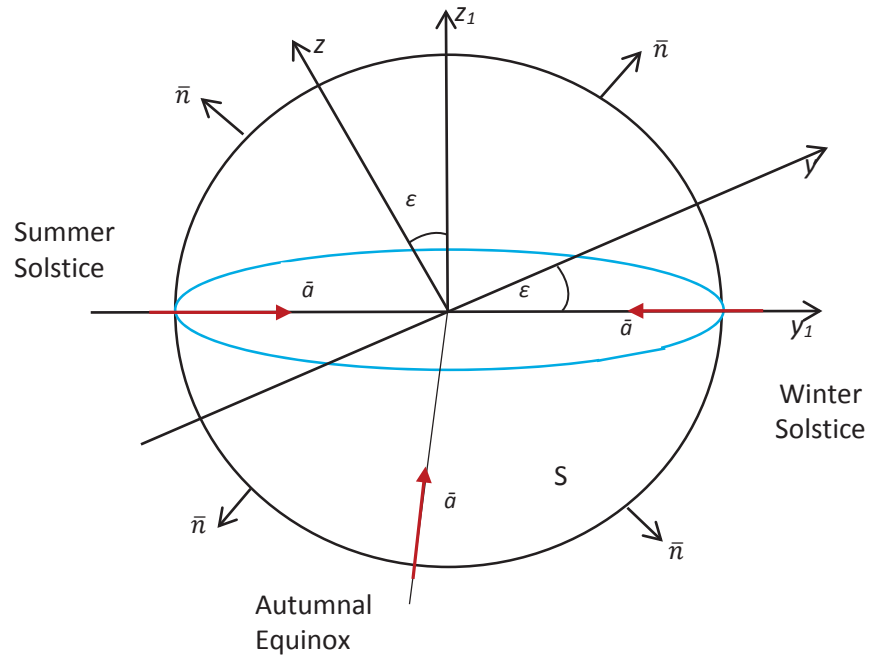


Fig. 2.6 The direction of the radiation vector from the Earth's point of view and the surface orientation.

The positively-oriented surface (S^+) in the chosen projection plane is the part of the sphere closer to the observer. The negatively-oriented surface (S^-) is the part of the sphere pointing away from the observer.

Sunlight is received by both sides of the surface. However, for the computations this needs to be spread into two parts. The illumination area for a positively-oriented surface and for a negatively-oriented surface for a certain belt is introduced in Figure 2.7.

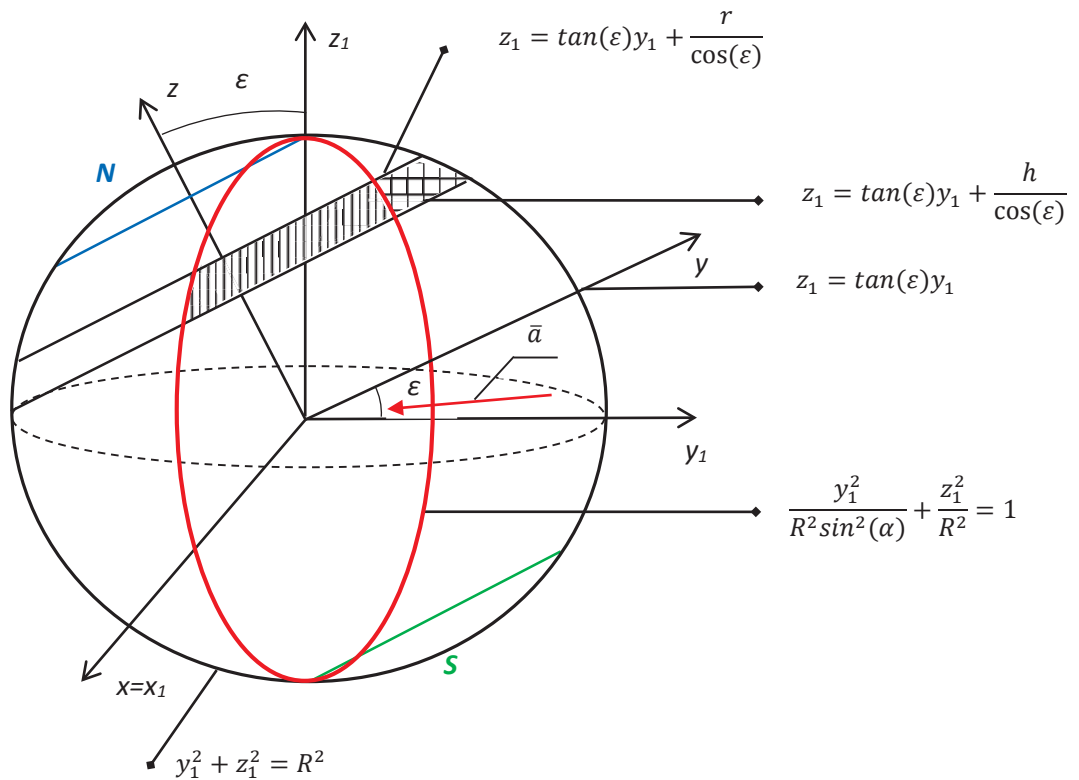


Fig. 2.7 The illumination area for a positively-oriented surface and for a negatively-oriented surface for the latitudinal belt.

In Figure 2.7, the forward- hatched illumination area is on the negatively-oriented surface, so it is a strip coming from the side located further from the observer (D^-). The back- hatched illumination area is on the positively-oriented surface, which is a small piece on the side located closer to the observer (D^+).

For different latitudes the light boundaries will be different. In addition, they may vary with time for some latitudinal belts. In order to model this, the angle β was assigned in terms of an obliquity angle (ϵ) and the angle of the Earth's rotation around the Sun (α) (see Figure 2.8).

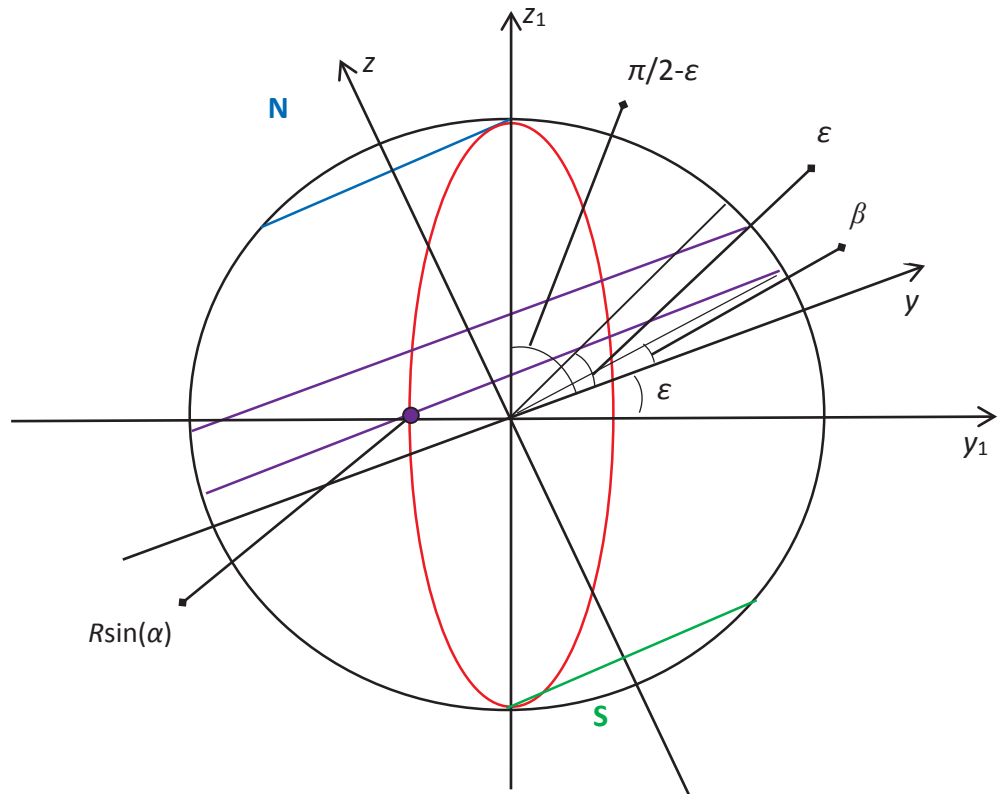


Fig. 2.8 The determination of illumination areas for different latitudinal belts.

In Figure 2.8:

$$\sin(\beta) = \sin(\epsilon)\sin(\alpha),$$

$$\beta^\circ = \frac{180^\circ}{\pi} \arcsin(\sin(\alpha) \sin(\epsilon)).$$

The computations were performed for the period of time from the winter solstice to the vernal equinox. This corresponds to the first quadrant of the imaginary circle (Figure 2.1), where the angle β ranges from 0° to $23^\circ 26'$. For the other three quarters of the year, we simply rearrange the results obtained from the first set of computations. A more detailed description of this process is given later in Section 2.8.

From Figure 2.8, one can determine that the angle β can be less than or equal to the angle ϵ . The illumination area is different for these two cases. Also, the latitudinal belts can be located above the angle ϵ or above the polar circle ($90^\circ - \epsilon$). For these cases the area differs as well. Thus, there can be four possible types of illumination areas which are listed below. In addition, as time progresses, the point $R\sin(\alpha)$ shifts along the y_1 coordinate axes (Figure 2.8) and may result in the illumination area changing from one type to another for some latitudinal belts.

The four types are characterized as:

$$0 - \beta,$$

$$\beta - \varepsilon,$$

$$\varepsilon - \left(\frac{\pi}{2} - \varepsilon\right),$$

$$\left(\frac{\pi}{2} - \varepsilon\right) - \frac{\pi}{2}.$$

The illumination areas for each latitudinal belt for the period of time from the winter solstice to the vernal equinox are given in Tables 2.1-2.2.

Table 2.1 The illumination areas for 0°-50° latitudinal belts for the period of time from the winter solstice to the vernal equinox.

α	Latitudinal belt				
	0°-10°	10°-20°	20°-30°	30°-40°	40°-50°
10°	$\beta-\varepsilon$	$\beta-\varepsilon$	$\varepsilon-(\pi/2-\varepsilon)$	$\varepsilon-(\pi/2-\varepsilon)$	$\varepsilon-(\pi/2-\varepsilon)$
20°	$0-\beta$	$\beta-\varepsilon$	$\varepsilon-(\pi/2-\varepsilon)$	$\varepsilon-(\pi/2-\varepsilon)$	$\varepsilon-(\pi/2-\varepsilon)$
30°	$0-\beta$	$\beta-\varepsilon$	$\varepsilon-(\pi/2-\varepsilon)$	$\varepsilon-(\pi/2-\varepsilon)$	$\varepsilon-(\pi/2-\varepsilon)$
40°	$0-\beta$	$\beta-\varepsilon$	$\varepsilon-(\pi/2-\varepsilon)$	$\varepsilon-(\pi/2-\varepsilon)$	$\varepsilon-(\pi/2-\varepsilon)$
50°	$0-\beta$	$0-\beta$	$\varepsilon-(\pi/2-\varepsilon)$	$\varepsilon-(\pi/2-\varepsilon)$	$\varepsilon-(\pi/2-\varepsilon)$
60°	$0-\beta$	$0-\beta$	$\varepsilon-(\pi/2-\varepsilon)$	$\varepsilon-(\pi/2-\varepsilon)$	$\varepsilon-(\pi/2-\varepsilon)$
70°	$0-\beta$	$0-\beta$	$\varepsilon-(\pi/2-\varepsilon)$	$\varepsilon-(\pi/2-\varepsilon)$	$\varepsilon-(\pi/2-\varepsilon)$
80°	$0-\beta$	$0-\beta$	$\varepsilon-(\pi/2-\varepsilon)$	$\varepsilon-(\pi/2-\varepsilon)$	$\varepsilon-(\pi/2-\varepsilon)$
90°	$0-\beta$	$0-\beta$	$\varepsilon-(\pi/2-\varepsilon)$	$\varepsilon-(\pi/2-\varepsilon)$	$\varepsilon-(\pi/2-\varepsilon)$

Table 2.2 The illumination areas for 50°-90° latitudinal belts for the period of time from the winter solstice to the vernal equinox.

α	Latitudinal belt			
	50°-60°	60°-70°	70°-80°	80°-90°
10°	$\varepsilon-(\pi/2-\varepsilon)$	$\varepsilon-(\pi/2-\varepsilon)$	$(\pi/2-\varepsilon)-\pi/2$	$(\pi/2-\varepsilon)-\pi/2$
20°	$\varepsilon-(\pi/2-\varepsilon)$	$\varepsilon-(\pi/2-\varepsilon)$	$(\pi/2-\varepsilon)-\pi/2$	$(\pi/2-\varepsilon)-\pi/2$
30°	$\varepsilon-(\pi/2-\varepsilon)$	$\varepsilon-(\pi/2-\varepsilon)$	$(\pi/2-\varepsilon)-\pi/2$	$(\pi/2-\varepsilon)-\pi/2$
40°	$\varepsilon-(\pi/2-\varepsilon)$	$\varepsilon-(\pi/2-\varepsilon)$	$(\pi/2-\varepsilon)-\pi/2$	$(\pi/2-\varepsilon)-\pi/2$
50°	$\varepsilon-(\pi/2-\varepsilon)$	$\varepsilon-(\pi/2-\varepsilon)$	$(\pi/2-\varepsilon)-\pi/2$	$(\pi/2-\varepsilon)-\pi/2$
60°	$\varepsilon-(\pi/2-\varepsilon)$	$\varepsilon-(\pi/2-\varepsilon)$	$(\pi/2-\varepsilon)-\pi/2$	$(\pi/2-\varepsilon)-\pi/2$
70°	$\varepsilon-(\pi/2-\varepsilon)$	$\varepsilon-(\pi/2-\varepsilon)$	$(\pi/2-\varepsilon)-\pi/2$	$(\pi/2-\varepsilon)-\pi/2$
80°	$\varepsilon-(\pi/2-\varepsilon)$	$\varepsilon-(\pi/2-\varepsilon)$	$(\pi/2-\varepsilon)-\pi/2$	$(\pi/2-\varepsilon)-\pi/2$
90°	$\varepsilon-(\pi/2-\varepsilon)$	$\varepsilon-(\pi/2-\varepsilon)$	$(\pi/2-\varepsilon)-\pi/2$	$(\pi/2-\varepsilon)-\pi/2$

It should be noted that sometimes the angle β lies within the latitudinal belts. In these cases, that illumination area which results in the greater overlap with the latitudinal belt is chosen.

2.2. The illumination area for the Northern Hemisphere latitudinal belts

The illumination area change for all the latitudinal belts is illustrated in Figures 2.9-2.17. In each of the following figures (except Figure 2.9), the graphs in cases a-c are shown for the values of $\alpha=20^\circ$, $\alpha=40^\circ$ and $\alpha=60^\circ$, respectively. In the Figure 2.9, the first case corresponds to $\alpha=10^\circ$ instead. This was done in order to better demonstrate the change of the illumination area for some latitudinal belts with time.

The illumination area change for the 0° - 10° latitudinal belt is illustrated in Figure 2.9. For this latitudinal belt the illumination starts from the type β - ε and then changes to the type 0 - β , with no further change until the vernal equinox.

The illumination area change for the 10° - 20° latitudinal belt is illustrated in Figure 2.10. Here the illumination area also starts from the β - ε type which remains for a while and then shifts to the 0 - β type (similar to the previous case).

For the area lying between 23° (ε) and 67° (the polar circle), the illumination area remains $\varepsilon - (\pi/2 - \varepsilon)$ for the whole period observed. However, since a 10° division was used this illumination area has been applied for all the latitudinal belts lying between 20° and 70° . This is shown in Figures 2.11–2.15.

The illumination areas for the 70° - 80° and 80° - 90° latitudinal belts are illustrated in Figures 2.16-2.17. For polar latitudes the illumination area is $(\pi/2 - \varepsilon) - \pi/2$ or there is no radiation received at all (polar night).

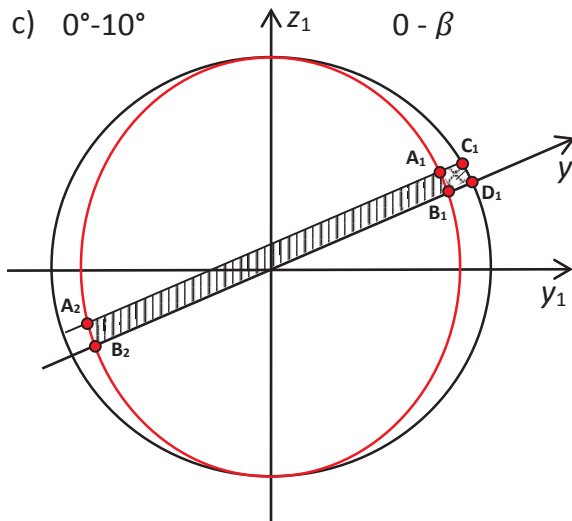
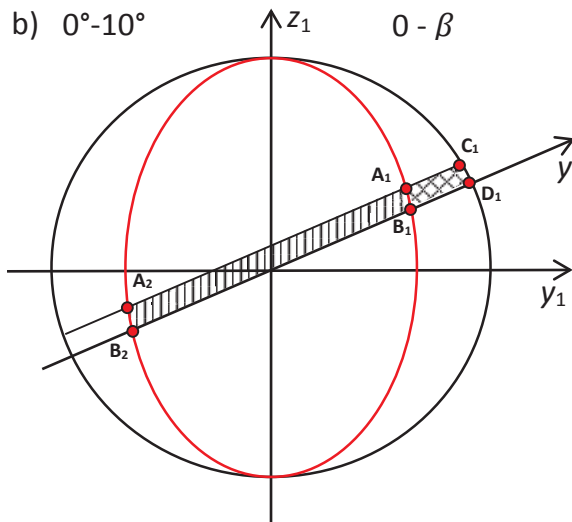
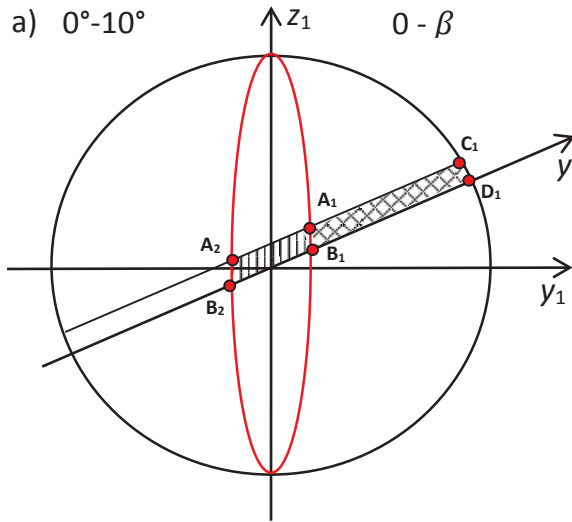


Fig. 2.9 Illumination areas for $0^\circ-10^\circ\text{N}$ latitudinal belt for $\alpha=10^\circ$, $\alpha=40^\circ$ and $\alpha=60^\circ$ (a-c)

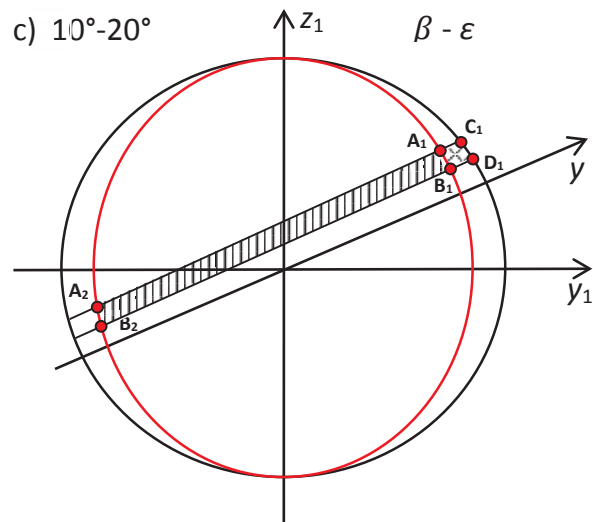
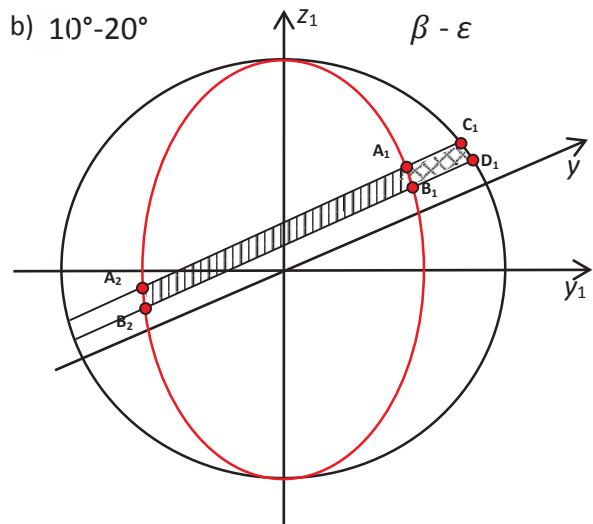
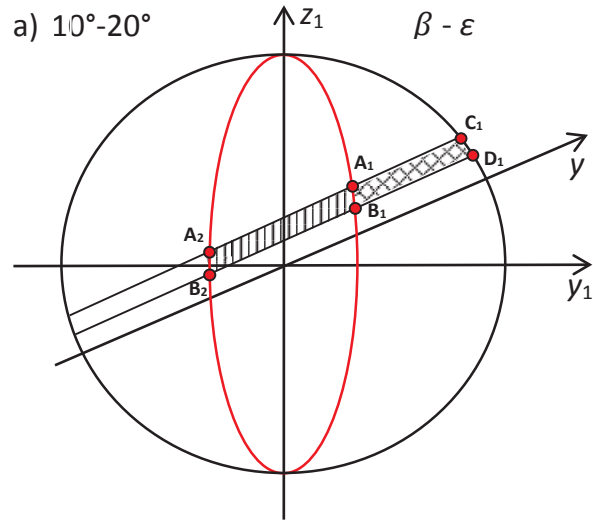


Fig. 2.10 Illumination areas for $10^{\circ}-20^{\circ}$ N latitudinal belt for $\alpha=20^{\circ}$, $\alpha=40^{\circ}$ and $\alpha=60^{\circ}$ (a-c)

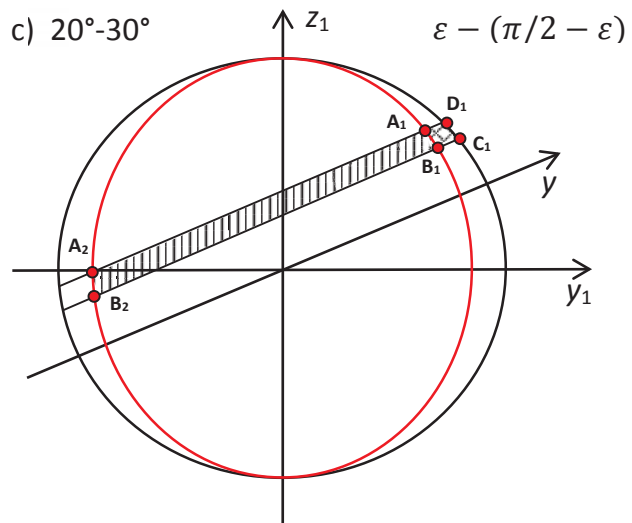
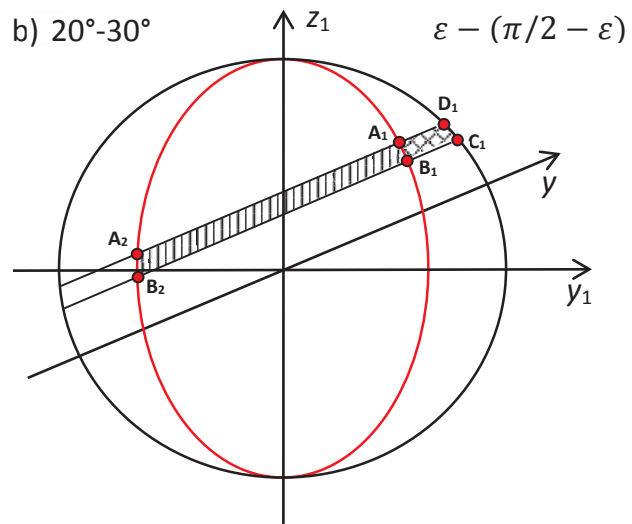
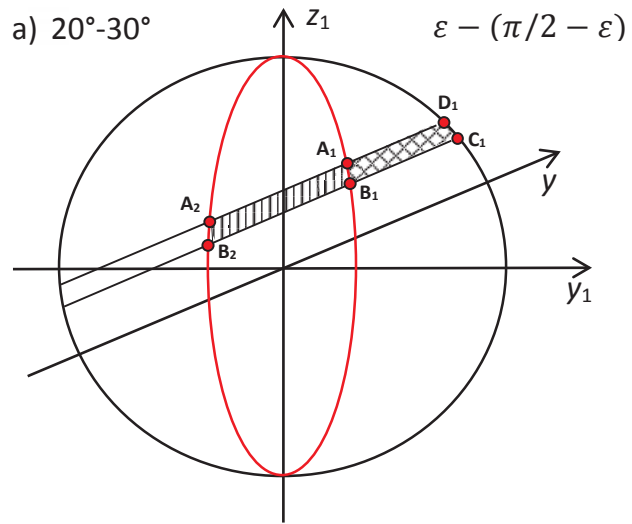


Fig. 2.11 Illumination areas for $20^{\circ}\text{-}30^{\circ}\text{N}$ latitudinal belt for $\alpha=20^{\circ}$, $\alpha=40^{\circ}$ and $\alpha=60^{\circ}$ (a-c)

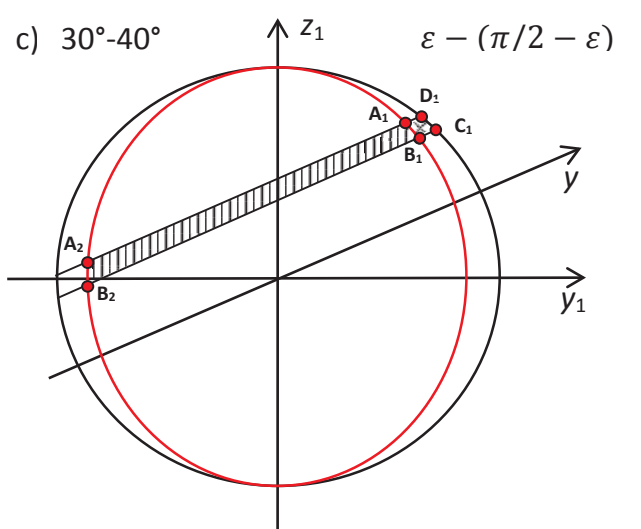
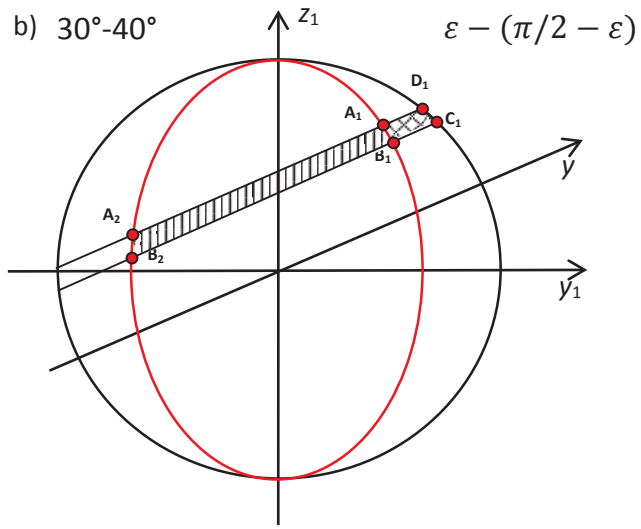
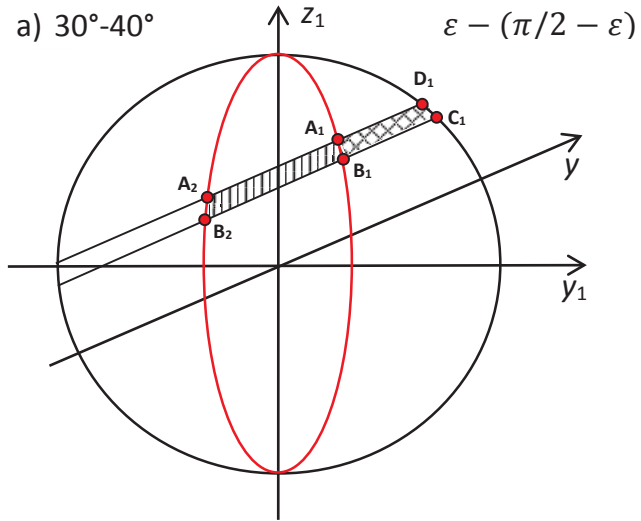


Fig. 2.12 Illumination areas for $30^\circ\text{-}40^\circ\text{N}$ latitudinal belt for $\alpha=20^\circ$, $\alpha=40^\circ$ and $\alpha=60^\circ$ (a-c)

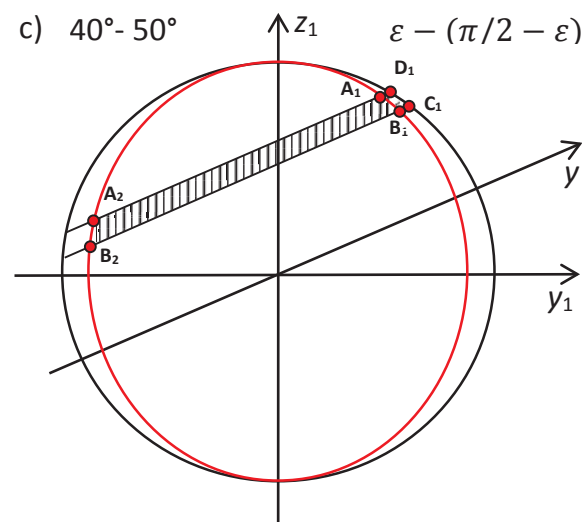
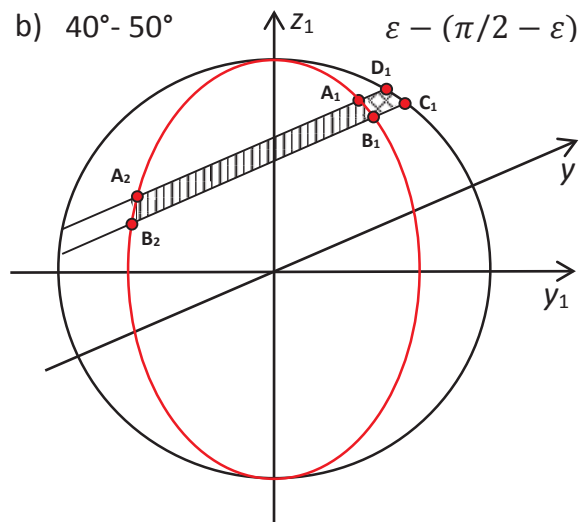
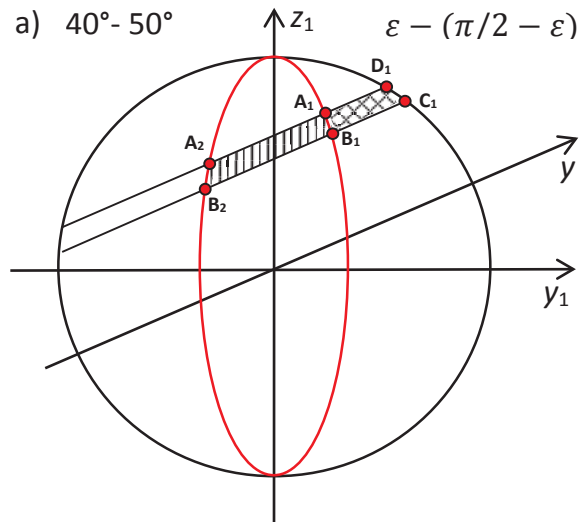


Fig. 2.13 Illumination areas for $40^\circ - 50^\circ$ N latitudinal belt for $\alpha=20^\circ$, $\alpha=40^\circ$ and $\alpha=60^\circ$ (a-c)

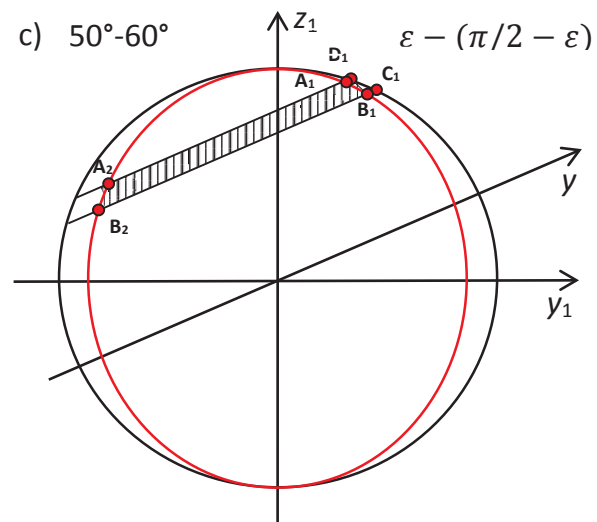
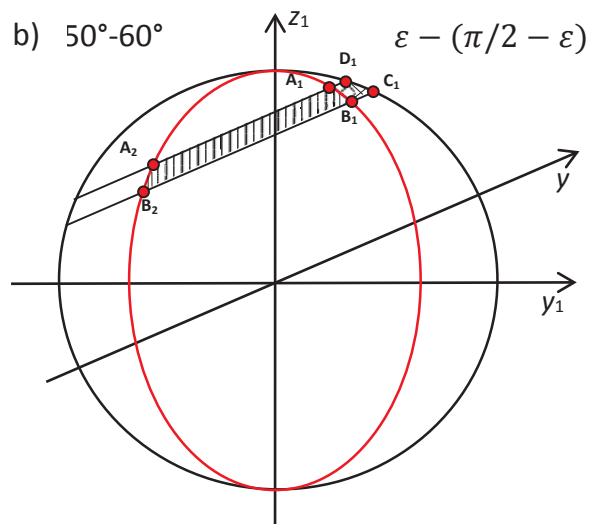
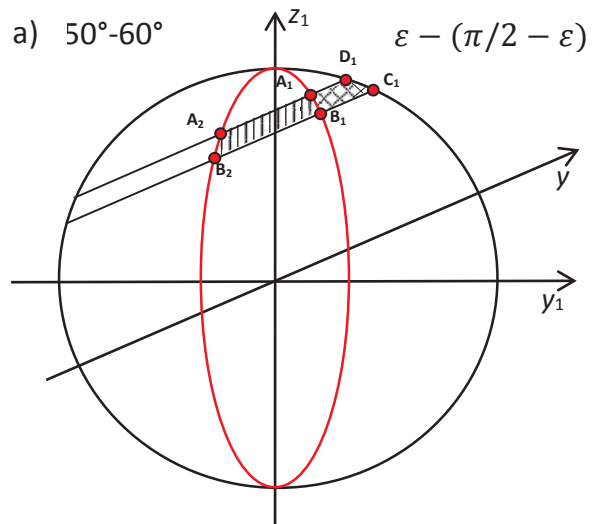


Fig. 2.14 Illumination areas for $50^{\circ}\text{-}60^{\circ}\text{N}$ latitudinal belt for $\alpha=20^{\circ}$, $\alpha=40^{\circ}$ and $\alpha=60^{\circ}$ (a-c)

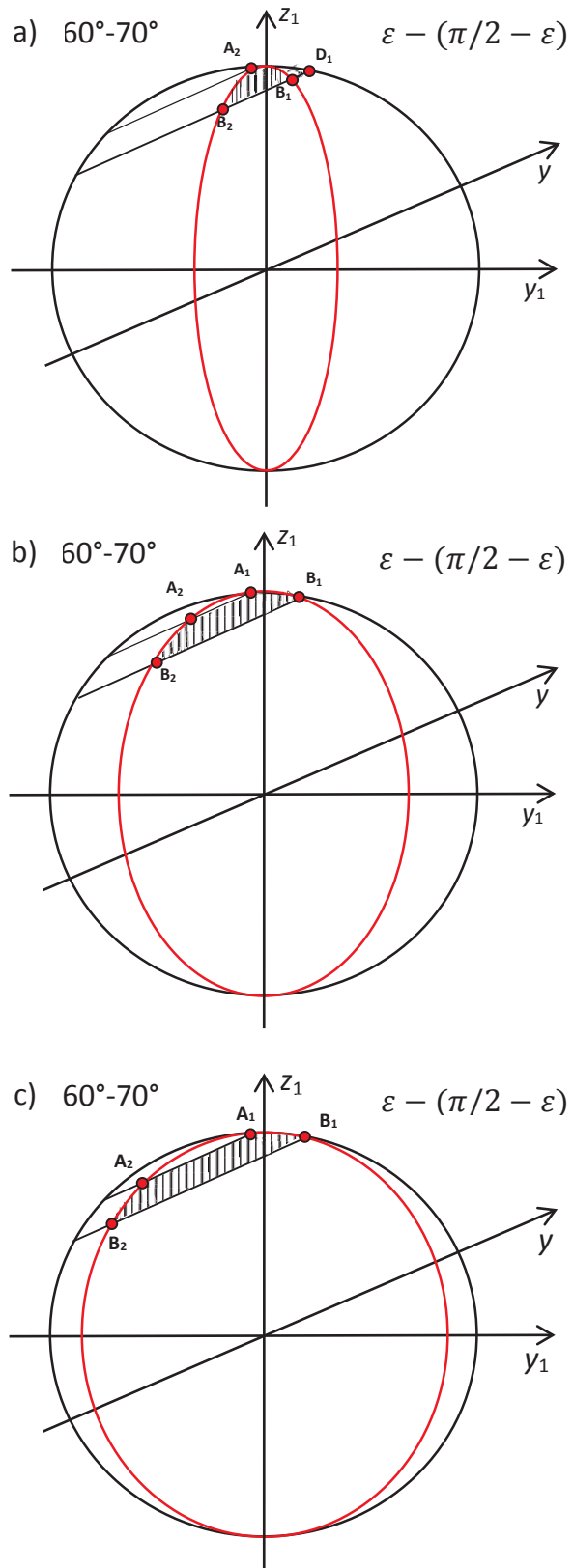


Fig. 2.15 Illumination areas for $60^\circ-70^\circ\text{N}$ latitudinal belt for $\alpha=20^\circ$, $\alpha=40^\circ$ and $\alpha=60^\circ$

(a-c)

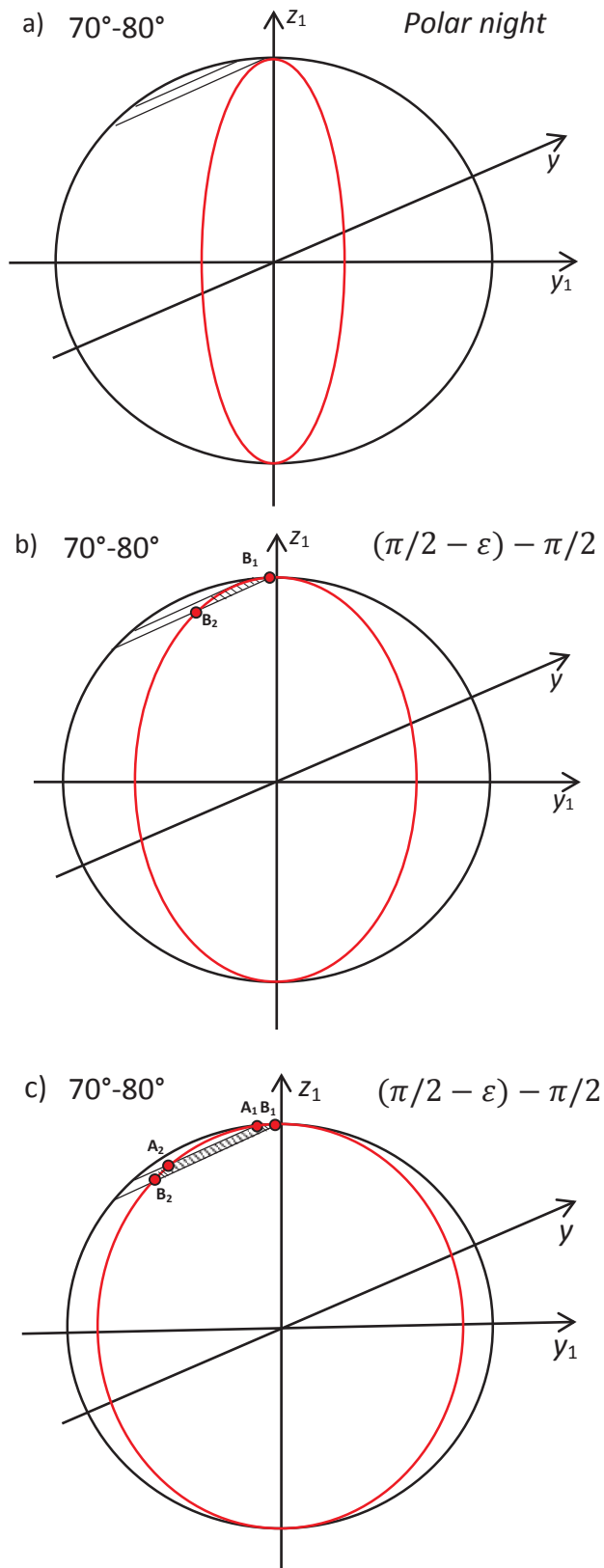


Fig. 2.16 Illumination areas for $70^\circ-80^\circ\text{N}$ latitudinal belt for $\alpha=20^\circ$, $\alpha=40^\circ$ and $\alpha=60^\circ$ (a-c)

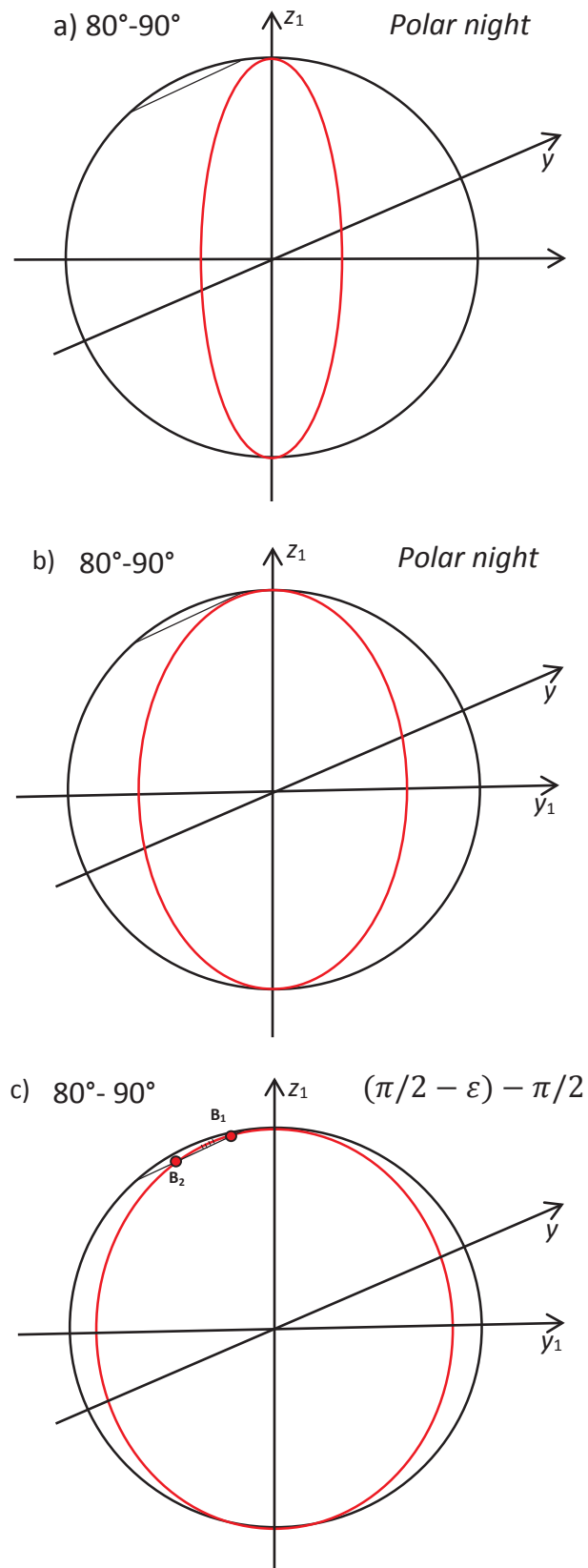


Fig. 2.17 Illumination areas for $80^\circ-90^\circ\text{N}$ latitudinal belt for $\alpha=20^\circ$, $\alpha=40^\circ$ and $\alpha=60^\circ$ (a-c)

2.3. The illumination areas for the Southern Hemisphere latitudinal belts

The illumination areas for the Southern Hemisphere obey different rules. For all the latitudinal belts from the equator to 40° inclusively there is one type of illumination area (referred as C_2-D_2 from this point onwards). An example for $30^\circ-40^\circ$ latitudinal belt is introduced in Figure 2.18. Here we can see that the same type of the illumination area remains for the whole period observed.

For all the latitudinal belts lying between 40° and 67° (due to the 10° steps, 70° was actually used) there is a different type of illumination area (further referred as D_2-C_2). An example for D_2-C_2 illumination area is introduced in Figure 2.19. In this case we can also see that there are no changes in the type of illumination area.

The examples for the polar areas are introduced in Figures 2.20-2.21. Here we can notice that the type of illumination area is different for $70^\circ-80^\circ$ and $80^\circ-90^\circ$ latitudinal belts and also changes with time. Starting from polar day at the winter solstice, the amount of radiation is being reduced gradually as the time progresses to the vernal equinox.

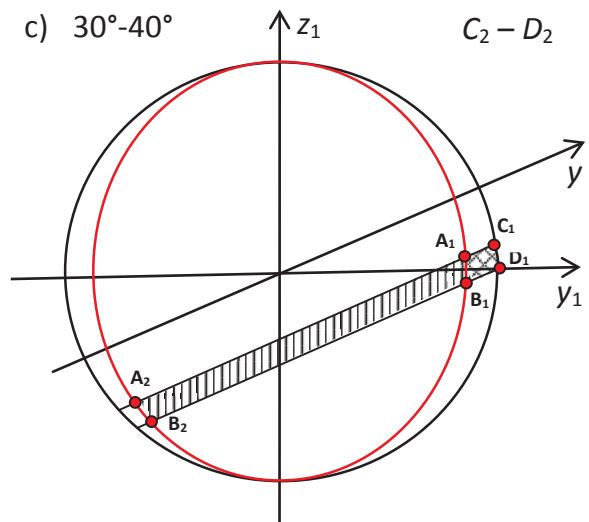
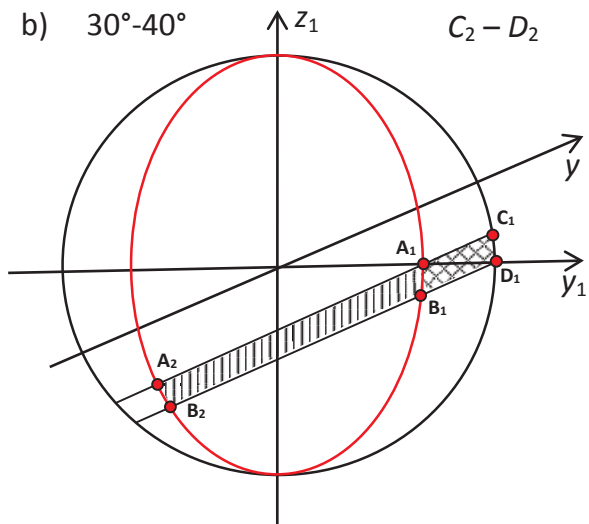
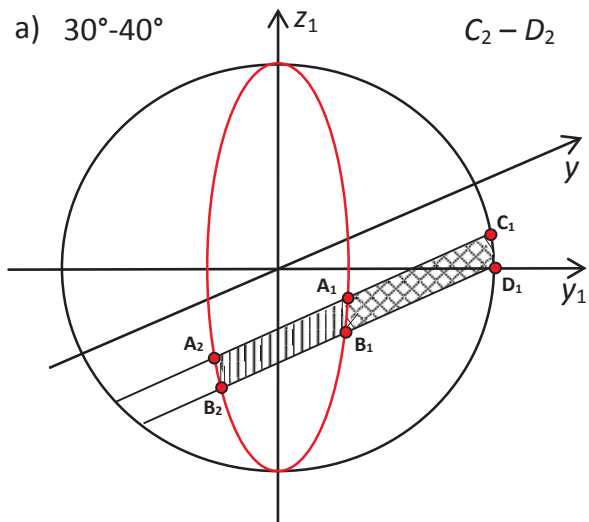


Fig. 2.18 Illumination areas for $30^{\circ}-40^{\circ}$ S latitudinal belt for $\alpha=20^{\circ}$, $\alpha=40^{\circ}$ and $\alpha=60^{\circ}$ (a-c)

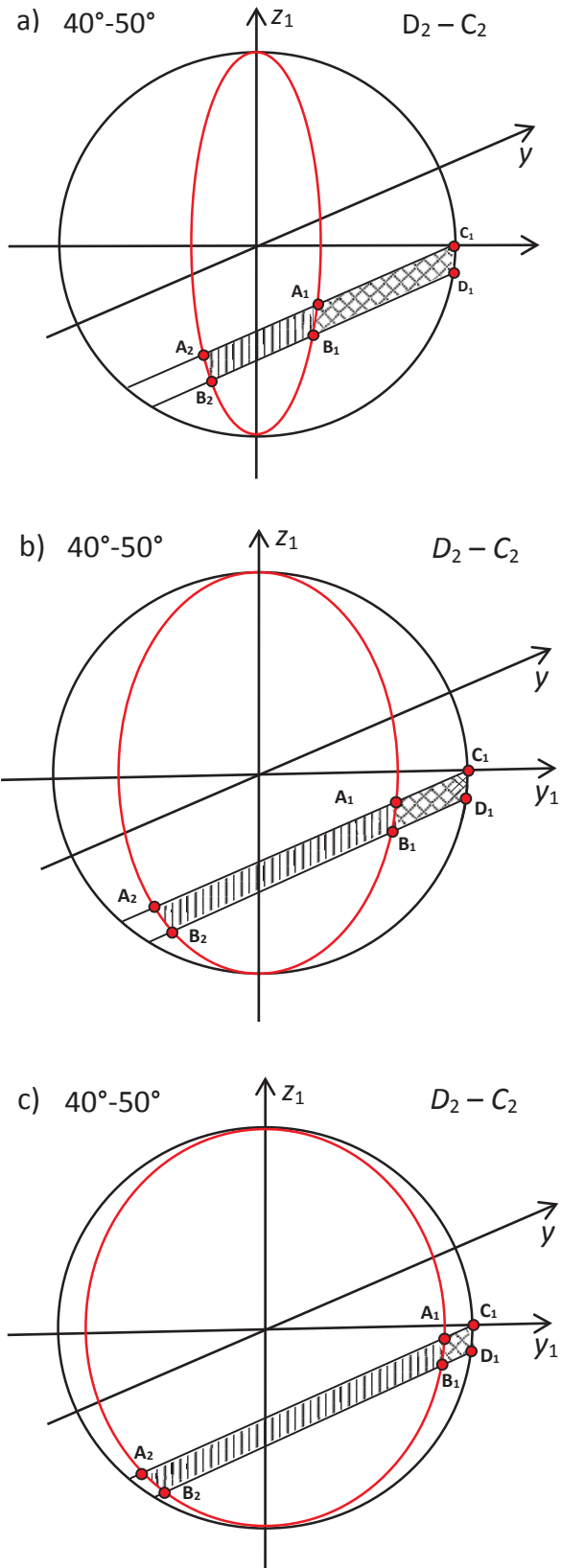


Fig. 2.19 Illumination areas for $40^{\circ}-50^{\circ}$ S latitudinal belt for $\alpha=20^{\circ}$, $\alpha=40^{\circ}$ and $\alpha=60^{\circ}$ (a-c)

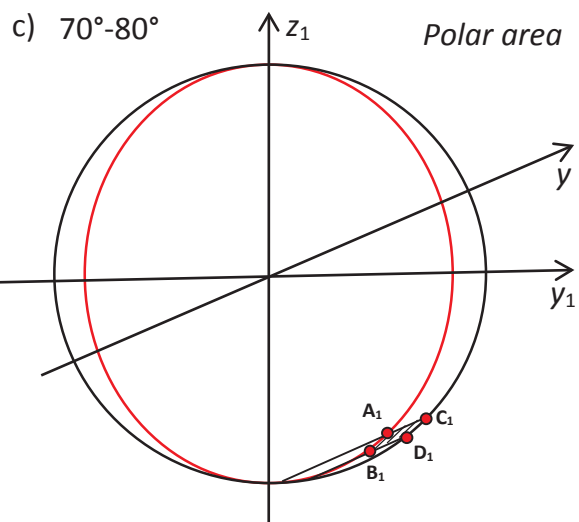
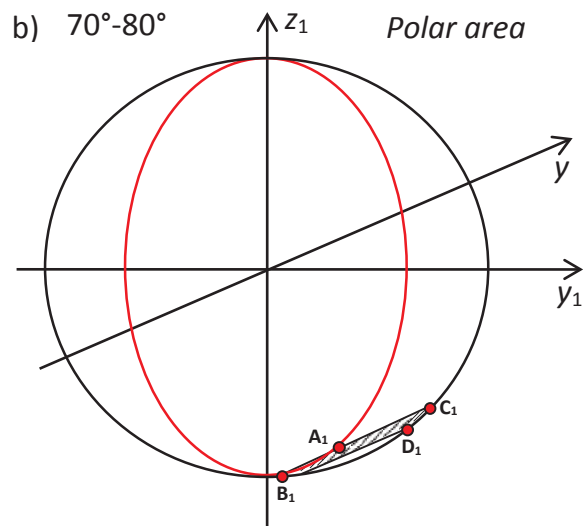
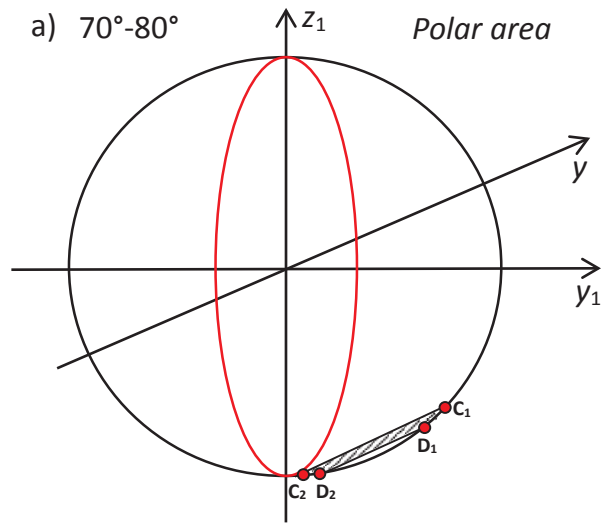


Fig. 2.20 Illumination areas for 70° - 80° S latitudinal belt for $\alpha=20^{\circ}$, $\alpha=40^{\circ}$ and $\alpha=60^{\circ}$ (a-c)

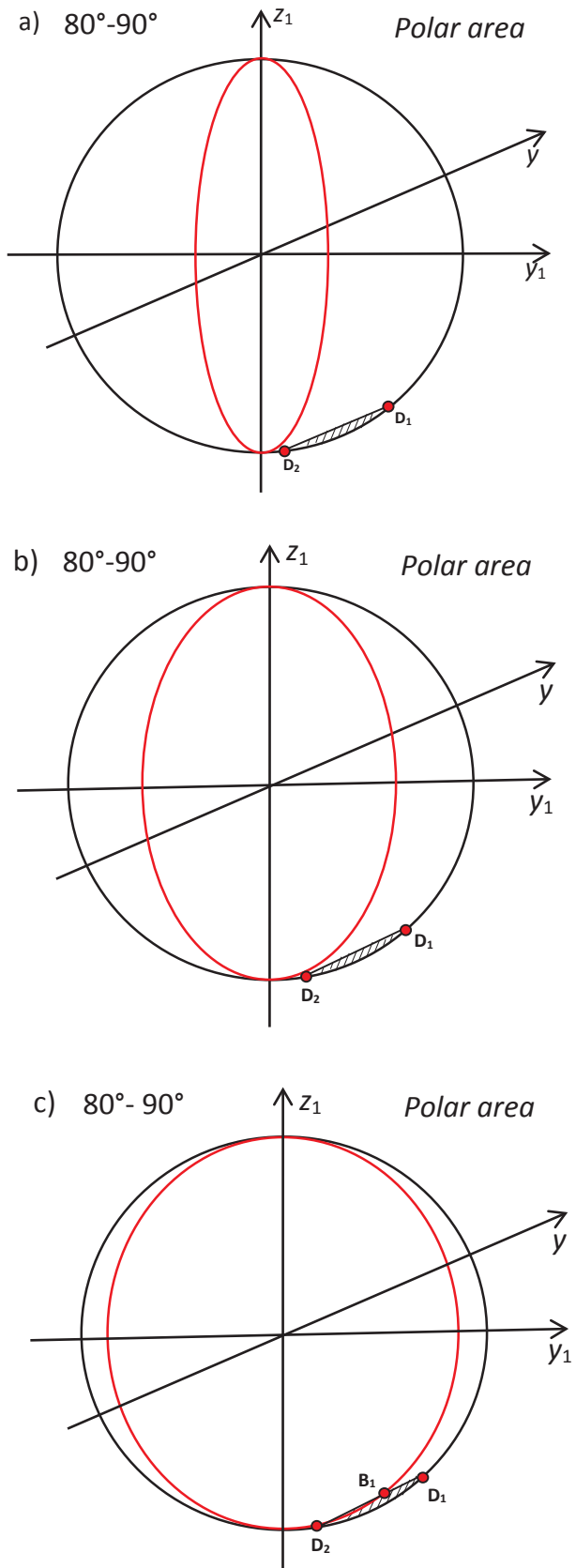


Fig. 2.21 Illumination areas for $80^\circ-90^\circ$ S latitudinal belt for $\alpha=20^\circ$, $\alpha=40^\circ$ and $\alpha=60^\circ$ (a-c)

2.4. Radiation Calculation

The amount of radiation received per m² in the current latitudinal belt (daily average) is the total amount of radiation divided by the surface area of latitudinal belt: $I=Flux/S_{belt}$. The details of the surface area of the latitudinal belt calculation are presented in Section 2.7.

The radiation flux through the surface can be calculated as the product of the radiation vector (\bar{a}) and the outward unit normal vector (\bar{n}) to the surface (S) integrated over the chosen side of the surface (see Figure 2.6):

$$Flux = \iint_S (\bar{a} \cdot \bar{n}) dS. \quad (2.1)$$

This also can be written in coordinate form. In order to calculate the flux, the integral was separated into an integral over the positively-oriented surface and an integral over the negatively-oriented surface.

$$\begin{aligned} Flux &= \iint_S (\bar{a} \cdot \bar{n}) dS = \iint_S ax_1 dy_1 dz_1 + ay_1 dx_1 dz_1 + az_1 dx_1 dy_1 = \iint_{S^-} ax_1 dy_1 dz_1 \\ &+ ax_1 dy_1 dz_1 + az_1 dx_1 dy_1 + \iint_{S^+} ax_1 dy_1 dz_1 + ay_1 dx_1 dz_1 + az_1 dx_1 dy_1. \end{aligned} \quad (2.2)$$

For the positively-oriented surface (S^+) and for the negatively-oriented surface (S^-) a surface integral was calculated as a double integral over the illumination area. The equation of the sphere ($x_1^2+y_1^2+z_1^2=R^2$) was used as the equation of the surface. The lower ($z_1\alpha$, $y_1\alpha$) and upper ($z_1\beta$, $y_1\beta$) limits of integration were derived from the equations shown in Figure 2.4.

$$\begin{aligned} \iint_{S^+} ax_1 dy_1 dz_1 + ay_1 dx_1 dz_1 + az_1 dx_1 dy_1 &= \iint_{D^+} (F \sin \alpha - F \cos \alpha \frac{\partial x_1}{\partial y_1}) dy_1 dz_1 \\ &= \iint_{D^+} (F \sin \alpha - F \cos \alpha \frac{y_1}{\sqrt{R^2 - y_1^2 - z_1^2}}) dy_1 dz_1 \\ &= F \sin \alpha - F \cos \alpha \int_{z_1\alpha}^{z_1\beta} dz_1 \int_{y_1\alpha}^{y_1\beta} \frac{y_1}{\sqrt{R^2 - y_1^2 - z_1^2}} dy_1 \end{aligned} \quad (2.3)$$

$$\text{where } x_1 = \sqrt{R^2 - y_1^2 - z_1^2}, \quad \frac{\partial x_1}{\partial y_1} = \frac{y_1}{\sqrt{R^2 - y_1^2 - z_1^2}}.$$

$$\begin{aligned}
\iint_{S^-} ax_1 dy_1 dz_1 + ay_1 dx_1 dz_1 + az_1 dx_1 dy_1 &= \iint_{D^-} (F \sin \alpha - F \cos \alpha \frac{\partial x_1}{\partial y_1}) dy_1 dz_1 \\
&= \iint_{D^-} (F \sin \alpha + F \cos \alpha \frac{y_1}{\sqrt{R^2 - y_1^2 - z_1^2}}) dy_1 dz_1 \tag{2.4} \\
&= F \sin \alpha + F \cos \alpha \int_{z_1 \alpha}^{z_1 \beta} dz_1 \int_{y_1 \alpha}^{y_1 \beta} \frac{y_1}{\sqrt{R^2 - y_1^2 - z_1^2}} dy_1,
\end{aligned}$$

where $x_1 = -\sqrt{R^2 - y_1^2 - z_1^2}$, $\frac{\partial x_1}{\partial y_1} = -\frac{y_1}{\sqrt{R^2 - y_1^2 - z_1^2}}$.

2.5. Limits of integration for the Northern Hemisphere

For each illumination area the surface of integration has been spread out into areas convenient for integration.

The illumination area $0 - \beta$ is shown in Figure 2.22.

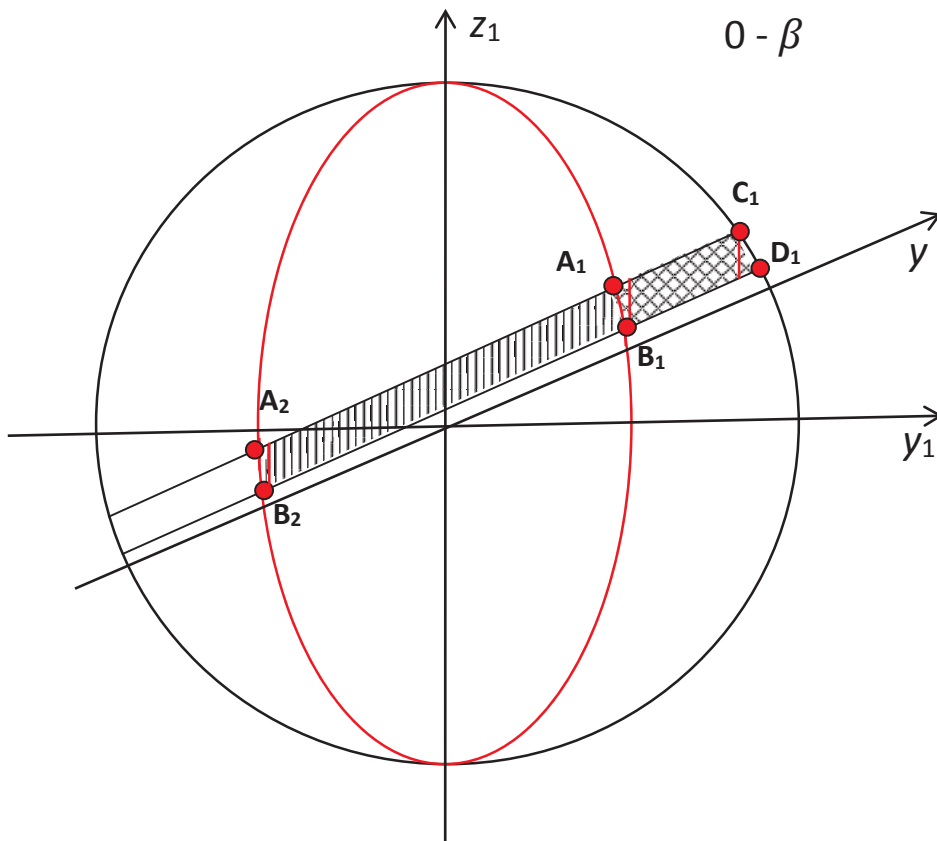


Fig. 2.22 The area of integration for the $0 - \beta$ illumination area.

The red vertical lines separate the total area into the subsequent areas over which the integration was performed. The limits of integration are as described in Table 2.3.

Table 2.3 The limits of integration for the $0 - \beta$ illumination area.

Side of the surface	Limits for y_1 ($y_1\alpha$ and $y_1\beta$)	Limits for z_1 ($z_1\alpha$ and $z_1\beta$)
S^-	$y_1A_2 \leq y_1 \leq y_1B_2$	$-R\sqrt{1 - \frac{y_1^2}{R^2 \sin^2(\alpha)}} \leq z_1 \leq \tan(\varepsilon)y_1 + \frac{r}{\cos(\varepsilon)}$
	$y_1B_2 \leq y_1 \leq y_1C_1$	$\tan(\varepsilon)y_1 + \frac{h}{\cos(\varepsilon)} \leq z_1 \leq \tan(\varepsilon)y_1 + \frac{r}{\cos(\varepsilon)}$
	$y_1C_1 \leq y_1 \leq y_1D_1$	$\tan(\varepsilon)y_1 + \frac{h}{\cos(\varepsilon)} \leq z_1 \leq \sqrt{R^2 - y_1^2}$
S^+	$y_1A_1 \leq y_1 \leq y_1B_1$	$R\sqrt{1 - \frac{y_1^2}{R^2 \sin^2(\alpha)}} \leq z_1 \leq \tan(\varepsilon)y_1 + \frac{r}{\cos(\varepsilon)}$
	$y_1B_1 \leq y_1 \leq y_1C_1$	$\tan(\varepsilon)y_1 + \frac{h}{\cos(\varepsilon)} \leq z_1 \leq \tan(\varepsilon)y_1 + \frac{r}{\cos(\varepsilon)}$
	$y_1C_1 \leq y_1 \leq y_1D_1$	$\tan(\varepsilon)y_1 + \frac{h}{\cos(\varepsilon)} \leq z_1 \leq \sqrt{R^2 - y_1^2}$

Here the limits of integration with respect to y_1 are as follows:

$$y_1C_1 = \frac{-r + (r \cos(\varepsilon) + \sqrt{r^2 \cos^2(\varepsilon) + R^2 \sin^2(\varepsilon) - r^2}) \cos(\varepsilon)}{\sin(\varepsilon)}, \quad (2.5)$$

$$z_1C_1 = \sqrt{R^2 - \frac{(-r + (r \cos(\varepsilon) + \sqrt{r^2 \cos^2(\varepsilon) + R^2 \sin^2(\varepsilon) - r^2}) \cos(\varepsilon))^2}{\sin^2(\varepsilon)}}, \quad (2.6)$$

$$y_1D_1 = \frac{-h + (h \cos(\varepsilon) + \sqrt{h^2 \cos^2(\varepsilon) + R^2 \sin^2(\varepsilon) - h^2}) \cos(\varepsilon)}{\sin(\varepsilon)}, \quad (2.7)$$

$$z_1D_1 = \sqrt{R^2 - \frac{(-h + (h \cos(\varepsilon) + \sqrt{h^2 \cos^2(\varepsilon) + R^2 \sin^2(\varepsilon) - h^2}) \cos(\varepsilon))^2}{\sin^2(\varepsilon)}}, \quad (2.8)$$

$$\begin{aligned} y_1A_1 = & [(\sin(\varepsilon)r \cos(\alpha) + (\sin^2(\varepsilon)r^2 \cos^2(\alpha) + \cos^4(\varepsilon)R^2 - r^2 \cos^2(\varepsilon) \\ & + R^2 \cos^2(\alpha) \cdot \cos^2(\varepsilon) - \cos^2(\alpha) - \cos^2(\alpha) \cdot \cos^4(\varepsilon)R^2 \\ & + \cos^2(\alpha) \cos^2(\varepsilon)r^2)^{1/2}) \times \cos(\alpha)] / (-\cos^2(\varepsilon) - \sin^2(\alpha) \\ & + \cos^2(\varepsilon) \sin^2(\alpha)), \end{aligned} \quad (2.9)$$

$$\begin{aligned}
z_1A_1 &= [\tan(\varepsilon)(\sin(\varepsilon)r \cos(\alpha) + (\sin^2(\varepsilon)r^2 \cos^2(\alpha) + \cos^4(\varepsilon)R^2 - r^2 \cos^2(\varepsilon) \\
&+ R^2 \cos^2(\alpha) \cos^2(\varepsilon) - \cos^2(\alpha)r^2 - \cos^2(\alpha) \cos^4(\varepsilon)R^2 \\
&+ \cos^2(\alpha) \cos^2(\varepsilon)r^2)^{1/2}) \times \cos(\alpha)] / (-\cos^2(\varepsilon) - \sin^2(\alpha) + \sin^2(\alpha) \cos^2(\varepsilon)) \quad (2.10) \\
&+ \frac{r}{\cos(\varepsilon)},
\end{aligned}$$

$$\begin{aligned}
y_1A_2 &= [(\sin(\varepsilon)r \cos(\alpha) - (\sin^2(\varepsilon)r^2 \cos^2(\alpha) + \cos^4(\varepsilon)R^2 - r^2 \cos^2(\varepsilon) \\
&+ R^2 \cos^2(\alpha) \cos^2(\varepsilon) - \cos^2(\alpha)r^2 - \cos^2(\alpha) \cos^4(\varepsilon)R^2 \\
&+ \cos^2(\alpha) \cos^2(\varepsilon)r^2)^{1/2}) \times \cos(\alpha)] / (-\cos^2(\varepsilon) - \sin^2(\alpha) \\
&+ \cos^2(\varepsilon) \sin^2(\alpha)), \quad (2.11)
\end{aligned}$$

$$\begin{aligned}
z_1A_2 &= [\tan(\varepsilon)(\sin(\varepsilon)r \cos(\alpha) - (\sin^2(\varepsilon)r^2 \cos^2(\alpha) + \cos^4(\varepsilon)R^2 - r^2 \cos^2(\varepsilon) \\
&+ R^2 \cos^2(\alpha) \cos^2(\varepsilon) - \cos^2(\alpha)r^2 - \cos^2(\alpha) \cos^4(\varepsilon)R^2 \\
&+ \cos^2(\alpha) \cos^2(\varepsilon)r^2)^{1/2}) \times \cos(\alpha)] / (-\cos^2(\varepsilon) - \sin^2(\alpha) + \sin^2(\alpha) \cos^2(\varepsilon)) \quad (2.12) \\
&+ \frac{r}{\cos(\varepsilon)},
\end{aligned}$$

$$\begin{aligned}
y_1B_1 &= [(\sin(\varepsilon)h \cos(\alpha) + (\sin^2(\varepsilon)h^2 \cos^2(\alpha) + \cos^4(\varepsilon)R^2 - h^2 \cos^2(\varepsilon) \\
&+ R^2 \cos^2(\alpha) \cos^2(\varepsilon) - \cos^2(\alpha)h^2 - \cos^2(\alpha) \cos^4(\varepsilon)R^2 \\
&+ \cos^2(\alpha) \cos^2(\varepsilon)h^2)^{1/2}) \times \cos(\alpha)] / (-\cos^2(\varepsilon) - \sin^2(\alpha) \\
&+ \cos^2(\varepsilon) \sin^2(\alpha)), \quad (2.13)
\end{aligned}$$

$$\begin{aligned}
z_1B_1 &= [\tan(\varepsilon)(\sin(\varepsilon)h \cos(\alpha) + (\sin^2(\varepsilon)h^2 \cos^2(\alpha) + \cos^4(\varepsilon)R^2 - h^2 \cos^2(\varepsilon) \\
&+ R^2 \cos^2(\alpha) \cos^2(\varepsilon) - \cos^2(\alpha)h^2 - \cos^2(\alpha) \cos^4(\varepsilon)R^2 \\
&+ \cos^2(\alpha) \cos^2(\varepsilon)h^2)^{1/2}) \times \cos(\alpha)] / (-\cos^2(\varepsilon) - \sin^2(\alpha) + \sin^2(\alpha) \cos^2(\varepsilon)) \quad (2.14) \\
&+ \frac{h}{\cos(\varepsilon)},
\end{aligned}$$

$$\begin{aligned}
y_1B_2 &= [(\sin(\varepsilon)h \cos(\alpha) - (\sin^2(\varepsilon)h^2 \cos^2(\alpha) + \cos^4(\varepsilon)R^2 - h^2 \cos^2(\varepsilon) \\
&+ R^2 \cos^2(\alpha) \cos^2(\varepsilon) - \cos^2(\alpha)h^2 - \cos^2(\alpha) \cos^4(\varepsilon)R^2 \\
&+ \cos^2(\alpha) \cos^2(\varepsilon)h^2)^{1/2}) \cos(\alpha)] / (-\cos^2(\varepsilon) - \sin^2(\alpha) + \cos^2(\varepsilon) \sin^2(\alpha)), \quad (2.15)
\end{aligned}$$

$$\begin{aligned}
z_1B_2 &= [\tan(\varepsilon)(\sin(\varepsilon)h \cos(\alpha) - (\sin^2(\varepsilon)h^2 \cos^2(\alpha) + \cos^4(\varepsilon)R^2 \\
&- h^2 \cos^2(\varepsilon) + R^2 \cos^2(\alpha) \cos^2(\varepsilon) - \cos^2(\alpha)h^2 - \cos^2(\alpha) \cos^4(\varepsilon)R^2 \\
&+ \cos^2(\alpha) \cos^2(\varepsilon)h^2)^{1/2}) \times \cos(\alpha)] / (-\cos^2(\varepsilon) - \sin^2(\alpha) + \sin^2(\alpha) \cos^2(\varepsilon)) \quad (2.16) \\
&+ \frac{h}{\cos(\varepsilon)}.
\end{aligned}$$

These limits of integration are used in all the following cases for both the Northern and the Southern Hemispheres.

The division of areas of integration for β - ε is introduced in Figure 2.23.

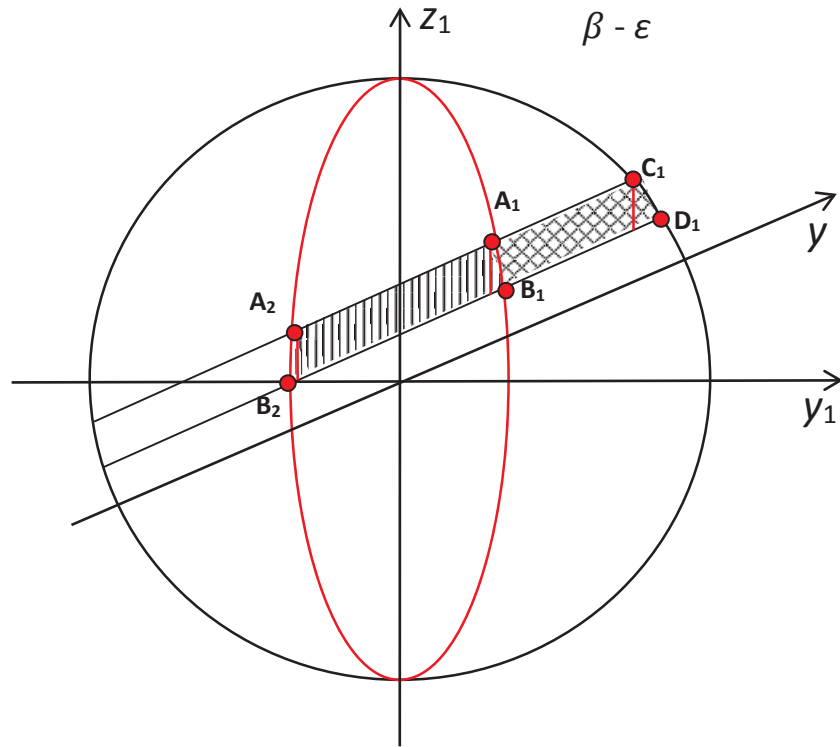


Fig. 2.23 The area of integration for the $\beta - \varepsilon$ illumination areas.

The illumination area $\varepsilon - (\pi/2 - \varepsilon)$ is represented by three different types. All the latitudinal belts from 20° to 60° belong to the first type which is shown in Figure 2.24. The illumination area here duplicates the $\beta - \varepsilon$ one, with the only difference being that it is located above the angle ε .

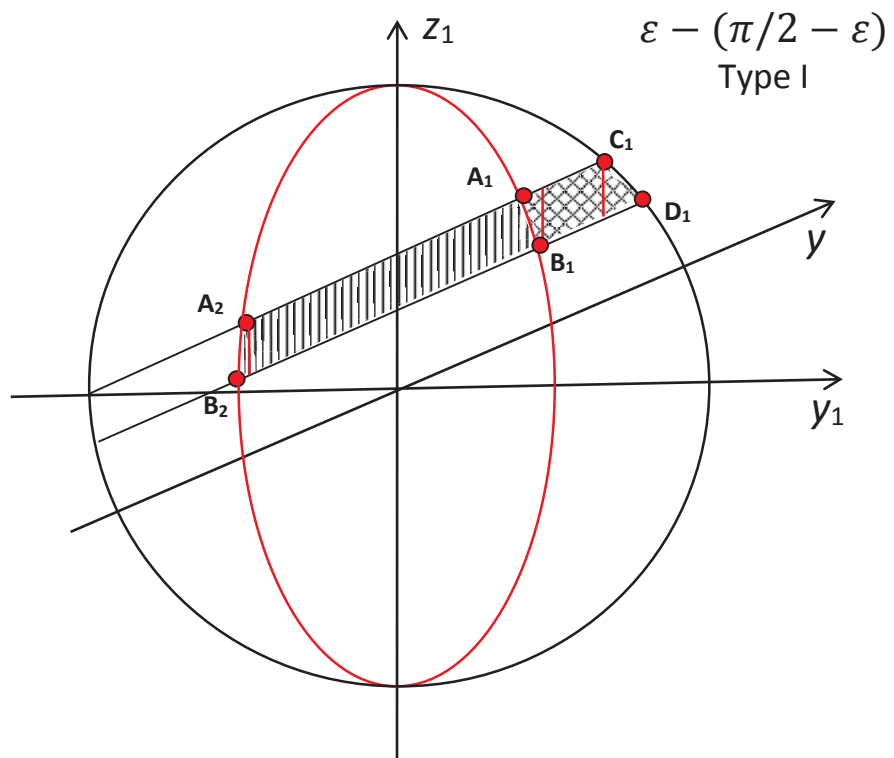


Fig. 2.24 The area of integration for the $\varepsilon - (\pi/2 - \varepsilon)$ Type I illumination areas.

The limits of integration for these two illumination areas are described in Table 2.4.

Table 2.4 The limits of integration for the β - ε and $\varepsilon - (\pi/2 - \varepsilon)$ Type I illumination areas.

Side of the surface	Limits for y_1 ($y_1\alpha$ and $y_1\beta$)	Limits for z_1 ($z_1\alpha$ and $z_1\beta$)
S^-	$y_1B_2 \leq y_1 \leq y_1A_2$	$\tan(\varepsilon)y_1 + \frac{h}{\cos(\varepsilon)} \leq z_1 \leq R\sqrt{1 - \frac{y_1^2}{R^2 \sin^2(\alpha)}}$
	$y_1A_2 \leq y_1 \leq y_1C_1$	$\tan(\varepsilon)y_1 + \frac{h}{\cos(\varepsilon)} \leq z_1 \leq \tan(\varepsilon)y_1 + \frac{r}{\cos(\varepsilon)}$
	$y_1C_1 \leq y_1 \leq y_1D_1$	$\tan(\varepsilon)y_1 + \frac{h}{\cos(\varepsilon)} \leq z_1 \leq \sqrt{R^2 - y_1^2}$
S^+	$y_1A_1 \leq y_1 \leq y_1B_1$	$R\sqrt{1 - \frac{y_1^2}{R^2 \sin^2(\alpha)}} \leq z_1 \leq \tan(\varepsilon)y_1 + \frac{r}{\cos(\varepsilon)}$
	$y_1B_1 \leq y_1 \leq y_1C_1$	$\tan(\varepsilon)y_1 + \frac{h}{\cos(\varepsilon)} \leq z_1 \leq \tan(\varepsilon)y_1 + \frac{r}{\cos(\varepsilon)}$
	$y_1C_1 \leq y_1 \leq y_1D_1$	$\tan(\varepsilon)y_1 + \frac{h}{\cos(\varepsilon)} \leq z_1 \leq \sqrt{R^2 - y_1^2}$

The illumination area for the 60° - 70° latitudinal belt for a small values of α is represented by the second type of $\varepsilon - (\pi/2 - \varepsilon)$ illumination area shown in Figure 2.25. For larger values of α (see Figure 2.15) this latitudinal belt belongs to the third type of $\varepsilon - (\pi/2 - \varepsilon)$ illumination area which is shown in Figure 2.26.

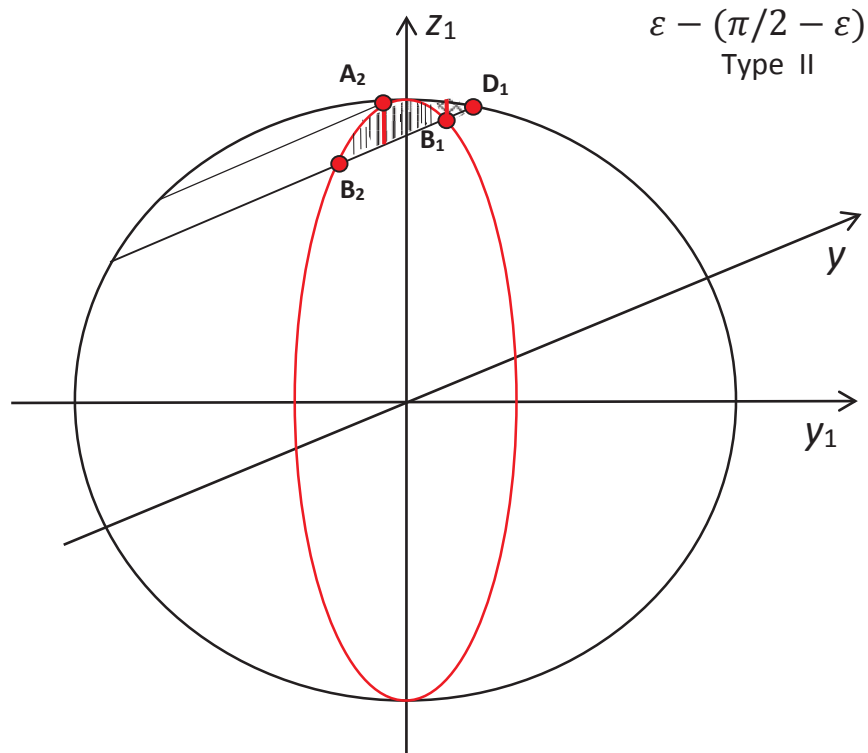


Fig. 2.25 The area of integration for the $\varepsilon - (\pi/2 - \varepsilon)$ Type II illumination areas.

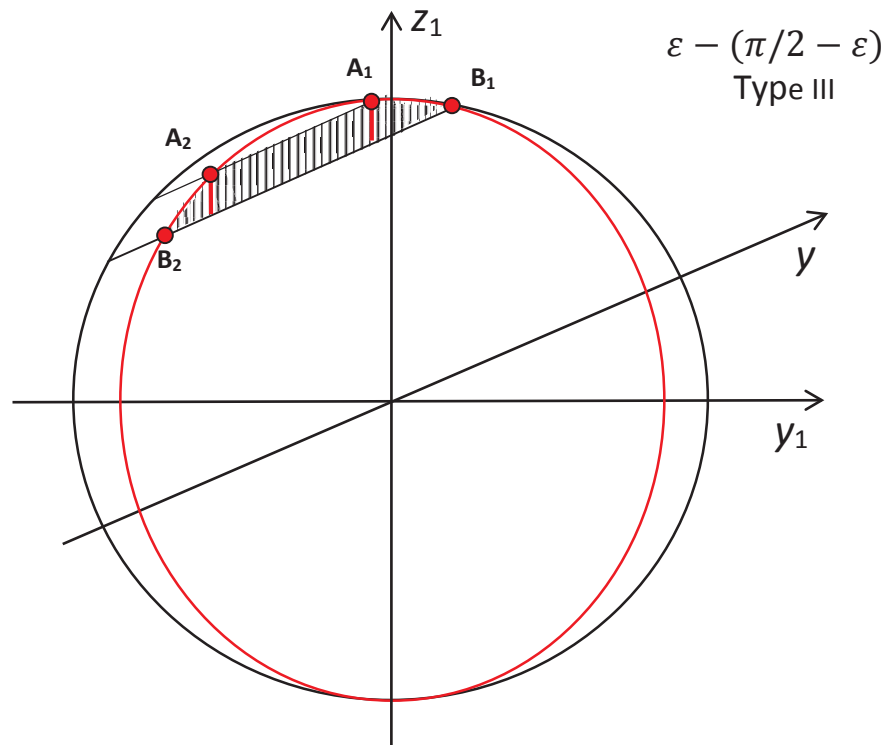


Fig. 2.26 The area of integration for the $\varepsilon - (\pi/2 - \varepsilon)$ Type III illumination areas.

The limits of integration for the second and third types of $\varepsilon - (\pi/2 - \varepsilon)$ illumination area are introduced in Tables 2.5-2.6.

Table 2.5 The limits of integration for the $\varepsilon - (\pi/2 - \varepsilon)$ Type II illumination area.

Side of the surface	Limits for y_1 ($y_1\alpha$ and $y_1\beta$)	Limits for z_1 ($z_1\alpha$ and $z_1\beta$)
S^-	$y_1B_2 \leq y_1 \leq y_1A_2$	$\tan(\varepsilon)y_1 + \frac{h}{\cos(\varepsilon)} \leq z_1 \leq R\sqrt{1 - \frac{y_1^2}{R^2 \sin^2(\alpha)}}$
	$y_1A_2 \leq y_1 \leq y_1D_1$	$\tan(\varepsilon)y_1 + \frac{h}{\cos(\varepsilon)} \leq z_1 \leq \sqrt{R^2 - y_1^2}$
S^+	$y_1A_2 \leq y_1 \leq y_1B_1$	$R\sqrt{1 - \frac{y_1^2}{R^2 \sin^2(\alpha)}} \leq z_1 \leq \sqrt{R^2 - y_1^2}$
	$y_1B_1 \leq y_1 \leq y_1D_1$	$\tan(\varepsilon)y_1 + \frac{h}{\cos(\varepsilon)} \leq z_1 \leq \sqrt{R^2 - y_1^2}$

Table 2.6 The limits of integration for the $\varepsilon - (\pi/2 - \varepsilon)$ Type III illumination area.

Side of the surface	Limits for y_1 ($y_1\alpha$ and $y_1\beta$)	Limits for z_1 ($z_1\alpha$ and $z_1\beta$)
S^-	$y_1B_2 \leq y_1 \leq y_1A_2$	$\tan(\varepsilon)y_1 + \frac{h}{\cos(\varepsilon)} \leq z_1 \leq R\sqrt{1 - \frac{y_1^2}{R^2 \sin^2(\alpha)}}$
	$y_1A_2 \leq y_1 \leq y_1A_1$	$\tan(\varepsilon)y_1 + \frac{h}{\cos(\varepsilon)} \leq z_1 \leq \tan(\varepsilon)y_1 + \frac{r}{\cos(\varepsilon)}$
	$y_1A_1 \leq y_1 \leq y_1B_1$	$\tan(\varepsilon)y_1 + \frac{h}{\cos(\varepsilon)} \leq z_1 \leq \sqrt{R^2 - y_1^2}$

For the polar regions there are two different types of the illumination area $(\pi/2 - \varepsilon) - \pi/2$ (see Figures 2.27-2.28).

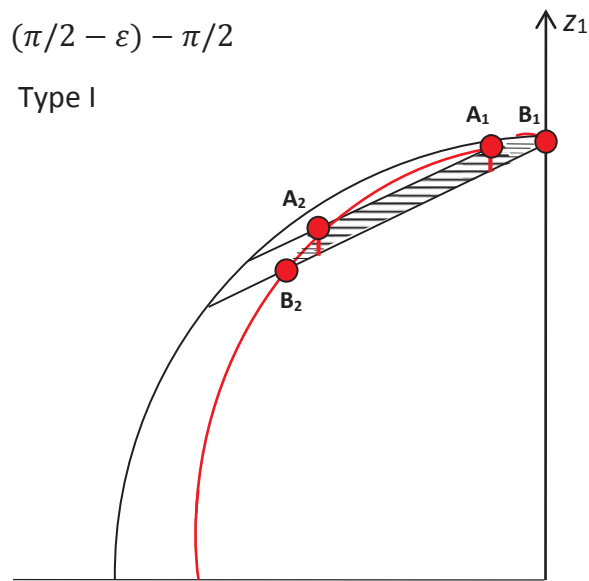


Fig. 2.27 The area of integration for the $(\pi/2 - \varepsilon) - \pi/2$ Type I illumination area.

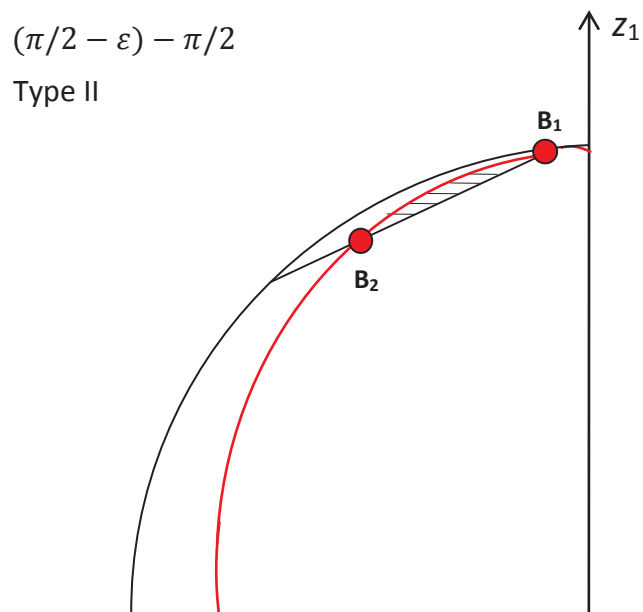


Fig. 2.28 The area of integration for the $(\pi/2 - \varepsilon) - \pi/2$ Type II illumination area.

The limits of integration for two types of $(\pi/2 - \varepsilon) - \pi/2$ illumination area are described in Tables 2.7-2.8. Note that for the polar regions in the Northern Hemisphere the radiation is received only by the positively-oriented surface.

Table 2.7 The limits of integration for the $(\pi/2 - \varepsilon) - \pi/2$ Type I illumination area.

Side of the surface	Limits for y_1 ($y_1\alpha$ and $y_1\beta$)	Limits for z_1 ($z_1\alpha$ and $z_1\beta$)
S^+	$y_1B_2 \leq y_1 \leq y_1A_2$	$\tan(\varepsilon)y_1 + \frac{h}{\cos(\varepsilon)} \leq z_1 \leq \sqrt{R^2 - y_1^2}$
	$y_1A_2 \leq y_1 \leq y_1C_1$	$\tan(\varepsilon)y_1 + \frac{h}{\cos(\varepsilon)} \leq z_1 \leq \tan(\varepsilon)y_1 + \frac{r}{\cos(\varepsilon)}$
	$y_1C_1 \leq y_1 \leq y_1D_1$	$\tan(\varepsilon)y_1 + \frac{h}{\cos(\varepsilon)} \leq z_1 \leq \sqrt{R^2 - y_1^2}$

Table 2.8 The limits of integration for the $(\pi/2 - \varepsilon) - \pi/2$ Type II illumination area.

Side of the surface	Limits for y_1 ($y_1\alpha$ and $y_1\beta$)	Limits for z_1 ($z_1\alpha$ and $z_1\beta$)
S^+	$y_1B_2 \leq y_1 \leq y_1A_2$	$\tan(\varepsilon)y_1 + \frac{h}{\cos(\varepsilon)} \leq z_1 \leq R\sqrt{1 - \frac{y_1^2}{R^2 \sin^2(\alpha)}}$

2.6. Limits of integration for the Southern Hemisphere

For the calculation of the amount of insolation for the Southern Hemisphere the illumination areas below equator need to be considered. However, for computational simplicity the symmetrical areas in the Northern Hemisphere were used (see the examples below).

An example for C_2 - D_2 symmetrical illumination area is illustrated in Figure 2.29.

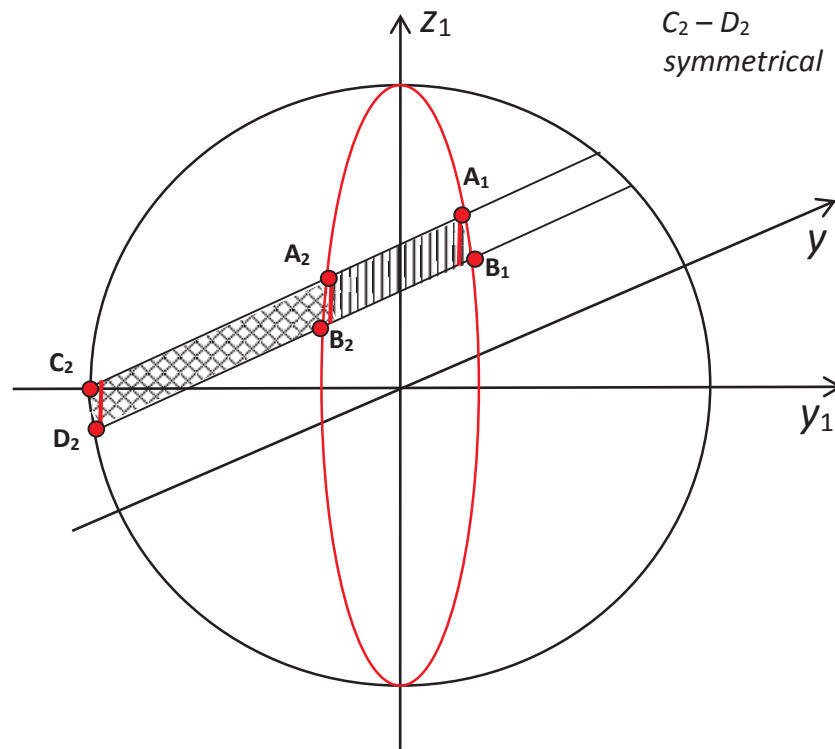


Fig. 2.29 The areas of integration for the C_2-D_2 symmetrical illumination area.

An example for C_2-D_2 symmetrical illumination area is illustrated in Figure 2.29.

The limits of integration are introduced in Table 2.9.

Table 2.9 The limits of integration for C_2 - D_2 symmetrical illumination area.

Side of the surface	Limits for y_1 ($y_1\alpha$ and $y_1\beta$)	Limits for z_1 ($z_1\alpha$ and $z_1\beta$)
S^-	$y_1C_2 \leq y_1 \leq y_1D_2$	$\sqrt{R^2 - y_1^2} \leq z_1 \leq \tan(\varepsilon)y_1 + \frac{r}{\cos(\varepsilon)}$
	$y_1D_2 \leq y_1 \leq y_1A_1$	$\tan(\varepsilon)y_1 + \frac{h}{\cos(\varepsilon)} \leq z_1 \leq \tan(\varepsilon)y_1 + \frac{r}{\cos(\varepsilon)}$
	$y_1A_1 \leq y_1 \leq y_1B_1$	$\tan(\varepsilon)y_1 + \frac{h}{\cos(\varepsilon)} \leq z_1 \leq R\sqrt{1 - \frac{y_1^2}{R^2 \sin^2(\alpha)}}$
S^+	$y_1D_2 \leq y_1 \leq y_1C_2$	$\sqrt{R^2 - y_1^2} \leq z_1 \leq \tan(\varepsilon)y_1 + \frac{r}{\cos(\varepsilon)}$
	$y_1D_2 \leq y_1 \leq y_1B_2$	$\tan(\varepsilon)y_1 + \frac{h}{\cos(\varepsilon)} \leq z_1 \leq \tan(\varepsilon)y_1 + \frac{r}{\cos(\varepsilon)}$
	$y_1B_2 \leq y_1 \leq y_1A_2$	$R\sqrt{1 - \frac{y_1^2}{R^2 \sin^2(\alpha)}} \leq z_1 \leq \tan(\varepsilon)y_1 + \frac{r}{\cos(\varepsilon)}$

Here the coordinates of the points C_2 and D_2 are the following:

$$y_1C_2 = \frac{-r + (r \cos(\varepsilon) - \sqrt{r^2 \cos^2(\varepsilon) + R^2 \sin^2(\varepsilon) - r^2}) \cos(\varepsilon)}{\sin(\varepsilon)}, \quad (2.17)$$

$$z_1C_2 = \sqrt{R^2 - \frac{(-r + (r \cos(\varepsilon) - \sqrt{r^2 \cos^2(\varepsilon) + R^2 \sin^2(\varepsilon) - r^2}) \cos(\varepsilon))^2}{\sin^2(\varepsilon)}}, \quad (2.18)$$

$$y_1D_2 = \frac{-h + (h \cos(\varepsilon) - \sqrt{h^2 \cos^2(\varepsilon) + R^2 \sin^2(\varepsilon) - h^2}) \cos(\varepsilon)}{\sin(\varepsilon)}, \quad (2.19)$$

$$z_1D_2 = \sqrt{R^2 - \frac{(-h + (h \cos(\varepsilon) - \sqrt{h^2 \cos^2(\varepsilon) + R^2 \sin^2(\varepsilon) - h^2}) \cos(\varepsilon))^2}{\sin^2(\varepsilon)}}. \quad (2.20)$$

An example for D_2 - C_2 symmetrical illumination area is illustrated in Figure 2.30.

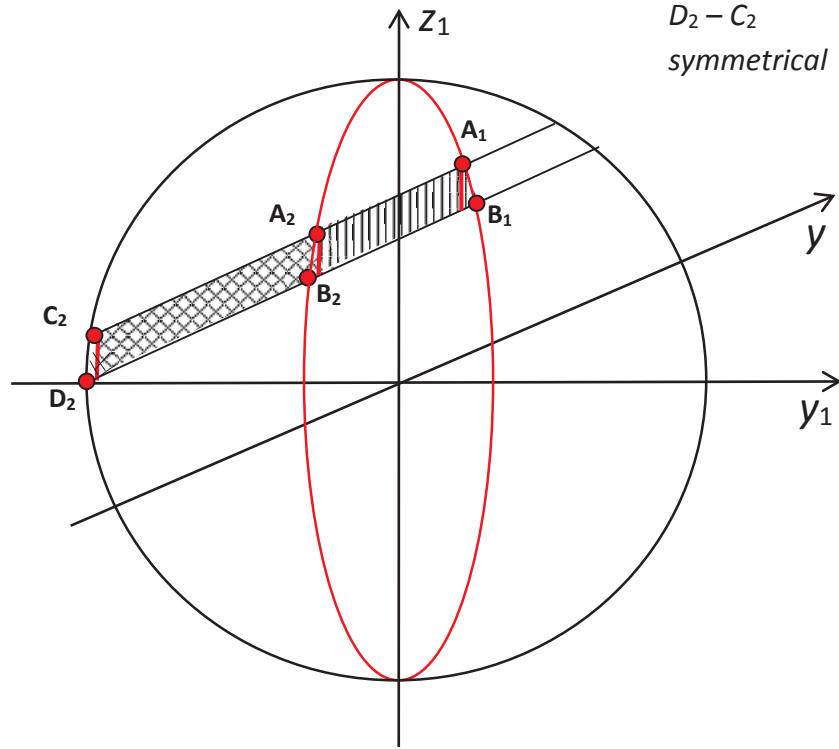


Fig. 2.30 The areas of integration for the D_2-C_2 symmetrical illumination area.

Here the limits of integration are given in Table 2.10.

Table 2.10 The limits of integration for D_2-C_2 symmetrical illumination area.

Side of the surface	Limits for y_1 ($y_1\alpha$ and $y_1\beta$)	Limits for $z_1(z_1\alpha$ and $z_1\beta$)
S^-	$y_1D_2 \leq y_1 \leq y_1C_2$	$\tan(\varepsilon)y_1 + \frac{h}{\cos(\varepsilon)} \leq z_1 \leq \sqrt{R^2 - y_1^2}$
	$y_1C_2 \leq y_1 \leq y_1A_1$	$\tan(\varepsilon)y_1 + \frac{h}{\cos(\varepsilon)} \leq z_1 \leq \tan(\varepsilon)y_1 + \frac{r}{\cos(\varepsilon)}$
	$y_1A_1 \leq y_1 \leq y_1B_1$	$\tan(\varepsilon)y_1 + \frac{h}{\cos(\varepsilon)} \leq z_1 \leq R\sqrt{1 - \frac{y_1^2}{R^2 \sin^2(\alpha)}}$
S^+	$y_1D_2 \leq y_1 \leq y_1C_2$	$\tan(\varepsilon)y_1 + \frac{h}{\cos(\varepsilon)} \leq z_1 \leq \sqrt{R^2 - y_1^2}$
	$y_1C_2 \leq y_1 \leq y_1B_2$	$\tan(\varepsilon)y_1 + \frac{h}{\cos(\varepsilon)} \leq z_1 \leq \tan(\varepsilon)y_1 + \frac{r}{\cos(\varepsilon)}$
	$y_1B_2 \leq y_1 \leq y_1A_2$	$\tan(\varepsilon)y_1 + \frac{h}{\cos(\varepsilon)} \leq z_1 \leq R\sqrt{1 - \frac{y_1^2}{R^2 \sin^2(\alpha)}}$

For the polar latitudes there are four different types of illumination areas (see Figures 2.31-2.34).

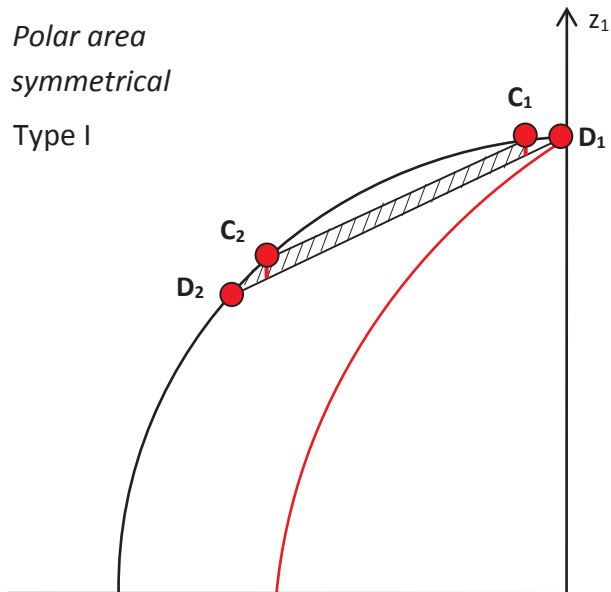


Fig. 2.31 The areas of integration for the *polar symmetrical* Type I illumination area.

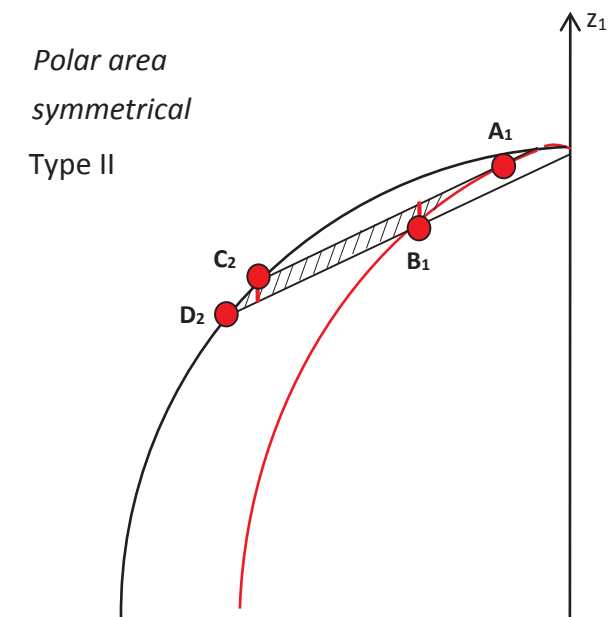


Fig. 2.32 The areas of integration for the *polar symmetrical* Type II illumination area.

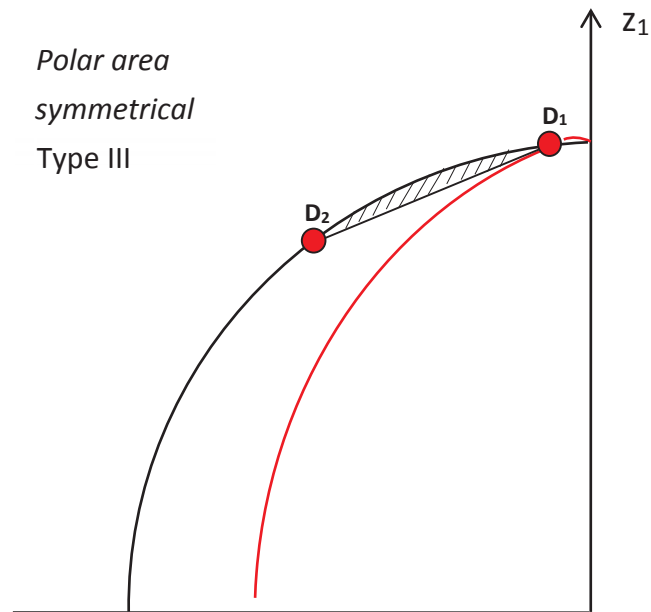


Fig. 2.33 The areas of integration for the *polar symmetrical* Type III illumination area.

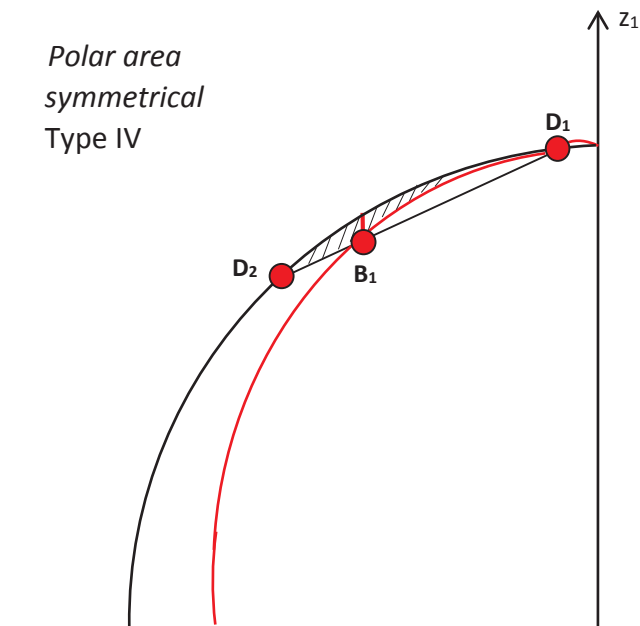


Fig. 2.34 The areas of integration for the *polar symmetrical* Type IV illumination area.

The limits of integration are shown in Tables 2.11–2.14. Note that for the Southern Hemisphere polar regions the radiation is received only by the negatively-oriented surface.

Table 2.11 The limits of integration for the *polar symmetrical* Type I illumination area.

Side of the surface	Limits for y_1 ($y_1\alpha$ and $y_1\beta$)	Limits for z_1 ($z_1\alpha$ and $z_1\beta$)
S^-	$y_1D_2 \leq y_1 \leq y_1C_2$	$\tan(\varepsilon)y_1 + \frac{h}{\cos(\varepsilon)} \leq z_1 \leq \sqrt{R^2 - y_1^2}$
	$y_1C_2 \leq y_1 \leq y_1C_1$	$\tan(\varepsilon)y_1 + \frac{h}{\cos(\varepsilon)} \leq z_1 \leq \tan(\varepsilon)y_1 + \frac{r}{\cos(\varepsilon)}$
	$y_1C_1 \leq y_1 \leq y_1D_1$	$\tan(\varepsilon)y_1 + \frac{h}{\cos(\varepsilon)} \leq z_1 \leq \sqrt{R^2 - y_1^2}$

Table 2.12 The limits of integration for the *polar symmetrical* Type II illumination area.

Side of the surface	Limits for y_1 ($y_1\alpha$ and $y_1\beta$)	Limits for z_1 ($z_1\alpha$ and $z_1\beta$)
S^-	$y_1D_2 \leq y_1 \leq y_1C_2$	$\tan(\varepsilon)y_1 + \frac{h}{\cos(\varepsilon)} \leq z_1 \leq \sqrt{R^2 - y_1^2}$
	$y_1C_2 \leq y_1 \leq y_1B_1$	$\tan(\varepsilon)y_1 + \frac{h}{\cos(\varepsilon)} \leq z_1 \leq \tan(\varepsilon)y_1 + \frac{r}{\cos(\varepsilon)}$
	$y_1B_1 \leq y_1 \leq y_1A_1$	$R\sqrt{1 - \frac{y_1^2}{R^2 \sin^2(\alpha)}} \leq z_1 \leq \tan(\varepsilon)y_1 + \frac{r}{\cos(\varepsilon)}$

Table 2.13 The limits of integration for the *polar symmetrical* Type III illumination area.

Side of the surface	Limits for y_1 ($y_1\alpha$ and $y_1\beta$)	Limits for z_1 ($z_1\alpha$ and $z_1\beta$)
S^-	$y_1D_2 \leq y_1 \leq y_1D_1$	$\tan(\varepsilon)y_1 + \frac{h}{\cos(\varepsilon)} \leq z_1 \leq \sqrt{R^2 - y_1^2}$

Table 2.14 The limits of integration for the *polar symmetrical* Type IV illumination area.

Side of the surface	Limits for y_1 ($y_1\alpha$ and $y_1\beta$)	Limits for $z_1(z_1\alpha$ and $z_1\beta$)
S^-	$y_1D_2 \leq y_1 \leq y_1B_1$	$\tan(\varepsilon)y_1 + \frac{h}{\cos \varepsilon} \leq z_1 \leq \sqrt{R^2 - y_1^2}$
	$y_1B_1 \leq y_1 \leq y_1D_1$	$R\sqrt{1 - \frac{y_1^2}{R^2 \sin^2 \alpha}} \leq z_1 \leq \sqrt{R^2 - y_1^2}$

2.7. The approximation technique

After attempting to calculate the double integrals in Maple software it was discovered that the software fails to do so due to the combination of the complexity of the integrand and the limits of integration. Thus an approximation technique was applied to the intervals bordered by an ellipse and circle.

The parts of an ellipse and circle were approximated by a straight line of a form:

$$z_1 = ky_1 + b, \quad (2.21)$$

where k and b are the coefficients. Since the latitudinal belts are thin, compared to the earth's circumference, the approximation will not have a major impact on the computational results.

2.7.1. The approximation of the latitudinal belts in the Northern Hemisphere

The approximation for area $0 - \beta$ is shown in Figure 2.35. The changed limits of integration are shown in Table 2.15.

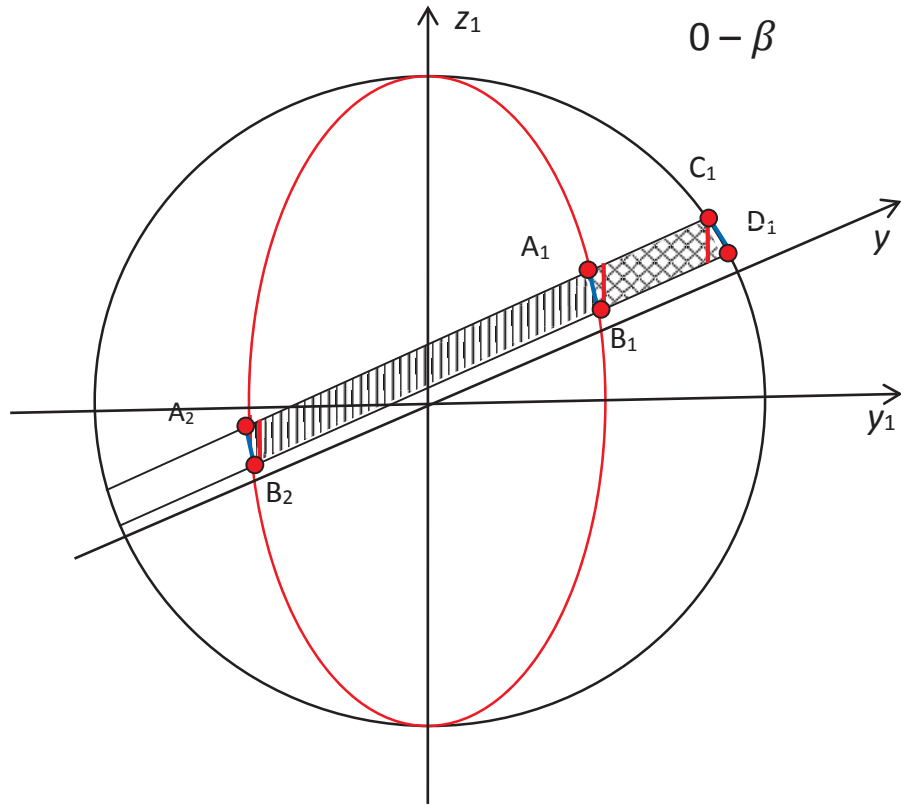


Fig. 2.35 The approximation of the $0 - \beta$ illumination area.

Table 2.15 The updated limits of integration for $0 - \beta$ illumination area.

Side of the surface	Limits for y_1 ($y_1\alpha$ and $y_1\beta$)	Limits for z_1 ($z_1\alpha$ and $z_1\beta$)
S^-	$y_1A_2 \leq y_1 \leq y_1B_2$	$k_{A_2B_2}y_1 + b_{A_2B_2} \leq z_1 \leq \tan(\varepsilon)y_1 + \frac{r}{\cos(\varepsilon)}$
	$y_1B_2 \leq y_1 \leq y_1C_1$	$\tan(\varepsilon)y_1 + \frac{h}{\cos(\varepsilon)} \leq z_1 \leq \tan(\varepsilon)y_1 + \frac{r}{\cos(\varepsilon)}$
	$y_1C_1 \leq y_1 \leq y_1D_1$	$\tan(\varepsilon)y_1 + \frac{h}{\cos(\varepsilon)} \leq z_1 \leq k_{C_1D_1}y_1 + b_{C_1D_1}$
S^+	$y_1A_1 \leq y_1 \leq y_1B_1$	$k_{A_1B_1}y_1 + b_{A_1B_1} \leq z_1 \leq \tan(\varepsilon)y_1 + \frac{r}{\cos(\varepsilon)}$
	$y_1B_1 \leq y_1 \leq y_1C_1$	$\tan(\varepsilon)y_1 + \frac{h}{\cos(\varepsilon)} \leq z_1 \leq \tan(\varepsilon)y_1 + \frac{r}{\cos(\varepsilon)}$
	$y_1C_1 \leq y_1 \leq y_1D_1$	$\tan(\varepsilon)y_1 + \frac{h}{\cos(\varepsilon)} \leq z_1 \leq k_{C_1D_1}y_1 + b_{C_1D_1}$

In Table 2.15, the coefficients k_{ij} and b_{ij} were found as follows:

$$k_{ij} = \frac{(z_{1i} - z_{1j})}{y_{1i} - y_{1j}}, \quad (2.22)$$

$$b_{ij} = z_{1i} - k_{ij}y_{1i}, \quad (2.23)$$

where i and j are the beginning and the end of the line.

The approximation of $\beta - \varepsilon$ and $\varepsilon - (\pi/2 - \varepsilon)$ Type I are shown in Figure 2.36-2.37.

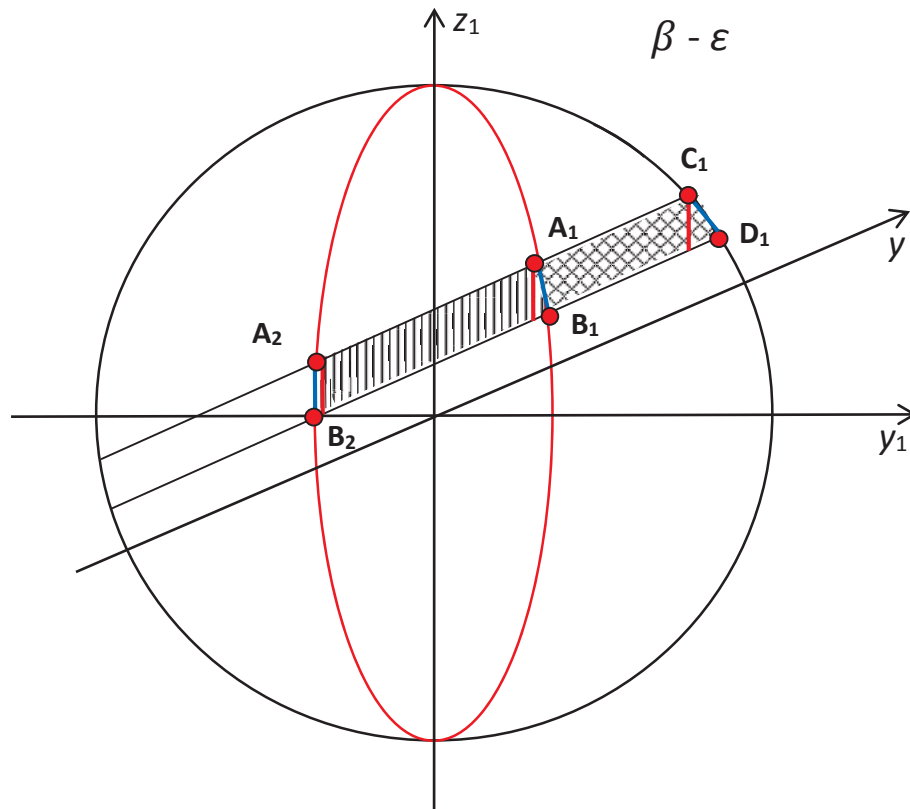


Fig. 2.36 The approximation of the $\beta - \varepsilon$ illumination area.

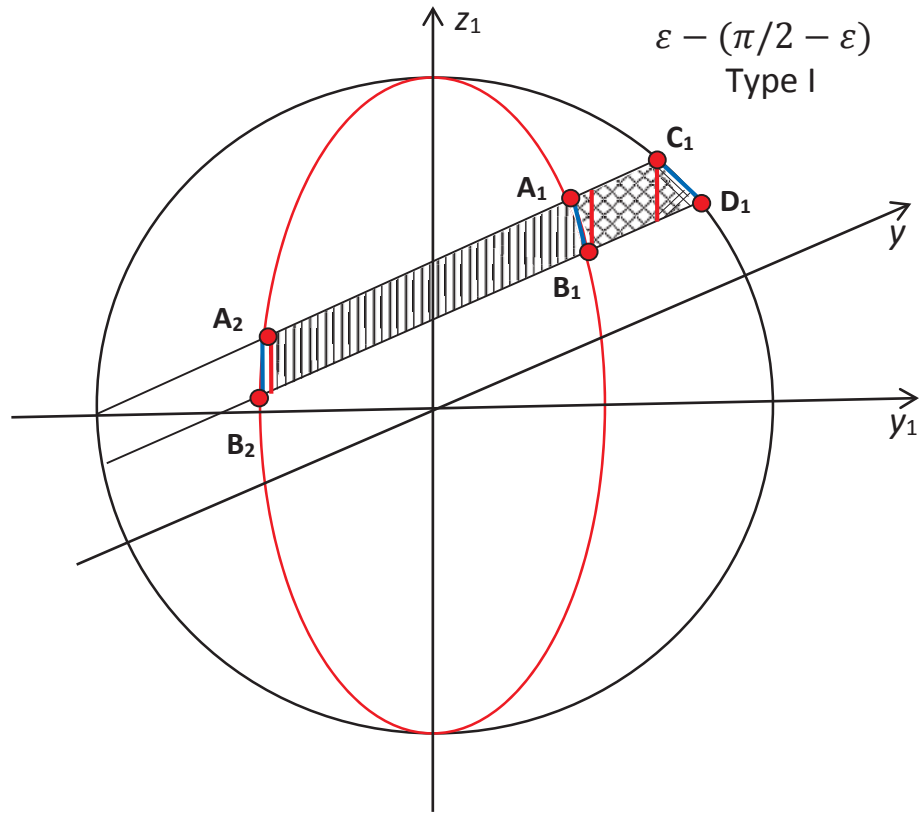


Fig. 2.37 The approximation of the $\varepsilon - (\pi/2 - \varepsilon)$ Type I illumination area. The changes of the limits of integration for these two illumination areas are shown in Table 2.16.

Table 2.16 The updated limits of integration for β - ε and $\varepsilon - (\pi/2 - \varepsilon)$ Type I illumination areas.

Side of the surface	Limits for y_1 ($y_1\alpha$ and $y_1\beta$)	Limits for z_1 ($z_1\alpha$ and $z_1\beta$)
S^-	$y_1B_2 \leq y_1 \leq y_1A_2$	$\tan(\varepsilon)y_1 + \frac{h}{\cos(\varepsilon)} \leq z_1 \leq k_{A_2B_2}y_1 + b_{A_2B_2}$
	$y_1A_2 \leq y_1 \leq y_1C_1$	$\tan(\varepsilon)y_1 + \frac{h}{\cos(\varepsilon)} \leq z_1 \leq \tan(\varepsilon)y_1 + \frac{r}{\cos(\varepsilon)}$
	$y_1C_1 \leq y_1 \leq y_1D_1$	$\tan(\varepsilon)y_1 + \frac{h}{\cos(\varepsilon)} \leq z_1 \leq k_{C_1D_1}y_1 + b_{C_1D_1}$
S^+	$y_1A_1 \leq y_1 \leq y_1B_1$	$k_{A_1B_1}y_1 + b_{A_1B_1} \leq z_1 \leq \tan(\varepsilon)y_1 + \frac{r}{\cos(\varepsilon)}$
	$y_1B_1 \leq y_1 \leq y_1C_1$	$\tan(\varepsilon)y_1 + \frac{h}{\cos(\varepsilon)} \leq z_1 \leq \tan(\varepsilon)y_1 + \frac{r}{\cos(\varepsilon)}$
	$y_1C_1 \leq y_1 \leq y_1D_1$	$\tan(\varepsilon)y_1 + \frac{h}{\cos(\varepsilon)} \leq z_1 \leq k_{C_1D_1}y_1 + b_{C_1D_1}$

The approximation of two other types of $\varepsilon - (\pi/2 - \varepsilon)$ illumination area are introduced in Figures 2.38-2.39.

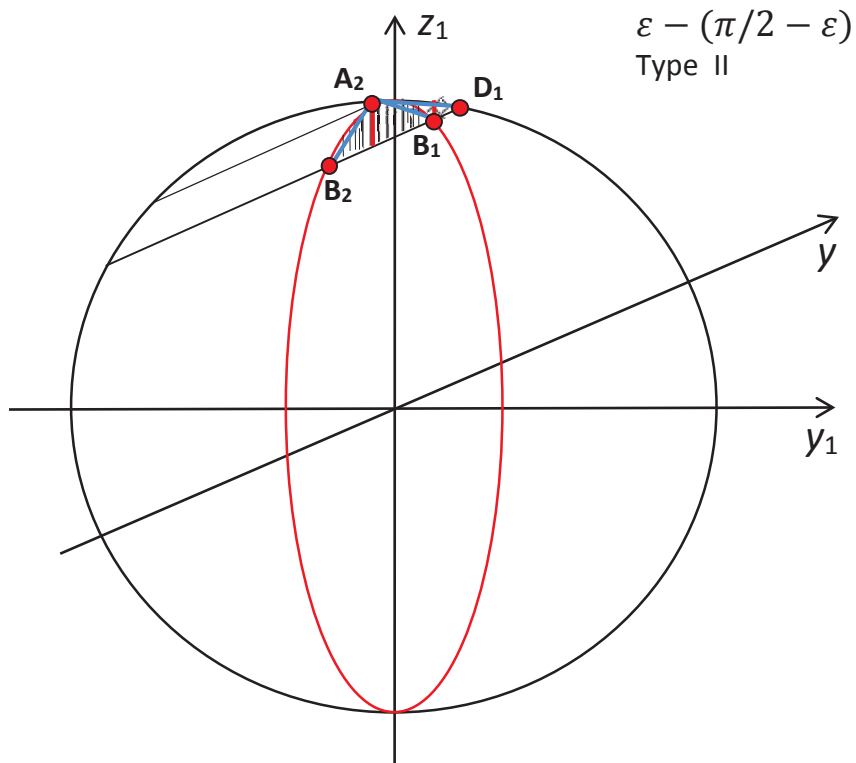


Fig. 2.38 The approximation of the $\varepsilon - (\pi/2 - \varepsilon)$ Type II illumination area.

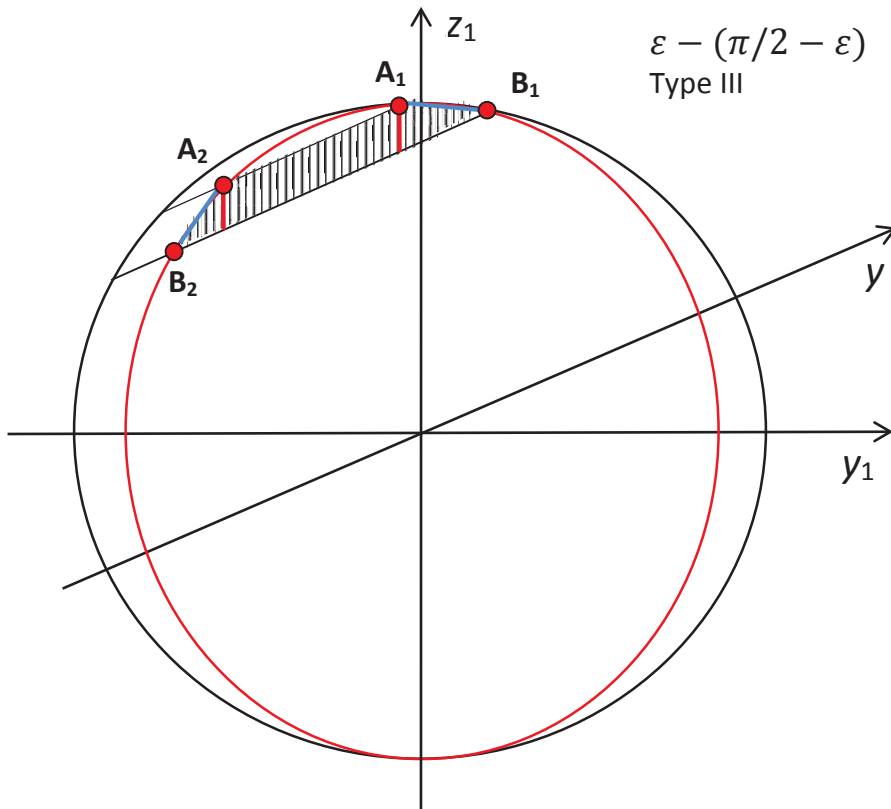


Fig. 2.39 The approximation of the $\varepsilon - (\pi/2 - \varepsilon)$ Type III illumination area.

The changes of the limits of integration are shown in Table 2.17 and Table 2.18, respectively.

Table 2.17 The updated limits of integration for the $\varepsilon - (\pi/2 - \varepsilon)$ Type II illumination area.

Side of the surface	Limits for y_1 ($y_1\alpha$ and $y_1\beta$)	Limits for z_1 ($z_1\alpha$ and $z_1\beta$)
S^-	$y_1B_2 \leq y_1 \leq y_1A_2$	$\tan(\varepsilon)y_1 + \frac{h}{\cos(\varepsilon)} \leq z_1 \leq k_{A_2B_2}y_1 + b_{A_2B_2}$
	$y_1A_2 \leq y_1 \leq y_1D_1$	$\tan(\varepsilon)y_1 + \frac{h}{\cos(\varepsilon)} \leq z_1 \leq k_{A_2D_1}y_1 + b_{A_2D_1}$
S^+	$y_1A_2 \leq y_1 \leq y_1B_1$	$k_{A_2B_1}y_1 + b_{A_2B_1} \leq z_1 \leq k_{A_2D_1}y_1 + b_{A_2D_1}$
	$y_1B_1 \leq y_1 \leq y_1D_1$	$\tan(\varepsilon)y_1 + \frac{h}{\cos(\varepsilon)} \leq z_1 \leq k_{A_2D_1}y_1 + b_{A_2D_1}$

Table 2.18 The updated limits of integration for the $\varepsilon - (\pi/2 - \varepsilon)$ Type III illumination area.

Side of the surface	Limits for y_1 ($y_1\alpha$ and $y_1\beta$)	Limits for z_1 ($z_1\alpha$ and $z_1\beta$)
S^-	$y_1B_2 \leq y_1 \leq y_1A_2$	$\tan(\varepsilon)y_1 + \frac{h}{\cos(\varepsilon)} \leq z_1 \leq k_{A_2B_2}y_1 + b_{A_2B_2}$
	$y_1A_2 \leq y_1 \leq y_1A_1$	$\tan(\varepsilon)y_1 + \frac{h}{\cos(\varepsilon)} \leq z_1 \leq \tan(\varepsilon)y_1 + \frac{r}{\cos(\varepsilon)}$
	$y_1A_1 \leq y_1 \leq y_1B_1$	$\tan(\varepsilon)y_1 + \frac{h}{\cos(\varepsilon)} \leq z_1 \leq k_{A_1B_1}y_1 + b_{A_1B_1}$

The approximation for first type of $(\pi/2 - \varepsilon) - \pi/2$ illumination area is introduced in Figure 2.40. The second type did not require the approximation.

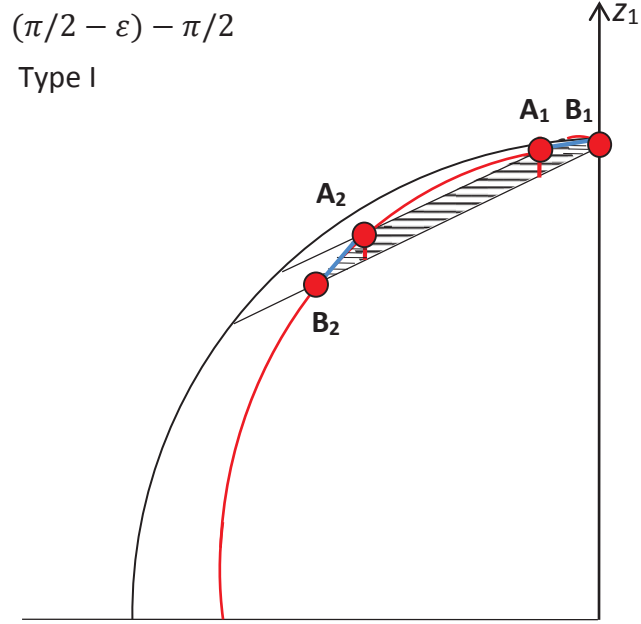


Fig. 2.40 The approximation of the $(\pi/2 - \varepsilon) - \pi/2$ Type I illumination area.

The changed limits of integration are shown in Table 2.19.

Table 2.19 The updated limits of integration for the $(\pi/2 - \varepsilon) - \pi/2$ Type I illumination area.

Side of the surface	Limits for y_1 ($y_1\alpha$ and $y_1\beta$)	Limits for z_1 ($z_1\alpha$ and $z_1\beta$)
S^+	$y_1B_2 \leq y_1 \leq y_1A_2$	$\tan(\varepsilon)y_1 + \frac{h}{\cos(\varepsilon)} \leq z_1 \leq k_{A_2B_2}y_1 + b_{A_2B_2}$
	$y_1A_2 \leq y_1 \leq y_1C_1$	$\tan(\varepsilon)y_1 + \frac{h}{\cos(\varepsilon)} \leq z_1 \leq \tan(\varepsilon)y_1 + \frac{r}{\cos(\varepsilon)}$
	$y_1C_1 \leq y_1 \leq y_1D_1$	$\tan(\varepsilon)y_1 + \frac{h}{\cos(\varepsilon)} \leq z_1 \leq k_{C_1D_1}y_1 + b_{C_1D_1}$

2.7.2. The approximation of the latitudinal belts in the Southern Hemisphere

The approximated area C_2-D_2 is shown in Figure 2.41.

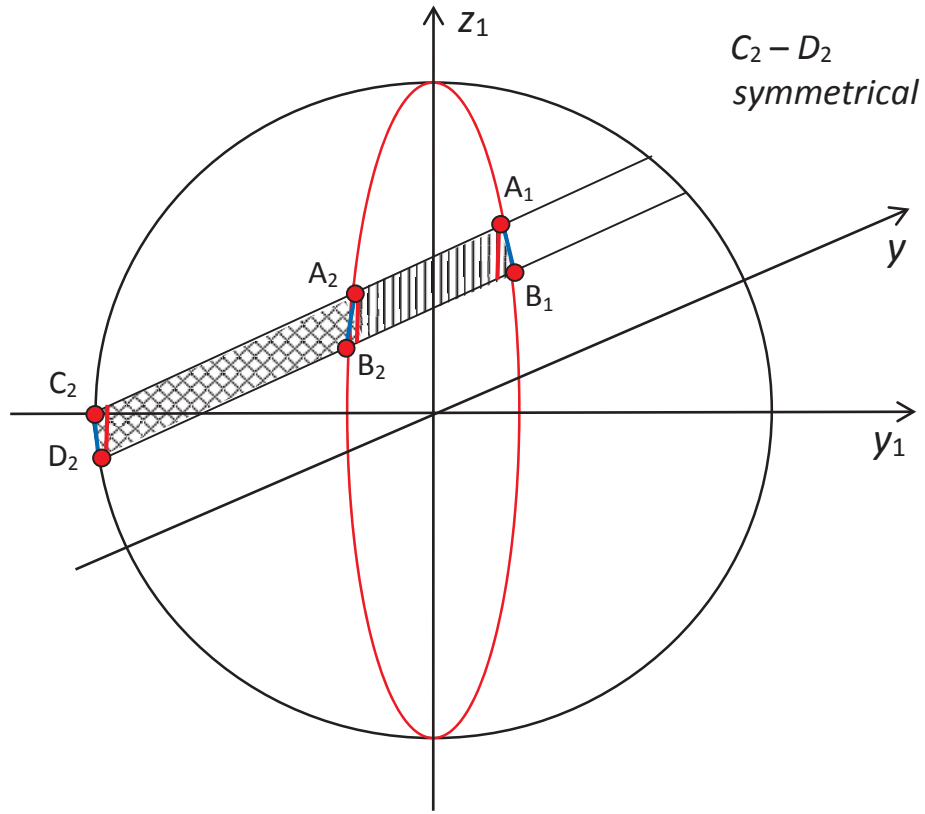


Fig. 2.41 The approximation of the C_2 - D_2 symmetrical illumination area.

The change of the limits of integration is shown in Table 2.20.

Table 2.20 The updated limits of integration for C_2 - D_2 symmetrical illumination area.

Side of the surface	Limits for y_1 ($y_1\alpha$ and $y_1\beta$)	Limits for z_1 ($z_1\alpha$ and $z_1\beta$)
S^-	$y_1C_2 \leq y_1 \leq y_1D_2$	$k_{C_2D_2}y_1 + b_{C_2D_2} \leq z_1 \leq \tan(\varepsilon)y_1 + \frac{r}{\cos(\varepsilon)}$
	$y_1D_2 \leq y_1 \leq y_1A_1$	$\tan(\varepsilon)y_1 + \frac{h}{\cos(\varepsilon)} \leq z_1 \leq \tan(\varepsilon)y_1 + \frac{r}{\cos(\varepsilon)}$
	$y_1A_1 \leq y_1 \leq y_1B_1$	$\tan(\varepsilon)y_1 + \frac{h}{\cos(\varepsilon)} \leq z_1 \leq k_{A_1B_1}y_1 + b_{A_1B_1}$
S^+	$y_1D_2 \leq y_1 \leq y_1C_2$	$k_{C_2D_2}y_1 + b_{C_2D_2} \leq z_1 \leq \tan(\varepsilon)y_1 + \frac{r}{\cos(\varepsilon)}$
	$y_1D_2 \leq y_1 \leq y_1B_2$	$\tan(\varepsilon)y_1 + \frac{h}{\cos(\varepsilon)} \leq z_1 \leq \tan(\varepsilon)y_1 + \frac{r}{\cos(\varepsilon)}$
	$y_1B_2 \leq y_1 \leq y_1A_2$	$k_{A_2B_2}y_1 + b_{A_2B_2} \leq z_1 \leq \tan(\varepsilon)y_1 + \frac{r}{\cos(\varepsilon)}$

The approximated area D_2-C_2 is shown in Figure 2.42.

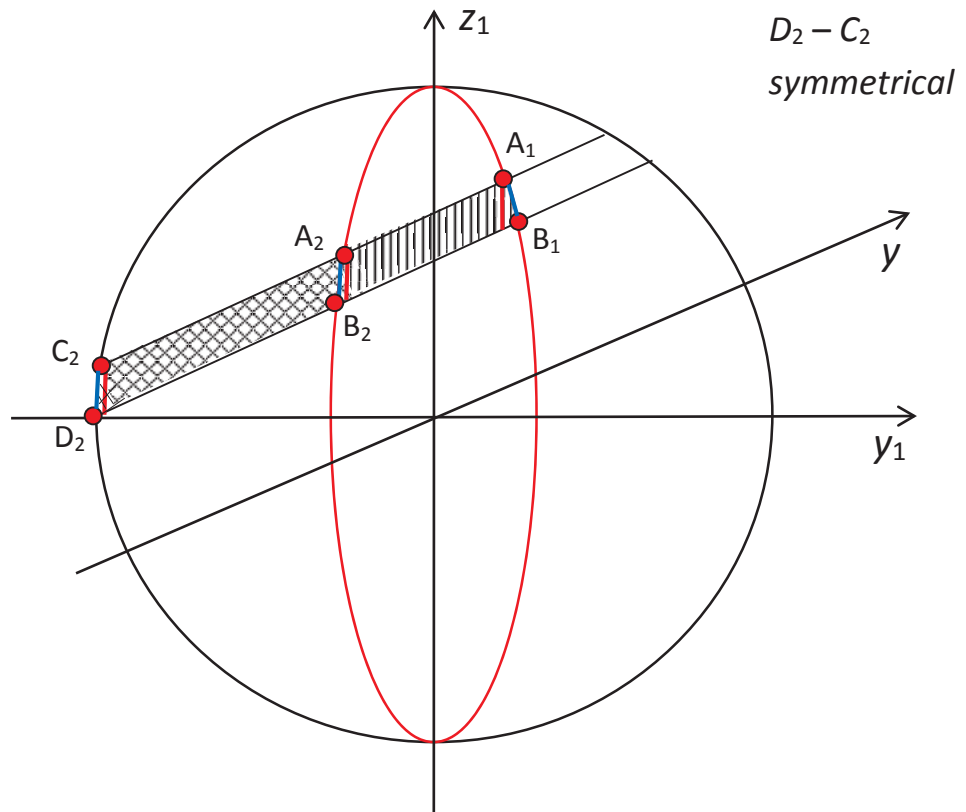


Fig. 2.42 The approximation of the D_2-C_2 symmetrical illumination area.

The updated limits of integration are presented in Table 2.21.

Table 2.21 The updated limits of integration for D_2 - C_2 symmetrical illumination area.

Side of the surface	Limits for y_1 ($y_1\alpha$ and $y_1\beta$)	Limits for z_1 ($z_1\alpha$ and $z_1\beta$)
S^-	$y_1D_2 \leq y_1 \leq y_1C_2$	$\tan(\varepsilon)y_1 + \frac{h}{\cos(\varepsilon)} \leq z_1 \leq k_{C_2D_2}y_1 + b_{C_2D_2}$
	$y_1C_2 \leq y_1 \leq y_1A_1$	$\tan(\varepsilon)y_1 + \frac{h}{\cos(\varepsilon)} \leq z_1 \leq \tan(\varepsilon)y_1 + \frac{r}{\cos(\varepsilon)}$
	$y_1A_1 \leq y_1 \leq y_1B_1$	$\tan(\varepsilon)y_1 + \frac{h}{\cos(\varepsilon)} \leq z_1 \leq k_{A_1B_1}y_1 + b_{A_1B_1}$
S^+	$y_1D_2 \leq y_1 \leq y_1C_2$	$\tan(\varepsilon)y_1 + \frac{h}{\cos(\varepsilon)} \leq z_1 \leq k_{C_2D_2}y_1 + b_{C_2D_2}$
	$y_1C_2 \leq y_1 \leq y_1B_2$	$\tan(\varepsilon)y_1 + \frac{h}{\cos(\varepsilon)} \leq z_1 \leq \tan(\varepsilon)y_1 + \frac{r}{\cos(\varepsilon)}$
	$y_1B_2 \leq y_1 \leq y_1A_2$	$\tan(\varepsilon)y_1 + \frac{h}{\cos(\varepsilon)} \leq z_1 \leq k_{A_2B_2}y_1 + b_{A_2B_2}$

The approximations for the first, second and four types of polar area are introduced in Figures 2.43-2.45. The third one does not require any approximation. The change of the limits of integration is shown in Tables 2.22–2.24.

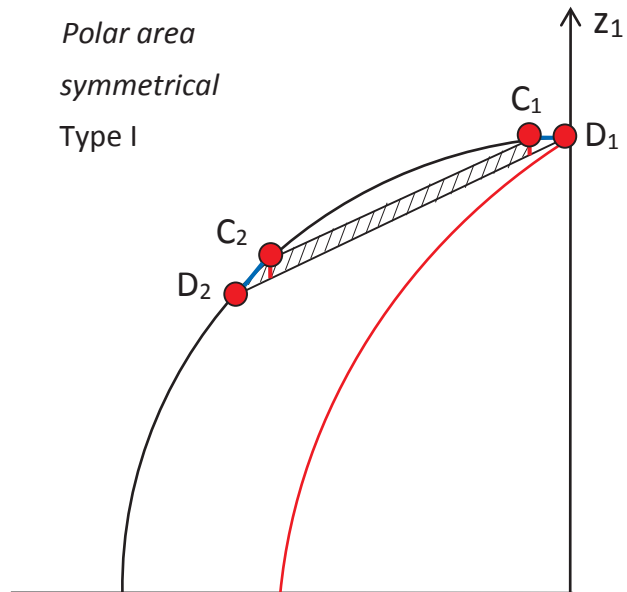


Fig. 2.43 The approximation of the *polar symmetrical Type I* illumination area.

Table 2.22 The updated limits of integration for the *polar symmetrical Type I* illumination area.

Side of the surface	Limits for y_1 ($y_1\alpha$ and $y_1\beta$)	Limits for z_1 ($z_1\alpha$ and $z_1\beta$)
S^-	$y_1D_2 \leq y_1 \leq y_1C_2$	$\tan(\varepsilon)y_1 + \frac{h}{\cos(\varepsilon)} \leq z_1 \leq k_{C_2D_2}y_1 + b_{C_2D_2}$
	$y_1C_2 \leq y_1 \leq y_1C_1$	$\tan(\varepsilon)y_1 + \frac{h}{\cos(\varepsilon)} \leq z_1 \leq \tan(\varepsilon)y_1 + \frac{r}{\cos(\varepsilon)}$
	$y_1C_1 \leq y_1 \leq y_1D_1$	$\tan(\varepsilon)y_1 + \frac{h}{\cos(\varepsilon)} \leq z_1 \leq k_{C_1D_1}y_1 + b_{C_1D_1}$

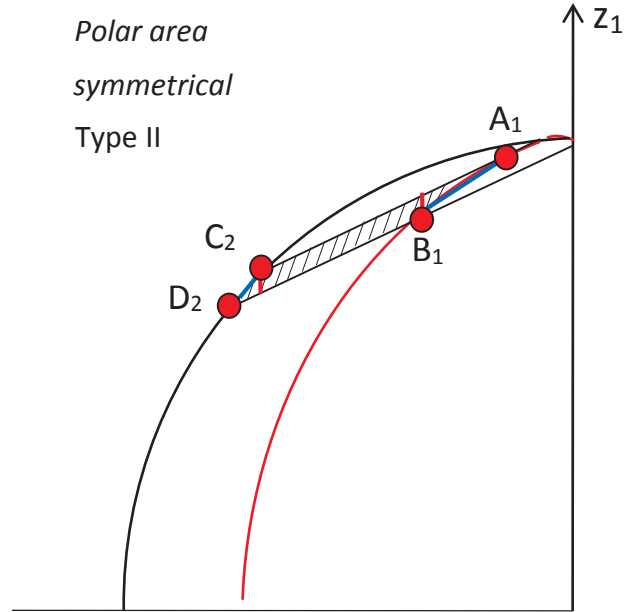


Fig. 2.44 The approximation of the *polar symmetrical* Type II illumination area.

Table 2.23 The updated limits of integration for the *polar symmetrical* Type II illumination area.

Side of the surface	Limits for y_1 ($y_1\alpha$ and $y_1\beta$)	Limits for z_1 ($z_1\alpha$ and $z_1\beta$)
S^-	$y_1D_2 \leq y_1 \leq y_1C_2$	$\tan(\varepsilon)y_1 + \frac{h}{\cos(\varepsilon)} \leq z_1 \leq k_{C_2D_2}y_1 + b_{C_2D_2}$
	$y_1C_2 \leq y_1 \leq y_1B_1$	$\tan(\varepsilon)y_1 + \frac{h}{\cos(\varepsilon)} \leq z_1 \leq \tan(\varepsilon)y_1 + \frac{r}{\cos(\varepsilon)}$
	$y_1B_1 \leq y_1 \leq y_1A_1$	$k_{A_1B_1}y_1 + b_{A_1B_1} \leq z_1 \leq \tan(\varepsilon)y_1 + \frac{r}{\cos(\varepsilon)}$

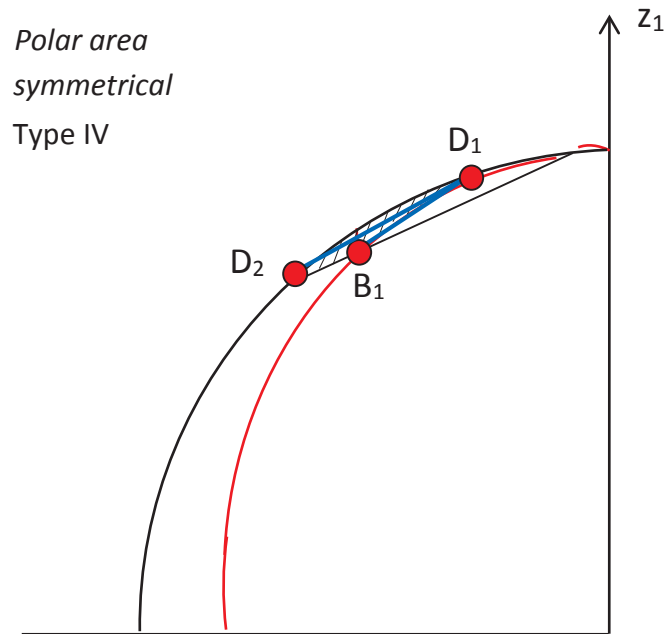


Fig. 2.45 The approximation of the *polar symmetrical* Type IV illumination area.

Table 2.24 The updated limits of integration for the *polar symmetrical* Type IV illumination area.

Side of the surface	Limits for y_1 ($y_1\alpha$ and $y_1\beta$)	Limits for z_1 ($z_1\alpha$ and $z_1\beta$)
S^-	$y_1D_2 \leq y_1 \leq y_1B_1$	$\tan(\varepsilon)y_1 + \frac{h}{\cos \varepsilon} \leq z_1 \leq k_{D_1D_2}y_1 + b_{D_1D_2}$
	$y_1B_1 \leq y_1 \leq y_1D_1$	$k_{B_1D_1}y_1 + b_{B_1D_1} \leq z_1 \leq k_{D_1D_2}y_1 + b_{D_1D_2}$

2.8. The calculation of the area of the latitudinal belt

The projection of a latitudinal belt in YOZ plane and XOY plane are shown in Figure 2.46.

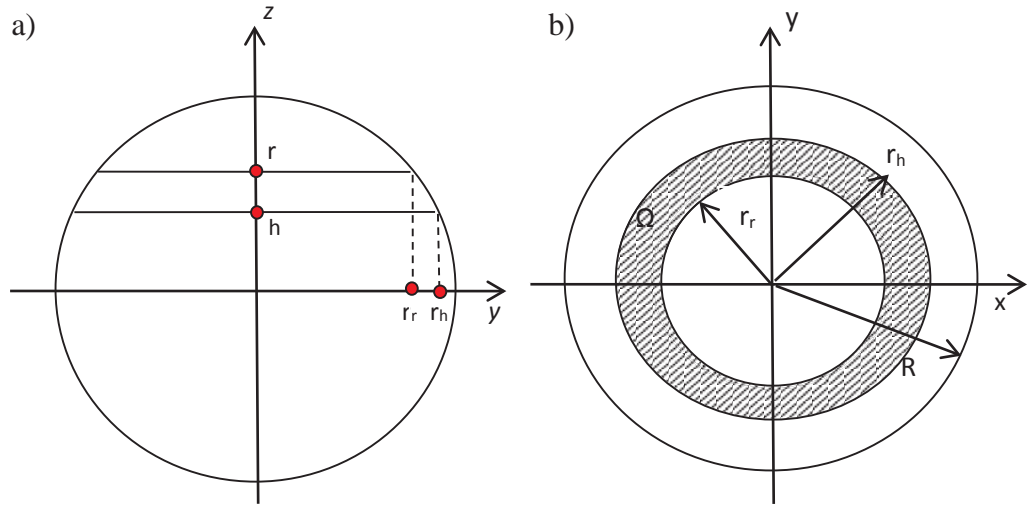


Fig. 2.46 The projection of latitudinal belt in YOZ plane (a) and XOY plane (b).

For computational simplicity the calculations were performed in the XOY plane. The latitudinal belt area was calculated as follows:

$$\begin{aligned}
 S_{belt} &= \iint_{\Omega} \sqrt{1 + \left(\frac{\partial z}{\partial x}\right)^2 + \left(\frac{\partial z}{\partial y}\right)^2} dx dy = \iint_{\Omega} \sqrt{1 + \frac{x^2}{R^2 - x^2 - y^2} + \frac{y^2}{R^2 - x^2 - y^2}} dx dy \\
 &= \iint_{\Omega} \frac{R}{\sqrt{R^2 - x^2 - y^2}} dx dy = \iint_{\Omega_1} \frac{R \rho d\rho d\varphi}{\sqrt{R^2 - \rho^2}} = R \int_0^{2\pi} d\varphi \int_{r_r}^{r_h} \frac{\rho d\rho}{\sqrt{R^2 - \rho^2}} \\
 &= -2\pi R [\sqrt{R^2 - \rho^2}]_{r_r}^{r_h} = 2\pi R(r - h), \tag{2.24}
 \end{aligned}$$

where $x = \rho \cos(\varphi)$, $y = \rho \sin(\varphi)$, $z = \sqrt{R^2 - x^2 - y^2}$, $r_r = \sqrt{R^2 - r^2}$ and $r_h = \sqrt{R^2 - h^2}$ (see Fig. 2.46a) are the radii of upper and lower limits of the belt, respectively.

2.9. Computation and results

In order to get the amount of radiation per square metre (I), the surface areas of the belt and the double integrals were calculated for each latitudinal belt of a width of 10° for the Northern and Southern Hemisphere using the Maple software. The time step for α was chosen to be 10° (~ 10 days). The Maple worksheet for the b-e and e-(Pi/2-E) illumination areas for the Northern Hemisphere is given in Appendix 1 as an example.

The calculations were performed for the period of time from the winter solstice to the

vernal equinox. This corresponds to the first quadrant of the earth orbit starting from the winter solstice ($\alpha=0^\circ$) and going anticlockwise (see Fig. 2.1) to the vernal equinox ($\alpha=90^\circ$). Note that for the winter solstice the computations were actually performed for $\alpha=0.00001^\circ$, since for $\alpha=0^\circ$ a division by zero occurs in the equation of the ellipse which represents a change of the amount of light received by any particular area throughout the year (see Figure 2.4).

Thus a set of nine radiation values has been obtained for both Hemispheres, further referred to as N (0° - 90°) and S (0° - 90°). The amount of radiation per square metre (I) for the rest of the year was obtained as shown in Table 2.25 by combining these sets and rearranging data in them.

Table 2.25 Calculations of the insolation for the whole year period for the Northern and Southern Hemispheres.

Quadrant of circle and the corresponding period of time	Radiation values	
	Northern Hemisphere	Southern Hemisphere
I (winter solstice-vernal equinox)	N (0° - 90°)	S (90° - 0°)
II (vernal equinox- summer solstice)	S (0° - 90°)	N (90° - 0°)
III (summer solstice- autumnal equinox)	S (0° - 90°)	N (0° - 90°)
IV (autumnal equinox- winter solstice)	N (90° - 0°)	S (90° - 0°)

Note also that it is easy to modify the procedure for thinner belts for more accuracy. After applying the approximation technique the computations were performed in the Maple software. The amount of insolation for any particular time of the year for any latitudinal belt was calculated from the previously derived formulae. The results for a complete year cycle for the Northern Hemispheres are shown in Figures 2.47-2.48.

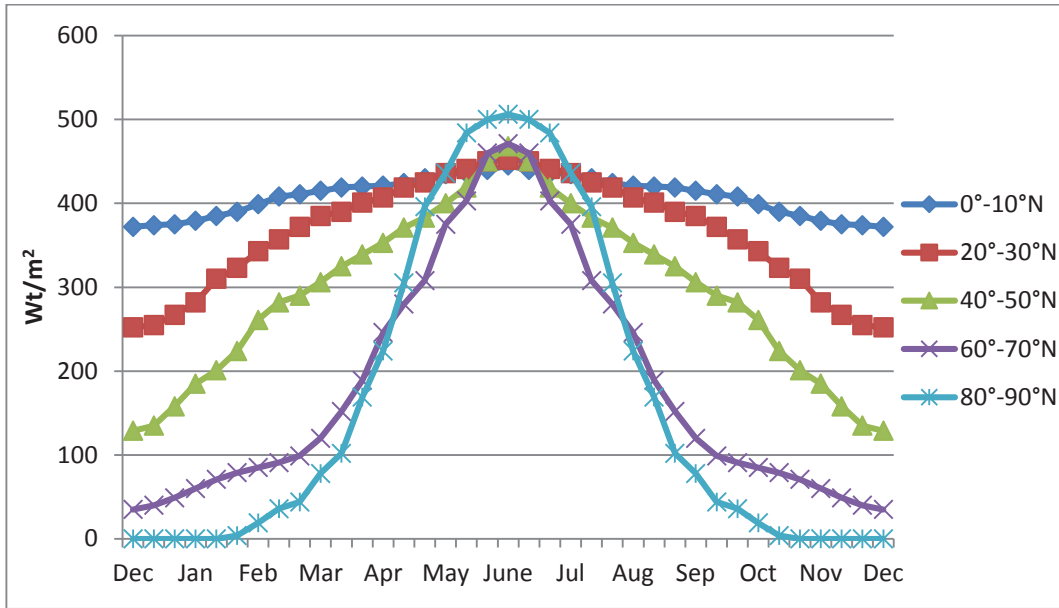


Fig. 2.47 The amount of radiation received by odd latitudinal belts in the Northern Hemisphere.

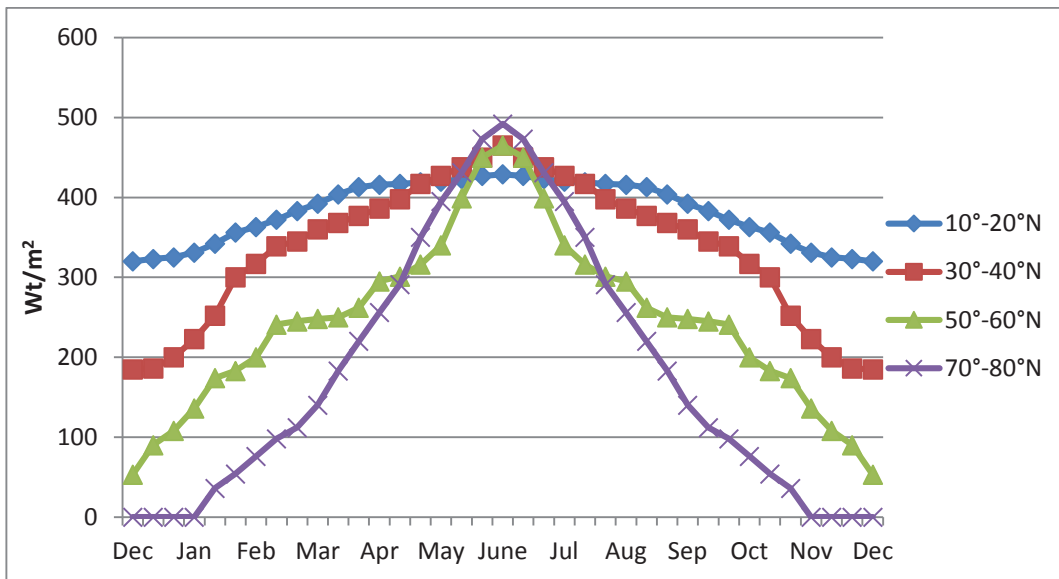


Fig.2.48 The amount of radiation received by even latitudinal belts in the Northern Hemisphere.

The results for a complete year cycle for the Southern Hemispheres are shown in Figures 2.49-2.50.

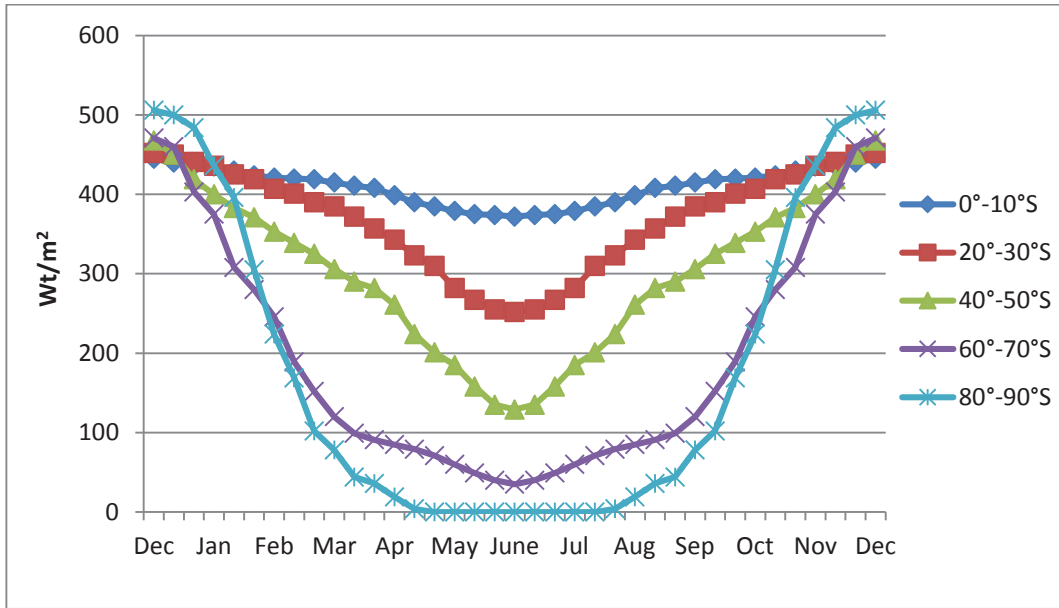


Fig. 2.49 The amount of radiation received by odd latitudinal belts in the Southern Hemisphere.

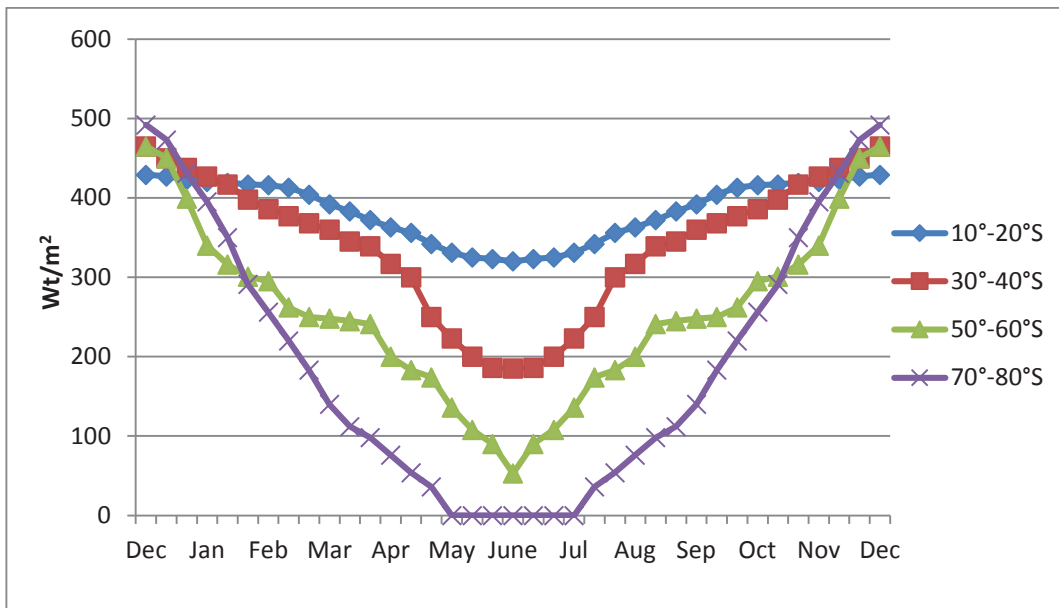


Fig. 2.50 The amount of radiation received by even latitudinal belts in the Southern Hemisphere.

Note that smoother curves would result from using a smaller step size for α .

We have also calculated the annual average value for each latitudinal belt and compare it with satellite data. This data was obtained from the NASA Langley Research Centre Atmospheric Science Data Centre Surface meteorological and Solar Energy (SSE)

web portal supported by the NASA LaRC POWER Project¹.

Note that the data in the source is given in terms of 1° resolution so we have averaged this over the 10° latitudinal belt. The results of comparison are shown in Table 2.26.

Table 2.26 Comparison of the obtained results with satellite data.

Latitudinal belt	Satellite data (Wt/m ²)	Proposed model (Wt/m ²)	Accuracy
0°-10°	415.00	408.40	0.99
10°-20°	398.45	381.65	0.97
20°-30°	378.29	376.20	0.99
30°-40°	359.76	346.50	0.99
40°-50°	304.33	300.83	0.99
50°-60°	257.78	251.33	0.97
60°-70°	220.00	213.22	0.97
70°-80°	182.02	172.50	0.95
80°-90°	169.89	159.17	0.94
Average			0.97

The results show very good agreement for equatorial and middle latitudes region with an average accuracy of 98%. Slightly less agreement (94.5%) can be observed in the polar regions which are known to be difficult to model. The average accuracy of the model is 97%.

In this Chapter, we have presented the novel insolation model for calculating the insolation at the top of the atmosphere. The full model description and the approach for calculating insolation are introduced. We have also described an approximation technique used and the computational procedure. Finally, the results for the amount of insolation for every latitudinal belt at any particular time and a comparison of the annual averages with satellite data are presented.

¹ https://eosweb.larc.nasa.gov/sse/global/text/22yr_toa_dwn

Chapter 3 Incorporation of the proposed model into global climate model C-GOLDSTEIN

In Chapter 2, a new insolation model has been proposed where the radiation is modelled as a flux coming from space. The amount of insolation received by every latitudinal belt throughout the year has been obtained. After comparison with satellite data from NASA, very good agreement was observed for equatorial and middle latitudes regions, with slightly less agreement for the polar regions. The average accuracy of the model is 97%.

In this Chapter we aim to incorporate the proposed insolation model into the Earth System Model of Intermediate Complexity C-GOLDSTEIN. The purpose of this is to incorporate seasonal variations of insolation into C-GOLDSTEIN, as well as testing the performance of the proposed model in the context of a global climate model.

C-GOLDSTEIN is an EMIC developed by (Marsh, et al., 2002), which allows forecasts in the order of millennia within a relatively short computational time. A full description of the model is provided in Section 1.3.2. Here, we focus only on those parts which are related to computing insolation. Tests of running C-GOLDSTEIN with the annual average insolation obtained from the model proposed in Chapter 2, as well as their comparison with the yearly averages used previously in C-GOLDSTEIN, are discussed in Section 3.1. The details of the incorporation of seasonal variations of insolation into the C-GOLDSTEIN software are given in Section 3.2.

3.1. The verification and comparison of the results for the annual average insolation

The annual amount of radiation received in the original version of C-GOLDSTEIN was approximated by the second order Legendre polynomials (North, 1975):

$$S(x) \cong 1 + S_2 P_2(x), \tag{3.1}$$

where $S(x)$ is the mean annual distribution of radiation reaching the top of the atmosphere, x is the sine of latitude, $S_2 = -0.477$ is a constant, and $P_2(x) = \frac{1}{2}(3x^2 - 1)$ is the second Legendre polynomial (North, et al., 1981). These calculations were initially

performed in one of the subroutines of the global climate model where the atmosphere is initialized prior to the start of iterations. The average annual values used there were replaced by the annual average values obtained from our proposed model (see Table 2.25) and the software was then run. The results for the new annual temperature distribution are presented in Figure 3.1. Note that C-GOLDSTEIN has a latitudinal resolution of 20° near the polar regions. Thus, we chose to extend the value for the 70°-80° belt to the 80°-90° latitudinal belt.

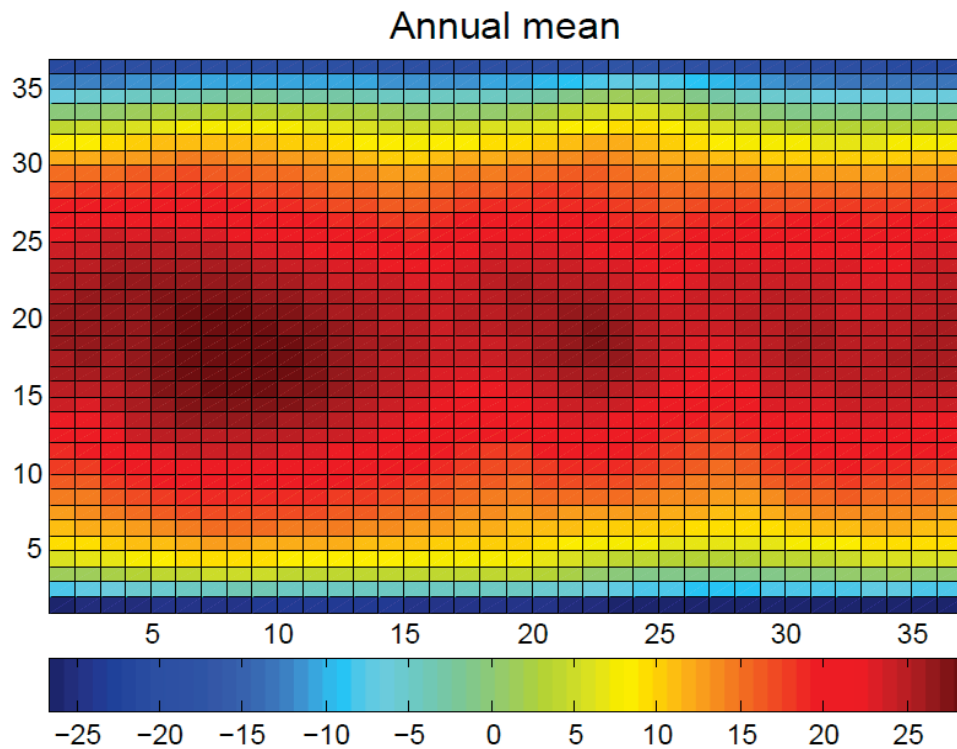


Fig. 3.1 The annual mean temperature distribution.

The results were then compared with the annual mean distribution temperature map obtained from NOAA-CIRES Climate Diagnostics Center, Boulder, Colorado².

The comparison indicates that, in general, the temperature distribution is realistic. The hot spots related to the continents are evident in the centre of the map. Also, the average annual temperature for the South pole region is lower than that for the North pole region and this can also be observed in the real temperature map.

Then the yearly averages of the proposed model compared previously (Table 2.26) with satellite data from NASA have also been compared with annual average results

² http://www-das.uwyo.edu/~geerts/cwx/notes/chap16/geo_clim.html

obtained from the initial component of C-GOLDSTEIN. The comparison of the results is shown in Table 3.1.

Table 3.1 The comparison of the results of initial and proposed insolation models.

Latitudinal belt	Satellite data (Wt/m ²)	Proposed insolation model (Wt/m ²)	The insolation component of C-GOLDSTEIN (Wt/m ²)	Accuracy	
				Proposed insolation model	The insolation component of C-GOLDSTEIN
0°-10°	415.00	408.40	420.67	0.99	0.99
10°-20°	398.45	381.65	407.33	0.97	0.98
20°-30°	378.29	376.20	380.33	0.99	0.99
30°-40°	359.76	346.50	339.00	0.99	0.94
40°-50°	304.33	300.83	295.00	0.99	0.97
50°-60°	257.78	251.33	253.00	0.97	0.98
60°-70°	220.00	213.22	217.00	0.97	0.99
70°-80°	182.02	172.50	192.00	0.95	0.95
80°-90°	169.89	172.50	192.00	0.98	0.87
Average				0.9785	0.96

The results obtained indicate a 2% increase in the average accuracy compared to the insolation values used previously in C-GOLDSTEIN. Also, there is a significant increase in accuracy for the furthest polar belt.

3.2. Incorporation of seasonal variations of insolation into C-GOLDSTEIN

Note that the integral formulae resulting from the proposed model in Chapter 2 cannot be evaluated exactly in any computational code. Therefore, some kind of

approximation needs to be used for the incorporation of the data from Figures 2.47-2.50 into the code of C-GOLDSTEIN. In Sections 3.2.1 and 3.2.2, a curve fitting procedure used for this purpose is described. In Section 3.2.3, the process of code implementation and the results of seasonal simulations of insolation within C-GOLDSTEIN are provided.

3.2.1. A curve fitting procedure for latitudinal belts in the Northern Hemisphere

The amount of insolation for every latitudinal belt throughout the year is presented in Figures 2.47-2.50. In order to allow the incorporation of those curves into the code of the C-GOLDSTEIN, they were approximated by functions of several different types. Note that this time the approximation for the 70°-80° and 80°-90° latitudinal belts was done separately in order to obtain higher accuracy for the seasonal variations of insolation. The averaged value was then used over the 70°-90° region in the code for each time step.

The curves corresponding to the first two latitudinal belts (0°-10° and 10°-20°), which have the least variation, were approximated by a wave function. The curves corresponding to the remaining latitudinal belts were approximated by piecewise continuous functions. In particular, the 30°-40°, 40°-50°, 60°-70° and 70°-80° latitudinal belt curves were best approximated by straight line sections; the best fit for the 20°-30° latitudinal belt was a combination of a wave function and the straight lines. The remaining latitudinal belts which displayed a more complicated shape (50°-60° and 80°-90°) were approximated by the combination of several wave functions and straight lines.

The approximation functions are given below. The number of intervals is 37, since the calculations in Chapter 2 were performed for the time step corresponding to $\alpha=10^\circ$, plus one additional step required to return to the original position.

$$0^\circ\text{-}10^\circ: y_1(t) = A_{1,1} \sin(\omega_{1,1}t + \varphi_{1,1}) + B_{1,1}, \quad (3.2)$$

$$10^\circ\text{-}20^\circ: y_2(t) = A_{1,2} \sin(\omega_{1,2}t + \varphi_{1,2}) + B_{1,2}, \quad (3.3)$$

$$20^\circ\text{-}30^\circ: y_3(t) = \begin{cases} E_3, & t = 1, \\ C_{1,3}t + D_{1,3}, & 2 \leq t \leq 4, \\ A_{1,3}\sin(\omega_{1,3}t + \varphi_{1,3}) + B_{1,3}, & 5 \leq t \leq 33, \\ C_{2,3}t + D_{2,3}, & 34 \leq t \leq 36, \\ E_3, & t = 37. \end{cases} \quad (3.4)$$

$$30^\circ\text{-}40^\circ: y_4(t) = \begin{cases} E_4, & t = 1, \\ C_{1,4}t + D_{1,4}, & 2 \leq t \leq 5, \\ C_{3,4}t + D_{3,4}, & 6 \leq t \leq 19, \\ C_{4,4}t + D_{4,4}, & 20 \leq t \leq 32, \\ C_{2,4}t + D_{2,4}, & 33 \leq t \leq 36, \\ E_4, & t = 37. \end{cases} \quad (3.5)$$

$$40^\circ\text{-}50^\circ: y_5(t) = \begin{cases} C_{1,5}t + D_{1,5}, & 1 \leq t \leq 19, \\ C_{2,5}t + D_{2,5}, & 20 \leq t \leq 37. \end{cases} \quad (3.6)$$

$$50^\circ\text{-}60^\circ: y_6(t) = \begin{cases} C_{1,6}t + D_{1,6}, & 1 \leq t \leq 8, \\ A_{2,6}\sin(\omega_{2,6}t + \varphi_{2,6}) + B_{2,6}, & 9 \leq t \leq 16, \\ A_{1,6}\sin(\omega_{1,6}t + \varphi_{1,6}) + B_{1,6}, & 17 \leq t \leq 21, \\ A_{3,6}\sin(\omega_{3,6}t + \varphi_{3,6}) + B_{3,6}, & 22 \leq t \leq 29, \\ C_{2,6}t + D_{2,6}, & 30 \leq t \leq 37. \end{cases} \quad (3.7)$$

$$60^\circ\text{-}70^\circ: y_7(t) = \begin{cases} C_{1,7}t + D_{1,7}, & 1 \leq t \leq 9, \\ C_{3,7}t + D_{3,7}, & 10 \leq t \leq 19, \\ C_{4,7}t + D_{4,7}, & 20 \leq t \leq 28, \\ C_{2,7}t + D_{2,7}, & 29 \leq t \leq 37. \end{cases} \quad (3.8)$$

$$70^\circ\text{-}80^\circ: y_8(t) = \begin{cases} E_8, & 1 \leq t \leq 6, \\ C_{1,8}t + D_{1,8}, & 5 \leq t \leq 9, \\ C_{3,8}t + D_{3,8}, & 10 \leq t \leq 19, \\ C_{4,8}t + D_{4,8}, & 20 \leq t \leq 28, \\ C_{2,8}t + D_{2,8}, & 29 \leq t \leq 33, \\ E_8, & 34 \leq t \leq 37. \end{cases} \quad (3.9)$$

$$80^\circ\text{-}90^\circ: y_9(t) = \begin{cases} E_9, & 1 \leq t \leq 6, \\ A_{2,9}\sin(\omega_{2,9}t + \varphi_{2,9}) + B_{2,9}, & 7 \leq t \leq 12, \\ C_{1,9}t + D_{1,9}, & 13 \leq t \leq 14, \\ A_{1,9}\sin(\omega_{1,9}t + \varphi_{1,9}) + B_{1,9}, & 15 \leq t \leq 23, \\ C_{2,9}t + D_{2,9}, & 24 \leq t \leq 25, \\ A_{3,9}\sin(\omega_{3,9}t + \varphi_{3,9}) + B_{3,9}, & 26 \leq t \leq 31, \\ E_9, & 32 \leq t \leq 37. \end{cases} \quad (3.10)$$

Here the coefficients found for an optimal fit for the straight lines are the slopes (3.11) and the intercepts (3.12). The coefficients of the straight lines were found by simply interpolating two given points. E_i , $i \in \{3,4,8,9\}$, is the constant obtained from the original plot.

$$C_{j,i}, i \in \begin{cases} \{3,4,5,6,7,8,9\}, & j = 1,2, \\ \{7,8\}, & j = 3,4. \end{cases} \quad (3.11)$$

$$D_{j,i}, i \in \begin{cases} \{3,4,5,6,7,8,9\}, & j = 1,2, \\ \{7,8\}, & j = 3,4. \end{cases} \quad (3.12)$$

The coefficients to be chosen for an optimal fit for the wave functions are the amplitudes (3.13), vertical shifts (3.14), angular velocities (3.15), and phases (3.16).

$$A_{j,i}, i \in \begin{cases} \{1,2,3,6,9\}, & j = 1, \\ \{6,9\}, & j = 2,3. \end{cases} \quad (3.13)$$

$$B_{j,i}, i \in \begin{cases} \{1,2,3,6,9\}, & j = 1, \\ \{6,9\}, & j = 2,3. \end{cases} \quad (3.14)$$

$$\varphi_{j,i}, i \in \begin{cases} \{1,2,3,6,9\}, & j = 1, \\ \{6,9\}, & j = 2,3. \end{cases} \quad (3.15)$$

$$\omega_{j,i}, i \in \begin{cases} i \in \{1,2,3,6,9\}, & j = 1, \\ i \in \{6,9\}, & j = 2,3. \end{cases} \quad (3.16)$$

In order to find the amplitudes and the vertical shifts of the wave function, the ordinary least square method was used. The angular velocities were fixed as $\omega_{i,j} = \frac{2\pi}{k_{i,j}}$, where $k_{i,j}$ denotes the number of intervals over which the wave function is defined. The values for i and j indexes for k are the same as for $\omega_{i,j}$ (3.16). The values for the phases ($\varphi_{j,i}$) were chosen manually after examining the plot obtained after the first round of optimisation.

Let λ denote the combination of all $A_{j,i}$ and $B_{j,i}$. Then for each $i \in \{1,2,3,6,9\}$,

$$F_i(\lambda) = \text{minimise } \sum_{t=1}^n (y_i(t) - f_i(t))^2. \quad (3.17)$$

where $f_i(t)$ is the amount of insolation obtained from the proposed insolation model for the latitudinal belt i , $y_i(t)$ is the approximated value obtained for the latitudinal belt i ; n is the number of intervals, and t is time.

The optimisation was performed in MS Excel using ‘The Solver’ add-in. The Generalised Reduced Gradient (GRG) non-linear solving method was used. Estimates for the amplitudes ($\overline{A_{i,j}}$) and estimates for the vertical shifts ($\overline{B_{i,j}}$) were calculated as follows:

$$\overline{A_{l,j}} = 0.5\max(\sum_{t=k}^m y_i(t)) - 0.5\min(\sum_{t=k}^m y_i(t)), \quad (3.18)$$

$$\overline{B_{l,j}} = 0.5 \max(\sum_{t=k}^m y_i(t)) + 0.5\min(\sum_{t=k}^m y_i(t)), \quad (3.19)$$

for each $i \in \{1,2,3,6,9\}$.

For each $j \in \{1,2,3\}$, k and m are the beginning and endpoints of the domain over which the corresponding wave functions are defined. Based on these, upper bounds for each amplitude and lower bounds for each vertical shift were then chosen so as to allow a reasonable range for the parameters to be optimised. Note that the Solver command only determines locally optimal solutions and without the specified bounds, a physically unreasonable solution can result.

After performing the optimisation in this way, an optimal solution was reached. In case of the optimal value reaching the constraint value, the corresponding bounds were shifted further in order to allow an improved and physically reasonable solution to be obtained. The resulting curves are presented in Figures 3.2-3.10.

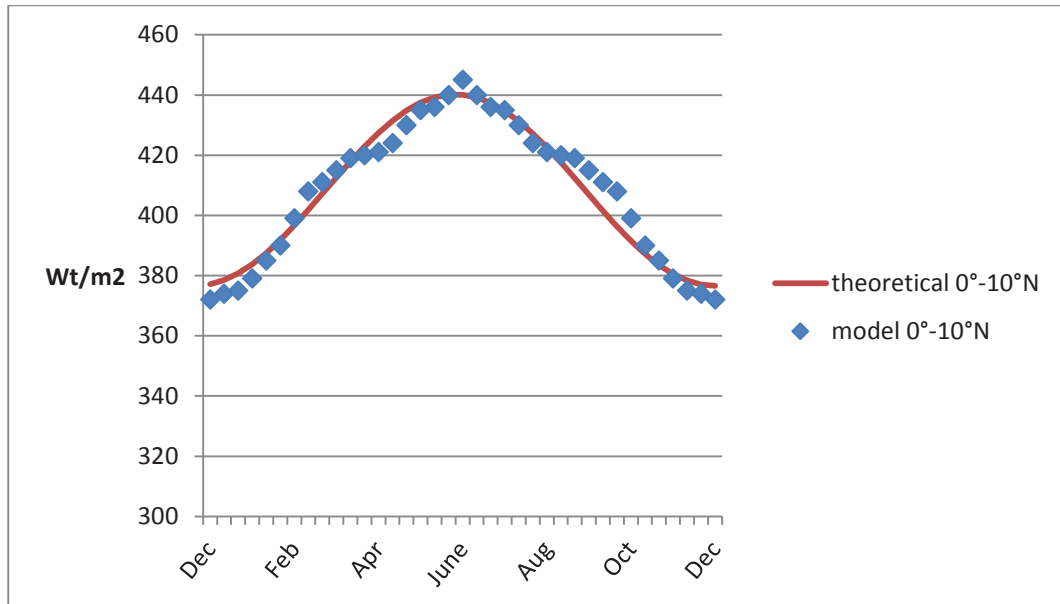


Fig. 3.2 Curve fitting for 0°-10°N latitudinal belt.

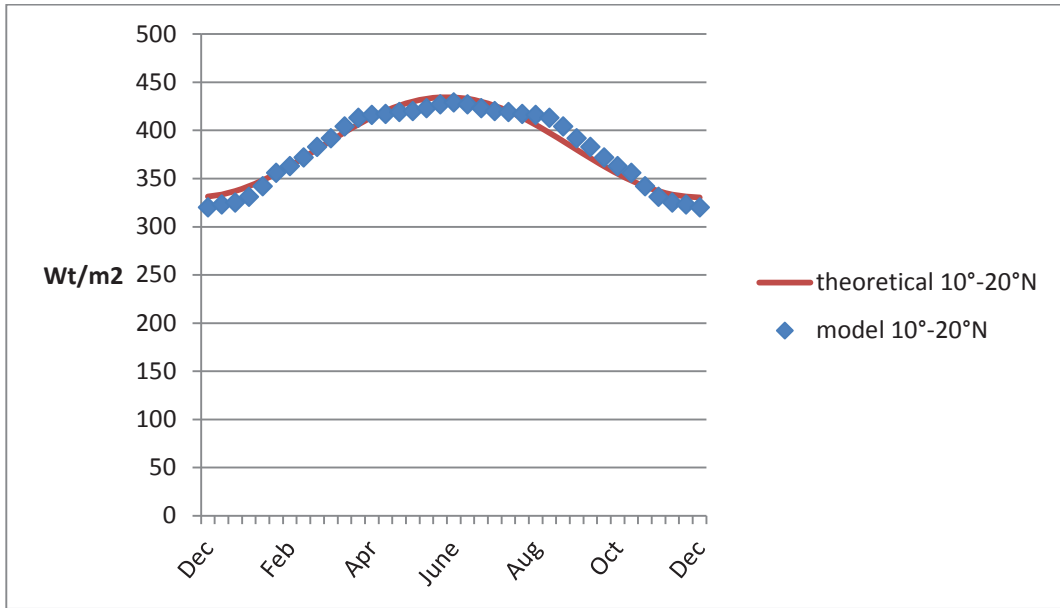


Fig. 3.3 Curve fitting for 10°-20°N latitudinal belt.

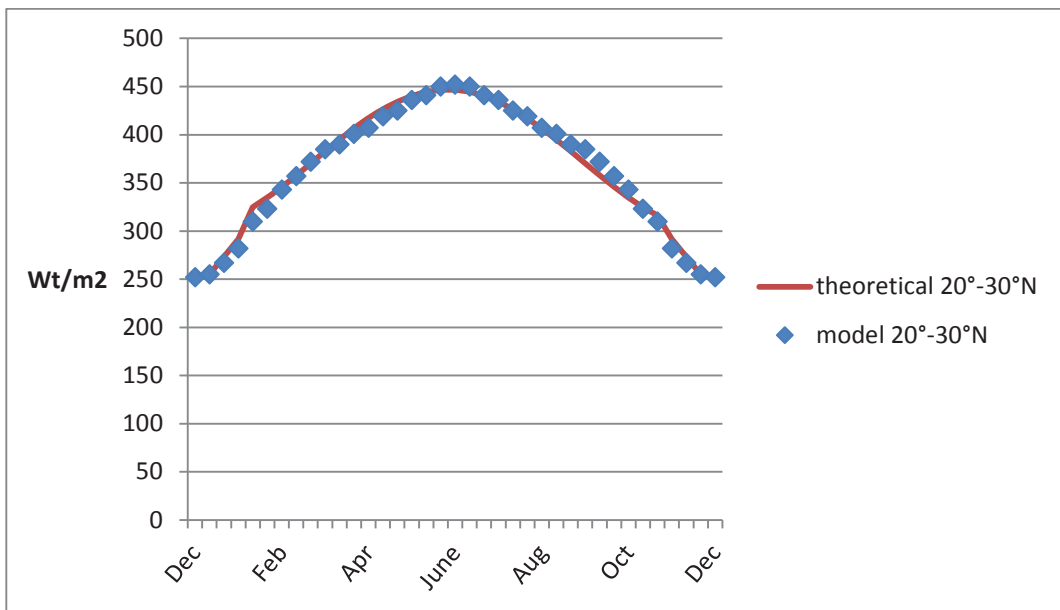


Fig. 3.4 Curve fitting for 20°-30°N latitudinal belt.

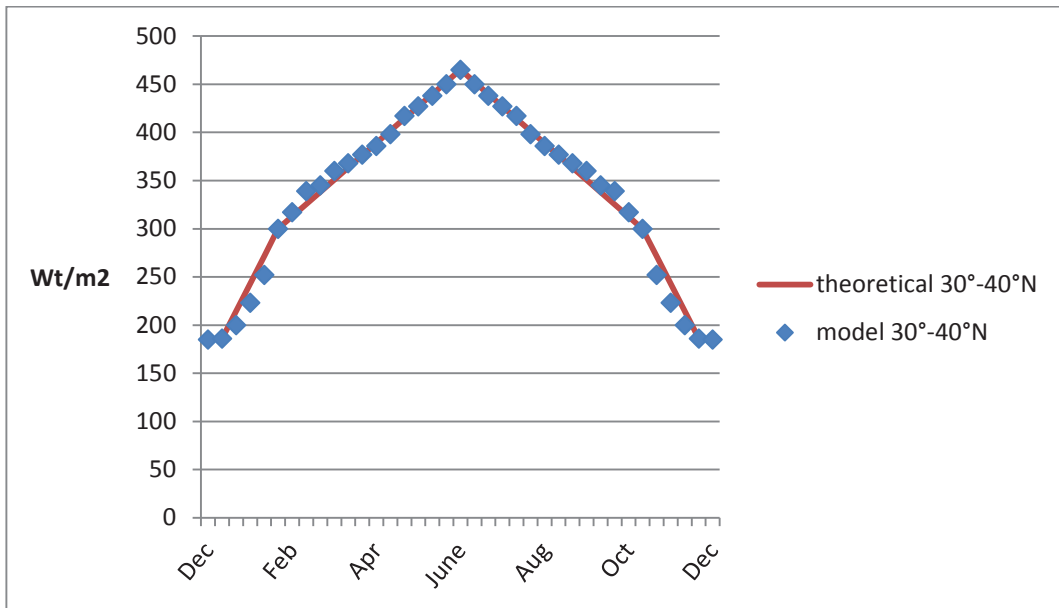


Fig. 3.5 Curve fitting for 30°-40°N latitudinal belt.

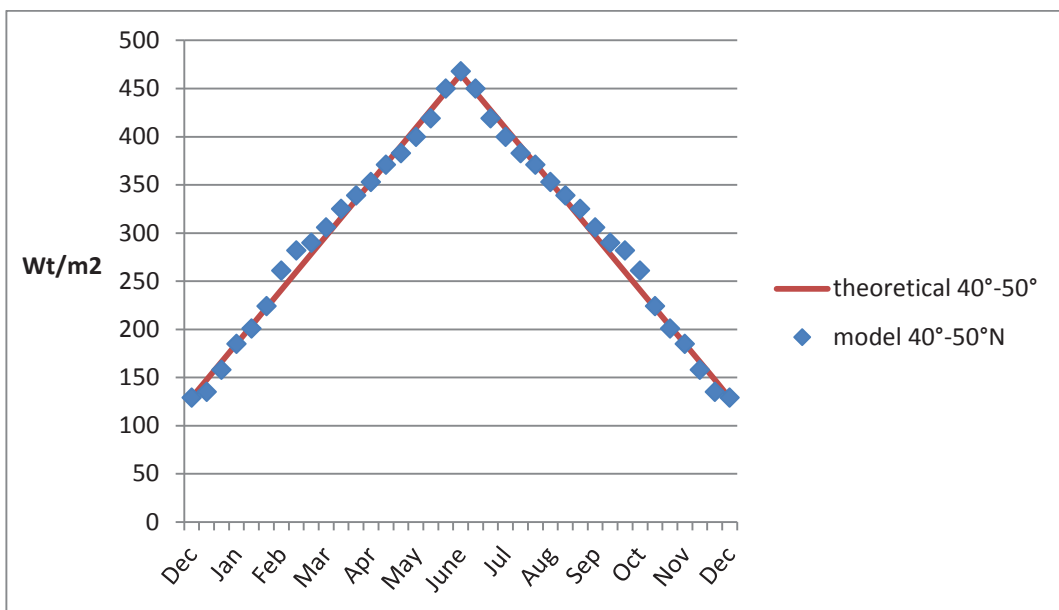


Fig. 3.6 Curve fitting for 40°-50°N latitudinal belt.

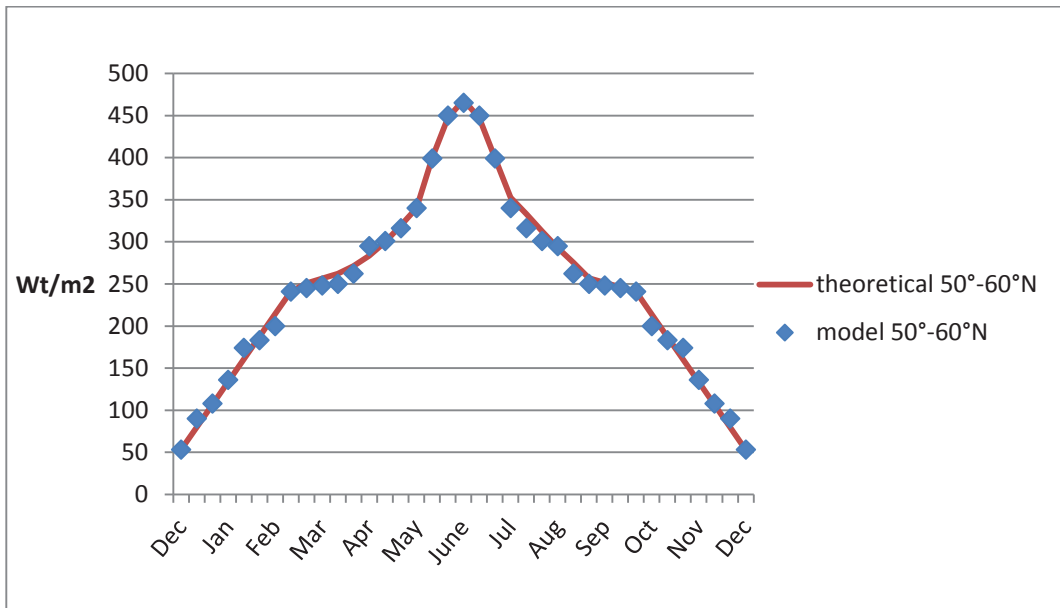


Fig. 3.7 Curve fitting for 50°-60°N latitudinal belt.

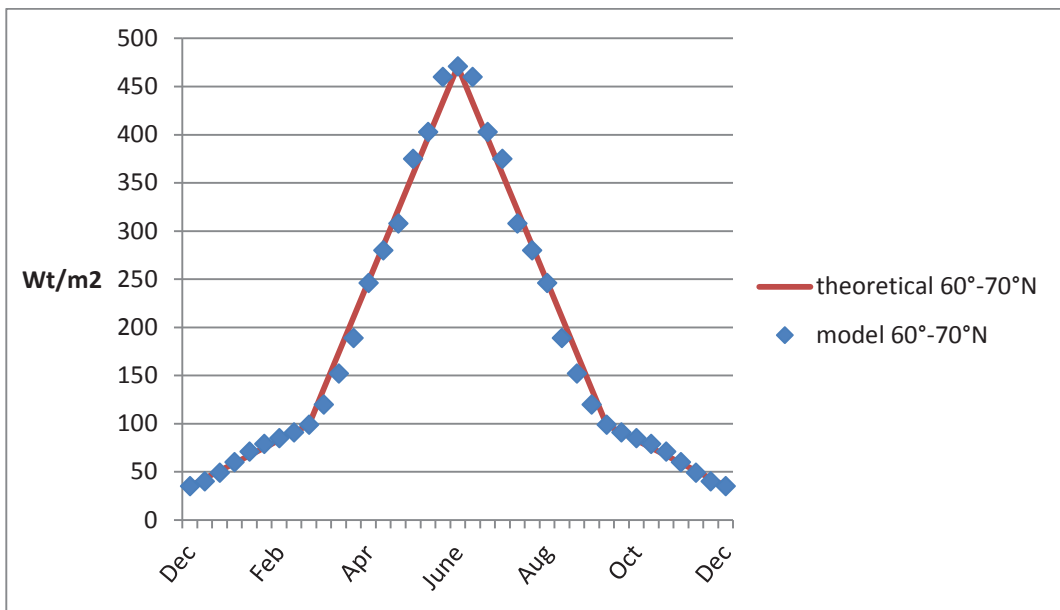


Fig. 3.8 Curve fitting for 60°-70°N latitudinal belt.

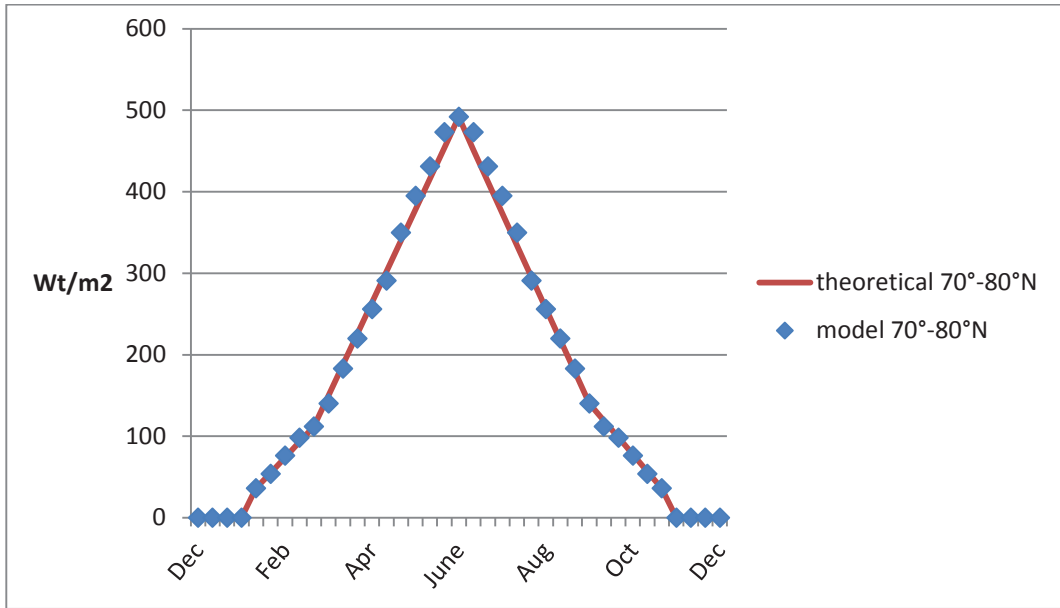


Fig. 3.9 Curve fitting for 70°-80°N latitudinal belt.

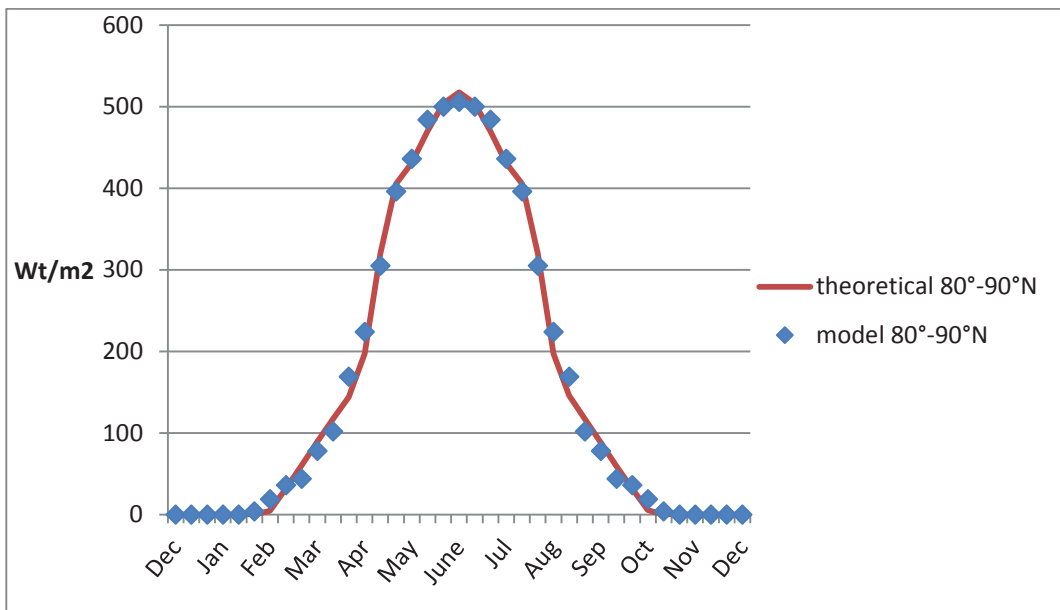


Fig. 3.10 Curve fitting for 80°-90°N latitudinal belt.

The coefficients used for the straight line sections are listed in Tables 3.2-3.3. The optimised coefficients for the wave functions can be found in Tables 3.4-3.6. Finally, the information about the total error estimate is provided in Table 3.7.

Table 3.2 The coefficients of the straight lines ($C_{1,i}$, $C_{2,i}$, $D_{1,i}$, $D_{2,i}$, E_i).

Latitudinal belt	i	Coefficients				
		$C_{1,i}$	$D_{1,i}$	$C_{2,i}$	$D_{2,i}$	E_i
20°-30°	3	18.33	218.33	-18.33	914.89	252
30°-40°	4	28.5	129	-28.5	1212	185
40°-50°	5	18.67	110.33	-18.67	819.73	-
50°-60°	6	26.86	26.14	-26.86	1046.71	-
60°-70°	7	8	27	-8	331	-
70°-80°	8	19	-59	-20.8	722.4	0
80°-90°	9	87.25	-903.19	-87.25	2412.36	0

Table 3.3 The coefficients of the straight lines ($C_{3,i}$, $C_{4,i}$, $D_{3,i}$, $D_{4,i}$).

Latitudinal belt	i	Coefficients			
		$C_{3,i}$	$D_{3,i}$	$C_{4,i}$	$D_{4,i}$
30°-40°	4	12.7	223.85	-12.7	706.3
60°-70°	7	37.2	-235.8	-37.2	1177.8
70°-80°	8	38.89	-248.89	-38.89	1228.91

Table 3.4 The coefficients of wave functions ($A_{1,i}$, $B_{1,i}$, $\omega_{1,i}$, $\varphi_{1,i}$).

Latitudinal belt	i	Coefficients			
		$A_{1,i}$	$B_{1,i}$	$\omega_{1,i}$	$\varphi_{1,i}$
0°-10°	1	31.79	408.44	0.17	-1.57
10°-20°	2	52.05	382.59	0.17	-1.57
20°-30°	3	73.60	373.30	0.17	-1.57
50°-60°	6	56.07	412.54	0.9	9.6
80°-90°	9	57.65	459.93	0.7	0.84

Table 3.5 The coefficients of wave functions ($A_{2,i}$, $B_{2,i}$, $\omega_{2,i}$, $\varphi_{2,i}$).

Latitudinal belt	i	Coefficients			
		$A_{2,i}$	$B_{2,i}$	$\omega_{2,i}$	$\varphi_{2,i}$
50°-60°	6	100	345.68	0.3	1.59
80°-90°	9	168.84	67.39	0.17	-1.57

Table 3.6 The coefficients of wave functions ($A_{3,i}$, $B_{3,i}$, $\omega_{3,i}$, $\varphi_{3,i}$).

Latitudinal belt	i	Coefficients			
		$A_{3,i}$	$B_{3,i}$	$\omega_{3,i}$	$\varphi_{3,i}$
50°-60°	6	63.43	307.22	0.3	2.33
80°-90°	9	171.26	96.5	0.17	-1.57

Table 3.7. Total error estimation.

Latitudinal belt	F_i	Latitudinal belt	F_i	Latitudinal belt	F_i
0°-10°	812.05	30°-40°	2272.13	60°-70°	4875.2
10°-20°	2555.90	40°-50°	3386.1	70°-80°	3000.05
20°-30°	1775.21	50°-60°	3385.3	80°-90°	4065.32

In order to verify how well the values from the proposed model are replicated by the approximation, the R squared test was applied. The R^2 coefficient was computed using “Data Analysis” add-in in MS Excel. The “Regression” analysis tool was used. The results of the goodness of the fit for each latitudinal belt are presented in Table 3.8.

Table 3.8 The results of calculations of the R^2 coefficient for each latitudinal belt.

Latitudinal belt	R^2
0°-10°N	0.9783
10°-20°N	0.9560
20°-30°N	0.9892
30°-40°N	0.9914
40°-50°N	0.9911
50°-60°N	0.9951
60°-70°N	0.9939
70°-80°N	0.9981
80°-90°N	0.9958

The R^2 coefficient for all the latitudinal belts is greater than the required 95% confidence level. In particular, for the latitudinal belts from 30° onwards, its value is 99%. Thus the conclusion can be drawn that the fitted curves are appropriate for approximating the values obtained from the proposed model.

3.2.2. A curve fitting procedure for latitudinal belts in the Southern Hemisphere

For the Southern Hemisphere, the following changes were made to the curves. These essentially correspond to a shift of the curves for the northern hemisphere by 6 months.

$$0^\circ\text{-}10^\circ: y_1(t) = A_{1,1} \sin(\omega_{1,1}(t + 18) + \varphi_{1,1}) + B_{1,1}, \quad (3.20)$$

$$10^\circ\text{-}20^\circ: y_2(t) = A_{1,2} \sin(\omega_{1,2}(t + 18) + \varphi_{1,2}) + B_{1,2}, \quad (3.21)$$

$$20^\circ\text{-}30^\circ: y_3(t) = \begin{cases} A_{1,3} \sin(\omega_{1,3}(t + 18) + \varphi_{1,3}) + B_{1,3}, & 1 \leq t \leq 15, \\ C_{2,3}(t + 18) + D_{2,3}, & 16 \leq t \leq 18, \\ E_3, & 19 \leq t \leq 20, \\ C_{1,3}(t - 18) + D_{1,3}, & 21 \leq t \leq 23, \\ A_{1,3} \sin(\omega_{1,3}(t - 18) + \varphi_{1,3}) + B_{1,3}, & 24 \leq t \leq 37. \end{cases} \quad (3.22)$$

$$30^\circ\text{-}40^\circ: y_4(t) = \begin{cases} C_{4,4}(t+18) + D_{4,4}, & 1 \leq t \leq 14, \\ C_{2,4}(t+18) + D_{2,4}, & 15 \leq t \leq 18, \\ E_4, & 19 \leq t \leq 20, \\ C_{1,4}(t-18) + D_{1,4}, & 21 \leq t \leq 24, \\ C_{3,4}(t-18) + D_{3,4}, & 25 \leq t \leq 37. \end{cases} \quad (3.23)$$

$$40^\circ\text{-}50^\circ: y_5(t) = \begin{cases} C_{2,5}(t+18) + D_{2,5}, & 1 \leq t \leq 19, \\ C_{1,5}(t-18) + D_{1,5}, & 20 \leq t \leq 37. \end{cases} \quad (3.24)$$

$$50^\circ\text{-}60^\circ: y_6(t) = \begin{cases} A_{1,6}\sin(\omega_{1,6}(t+18) + \varphi_{1,6}) + B_{1,6}, & 1 \leq t \leq 3, \\ A_{3,6}\sin(\omega_{2,6}(t+18) + \varphi_{2,6}) + B_{2,6}, & 4 \leq t \leq 11, \\ C_{2,6}(t+18) + D_{2,6}, & 12 \leq t \leq 19, \\ C_{1,6}(t-18) + D_{1,6}, & 20 \leq t \leq 26, \\ A_{2,6}\sin(\omega_{2,6}(t-18) + \varphi_{2,6}) + B_{2,6}, & 27 \leq t \leq 34, \\ A_{1,6}\sin(\omega_{1,6}(t-18) + \varphi_{1,6}) + B_{1,6}, & 35 \leq t \leq 37. \end{cases} \quad (3.25)$$

$$60^\circ\text{-}70^\circ: y_7(t) = \begin{cases} C_{4,7}(t+18) + D_{4,7}, & 1 \leq t \leq 9, \\ C_{2,7}(t+18) + D_{2,7}, & 10 \leq t \leq 19, \\ C_{1,7}(t-18) + D_{1,7}, & 20 \leq t \leq 28, \\ C_{3,7}(t-18) + D_{3,7}, & 29 \leq t \leq 37. \end{cases} \quad (3.26)$$

$$70^\circ\text{-}80^\circ: y_8(t) = \begin{cases} C_{4,8}(t+18) + D_{4,8}, & 1 \leq t \leq 10, \\ C_{2,8}(t+18) + D_{2,8}, & 11 \leq t \leq 15, \\ E_8, & 16 \leq t \leq 22, \\ C_{1,8}(t-18) + D_{1,8}, & 23 \leq t \leq 27, \\ C_{3,8}(t-18) + D_{3,8}, & 28 \leq t \leq 37. \end{cases} \quad (3.27)$$

$$80^\circ\text{-}90^\circ: y_9(t) = \begin{cases} A_{1,9}\sin(\omega_{1,9}(t+18) + \varphi_{1,9}) + B_{1,9}, & 1 \leq t \leq 5, \\ C_{2,9}(t+18) + D_{2,9}, & 6 \leq t \leq 7, \\ A_{3,9}\sin(\omega_{3,9}(t+18) + \varphi_{3,9}) + B_{3,9}, & 8 \leq t \leq 13, \\ E_9, & 14 \leq t \leq 24, \\ A_{2,9}\sin(\omega_{2,9}(t-18) + \varphi_{2,9}) + B_{2,9}, & 25 \leq t \leq 30, \\ C_{1,9}(t-18) + D_{1,9}, & 31 \leq t \leq 32, \\ A_{1,9}\sin(\omega_{1,9}(t-18) + \varphi_{1,9}) + B_{1,9}, & 33 \leq t \leq 37. \end{cases} \quad (3.28)$$

The results of approximation are presented in Figures 3.11-3.19.

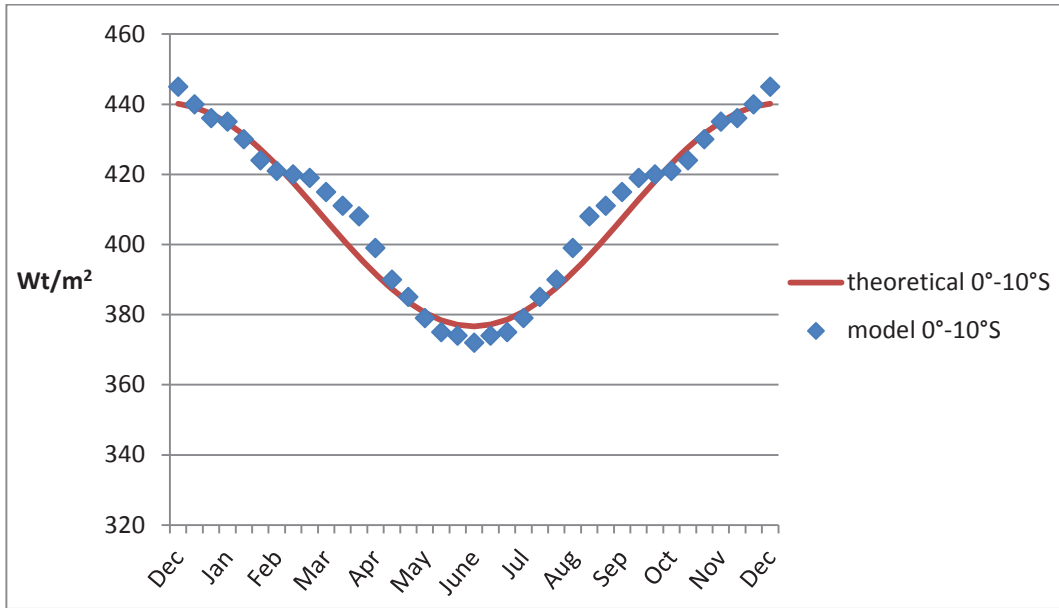


Fig. 3.11 Curve fitting for 0°-10°S latitudinal belt.

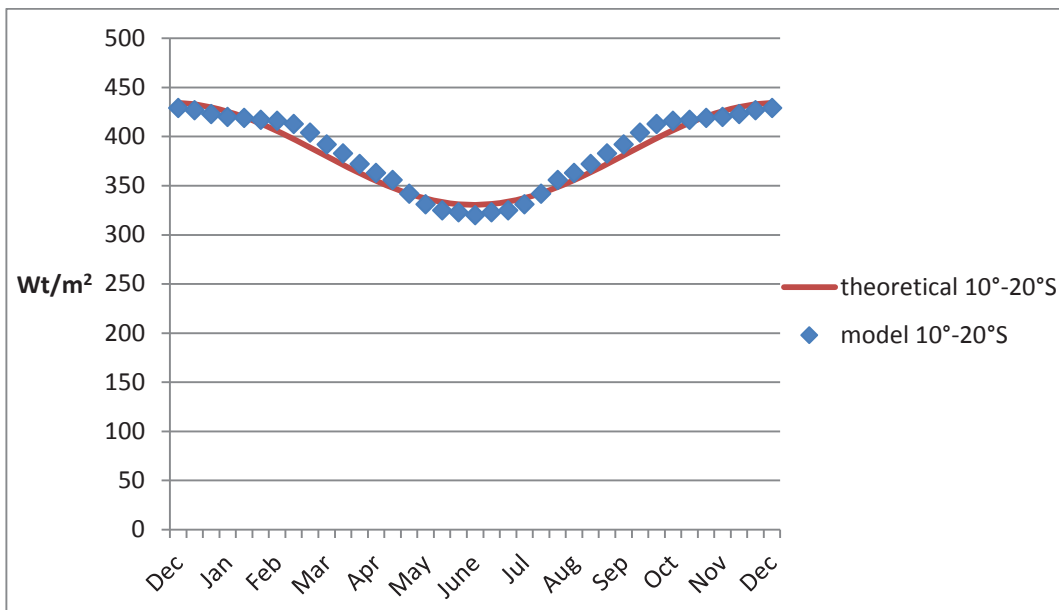


Fig. 3.12 Curve fitting for 10°-20°S latitudinal belt.

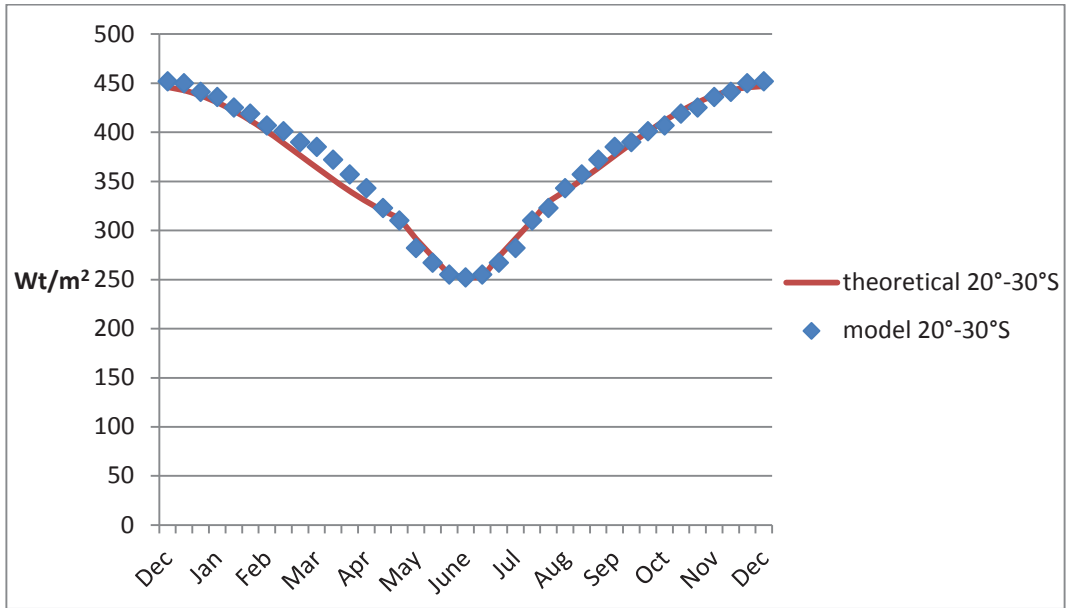


Fig. 3.13 Curve fitting for 20°-30°S latitudinal belt.

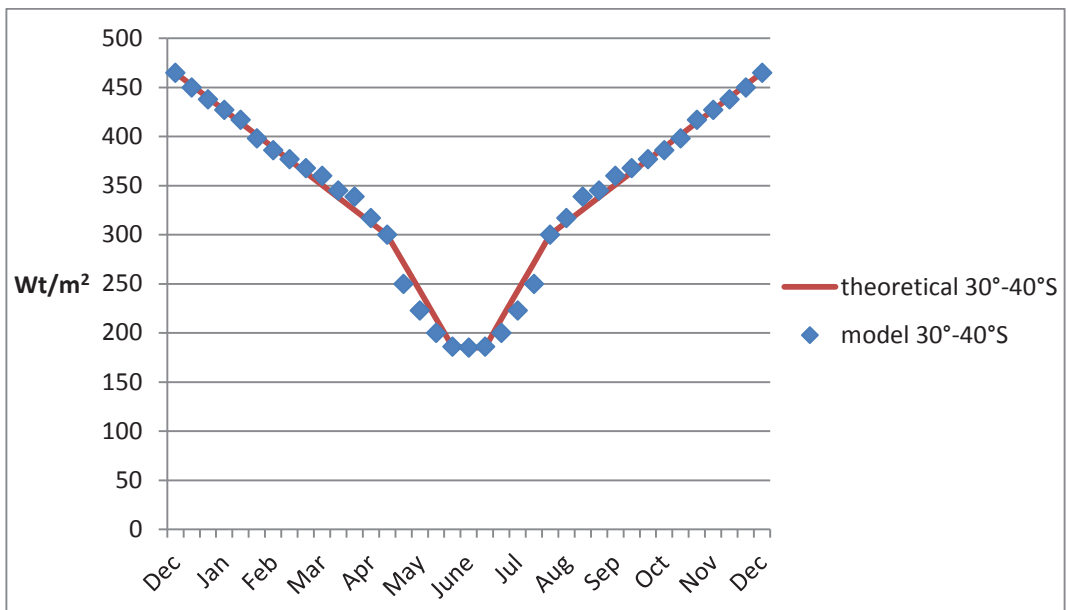


Fig. 3.14 Curve fitting for 30°-40°S latitudinal belt.

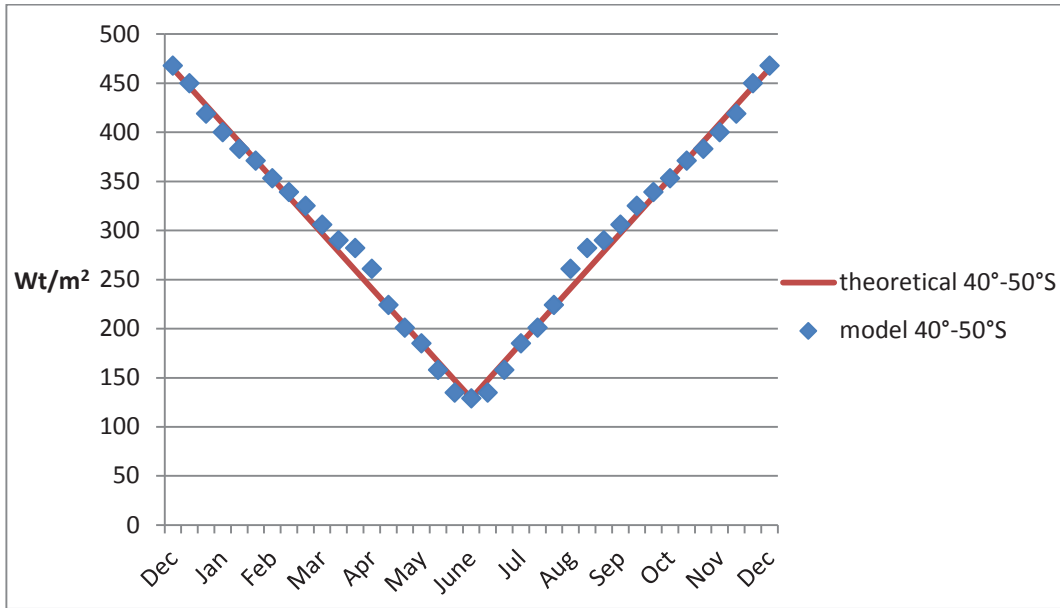


Fig. 3.15 Curve fitting for 40°-50°S latitudinal belt.

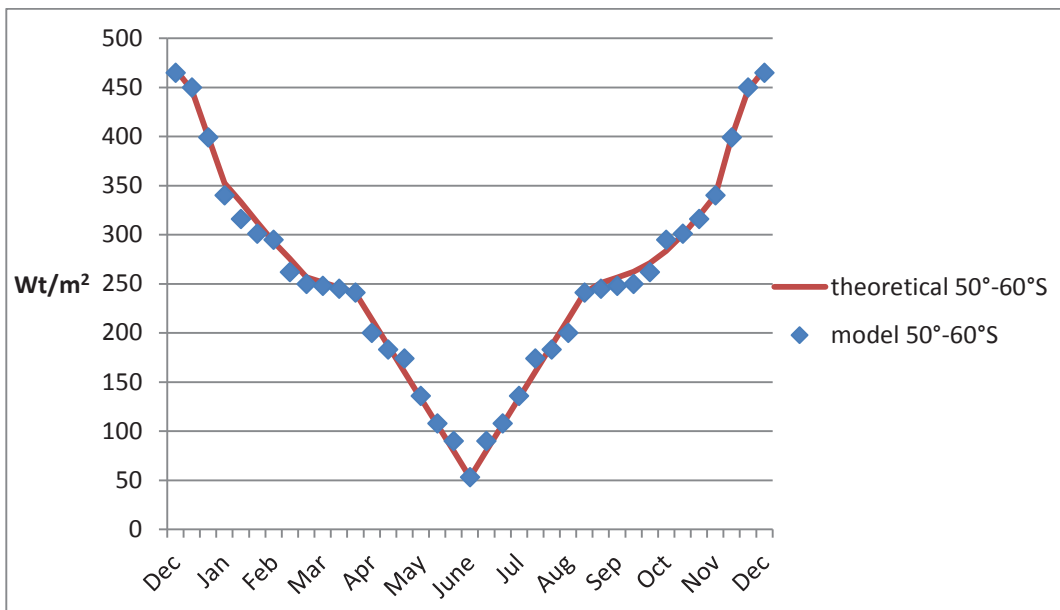


Fig. 3.16 Curve fitting for 50°-60°S latitudinal belt.

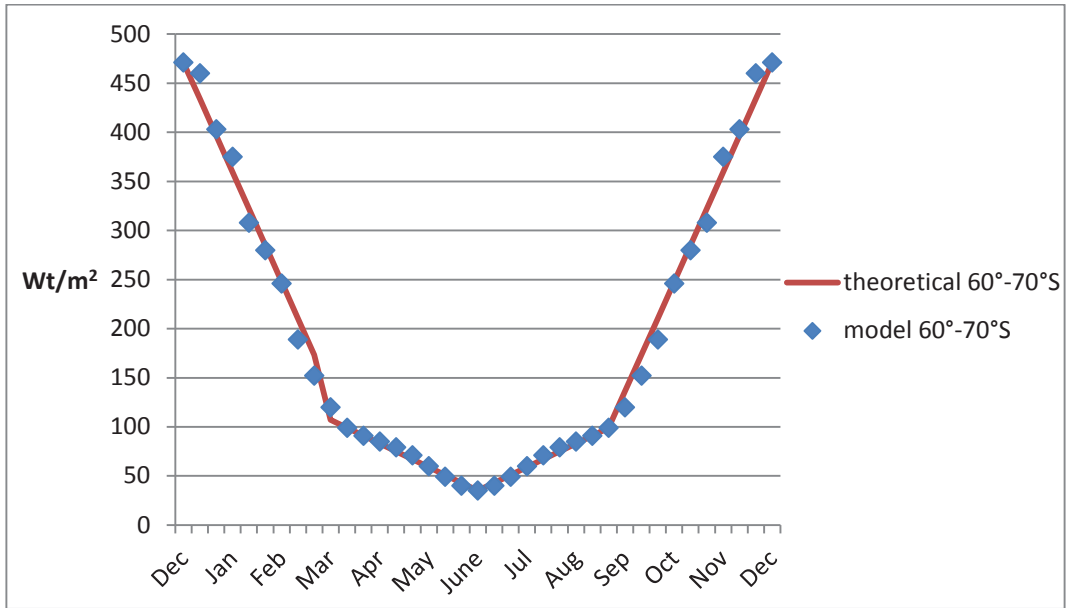


Fig. 3.17 Curve fitting for 60°-70°S latitudinal belt.

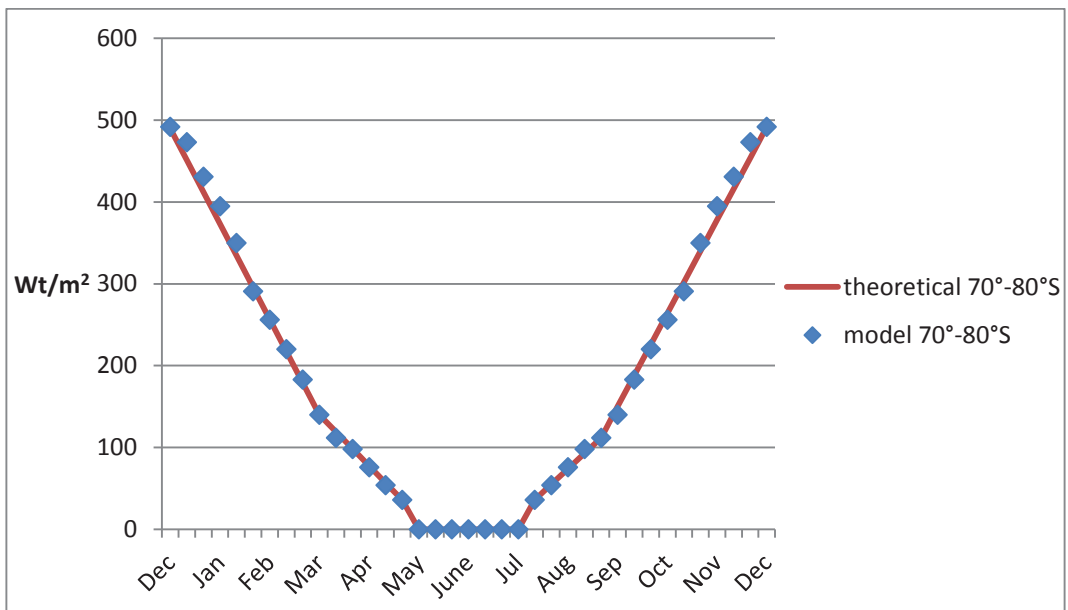


Fig. 3.18 Curve fitting for 70°-80°S latitudinal belt.

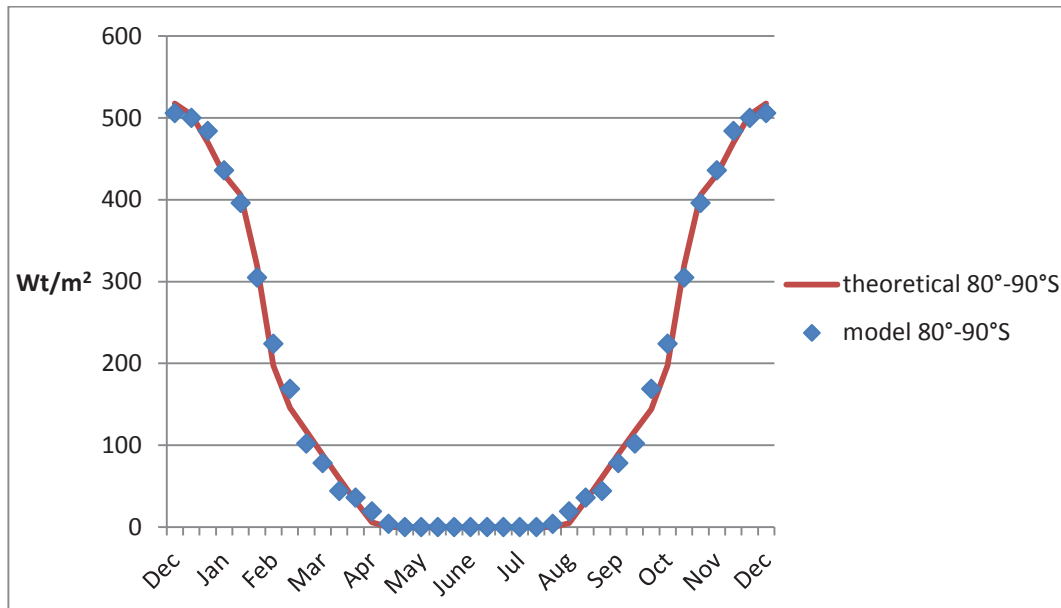


Fig. 3.19 Curve fitting for 80°-90°S latitudinal belt.

The results of R^2 coefficient for the Southern Hemisphere belt are introduced in Table 3.9.

Table 3.9 The results of calculations of the R^2 coefficient for each latitudinal belt.

Latitudinal belt	R^2
0°-10°S	0.9593
10°-20°S	0.9504
20°-30°S	0.9870
30°-40°S	0.9908
40°-50°S	0.9912
50°-60°S	0.9953
60°-70°S	0.9942
70°-80°S	0.9967
80°-90°S	0.9960

We note that for the Southern Hemisphere, the values of R^2 coefficient are also greater than the required level of 95%. Thus these curves can also be used for approximating the values obtained from the proposed model for the Southern Hemisphere.

3.2.3. Simulating the seasonal variations of insolation within C-GOLDSTEIN

The curves obtained in Section 3.2.2 have then been incorporated into the main loop of the C-GOLDSTEIN simulation model. This way the insolation computations are performed at each time step.

We then reinitialised the atmosphere starting from zero initial conditions and ran C-GOLDSTEIN in SPINUP mode leaving all other parameters set to zero (carbon dioxide rate of increase rate) in order to obtain the suitable initial conditions. This was done with the new annual averages as detailed in Section 3.1.

The model was then run with the modified code (see Appendix 2) using the results obtained after the SPINUP run as the initial conditions. The time step was reduced to 1 day for the ocean (compared to the initial 1.46 days). The ocean-atmosphere time step ratio was kept unchanged (the atmospheric time step is half of the ocean one). Note that a 360-day calendar was used for simplicity (i.e. each month has 30 days).

The results for the 21st day of each month are illustrated in Figures 3.20-3.31. The figures were obtained after small modification of the MATLAB plotting subroutine provided together with the model software.

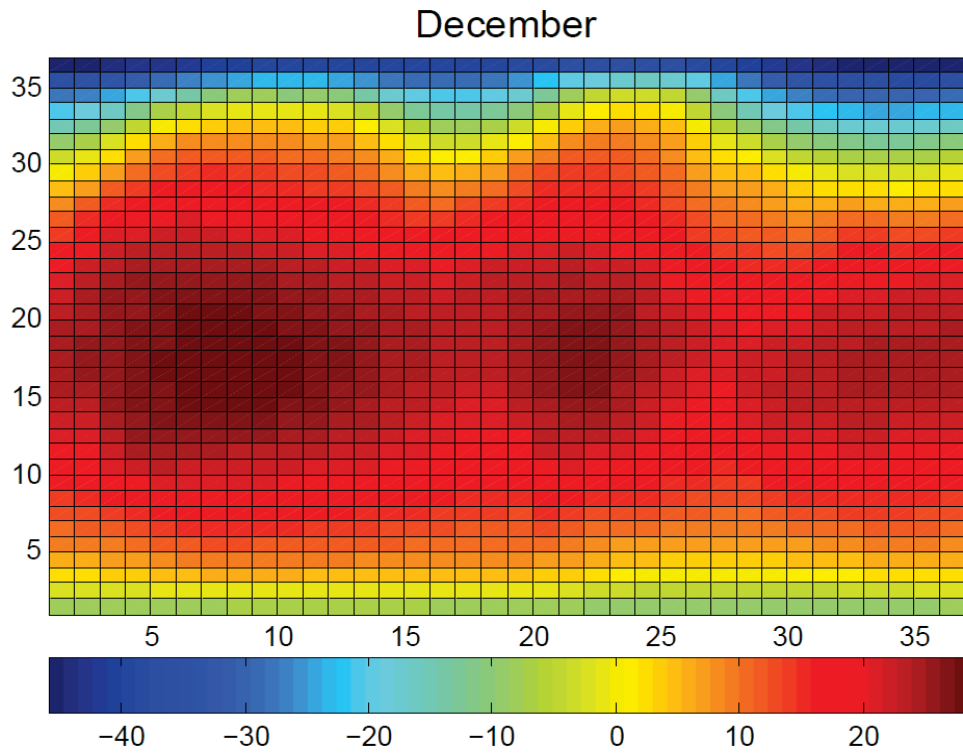


Fig. 3.20 Temperature distribution for December.

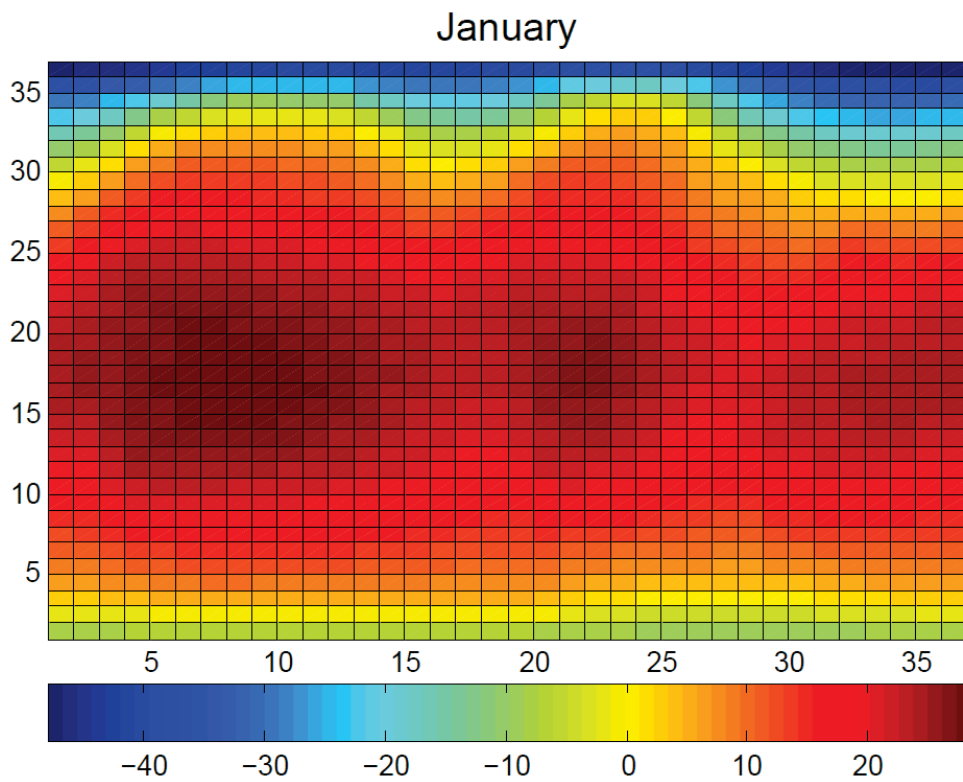


Fig. 3.21 Temperature distribution for January.

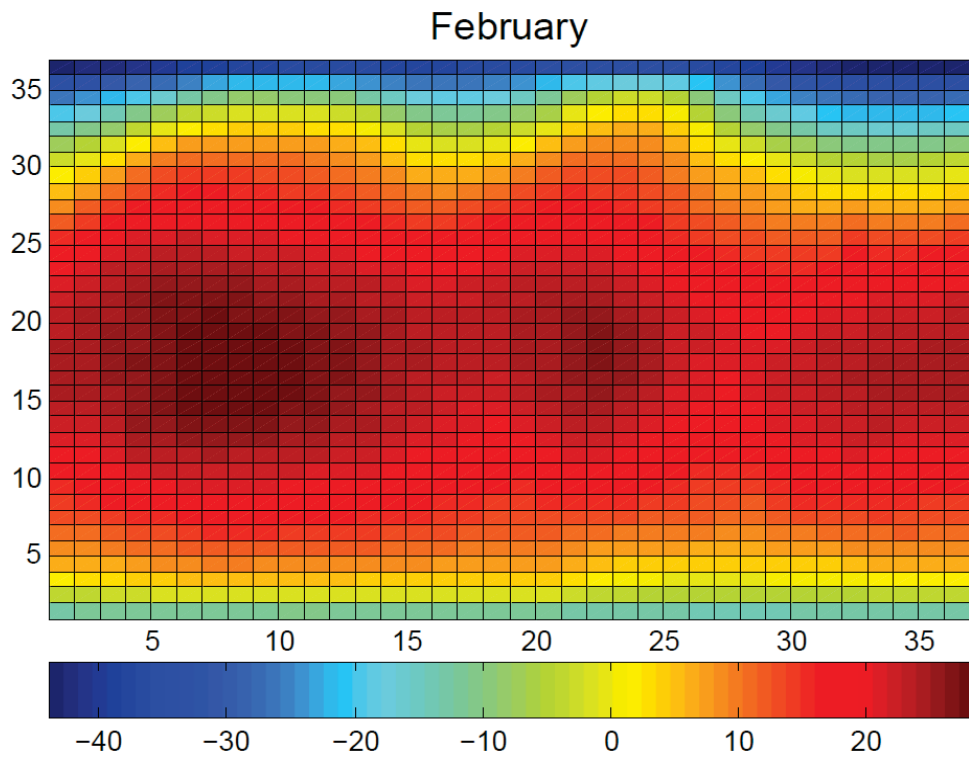


Fig. 3.22 Temperature distribution for February.

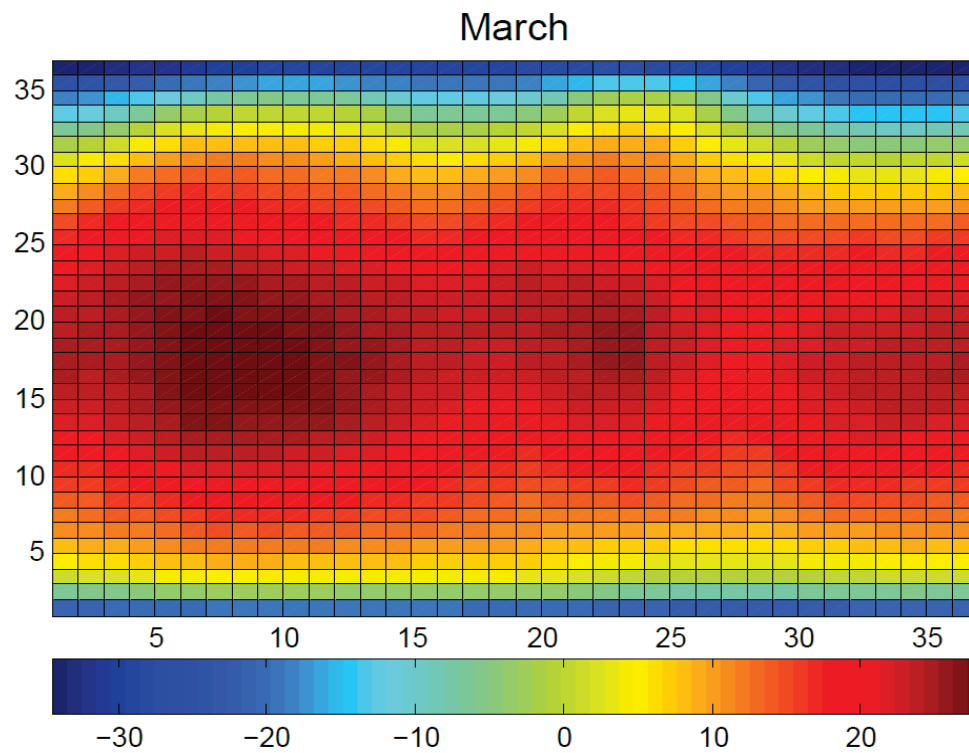


Fig. 3.23 Temperature distribution for March.

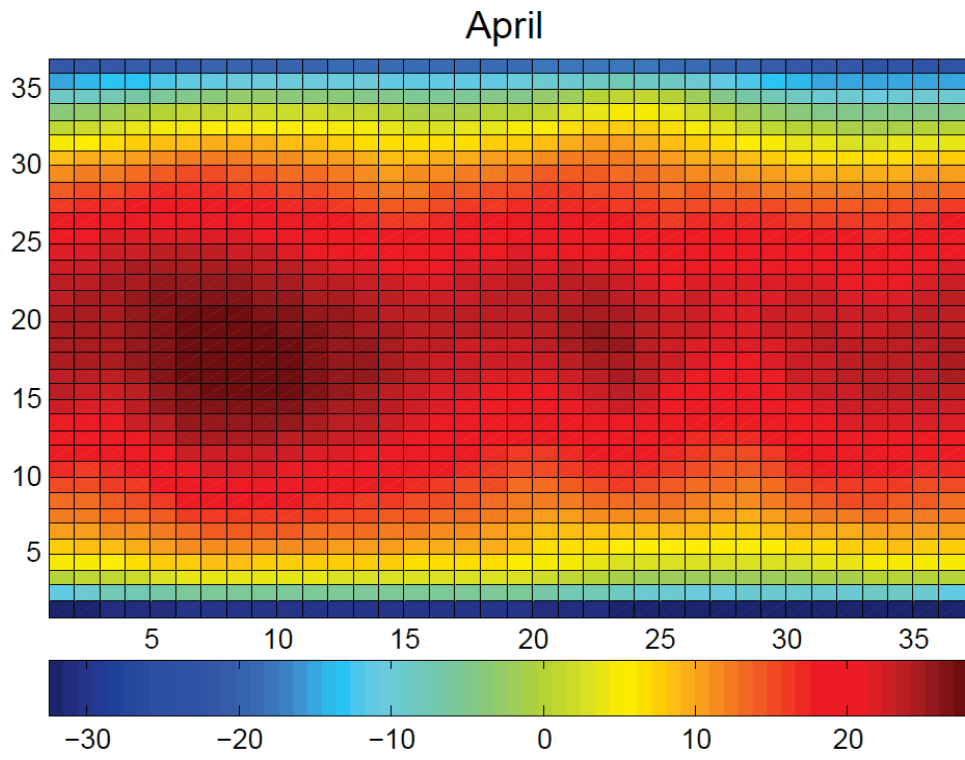


Fig. 3.24 Temperature distribution for April.

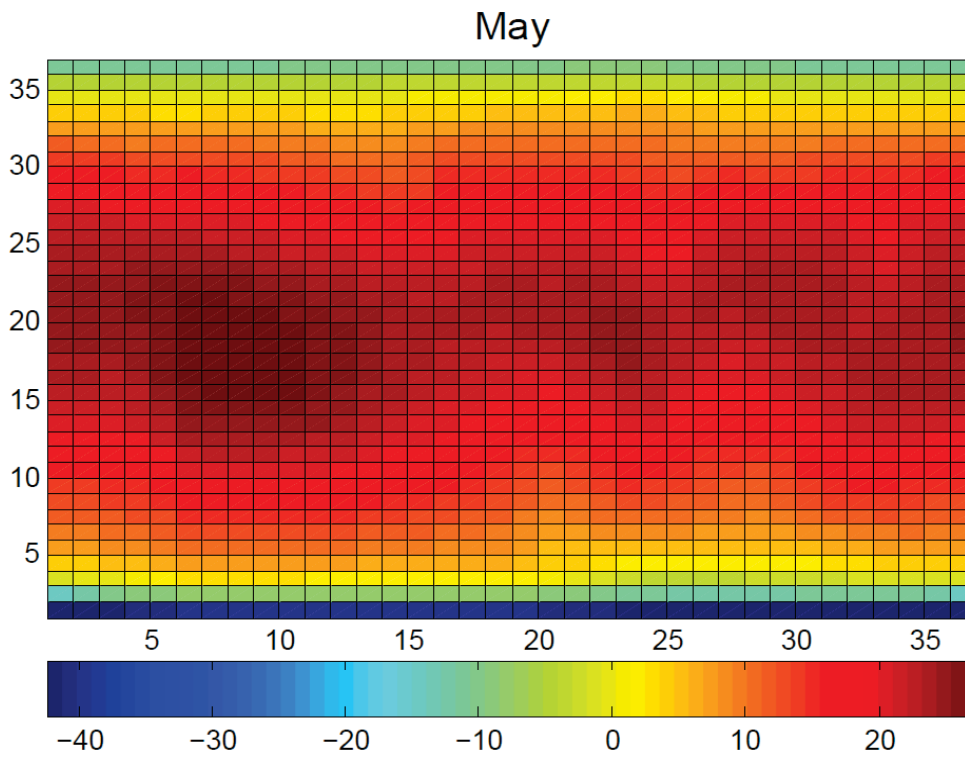


Fig. 3.25 Temperature distribution for May.

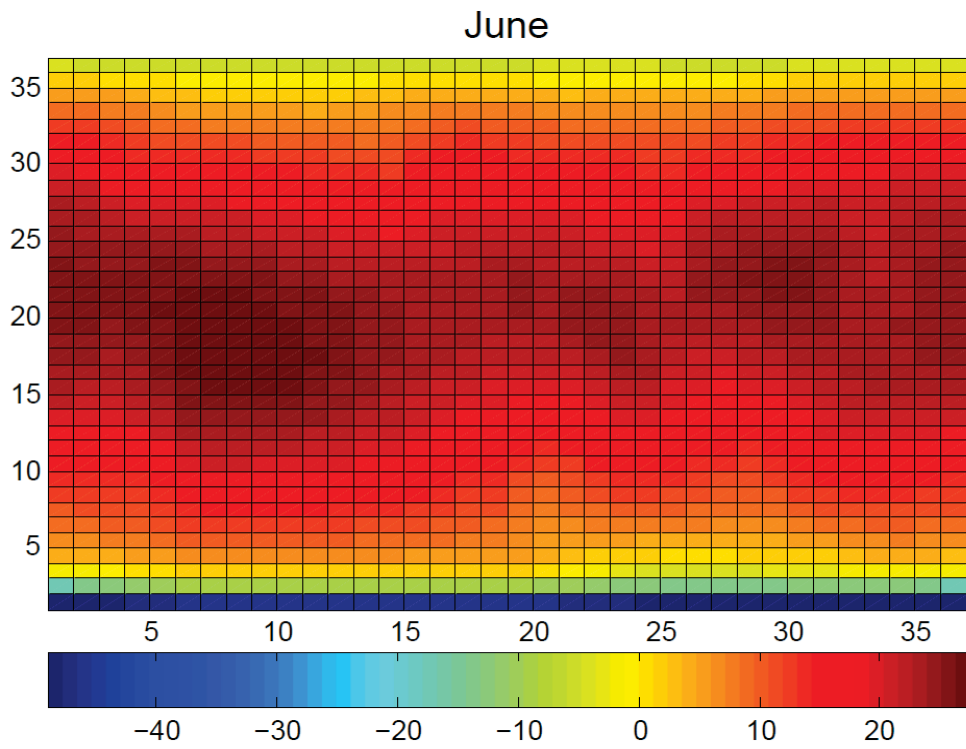


Fig. 3.26 Temperature distribution for June.

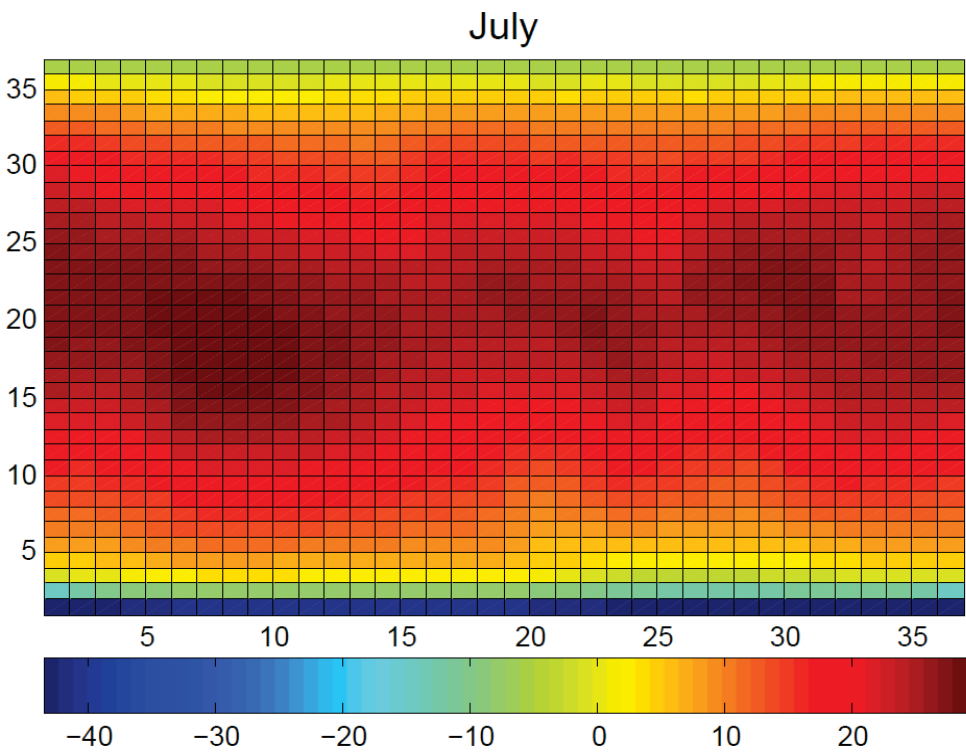


Fig. 3.27 Temperature distribution for July.

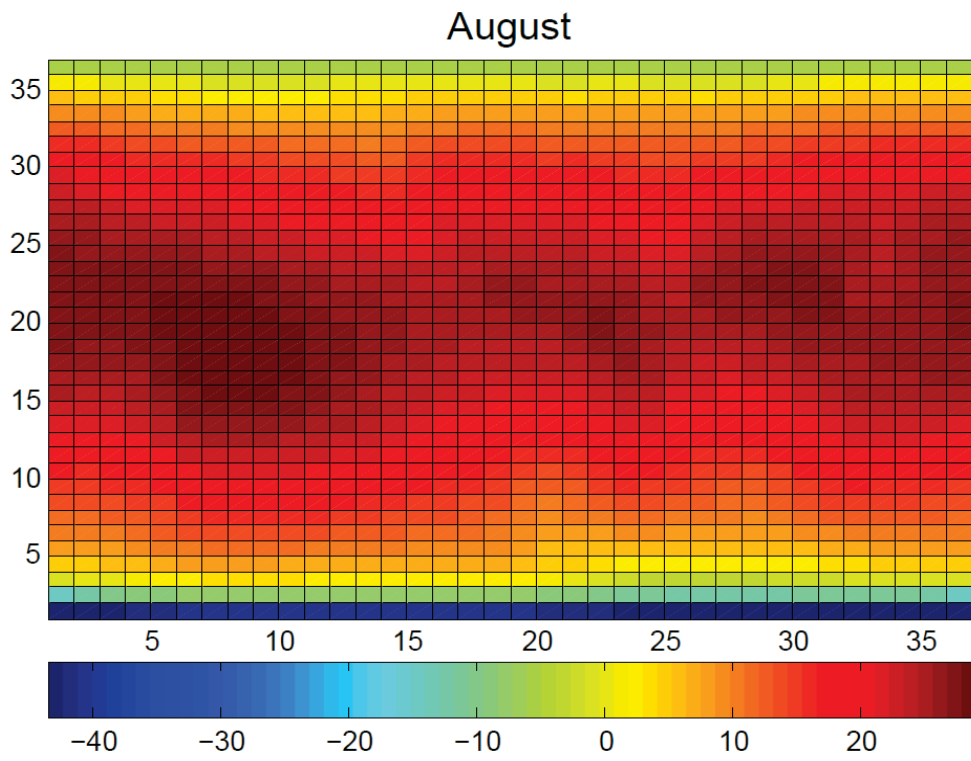


Fig. 3.28 Temperature distribution for August.

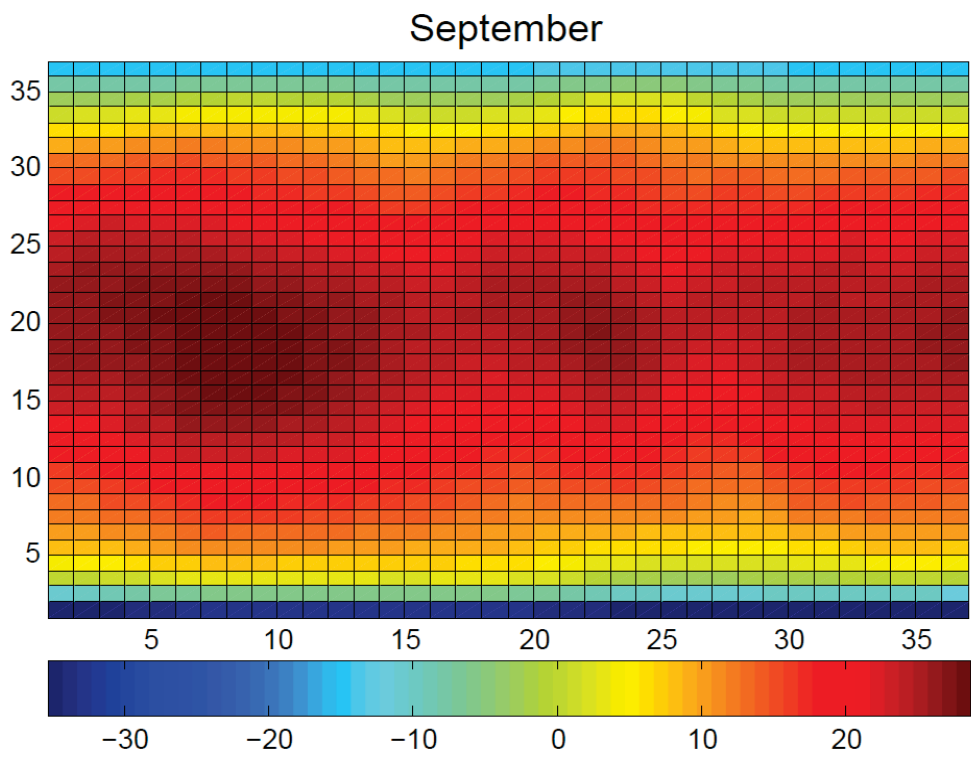


Fig. 3.29 Temperature distribution for September.

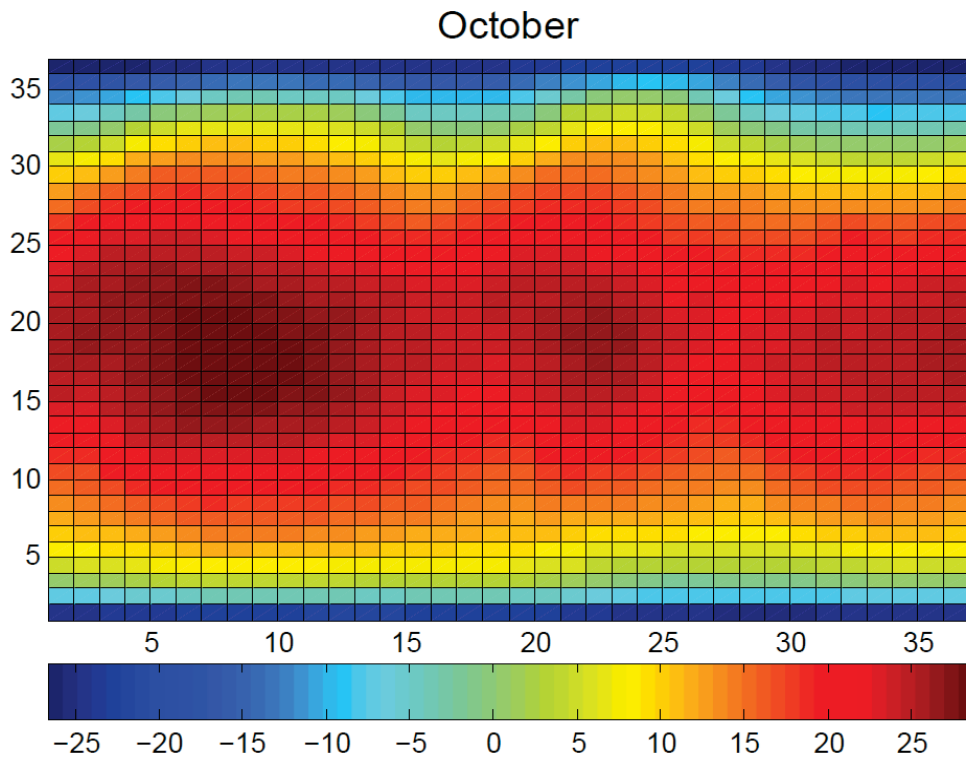


Fig. 3.30 Temperature distribution for October.

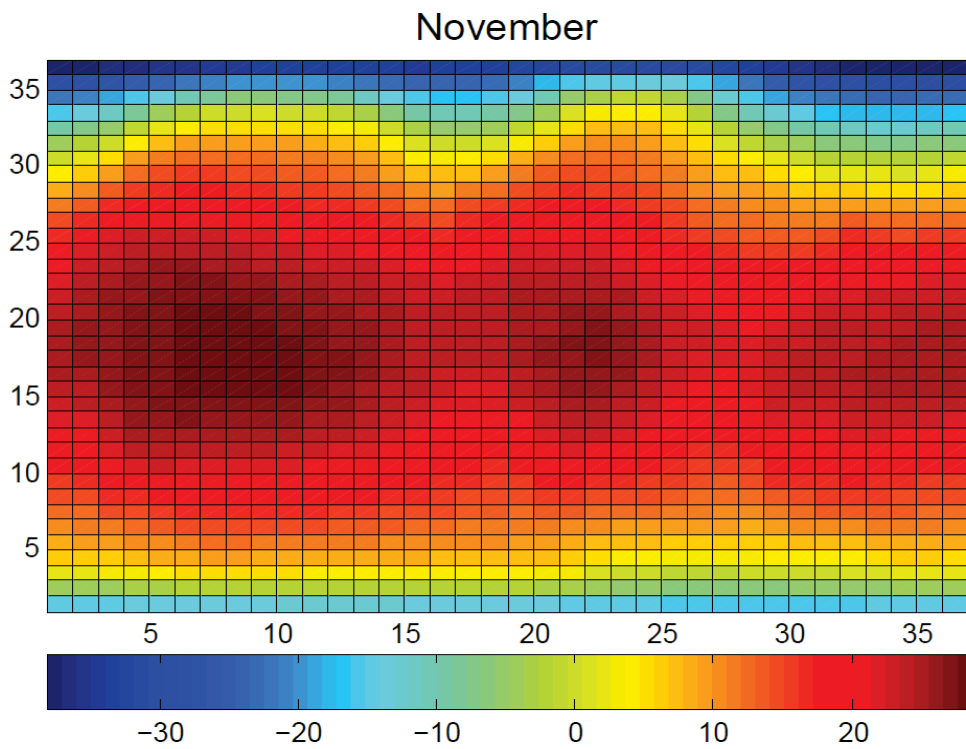


Fig. 3.31 Temperature distribution for November.

The results can be compared with the monthly temperature distribution maps from

NCEP (National Centres for Environmental Predictions)/NCAR Reanalysis Project³.

Clearly, the obtained temperature distributions are realistic and follow all the main patterns in the actual temperature distributions from NCEP/NCAR, such as the maintenance of hot temperature throughout the year for the equatorial regions, the rotation of the winter and summer seasons for the Northern and Southern Hemispheres, extreme low observed temperatures for the polar regions during their winter seasons, and distinct temperature variations due to the location of continents.

In this chapter, we compared the annual insolation averages previously used in C-GOLDSTEIN with those from the insolation model proposed in Chapter 2. We have run the C-GOLDSTEIN model with the new yearly averages and showed that realistic annual temperature distributions are obtained. We described a curve fitting procedure in order to allow us to incorporate the seasonal variations of insolation predicted by the new model into C-GOLDSTEIN. Finally, we have run C-GOLDSTEIN with the monthly variations of insolation and verified that the obtained temperature distributions are realistic for any time of year.

³ http://geog.uoregon.edu/envchange/clim_animations/flash/tmp2m.html

Conclusions and Future Work

In this thesis, a new approach for modelling insolation is proposed which uses the space perspective. The proposed model is then incorporated into an existing global climate model C-GOLDSTEIN, which allows for simulations of seasonal variations of insolation.

The first goal of the model development was to formulate the process of receiving the radiation by the Earth as a flux passing through a cross-section. We then chose the coordinate plane which was the most convenient for performing calculations and formulated the radiation vector. A major aspect of model development was also to derive the projections of the latitudinal belt in three different projection planes and to choose the one which provided us with the easiest projections.

The next objective was to model the change of illumination area for different latitudinal belts throughout the year, which was done by an introducing a new angle which was assigned in terms of an obliquity angle and the angle of the Earth's rotation around the Sun. Then we pictured the different illumination areas for different latitudinal belts and defined the limits of integration. Finally, we have calculated the amount of insolation received by any latitudinal belt in the Northern and Southern Hemispheres at any particular time by using the Maple software.

The annual values of insolation for each belt were then compared with the satellite data obtained from NASA. An average accuracy of the results obtained is 97%. The results show a very good agreement for the equatorial and middle latitude regions. Slightly less agreement can be observed for the polar regions, which are known to be difficult to model.

Next, we considered the task of incorporating the new insolation model into EMIC C-GOLDSTEIN, in which the annual average values of insolation were previously used. We first replaced the yearly averages of insolation in the C-GOLDSTEIN with those calculated from our model and made sure that this still yielded appropriate results for the global temperature distribution. Then, we incorporated our proposed model into the main loop of C-GOLDSTEIN so as to allow for seasonal variations of insolation.

Realistic monthly latitudinal temperature distributions have been obtained after running the C-GOLDSTEIN model with the new insolation component. The average

accuracy of modelling the insolation within C-GOLDSTEIN has been increased from 96% to 98%.

We note the Earth was assumed to be exactly spherical for the purposes of our proposed insolation model. Also, small variations in the distance between the Sun and the Earth while it traverses its orbit have not been considered in our proposed model so far. However, those effects are very small and their impact on the results is negligible, especially when used in an EMIC such as C-GOLDSTEIN. These effects can be easily incorporated into the model in the future.

The proposed modelling approach is an alternative to standard method based on the calculations on a celestial sphere as proposed in (Milankovitch, 1920). Both approaches can be easily employed within global climate models. The main advantage of the proposed model is that it will allow users in the future to explicitly incorporate the impact of more general space activity (such as solar flares, cosmic rays, gamma ray bursts etc.) on various Earth-based systems, which is not possible when the earth's point of view is used. Existing methods of modelling space activity do not incorporate these activities directly either. Instead, most of them formulate their likely impact on various chemical species in the atmosphere and incorporate this into a more general climate model.

The new approach allows for direct modelling of space activity and can be readily incorporated into existing global climate models. Hence, it opens a wide horizon for future work. For example, the effects of vortices that are generated during the solar flares can now be modelled and their impact can be incorporated. For this, the formulation of the radiation vector needs to be modified, i.e. it needs to be assigned as a function of the coordinates as well. Also, the orientation of mentioned external forces can now be taken into account. This will permit the investigating of the localized terrestrial effects of external forces.

Furthermore, new types of experiments can now be performed with the C-GOLDSTEIN climate model, because the calculations can now be performed for any particular time of the year. For instance, the investigation of consequences of random variations of insolation on temperature can now be examined.

Finally, since the proposed insolation model is fully analytic, it now gives researchers the opportunity to capture any possible variations in any of the input parameters and to investigate their impacts on climate.

In summary, the main contribution of the thesis is a new approach for modelling insolation at the top of the atmosphere, which allows for explicit incorporation of many different types of space activity on the Earth. This approach has been demonstrated to yield excellent results. Also, we have shown that it can be readily incorporated into existing global climate models. The future use of the proposed approach within comprehensive global climate models provides a new pathway for studying the possible effects of such activities on various Earth-based systems.

References

- Abramowitz, G., Leuning, R., Clark, M., & Pitman, A. (2008). Evaluating the Performance of Land Surface Models. *Journal of Climate*, 21(21).
- Adachi, Y. Coauthors, 2013: Basic performance of a new Earth System Model of the Meteorological Research Institute (MRI-ESM1). *Pap. Meteor. Geophys.*
- Adams, P. J., Seinfeld, J. H., Koch, D., Mickley, L., & Jacob, D. (2001). General circulation model assessment of direct radiative forcing by the sulfate-nitrate-ammonium-water inorganic aerosol system. *Journal of Geophysical Research: Atmospheres (1984–2012)*, 106(D1), 1097-1111.
- Alcamo, J. (1994). *IMAGE 2.0: Integrated modeling of global climate change* (Vol. 76): Kluwer Academic Pub.
- Alley, R. B., Clark, P. U., Huybrechts, P., & Joughin, I. (2005). Ice-sheet and sea-level changes. *Science*, 310(5747), 456-460.
- Austin, J., & Butchart, N. (2003). Coupled chemistry–climate model simulations for the period 1980 to 2020: Ozone depletion and the start of ozone recovery. *Quarterly Journal of the Royal Meteorological Society*, 129(595), 3225-3249.
- Bao, Q., Lin, P., Zhou, T., Liu, Y., Yu, Y., Wu, G., . . . Li, J. (2013). The flexible global ocean-atmosphere-land system model, spectral version 2: FGOALS-s2. *Advances in Atmospheric Sciences*, 30, 561-576.
- Berger, A. (1978). Long-term variations of daily insolation and Quaternary climatic changes. *Journal of the Atmospheric Sciences*, 35(12), 2362-2367.
- Boer, G., Flato, G., & Ramsden, D. (2000). A transient climate change simulation with greenhouse gas and aerosol forcing: projected climate to the twenty-first century. *Climate dynamics*, 16(6), 427-450.
- Bryan, K., & Lewis, L. (1979). A water mass model of the world ocean. *Journal of Geophysical Research: Oceans (1978–2012)*, 84(C5), 2503-2517.
- Budyko, M. I. (1969). The effect of solar radiation variations on the climate of the earth. *Tellus*, 21(5), 611-619.
- Calisto, M., Verronen, P., Rozanov, E., & Peter, T. (2012). Influence of a Carrington-like event on the atmospheric chemistry, temperature and dynamics. *Atmospheric chemistry and physics*, 12(18), 8679-8686.
- Carlsaw, K., Harrison, R., & Kirkby, J. (2002). Cosmic rays, clouds, and climate. *Science*, 298(5599), 1732-1737.
- Collins, W., Bellouin, N., Doutriaux-Boucher, M., Gedney, N., Halloran, P., Hinton, T., . . . Liddicoat, S. (2011). Development and evaluation of an Earth-system model–HadGEM2. *Geoscientific Model Development Discussions*, 4(2), 997-1062.
- Collins, W. D., Bitz, C. M., Blackmon, M. L., Bonan, G. B., Bretherton, C. S., Carton, J. A., . . . Henderson, T. B. (2006). The Community Climate System Model version 3 (CCSM3). *Journal of Climate*, 19(11).
- Cramer, W., Bondeau, A., Woodward, F. I., Prentice, I. C., Betts, R. A., Brovkin, V., . . . Friend, A. D. (2001). Global response of terrestrial ecosystem structure and function to CO₂ and climate change: results from six dynamic global vegetation models. *Global Change Biology*, 7(4), 357-373.
- Dickinson, R. E., Kennedy, P., & Henderson-Sellers, A. (1993). *Biosphere-atmosphere transfer scheme (BATS) version 1e as coupled to the NCAR community climate model*: National Center for Atmospheric Research, Climate and Global Dynamics Division.
- Donner, L. J., Wyman, B. L., Hemler, R. S., Horowitz, L. W., Ming, Y., Zhao, M., . . . Schwarzkopf, M. D. (2011). The Dynamical Core, Physical Parameterizations, and Basic Simulation Characteristics of the Atmospheric Component AM3 of the GFDL Global Coupled Model CM3. *Journal of Climate*, 24(13).

- Dufresne, J.-L., Foujols, M.-A., Denvil, S., Caubel, A., Marti, O., Aumont, O., . . . Benschila, R. (2013). Climate change projections using the IPSL-CM5 Earth System Model: from CMIP3 to CMIP5. *Climate dynamics*, 40(9-10), 2123-2165.
- Dunne, J. P., John, J. G., Adcroft, A. J., Griffies, S. M., Hallberg, R. W., Shevliakova, E., . . . Harrison, M. J. (2012). GFDL's ESM2 Global Coupled Climate-Carbon Earth System Models. Part I: Physical Formulation and Baseline Simulation Characteristics. *Journal of Climate*, 25(19).
- Dunne, J. P., John, J. G., Shevliakova, E., Stouffer, R. J., Krasting, J. P., Malyshev, S. L., . . . Cooke, W. (2013). GFDL's ESM2 Global Coupled Climate-Carbon Earth System Models. Part II: Carbon System Formulation and Baseline Simulation Characteristics*. *Journal of Climate*, 26(7).
- Eyring, V., Arblaster, J., Cionni, I., Sedláček, J., Perlwitz, J., Young, P., . . . Collins, W. J. (2013). Long-term ozone changes and associated climate impacts in CMIP5 simulations. *Journal of Geophysical Research: Atmospheres*, 118(10), 5029-5060.
- Flato, G. M., & Boer. (2001). Warming asymmetry in climate change simulations. *Geophysical research letters*, 28(1), 195-198.
- Foley, J., Prentice, I., Ramankutty, S., Levis, D., Pollard, S., Sitch, A., & Haxeltine. (1996). An integrated biosphere model of land surface processes, terrestrial carbon balance, and vegetation dynamics. *Global biogeochemical cycles*, 10(4), 603-628.
- Gallée, H., Van Ypersele, J., Fichet, T., Marsiat, I., Tricot, C., & Berger, A. (1992). Simulation of the last glacial cycle by a coupled, sectorially averaged climate-ice sheet model: 2. Response to insolation and CO₂ variations. *Journal of Geophysical Research: Atmospheres (1984–2012)*, 97(D14), 15713-15740.
- Gates, W. L., Henderson-Sellers, A., Boer, G. J., Folland, C. K., Kitoh, A., McAvaney, B. J., . . . Zeng, Q. (1996). *Climate models—evaluation*: Cambridge University Press, Cambridge, United Kingdom and New York, NY, USA.
- Gent, P. R., Danabasoglu, G., Donner, L. J., Holland, M. M., Hunke, E. C., Jayne, S. R., . . . Vertenstein, M. (2011). The Community Climate System Model Version 4. *Journal of Climate*, 24(19).
- Goosse, H., Brovkin, V., Fichet, T., Haarsma, R., Huybrechts, P., Jongma, J., . . . Campin, J.-M. (2010). Description of the Earth system model of intermediate complexity LOVECLIM version 1.2. *Geoscientific Model Development Discussions*, 3(1), 309-390.
- Gordon, C., Cooper, C., Senior, C. A., Banks, H., Gregory, J. M., Johns, T. C., . . . Wood, R. A. (2000). The simulation of SST, sea ice extents and ocean heat transports in a version of the Hadley Centre coupled model without flux adjustments. *Climate dynamics*, 16(2-3), 147-168.
- Gordon, C. T., & Stern, W. F. (1982). A description of the GFDL global spectral model. *Monthly Weather Review*, 110(7), 625-644.
- Harvey, L. (1992). A two-dimensional ocean model for long-term climatic simulations: Stability and coupling to atmospheric and sea ice models. *Journal of Geophysical Research: Oceans (1978–2012)*, 97(C6), 9435-9453.
- Hasumi, H., & Emori, S. (2004). K-1 coupled gcm (miroc) description. *Center for Climate System Research, University of Tokyo, Tokyo*.
- Haxeltine, A., & Prentice, I. C. (1996). BIOME3: An equilibrium terrestrial biosphere model based on ecophysiological constraints, resource availability, and competition among plant functional types. *Global biogeochemical cycles*, 10(4), 693-709.
- Horowitz, L. W., Walters, S., Mauzerall, D. L., Emmons, L. K., Rasch, P. J., Granier, C., . . . Tyndall, G. S. (2003). A global simulation of tropospheric ozone and related tracers: Description and evaluation of MOZART, version 2. *Journal of Geophysical Research: Atmospheres (1984–2012)*, 108(D24).
- Hurrell, J. W., Holland, M. M., Gent, P. R., Ghan, S., Kay, J. E., Kushner, P. J., . . . Marshall, S. (2013). The Community Earth System Model: A Framework for Collaborative

- Research. *Bulletin of the American Meteorological Society*, 94(9), 1339-1360. doi: 10.1175/bams-d-12-00121.1
- Ivanova, D., Mitchell, D. L., Arnott, W. P., & Poellot, M. (2001). A GCM parameterization for bimodal size spectra and ice mass removal rates in mid-latitude cirrus clouds. *Atmospheric research*, 59, 89-113.
- Jackman, C. H., Cerniglia, M. C., Nielsen, J. E., Allen, D. J., Zawodny, J. M., McPeters, R. D., . . . Rood, R. B. (1995). Two-dimensional and three-dimensional model simulations, measurements, and interpretation of the influence of the October 1989 solar proton events on the middle atmosphere. *Journal of Geophysical Research: Atmospheres (1984–2012)*, 100(D6), 11641-11660.
- Langner, J., & Rodhe, H. (1991). A global three-dimensional model of the tropospheric sulfur cycle. *Journal of Atmospheric Chemistry*, 13(3), 225-263.
- Lipscomb, W. H., Fyke, J. G., Vizcaíno, M., Sacks, W. J., Wolfe, J., Vertenstein, M., . . . Lawrence, D. M. (2013). Implementation and Initial Evaluation of the Glimmer Community Ice Sheet Model in the Community Earth System Model. *Journal of Climate*, 26(19), 7352-7371. doi: 10.1175/jcli-d-12-00557.1
- Liu, X., Easter, R. C., Ghan, S. J., Zaveri, R., Rasch, P., Shi, X., . . . Vitt, F. (2012). Toward a minimal representation of aerosols in climate models: Description and evaluation in the Community Atmosphere Model CAM5. *Geosci. Model Dev*, 5(3), 709-739.
- Maier-Reimer, E., Mikolajewicz, U., & Hasselmann, K. (1993). Mean circulation of the Hamburg LSG OGCM and its sensitivity to the thermohaline surface forcing. *Journal of Physical Oceanography*, 23(4), 731-757.
- Maier-Reimer, E. (1993). Geochemical cycles in an ocean general circulation model. Preindustrial tracer distributions. *Global biogeochemical cycles*, 7(3), 645-677.
- Manabe, S., Smagorinsky, J., & Strickler, R. F. (1965). Simulated climatology of a general circulation model with a hydrologic cycle 1. *Monthly Weather Review*, 93(12), 769-798.
- Manabe, S., & Stouffer, R. J. (1980). Sensitivity of a global climate model to an increase of CO₂ concentration in the atmosphere. *Journal of Geophysical Research: Oceans (1978–2012)*, 85(C10), 5529-5554.
- Manabe, S., & Wetherald, R. T. (1975). The effects of doubling the CO₂ concentration on the climate of a general circulation model.
- Marsh, R., Edwards, N. R., & Shepherd, J. G. (2002). Development of a fast climate model (CGOLDSTEIN) for Earth system science. *National Oceanography Centre, Southampton, European Way, Southampton SO14 3ZH*.
- Marsland, S., Haak, H., Jungclaus, J., Latif, M., & Röske, F. (2003). The Max-Planck-Institute global ocean/sea ice model with orthogonal curvilinear coordinates. *Ocean modelling*, 5(2), 91-127.
- Marti, O., Braconnot, P., Bellier, J., Benschila, R., Bony, S., Brockmann, P., . . . Dufresne, J. (2005). The new IPSL climate system model: IPSL-CM4. *Note du Pôle de Modélisation, IPSL*, 26, 1-86.
- Marti, O., Braconnot, P., Dufresne, J.-L., Bellier, J., Benschila, R., Bony, S., . . . Codron, F. (2010). Key features of the IPSL ocean atmosphere model and its sensitivity to atmospheric resolution. *Climate dynamics*, 34(1), 1-26.
- Martin, S. T. (2004). Effects of the physical state of tropospheric ammonium-sulfate-nitrate particles on global aerosol direct radiative forcing. *Atmospheric chemistry and physics*, 4(1), 183.
- McFarlane, N. A., Boer, G., Blanchet, J., & Lazare, M. (1992). The Canadian Climate Centre second-generation general circulation model and its equilibrium climate. *Journal of Climate*, 5(10), 1013-1044.
- Milanković, M. (1998). *Canon of insolation and the ice-age problem: Zavod za udžbenike i nastavna sredstva*.

- Milankovitch, M. (1920). *Théorie mathématique des phénomènes thermiques produits par la radiation solaire* (Vol. 339): Paris.
- Mitchell, J. F. (1983). The seasonal response of a general circulation model to changes in CO₂ and sea temperatures. *Quarterly Journal of the Royal Meteorological Society*, 109(459), 113-152.
- Mitchell, J. F., Senior, C., & Ingram, W. (1989). CO₂ and climate: a missing feedback?
- Mokhov, I., Eliseev, A., Handorf, D., & Petoukhov, V. Dethloff K, Weisheimer A, Khvorostyanov DV (2000) North Atlantic oscillation: diagnosis and modelling of interdecadal variability and its evolution. *Izv Atmos Ocean Phys*, 36(5), 555-565.
- Montoya, M., Griesel, A., Levermann, A., Mignot, J., Hofmann, M., Ganopolski, A., & Rahmstorf, S. (2005). The earth system model of intermediate complexity CLIMBER-3 α . Part I: description and performance for present-day conditions. *Climate dynamics*, 25(2-3), 237-263.
- Murnane, R., Sarmiento, J. L., & Le Quéré, C. (1999). Spatial distribution of air-sea CO₂ fluxes and the interhemispheric transport of carbon by the oceans. *Global biogeochemical cycles*, 13(2), 287-305.
- Myhre, G., Myhre, F., Stordal, T., Berglen, J., Sundet, I. S. A., & Isaksen. (2004). Uncertainties in the Radiative Forcing Due to Sulfate Aerosols. *Journal of the Atmospheric Sciences*, 61(5), 485-498.
- North, G. R. (1975). Analytical solution to a simple climate model with diffusive heat transport. *Journal of the Atmospheric Sciences*, 32(7), 1301-1307.
- North, G. R., Cahalan, R. F., & Coakley, J. A. (1981). Energy balance climate models. *Reviews of Geophysics*, 19(1), 91-121.
- North, G. R., & Coakley Jr, J. A. (1979). Differences between seasonal and mean annual energy balance model calculations of climate and climate sensitivity. *Journal of the Atmospheric Sciences*, 36(7), 1189-1204.
- Opsteegh, J., Haarsma, R., Selten, F., & Kattenberg, A. (1998). ECBILT: A dynamic alternative to mixed boundary conditions in ocean models. *Tellus A*, 50(3), 348-367.
- Penner, J., Eddleman, H., & Novakov, T. (1993). Towards the development of a global inventory for black carbon emissions. *Atmospheric Environment. Part A. General Topics*, 27(8), 1277-1295.
- Petoukhov, V., Ganopolski, A., Brovkin, V., Claussen, M., Eliseev, A., Kubatzki, C., & Rahmstorf, S. (2000). CLIMBER-2: a climate system model of intermediate complexity. Part I: model description and performance for present climate. *Climate dynamics*, 16(1), 1-17.
- Pham, M., Müller, J. F., Brasseur, G., Granier, C., & Megie, G. (1995). A three-dimensional study of the tropospheric sulfur cycle. *Journal of Geophysical Research: Atmospheres (1984–2012)*, 100(D12), 26061-26092.
- Raddatz, T., Reick, C., Knorr, W., Kattge, J., Roeckner, E., Schnur, R., . . . Jungclaus, J. (2007). Will the tropical land biosphere dominate the climate–carbon cycle feedback during the twenty-first century? *Climate dynamics*, 29(6), 565-574.
- Ramanathan, V., Pitcher, E. J., Malone, R. C., & Blackmon, M. L. (1983). The response of a spectral general circulation model to refinements in radiative processes. *Journal of the Atmospheric Sciences*, 40(3), 605-630.
- Reddy, M. S., Boucher, O., Bellouin, N., Schulz, M., Balkanski, Y., Dufresne, J. L., & Pham, M. (2005). Estimates of global multicomponent aerosol optical depth and direct radiative perturbation in the Laboratoire de Météorologie Dynamique general circulation model. *Journal of Geophysical Research: Atmospheres (1984–2012)*, 110(D10).
- Ritz, S. P., Stocker, T. F., & Joos, F. (2011). A Coupled Dynamical Ocean–Energy Balance Atmosphere Model for Paleoclimate Studies. *Journal of Climate*, 24(2).

- Rodger, C. J., Verronen, P. T., Clilverd, M. A., Seppälä, A., & Turunen, E. (2008). Atmospheric impact of the Carrington event solar protons. *Journal of Geophysical Research: Atmospheres (1984–2012)*, 113(D23).
- Roeckner, E., Brokopf, R., Esch, M., Giorgetta, M., Hagemann, S., Kornblueh, L., . . . Schulzweida, U. (2006). Sensitivity of simulated climate to horizontal and vertical resolution in the ECHAM5 atmosphere model. *Journal of Climate*, 19(16).
- Rotstayn, L., Jeffrey, S., Collier, M., Dravitzki, S., Hirst, A., Syktus, J., & Wong, K. (2012). Aerosol-and greenhouse gas-induced changes in summer rainfall and circulation in the Australasian region: a study using single-forcing climate simulations. *Atmospheric Chemistry & Physics*, 12(14).
- Rotty, R. M. (1987). Estimates of seasonal variation in fossil fuel CO₂ emissions. *Tellus B*, 39(1-2), 184-202.
- Salas-Méllia, D., Chauvin, F., Déqué, M., Douville, H., Gueremy, J., Marquet, P., . . . Tyteca, S. (2005). Description and validation of the CNRM-CM3 global coupled model. *Clim Dyn (in review)*.
- Schlesinger, M. E., & Mitchell, J. F. (1987). Climate model simulations of the equilibrium climatic response to increased carbon dioxide. *Reviews of Geophysics*, 25(4), 760-798.
- Schlesinger, M. E., & Zhao, Z.-C. (1989). Seasonal climatic changes induced by doubled CO₂ as simulated by the OSU atmospheric GCM/mixed-layer ocean model. *Journal of Climate*, 2(5), 459-495.
- Schmittner, A., Oschlies, A., Giraud, X., Eby, M., & Simmons, H. (2005). A global model of the marine ecosystem for long-term simulations: Sensitivity to ocean mixing, buoyancy forcing, particle sinking, and dissolved organic matter cycling. *Global biogeochemical cycles*, 19(3).
- Schulz, M., Schulz, C., Textor, S., Kinne, Y., Balkanski, S., Bauer, T., . . . Takemura. (2006). Radiative forcing by aerosols as derived from the AeroCom present-day and pre-industrial simulations. *Atmospheric chemistry and physics*, 6(12), 5225-5246.
- Sellers, P., Randall, D., Collatz, G., Berry, J., Field, C., Dazlich, D., . . . Bounoua, L. (1996). A revised land surface parameterization (SiB2) for atmospheric GCMs. Part I: Model formulation. *Journal of Climate*, 9(4), 676-705.
- Sellers, W. D. (1969). A global climatic model based on the energy balance of the earth-atmosphere system. *Journal of Applied Meteorology*, 8(3), 392-400.
- Shaffer, G., Olsen, S. M., & Pedersen, J. O. P. (2008). Presentation, calibration and validation of the low-order, DCESS Earth System model. *Geoscientific Model Development*, 1(1), 39-124.
- Shevliakova, E., Pacala, S. W., Malyshev, S., Hurtt, G. C., Milly, P., Caspersen, J. P., . . . Crevoisier, C. (2009). Carbon cycling under 300 years of land use change: Importance of the secondary vegetation sink. *Global biogeochemical cycles*, 23(2).
- Sitch, S., Smith, B., Prentice, I. C., Arneth, A., Bondeau, A., Cramer, W., . . . Sykes, M. T. (2003). Evaluation of ecosystem dynamics, plant geography and terrestrial carbon cycling in the LPJ dynamic global vegetation model. *Global Change Biology*, 9(2), 161-185.
- Sokolov, A. P., Schlosser, C. A., Dutkiewicz, S., Paltsev, S., Kicklighter, D. W., Jacoby, H. D., . . . Wang, C. (2005). MIT integrated global system model (IGSM) version 2: model description and baseline evaluation: MIT Joint Program on the Science and Policy of Global Change.
- Stier, P., Stier, J., Feichter, S., Kinne, S., Kloster, E., Vignati, J., . . . Petzold. (2005). The aerosol-climate model ECHAM5-HAM. *Atmospheric chemistry and physics*, 5(4), 1125-1156.
- Stoiber, R. E., Williams, S. N., & Huebert, B. (1987). Annual contribution of sulfur dioxide to the atmosphere by volcanoes. *Journal of Volcanology and Geothermal Research*, 33(1), 1-8.

- Stouffer, R., & Manabe, S. (1999). Response of a Coupled Ocean–Atmosphere Model to Increasing Atmospheric Carbon Dioxide: Sensitivity to the Rate of Increase. *Journal of Climate*, 12(8), 2224-2237.
- Strengers, B. J., Müller, C., Schaeffer, M., Haarsma, R. J., Severijns, C., Gerten, D., . . . Oostenrijk, R. (2010). Assessing 20th century climate–vegetation feedbacks of land-use change and natural vegetation dynamics in a fully coupled vegetation–climate model. *International Journal of Climatology*, 30(13), 2055-2065.
- Takata, K., Emori, S., & Watanabe, T. (2003). Development of the minimal advanced treatments of surface interaction and runoff. *Global and Planetary Change*, 38(1), 209-222.
- Tegen, I., & Fung, I. (1994). Modeling of mineral dust in the atmosphere: Sources, transport, and optical thickness. *Journal of Geophysical Research: Atmospheres (1984–2012)*, 99(D11), 22897-22914.
- Thomas, B. C., Arkenberg, K. R., Snyder, I., & Brock, R. (2011). Revisiting the Carrington Event: Updated modeling of atmospheric effects. *arXiv preprint arXiv:1111.5590*.
- Thomas, B. C., Jackman, C. H., & Melott, A. L. (2007). Modeling atmospheric effects of the September 1859 solar flare. *Geophysical research letters*, 34(6).
- Thomas, B. C., Melott, A. L., Fields, B. D., & Anthony-Twarog, B. J. (2008). Superluminous supernovae: no threat from η Carinae. *Astrobiology*, 8(1), 9-16.
- Thomas, B. C., Melott, A. L., Jackman, C. H., Laird, C. M., Medvedev, M. V., Stolarski, R. S., . . . Ejzak, L. M. (2005). Gamma-ray bursts and the Earth: Exploration of atmospheric, biological, climatic, and biogeochemical effects. *The Astrophysical Journal*, 634(1), 509.
- Tjiputra, J., Roelandt, C., Bentsen, M., Lawrence, D., Lorentzen, T., Schwinger, J., . . . Heinze, C. (2012). Evaluation of the carbon cycle components in the Norwegian Earth System Model (NorESM). *Geoscientific Model Development Discussions*, 5(4), 3035-3087.
- Usoskin, I. G., & Kovaltsov, G. A. (2006). Cosmic ray induced ionization in the atmosphere: Full modeling and practical applications. *Journal of Geophysical Research: Atmospheres (1984–2012)*, 111(D21).
- Verronen, P. T., Seppälä, A., Clilverd, M. A., Rodger, C. J., Kyrölä, E., Enell, C. F., . . . Turunen, E. (2005). Diurnal variation of ozone depletion during the October–November 2003 solar proton events. *Journal of Geophysical Research: Space Physics (1978–2012)*, 110(A9).
- Vichi, M., Manzini, E., Fogli, P. G., Alessandri, A., Patara, L., Scoccimarro, E., . . . Navarra, A. (2011). Global and regional ocean carbon uptake and climate change: sensitivity to a substantial mitigation scenario. *Climate dynamics*, 37(9-10), 1929-1947.
- Vizcaíno, M., Mikolajewicz, U., Gröger, M., Maier-Reimer, E., Schurgers, G., & Winguth, A. M. (2008). Long-term ice sheet–climate interactions under anthropogenic greenhouse forcing simulated with a complex Earth System Model. *Climate dynamics*, 31(6), 665-690.
- Voldoire, A. (2006). Quantifying the impact of future land-use changes against increases in GHG concentrations. *Geophysical research letters*, 33(4).
- Voldoire, A., Sanchez-Gomez, E., y Méliá, D. S., Decharme, B., Cassou, C., Sénési, S., . . . Chevallier, M. (2013). The CNRM-CM5. 1 global climate model: description and basic evaluation. *Climate dynamics*, 40(9-10), 2091-2121.
- Volodin, E., Dianskii, N., & Gusev, A. (2010). Simulating present-day climate with the INMCM4. 0 coupled model of the atmospheric and oceanic general circulations. *Izvestiya, Atmospheric and Oceanic Physics*, 46(4), 414-431.
- von Salzen, K., Scinocca, J. F., McFarlane, N. A., Li, J., Cole, J. N., Plummer, D., . . . Lazare, M. (2013). The Canadian fourth generation atmospheric global climate model (CanAM4). Part I: representation of physical processes. *Atmosphere-Ocean*, 51(1), 104-125.

- Washington, W., Weatherly, J., Meehl, G., Semtner Jr, A., Bettge, T., Craig, A., . . . James, R. (2000). Parallel climate model (PCM) control and transient simulations. *Climate dynamics*, 16(10-11), 755-774.
- Washington, W. M., & Meehl, G. A. (1983). General circulation model experiments on the climatic effects due to a doubling and quadrupling of carbon dioxide concentration. *Journal of Geophysical Research: Oceans (1978–2012)*, 88(C11), 6600-6610.
- Washington, W. M., & Meehl, G. A. (1996). High-latitude climate change in a global coupled ocean-atmosphere-sea ice model with increased atmospheric CO₂. *Journal of Geophysical Research: Atmospheres (1984–2012)*, 101(D8), 12795-12801.
- Watanabe, M., Suzuki, T., O'ishi, R., Komuro, Y., Watanabe, S., Emori, S., . . . Sekiguchi, M. (2010). Improved Climate Simulation by MIROC5: Mean States, Variability, and Climate Sensitivity. *Journal of Climate*, 23(23).
- Watanabe, S., Kawatani, Y., Tomikawa, Y., Miyazaki, K., Takahashi, M., & Sato, K. (2008). General aspects of a T213L256 middle atmosphere general circulation model. *Journal of Geophysical Research: Atmospheres (1984–2012)*, 113(D12).
- Wilson, C., & Mitchell, J. F. (1987). A doubled CO₂ climate sensitivity experiment with a global climate model including a simple ocean. *Journal of Geophysical Research: Atmospheres (1984–2012)*, 92(D11), 13315-13343.
- Woodward, F., Lomas, M. R., & Betts, R. A. (1998). Vegetation-climate feedbacks in a greenhouse world. *Philosophical Transactions of the Royal Society of London. Series B: Biological Sciences*, 353(1365), 29-39.
- Woodward, F. I., Smith, T. M., & Emanuel, W. R. (1995). A global land primary productivity and phytogeography model. *Global biogeochemical cycles*, 9(4), 471-490.
- Xin, X., Wu, T., Li, J., Wang, Z., Li, W., & Wu, F. (2013). How well does BCC_CSM1.1 reproduce the 20th century climate change over China. *Atmos. Oceanic Sci. Lett.*, 6(1), 21-26.
- Yeh, P. J.-F., & Eltahir, E. A. (2005). Representation of water table dynamics in a land surface scheme. Part I: Model development. *Journal of Climate*, 18(12).
- Yukimoto, S., Adachi, Y., & Hosaka, M. (2012). A new global climate model of the Meteorological Research Institute: MRI-CGCM3: model description and basic performance (special issue on recent development on climate models and future climate projections). *Journal of the Meteorological Society of Japan*, 90, 23-64.

Every reasonable effort has been made to acknowledge the owners of copyright material. I would be pleased to hear from any copyright owner who has been omitted or incorrectly acknowledged.

Appendix 1

Maple worksheet for calculating the amount of insolation per metre squared.

β - ε and $\varepsilon - (\pi/2 - \varepsilon)$ illumination areas

Northern Hemisphere

> **restart;**

Setting up time of the year, latitudinal belt, and general constants

In this example the calculations are performed for 40°-50° latitudinal belt and for $\alpha=30^\circ$

> **restart;**

> **R:=6371000; e:=23*Pi/180; rr:=R*sin(Pi*(5)/18);
r:=evalf(rr); hh:=R*sin(Pi*(4)/18); h:=evalf(hh);
a:=Pi*(3)/18; F:=1367;**

$$R := 6371000$$

$$e := \frac{23 \pi}{180}$$

$$rr := 6371000 \sin\left(\frac{5 \pi}{18}\right)$$

$$r := 0.4880469148 \cdot 10^7$$

$$hh := 6371000 \sin\left(\frac{2 \pi}{9}\right)$$

$$h := 0.4095199861 \cdot 10^7$$

$$a := \frac{\pi}{6}$$

$$F := 1367$$

Determining coordinates of the illumination area corner points

> **aa:=tan(e)*y1+r/cos(e)=sqrt(R^2-y1^2);s:=solve(aa, y1);**

$$aa := \tan\left(\frac{\pi}{13}\right)y1 + \frac{0.4880469148 \cdot 10^7}{\cos\left(\frac{\pi}{13}\right)} = \sqrt{40589641000000 - y1^2}$$

$$s := 0.2808228079 \cdot 10^7, -0.5144173511 \cdot 10^7$$

Point C₁

> **y1c1:=s[1]; z1c1:=sqrt(R^2-y1c1^2); y1c1:=evalf(y1c1);
z1c1:=evalf(z1c1);**

$$y1c1 := 0.2808228079 \cdot 10^7$$

$$z1c1 := 0.5718697060 \cdot 10^7$$

$$y1c1 := 0.2808228079 \cdot 10^7$$

$$z1c1 := 0.5718697060 \cdot 10^7$$

Point C₂

```
> y1c2:=s[2]; z1c2:=sqrt(R^2-y1c2^2); y1c2:=evalf(y1c2);
z1c2:=evalf(z1c2);
```

$$y1c2 := -0.5144173511 \cdot 10^7$$

$$z1c2 := 0.3758606110 \cdot 10^7$$

$$y1c2 := -0.5144173511 \cdot 10^7$$

$$z1c2 := 0.3758606110 \cdot 10^7$$

Point D₁

```
> bb:=tan(e)*y1+h/cos(e)=sqrt(R^2-y1^2);
t:=solve(bb, y1);
```

$$bb := \tan\left(\frac{\pi}{13}\right)y1 + \frac{0.4095199861 \cdot 10^7}{\cos\left(\frac{\pi}{13}\right)} = \sqrt{40589641000000 - y1^2}$$

$$t := 0.3758606109 \cdot 10^7, -0.5718697059 \cdot 10^7$$

```
> y1d1:=t[1]; z1d1:=sqrt(R^2-y1d1^2); y1d1:=evalf(y1d1);
z1d1:=evalf(z1d1);
```

$$y1d1 := 0.3758606109 \cdot 10^7$$

$$z1d1 := 0.5144173512 \cdot 10^7$$

$$y1d1 := 0.3758606109 \cdot 10^7$$

$$z1d1 := 0.5144173512 \cdot 10^7$$

Point D₂

```
> y1d2:=t[2]; z1d2:=sqrt(R^2-y1d2^2); y1d2:=evalf(y1d2);
z1d2:=evalf(z1d2);
```

$$y1d2 := -0.5718697059 \cdot 10^7$$

$$z1d2 := 0.2808228080 \cdot 10^7$$

$$y1d2 := -0.5718697059 \cdot 10^7$$

$$z1d2 := 0.2808228080 \cdot 10^7$$

Point A₁

```
> b:=(y1^2/(R^2*(sin^2)(a))+(tan(e)*y1+r/cos(e))^2/R^2=1);
v:=solve(b, y1);
```

$$b := \frac{y1^2}{10147410250000} + \frac{1}{40589641000000} \left(\tan\left(\frac{\pi}{13}\right)y1 + \frac{0.4880469148 \cdot 10^7}{\cos\left(\frac{\pi}{13}\right)} \right)^2 = 1$$

$$v := 0.1661288941 \cdot 10^7, -0.2271485684 \cdot 10^7$$

```
> y1a1:=v[1];
```

$$y1a1 := 0.1661288941 \cdot 10^7$$

```
> z1a1:=tan(e)*y1a1+r/cos(e); y1a1:=evalf(y1a1);  
z1a1:=evalf(z1a1);
```

$$z1a1 := 0.1661288941 \cdot 10^7 \tan\left(\frac{\pi}{13}\right) + \frac{0.4880469148 \cdot 10^7}{\cos\left(\frac{\pi}{13}\right)}$$

$$y1a1 := 0.1661288941 \cdot 10^7$$

$$z1a1 := 0.5436001952 \cdot 10^7$$

Point A₂

```
> y1a2:=v[2]; z1a2:=tan(e)*y1a2+r/cos(e);
```

```
y1a2:=evalf(y1a2); z1a2:=evalf(z1a2);
```

$$y1a2 := -0.2271485684 \cdot 10^7$$

$$z1a2 := -0.2271485684 \cdot 10^7 \tan\left(\frac{\pi}{13}\right) + \frac{0.4880469148 \cdot 10^7}{\cos\left(\frac{\pi}{13}\right)}$$

$$y1a2 := -0.2271485684 \cdot 10^7$$

$$z1a2 := 0.4466660066 \cdot 10^7$$

Point B₁

```
> f:=(y1^2/(R^2*(sin^2)(a)))+(tan(e)*y1+h/cos(e))^2/R^2=1;
```

```
m:=solve(f, y1);
```

```
> y1b1:=m[1];
```

```
z1b1:=tan(e)*y1b1+h/cos(e);
```

```
> y1b1:=evalf(y1b1); z1b1:=evalf(z1b1);
```

$$f := \frac{y1^2}{10147410250000} + \frac{1}{40589641000000} \left(\tan\left(\frac{\pi}{13}\right) y1 + \frac{0.4095199861 \cdot 10^7}{\cos\left(\frac{\pi}{13}\right)} \right)^2 = 1$$

$$m := 0.2127329808 \cdot 10^7, -0.2639345670 \cdot 10^7$$

$$y1b1 := 0.2127329808 \cdot 10^7$$

$$z1b1 := 0.2127329808 \cdot 10^7 \tan\left(\frac{\pi}{13}\right) + \frac{0.4095199861 \cdot 10^7}{\cos\left(\frac{\pi}{13}\right)}$$

$$y1b1 := 0.2127329808 \cdot 10^7$$

$$z1b1 := 0.4742100015 \cdot 10^7$$

Point B₂

```
> y1b2:=m[2]; z1b2:=tan(e)*y1b2+h/cos(e);
y1b2:=evalf(y1b2); z1b2:=evalf(z1b2);
```

Assigning Integrands

```
> A:=F*sin(a)-F*cos(a)*y1/(sqrt(R^2-y1^2-z1^2));
B:=F*sin(a)-F*cos(a)*(-y1)/(sqrt(R^2-y1^2-z1^2));
y1b2 := -0.2639345670 107
```

$$z1b2 := -0.2639345670 \cdot 10^7 \tan\left(\frac{\pi}{13}\right) + \frac{0.4095199861 \cdot 10^7}{\cos\left(\frac{\pi}{13}\right)}$$

$$y1b2 := -0.2639345670 \cdot 10^7$$

$$z1b2 := 0.3567220029 \cdot 10^7$$

$$A := 684 - \frac{684 \sqrt{3} y1}{\sqrt{40589641000000 - y1^2 - z1^2}}$$

$$B := 684 + \frac{684 \sqrt{3} y1}{\sqrt{40589641000000 - y1^2 - z1^2}}$$

Assigning Linear Approximation used

```
> Ka2b2:=(z1a2-z1b2)/(y1a2-y1b2); Ba2b2:=z1a2-Ka2b2*y1a2;
a2b2:=Ka2b2*y1+Ba2b2;
Ka2b2 := 2.445060815
```

$$Ba2b2 := 0.1002058070 \cdot 10^8$$

$$a2b2 := 2.445060815 y1 + 0.1002058070 \cdot 10^8$$

```
> Ka1b1:=(z1a1-z1b1)/(y1a1-y1b1); Ba1b1:=z1a1-Ka1b1*y1a1;
a1b1:=Ka1b1*y1+Ba1b1;
Ka1b1 := -1.488929375
```

$$Ba1b1 := 0.7909543857 \cdot 10^7$$

$$a1b1 := -1.488929375 y1 + 0.7909543857 \cdot 10^7$$

```
> Kc1d1:=(z1c1-z1d1)/(y1c1-y1d1); Bc1d1:=z1c1-Kc1d1*y1c1;
c1d1:=Kc1d1*y1+Bc1d1;
Kc1d1 := -0.6045210746
```

$$Bc1d1 := 0.7416330116 \cdot 10^7$$

$$c1d1 := -0.6045210746 y1 + 0.7416330116 \cdot 10^7$$

Evaluating total amount of insolation via double integrals

```
> k1:=int(A, z1=tan(e)*y1+h/cos(e)..a2b2) assuming
y1<y1a2, y1>y1b2;
```

$$k1 := 0.3969129147 \cdot 10^{10} + 1503.830739 \cdot yI$$

$$+ 1184.722752 \cdot yI \arcsin\left(\frac{1.029927831 (0.2393156643 \cdot yI + 0.4095199861 \cdot 10^7)}{\sqrt{0.4058964100 \cdot 10^{14} - 1 \cdot yI^2}}\right)$$

$$- 1184.722753 \cdot yI \arcsin\left(\frac{2.445060815 \cdot yI + 0.1002058070 \cdot 10^8}{\sqrt{0.4058964100 \cdot 10^{14} - 1 \cdot yI^2}}\right)$$

> **k1i:=int(k1, y1=y1b2..y1a2);**
k1i := 0.1971461177 10¹⁵

> **k2:=int(A, z1=h/cos(e)..r/cos(e)) assuming y1>y1a2, y1<y1c1;**

$$k2 := 0.553199154 \cdot 10^9 + 1184.722752 \cdot yI \arcsin\left(\frac{0.4217760310 \cdot 10^7}{\sqrt{0.4058964100 \cdot 10^{14} - 1 \cdot yI^2}}\right)$$

$$- 1184.722752 \cdot yI \arcsin\left(\frac{0.5026531004 \cdot 10^7}{\sqrt{0.4058964100 \cdot 10^{14} - 1 \cdot yI^2}}\right)$$

> **k2i:=int(k2, y1=y1a2..y1c1, numeric);**
k2i := 0.2437977778 10¹⁶

> **k3:=int(A, z1=tan(e)*y1+h/cos(e)..c1d1) assuming y1>y1c1, y1<y1d1;**

$$k3 := 0.2187821747 \cdot 10^{10} - 582.0832734 \cdot yI$$

$$+ 1184.722752 \cdot yI \arcsin\left(\frac{1.029927831 (0.2393156643 \cdot yI + 0.4095199861 \cdot 10^7)}{\sqrt{0.4058964100 \cdot 10^{14} - 1 \cdot yI^2}}\right)$$

$$+ 1184.722753 \cdot yI \arcsin\left(\frac{-0.7416330116 \cdot 10^7 + 0.6045210746 \cdot yI}{\sqrt{0.4058964100 \cdot 10^{14} - 1 \cdot yI^2}}\right)$$

> **k3i:=int(k3, y1=y1d1..y1c1, numeric);**
k3i := 0.7869899994 10¹⁵

> **k4:=int(B, z1=a1b1..tan(e)*y1+r/cos(e)) assuming y1>y1a1, y1<y1b1;**

$$k4 := -0.1971980792 \cdot 10^{10} + 1187.018550 \cdot yI$$

$$+ 1184.722753 \cdot yI \arcsin\left(\frac{1.488929375 \cdot yI - 0.7909543857 \cdot 10^7}{\sqrt{0.4058964100 \cdot 10^{14} - 1 \cdot yI^2}}\right)$$

$$+ 1184.722752 \cdot yI \arcsin\left(\frac{1.029927831 (0.2393156643 \cdot yI + 0.4880469148 \cdot 10^7)}{\sqrt{0.4058964100 \cdot 10^{14} - 1 \cdot yI^2}}\right)$$

> **k4i:=int(k4, y1=y1a1..y1b1, numeric);**
k4i := 0.2762799481 10¹⁵

> **k5:=int(B, z1=h/cos(e)..r/cos(e)) assuming y1>y1b1, y1<y1c1;**

$$k5 := 0.553199154 \cdot 10^9 - 1184.722752 \cdot yI \arcsin\left(\frac{0.4217760310 \cdot 10^7}{\sqrt{0.4058964100 \cdot 10^{14} - 1. \cdot yI^2}}\right) \\ + 1184.722752 \cdot yI \arcsin\left(\frac{0.5026531004 \cdot 10^7}{\sqrt{0.4058964100 \cdot 10^{14} - 1. \cdot yI^2}}\right)$$

> **k5i:=int(k5, y1=y1b1..y1c1, numeric);**
k5i := 0.8297604427 10¹⁵

> **k6:=int(B, z1=tan(e)*y1+h/cos(e)..c1d1) assuming y1<y1d1, y1>y1c1;**

$$k6 := 0.2187821747 \cdot 10^{10} - 582.0832734 \cdot yI \\ - 1184.722752 \cdot yI \arcsin\left(\frac{1.029927831 (0.2393156643 \cdot yI + 0.4095199861 \cdot 10^7)}{\sqrt{0.4058964100 \cdot 10^{14} - 1. \cdot yI^2}}\right) \\ - 1184.722753 \cdot yI \arcsin\left(\frac{-0.7416330116 \cdot 10^7 + 0.6045210746 \cdot yI}{\sqrt{0.4058964100 \cdot 10^{14} - 1. \cdot yI^2}}\right)$$

> **k6i:=int(k6, y1=y1c1..y1d1, numeric);**
k6i := 0.1312738322 10¹⁶

>
 > **i:=k1i+k2i+k3i+k4i+k5i+k6i;**
i := 0.5840892608 10¹⁶

Calculating surface area of latitudinal belt

> **G:=2*Pi*R*(r-h);**
G := 0.1000590125 10¹⁴ π

Calculating amount of insolation per unit area

> **Answer:=i/G; evalf(%);**
Answer := $\frac{583.7447784}{\pi}$
 185.8117339

Appendix 2

Revised C-GOLDSTEIN code to incorporate seasonal variations of insolation.

```
Appendix 2 Revised C-GOLDSTEIN code to incorporate seasonal
variations
of insolation
* mains.F main program for thermocline equation model goldstein
* variable depth 3/5/95
* extra outputs for global version 19/4/00
* #ifdef's added so that mains.f -> mains.F 6/5/2
*
      program goldstein
      include 'var.cmn'

      real avn, avs, sum, sums(8*maxl), tv(maxl,maxi,maxj,maxk),
rms
      real sum1, sum2, cor, pacsf, ty

c to average osc runs
c      real ats(maxl,maxi,maxj,maxk), au(3,maxi,maxj,maxk)
c      1      , afn(maxl,maxi,maxj,maxk)

      real opsi(0:maxj,0:maxk), ou(maxj,maxk), f1, f2
      real opsia(0:maxj,0:maxk), omina, omaxa,
      real opsip(0:maxj,0:maxk), ominp, omaxp
      real f3, f4, f5, f6,

      real zpsi(0:maxi,0:maxk), zu(maxi,maxk)

      integer nsteps, npstp, iwstp, itstp, iw, icount
      1      , i, j, k, l, istep, iterun, isol, isl, natm

      character ans,lout*3,lin*6,ext*3,conv*3

      logical flat, osc

      real hft(3), hfp(3), hfa(3), phfmax, tv2, tv3
      real psisl(0:maxi,0:maxj,isles),
ubisl(2,0:maxi+1,0:maxj,isles)
ctest1      ,erisl(isles,isles+1), psibc(2)
      1      ,erisl(isles+1,isles+1), psibc(2)

      real c13, c14, c15, c16, c17, c18
      real c19, d13, d14, d15, d16, d17
      real d18, d19, c23, c24, c25, c26
      real c27, c28, c29, d23, d24, d25
      real d26, d27, d28, d29, e3, e4
      real e8, e9, c34, c37, c38, d34
      real d37, d38, c44, c47, c48, d44
      real d47, d48, a11, a12, a13, a16
      real a19, b11, b12, b13, b16, b19
      real w11, w12, w13, w16, w19, f11
      real f12, f13, f16, f19, a26, a29
      real b26, b29, w26, w29, f26, f29
      real a36, a39, b36, b39, w36, w39
      real f36, f39, c36, c37, c46, d46
      real temp1, temp2, temp3, temp4
```

```

c
c for repeated runs forward or backward
c
c   open(20,file='output.553R')
c   do iterun=10,250,10
c   do iterun=240,0,-10
c   open(5,file='input.553')

   print*,'nsteps npstp iwstp itstp'
   read(5,*)nsteps,npstp,iwstp,itstp
   print*,'nsteps,npstp,iwstp,itstp'
   print*,'new or continuing run ?'
   read(5,'(a1)')ans
   print*,ans

   call gseto
c EMBM
   call gseta

   print*,'file extension for output (a3) ?'
   read(5,'(a3)')lout

   open(4,file='../results/'//lout//'. '//t')
   write(4,'(11(a11,3x))')
$           '%time'           '
$           ', ' Pac_T_d      ', ' Atl_T_d      '
$           ', ' Ind_T_d      ', ' Sou_T_d      '
$           ', ' Pac_T_u      ', ' Atl_T_u      '
$           ', ' Ind_T_u      ', ' Sou_T_u      '
$           ', ' drho/dz      ', ' speed        '

   open(14,file='../results/'//lout//'. '//s')
   write(14,'(11(a11,3x))')
$           '%time'           '
$           ', ' Pac_S_d      ', ' Atl_S_d      '
$           ', ' Ind_S_d      ', ' Sou_S_d      '
$           ', ' Pac_S_u      ', ' Atl_S_u      '
$           ', ' Ind_S_u      ', ' Sou_S_u      '
$           ', ' drho/dz      ', ' speed        '

   if(ans.eq.'n'.or.ans.eq.'N')then
* define an i.c. done in gset
   else
       print*,'input file extension for input (a6)'
       read(5,'(a6)')lin
       open(1,file='../results/'//lin)
       call inm(1)
       close(1)
c perturb the salinity
c   print*,'perturbing the i.c.'
c   do k=10 ,16
c   do i=9,11
c   do j=1,1
c       ts(1, i,j ,k ) = ts(1, i,j ,k ) + 0.2*(1-0.5*abs(
c   1       real(i-10)))
c   enddo
c   enddo
c   enddo

```



```

do k=1,kmax
  do j=1,jmax
    do i=1,imax
      do l=1,lmax
        ts1(l,i,j,k) = ts(l,i,j,k)
      enddo
      rho(i,j,k) = ec(1)*ts(1,i,j,k) +
ec(2)*ts(2,i,j,k)
1          + ec(3)*ts(1,i,j,k)**2 +
ec(4)*ts(1,i,j,k)**3
    enddo
  enddo
enddo
c EMBM atm
do j=1,jmax
  do i=1,imax
    tq1(1,i,j) = tq(1,i,j)
    tq1(2,i,j) = tq(2,i,j)
  enddo
enddo
c EMBM sea-ice
do j=1,jmax
  do i=1,imax
    varicel(1,i,j) = varice(1,i,j)
    varicel(2,i,j) = varice(2,i,j)
  enddo
enddo
endif

c periodic b.c. (required for implicit code)

do k=1,kmax
  do j=1,jmax
    rho(0,j,k) = rho(imax,j,k)
    rho(imax+1,j,k) = rho(1,j,k)
    do l=1,lmax
      ts(1,0,j,k) = ts(1,imax,j,k)
      ts(1,imax+1,j,k) = ts(1,1,j,k)
c for cimp.ne.1 need
      ts1(1,0,j,k) = ts(1,imax,j,k)
      ts1(1,imax+1,j,k) = ts(1,1,j,k)
    enddo
  enddo
enddo

c oscillating forcing

c   if(abs(sdal).gt. 1e-5)then
c     osc = .true.
c     print*,'oscillatory forcing amplitude',sdal
c     do k=1,kmax
c       do j=1,jmax
c         do i=1,imax
c           do l=1,lmax
c             ats(l,i,j,k)= 0
c             afn(l,i,j,k) = 0
c           enddo
c         do l=1,3

```

```

c             au(1,i,j,k) = 0
c             enddo
c             enddo
c             enddo
c             enddo
c             else
c             osc = .false.
c             endif

flat = .true.
do i=1,imax
  do j=1,jmax
    if(kl(i,j).gt.1.and.kl(i,j).le.kmax)flat = .false.
  enddo
enddo
if(flat)then
  print*,'flat bottom'
else
  print*,'topography present'
endif

call invert

#ifdef disle2
c code for multiple islands
  if(isles.ne.2)stop 'Makefile and var.cmn have different no.
isles'
#endif

do isol=1,isles

c set source term to 1 on the ith island (i+1th landmass) only

do j=0,jmax
  do i=1,imax
    k=i + j*imax
    if(gbold(k).eq.isol + 1)then
      gb(k) = 1.0
    else
      gb(k) = 0.0
    endif
  enddo
enddo
call ubarsolv(ubisl(1,0,0,isol),psisl(0,0,isol))

c find island path integral due to unit source on boundary
conditions

do isl=1,isles
  call island(ubisl(1,0,0,isol),erisl(isl,isol),isl,0)
enddo
enddo

print*,'island path integrals due to unit sources',
&      ((erisl(isl,isol),isl=1,isles),isol=1,isles)

call wind

```

```
iw = 1
icount = 0
```

c assigning the coefficients

```
c13=18.33
c14=28.5
c15=18.67
c16=26.86
c17=8
c18=19
c19=87.25
```

```
d13=218.33
d14=129
d15=110.33
d16=26.14
d17=27
d18=-59
d19=-903.19
```

```
c23=-18.33
c24=-28.5
c25=-18.67
c26=-26.86
c27=-8
c28=-20.8
c29=-87.25
```

```
d23=914.89
d24=1212
d25=819.73
d26=1046.71
d27=331
d28=722.4
d29=2412.36
```

```
e3=252
e4=185
e8=0
e9=0
```

```
c34=12.7
c36=5.75
c37=37.2
c38=38.89
```

```
d34=223.85
d36=199
d37=-235.8
d38=-248.89
```

```
c44=-12.7
c46=-5.25
c47=-37.2
c48=-38.89
```

d44=706.3
d46=398.5
d47=1177.8
d48=1228.91

a11=31.79
a12=52.05
a13=73.6
a16=56.07
a19=57.65

b11=408.44
b12=382.59
b13=373.3
b16=412.54
b19=459.93

w11=0.17
w12=0.17
w13=0.17
w16=0.9
w19=0.7

f11=-1.57
f12=-1.57
f13=-1.57
f16=9.6
f19=0.84

a26=100
a29=168.84

b26=345.68
b29=67.39

w26=0.3
w29=0.17

f26=1.59
f29=-1.57

a36=63.43
a39=171.26

b36=307.22
b39=96.5

w36=0.3
w39=0.17

f36=2.33
f39=-1.57

```
c      open(500,file='../results/'//lout//'.leto')
```

```
* time loop
```

```

do istep=1,nsteps
c   if (istep .gt. 119) then
c   write(500,*) 'istep= ', istep
sum = 0
      do j=1,jmax
      do i=1,imax
c         write(500,*) tq(1,i,j)
          sum = sum +tq(1,i,j)
      enddo
      enddo
write(500,*)sum/imax/jmax
c   endif

      ty = istep/9.7

c 80-90N
      if (ty.le.6) then
temp1=e9
      elseif (ty.le.12) then
temp1=a29*sin(w29*ty+f29)+b29
      elseif (ty.le.14) then
temp1=c19*ty+d19
      elseif (ty.le.23) then
temp1=a19*sin(w19*ty+f19)+b19
      elseif (ty.le.25) then
temp1=c29*ty+d29
      elseif (ty.le.31) then
temp1=a39*sin(w39*ty+f39)+b39
      elseif (ty.le.37) then
temp1=e9
      endif

c 70-80N
      if (ty.le.6) then
temp2=e8
      elseif (ty.le.9) then
temp2=c18*ty+d18
      elseif (ty.le.19) then
temp2=c38*ty+d38
      elseif (ty.le.28) then
temp2=c48*ty+d48
      elseif (ty.le.33) then
temp2=c28*ty+d28
      elseif (ty.le.37) then
temp2=e8
      endif

c 70-90N

      solfor(1)=0.5*(temp1+temp2)

c 60-70N
      if (ty.le.9) then
solfor(2)=c17*ty+d17
      elseif (ty.le.19) then
solfor(2)=c37*ty+d37
      elseif (ty.le.28) then
solfor(2)=c47*ty+d47

```

```
elseif (ty.le.37) then
solfor(2)=c27*ty+d27
endif
```

c 50-60N

```
if (ty.le.8) then
solfor(3)=c16*ty+d16
elseif (ty.le.11) then
solfor(3)=c36*ty+d36
elseif (ty.le.16) then
solfor(3)=a26*sin(w26*ty+f26)+b26
elseif (ty.le.21) then
solfor(3)=a16*sin(w16*ty+f16)+b16
elseif (ty.le.26) then
solfor(3)=a36*sin(w36*ty+f36)+b36
elseif (ty.le.29) then
solfor(3)=c46*ty+d46
elseif (ty.le.37) then
solfor(3)=c26*ty+d26
endif
```

```
solfor(4)=solfor(3)
```

c 40-50N

```
if (ty.le.19) then
solfor(5)=c15*ty+d15
elseif (ty.le.37) then
solfor(5)=c25*ty+d25
endif
```

```
solfor(6)=solfor(5)
```

c 30-40N

```
if (ty.le.1) then
solfor(7)=e4
elseif (ty.le.5) then
solfor(7)=c14*ty+d14
elseif (ty.le.19) then
solfor(7)=c34*ty+d34
elseif (ty.le.32) then
solfor(7)=c44*ty+d44
elseif (ty.le.36) then
solfor(7)=c24*ty+d24
elseif (ty.le.37) then
solfor(7)=e4
endif
```

```
solfor(8)=solfor(7)
```

```
solfor(9)=solfor(7)
```

c 20-30N

```
if (ty.le.1) then
solfor(10)=e3
elseif (ty.le.4) then
solfor(10)=c13*ty+d13
elseif (ty.le.33) then
solfor(10)=a13*sin(w13*ty+f13)+b13
elseif (ty.le.36) then
```

```

        solfor(10)=c23*ty+d23
        elseif (ty.le.37) then
        solfor(10)=e3
        endif

        solfor(11)=solfor(10)
        solfor(12)=solfor(10)

c 10-20N
        solfor(13)=a12*sin(w12*ty+f12)+b12

        solfor(14)=solfor(13)
        solfor(15)=solfor(13)

c 0-10N
        solfor(16)=a11*sin(w11*ty+f11)+b11

        solfor(17)=solfor(16)
        solfor(18)=solfor(16)

c 0-10S
        solfor(19)=a11*sin(w11*(ty+18)+f11)+b11
        solfor(20)=solfor(19)
        solfor(21)=solfor(19)

c 10-20S
        solfor(22)=a12*sin(w12*(ty+18)+f12)+b12
        solfor(23)=solfor(22)
        solfor(24)=solfor(22)

c 20-30S
        if (ty.le.15) then
        solfor(25)=a13*sin(w13*(ty+18)+f13)+b13
        elseif (ty.le.18) then
        solfor(25)=c23*(ty+18)+d23
        elseif (ty.le.20) then
        solfor(25)=e3
        elseif (ty.le.23) then
        solfor(25)=c13*(ty-18)+d13
        elseif (ty.le.37) then
        solfor(25)=a13*sin(w13*(ty-18)+f13)+b13
        endif

        solfor(26)=solfor(25)
        solfor(27)=solfor(25)

c 30-40S
        if (ty.le.14) then
        solfor(28)=c44*(ty+18)+d44
        elseif (ty.le.18) then
        solfor(28)=c24*(ty+18)+d24
        elseif (ty.le.20) then
        solfor(28)=e4
        elseif (ty.le.24) then
        solfor(28)=c14*(ty-18)+d14
        elseif (ty.le.37) then
        solfor(28)=c34*(ty-18)+d34
        endif

```

```

        solfor(29)=solfor(28)
        solfor(30)=solfor(28)

c 40-50S
    if (ty.le.19) then
        solfor(31)=c25*(ty+18)+d25
    elseif (ty.le.37) then
        solfor(31)=c15*(ty-18)+d15
    endif

        solfor(32)=solfor(31)

c 50-60S
    if (ty.le.3) then
        solfor(33)=a16*sin(w16*(ty+18)+f16)+b16
    elseif (ty.le.8) then
        solfor(33)=a36*sin(w36*(ty+18)+f36)+b36
    elseif (ty.le.11) then
        solfor(33)=c46*(ty+18)+d46
    elseif (ty.le.19) then
        solfor(33)=c26*(ty+18)+d26
    elseif (ty.le.26) then
        solfor(33)=c16*(ty-18)+d16
    elseif (ty.le.29) then
        solfor(33)=c36*(ty-18)+d36
    elseif (ty.le.34) then
        solfor(33)=a26*sin(w26*(ty-18)+f26)+b26
    elseif (ty.le.37) then
        solfor(33)=a16*sin(w16*(ty-18)+f16)+b16
    endif

        solfor(34)=solfor(33)

c 60-70S
    if (ty.le.9) then
        solfor(35)=c47*(ty+18)+d47
    elseif (ty.le.19) then
        solfor(35)=c27*(ty+18)+d27
    elseif (ty.le.28) then
        solfor(35)=c17*(ty-18)+d17
    elseif (ty.le.37) then
        solfor(35)=c37*(ty-18)+d37
    endif

c 70-80S
    if (ty.le.10) then
        temp3=c48*(ty+18)+d48
    elseif (ty.le.15) then
        temp3=c28*(ty+18)+d28
    elseif (ty.le.22) then
        temp3=e8
    elseif (ty.le.27) then
        temp3=c18*(ty-18)+d18
    elseif (ty.le.37) then
        temp3=c38*(ty-18)+d38
    endif

```



```

c 80-90S
    if (ty.le.5) then
        temp4=a19*sin(w19*(ty+18)+f19)+b19
    elseif (ty.le.7) then
        temp4=c29*(ty+18)+d29
    elseif (ty.le.13) then
        temp4=a39*sin(w39*(ty+18)+f39)+b39
    elseif (ty.le.24) then
        temp4=e9
    elseif (ty.le.30) then
        temp4=a29*sin(w29*(ty-18)+f29)+b29
    elseif (ty.le.32) then
        temp4=c19*(ty-18)+d19
    elseif (ty.le.37) then
        temp4=a19*sin(w19*(ty+-18)+f19)+b19
    endif

c 70-90S

    solfor(361)=0.5*(temp3+temp4)

c
    if(osc)call oscr
    if(.not.flat.or.osc.or.istep.eq.1)then
        call jbar
        call ubarsolv(ub,psi)

c find island path integral due to wind and jbar terms

        do isl=1,isles
            call island(ub,erisl(isl,isles+1),isl,1)
        enddo

#ifdef disle2
c solve system of simultaneous equations. Zero division here
might
c suggest not enough islands in the .psiles file

        psibc(1) = (- erisl(1,3)*erisl(2,2) +
erisl(2,3)*erisl(1,2))
            1 / (erisl(2,2)*erisl(1,1) -
erisl(2,1)*erisl(1,2))
        psibc(2) = (erisl(1,3)*erisl(2,1) -
erisl(2,3)*erisl(1,1))
            1 / (erisl(2,2)*erisl(1,1) -
erisl(2,1)*erisl(1,2))

c to artificially set flows around islands to zero set psibc() to
zero
c
        psibc(1) = 0
c
        psibc(2) = 0
#else
        psibc(1) = - erisl(1,2)/erisl(1,1)
#endif

        do j=1,jmax
            do i=0,imax+1

```

```

                do isl=1,isles
                    ub(1,i,j) = ub(1,i,j) +
ubisl(1,i,j,isl)*psibc(isl)
                    ub(2,i,j) = ub(2,i,j) +
ubisl(2,i,j,isl)*psibc(isl)
                enddo
            enddo
        enddo
c
c update diagnostic psi, not always necessary
c
        do j=0,jmax
            do i=0,imax
                do isl=1,isles
                    psi(i,j) = psi(i,j) +
psisl(i,j,isl)*psibc(isl)
                enddo
            enddo
        enddo
    endif

c update velocities

        call velc

c EMBM change E-P forcing
c     extra0 = extra0 + ?? check def'n same

ccc HYSTERESIS option
c gradual increase/decrease P-E in N.Atlantic
c plus/minus range0 Sv @ 0.05 Sv/1000 yr [after Rahmstorf 1996]
        extra0 = extra0 + (range0/real(nsteps))

ccc MELTWATER PULSE option
c reset extra0 to zero after 25/50/100 years:
        if(istep.ge.nsteps_extra0) extra0 = 0.0

c EMBM surface fluxes
c EMBM sea ice now updated in surflux to allow adjustment of
surface fluxes
        call surflux

#ifdef dimpo
        call tstipo(istep)
#else
        call tstepo(istep)
#endif

c EMBM update 1-layer atmosphere

        do natm = 1,ndta
#ifdef dimpa
        call tstipa
#else
        call tstepa

```

```

write(500,*) 'istep= ', istep, 'natm=',natm

      if (istep .eq. 252) then

open(500,file='../results/'///lout//'.leto')

sum = 0
write(500, *) istep
do j=1,jmax
  do i=1,imax
    write(500,*) tq(1,i,j)
    sum = sum +tq(1,i,j)
  enddo
enddo
write(500,*)sum/imax/jmax
close(500)
endif

#endif
c      if(mod(istep,npstp).lt.1) call diaga
      enddo

      t = istep*dt(kmax) + t0

      if(mod(istep,npstp).lt.2)then

print*
print*,'step ',istep,' t ',t,' dt ',dt(kmax)
print*,'psi on islands ',(psibc(isl),isl=1,isles)

      call diag
      if(mod(istep,npstp).eq.0)then
        do k=1,kmax
          do j=1,jmax
            do i=1,imax
              do l=1,lmax
                tv(1,i,j,k) = ts(1,i,j,k)
              enddo
            enddo
          enddo
        enddo
      else if(mod(istep,npstp).eq.1.and.istep.gt.1)then
c      open(7,file='../results/tmp.1')
        rms = 0
        do j=1,jmax
          do i=1,imax
            do k=1,kmax
              do l=1,lmax
                rms = rms + (tv(1,i,j,k) -
ts(1,i,j,k))**2
c      change = (tv(1,i,j,k) - ts(1,i,j,k))
c      if(j.eq.3.and.k.eq.kmax-
1)write(6,*)i,j,k,l,change
c      write(7,*)(tv(1,i,j,k) - ts(1,i,j,k))/dt(kmax)

```

```

                                enddo
                                enddo
                                enddo
                                enddo

c                                close (7)
                                rms = sqrt(rms/lmax/ntot/dt(kmax)/dt(kmax))
                                print*,'r.m.s. r.o.c.',rms
                                endif
                                endif

                                if(mod(istep,iwstp).eq.0)then
                                ext=conv(mod(iw,10))
                                open(2,file='../results/\\lout//'.//ext)
                                rewind 2
                                call outm(2)
                                close(2)
c write oscillating streamfunction
                                if(.not.flat.or.osc)then
                                open(2,file='../results/\\lout//'.psi.//ext)
                                do j=0,jmax
                                do i=0,imax
                                write(2,*)psi(i,j)
                                enddo
                                enddo
                                close(2)
                                endif
                                iw = iw + 1
                                endif

                                if(mod(istep,itstp).eq.0)then
c                                open(4,file='../results/\\lout//'.//t'
c 1                                ,access='append')
c for ibm no access parameter and don't close file faster on sg
too
                                open(4,file='../results/\\lout//'.//t')
                                open(14,file='../results/\\lout//'.//s')
                                open(40,file='../results/\\lout//'.//opsit')

                                call diag2(sums,avn,avs)
                                write(4,110)t,(sums(i),i=1,8),avn,avs
                                write(14,110)t,(sums(i),i=9,16),avn,avs

c EMBM
                                open(41,file='../results/\\lout//'.//airt')
                                open(42,file='../results/\\lout//'.//q')
                                call diag3(sum1,sum2)
                                write(41,110)t,sum1
                                write(42,110)t,sum2
c
                                close(4)

c                                if(osc)then
c                                open(8,file='../results/\\lout//'.osi')
c                                write(8,100)(ts(2,i,20,7 ),i=1,imax)
c                                write(8,100)( u(2,i, 1,7 ),i=1,imax)
c                                open(9,file='../results/\\lout//'.osj')
c                                write(9,100)(ts(2,1 ,j, 7),j=1,jmax)

```

```

c          open(12,file='../results/'//lout//'.osk'
c      1          ,access='append')
c          write(12,100)(ts(1,10,10,k ),k=1,kmax)
c          close(12)
c to average osc runs
c          if(osc)call oscav(ats,au,afn,icount)
c          endif

c Calculate meridional overturning streamfunction opsi on C grid
only

      do j=0,jmax
        do k=0,kmax
          opsi(j,k) = 0
          opsia(j,k) = 0
          opsip(j,k) = 0
        enddo
      enddo

      do 35 j=1,jmax-1
        do 40 k=1,kmax-1
          ou(j,k) = 0
          do 45 i=1,imax
            ou(j,k) = ou(j,k) + cv(j)*u(2,i,j,k)*dphi
45          continue
            opsi(j,k) = opsi(j,k-1) - dz(k)*ou(j,k)
40          continue
35          continue
c
c Pacific and Atlantic overturning streamfunctions
c
      ominp = 0
      omaxp = 0
      do j=jsf+1,jmax-1
        do k=1,kmax-1
          ou(j,k) = 0
          do i=ips(j),ipf(j)
            ou(j,k) = ou(j,k) + cv(j)*u(2,i,j,k)*dphi
          enddo
          opsip(j,k) = opsip(j,k-1) - dz(k)*ou(j,k)
          if(opsip(j,k).lt.ominp)ominp = opsip(j,k)
          if(opsip(j,k).gt.omaxp)omaxp = opsip(j,k)
        enddo
      enddo

      omina = 0
      omaxa = 0
      do j=jsf+1,jmax-1
c if continuing run, then just N.Atlantic
c      do j=10,jmax-1
c          do k=1,kmax-1
c excluding surface wind-driven cells (below 500m)
          do k=1,kmax-3
            ou(j,k) = 0
            do i=ias(j),iaf(j)
              ou(j,k) = ou(j,k) + cv(j)*u(2,i,j,k)*dphi
            enddo
            opsia(j,k) = opsia(j,k-1) - dz(k)*ou(j,k)

```

```

        if(opsia(j,k).lt.omin) omin = opsia(j,k)
        if(opsia(j,k).gt.omax) omax = opsia(j,k)
    enddo
enddo

write(40, '(6e15.5)') t, extra0, ominp, omexp, omin, omax

endif

c end time loop

    enddo
    close(500)

    close(4)
    close(14)
    close(40)
    close(41)
    close(42)
c   close(8)
c   close(9)

    call diagend(lout)

c put all the following junk into diagend when get round to it.??

c write out convective frequency array. Divide by 2*nsteps if
call co twice

    open(3, file='../results/'//lout//'.cost')
    if(nsteps.gt.0) write(3, '(e15.8)') ((cost(i,j)/nsteps
c   if(nsteps.gt.0) write(3, '(e15.8)') ((0.5*cost(i,j)/nsteps
1   , i=1, imax), j=1, jmax)
    close(3)

c write out barotropic streamfunction

    open(3, file='../results/'//lout//'.psi')
    do 60 j=0, jmax
        do 60 i=0, imax
            write(3, *) psi(i, j)
60   continue
    close(3)

c Calculate meridional overturning streamfunction opsi on C grid
only

    do j=0, jmax
        do k=0, kmax
            opsi(j,k) = 0
            opsia(j,k) = 0
            opsip(j,k) = 0
        enddo
    enddo

```

```

do 70 j=1,jmax-1
  do 80 k=1,kmax-1
    ou(j,k) = 0
    do 90 i=1,imax
      ou(j,k) = ou(j,k) + cv(j)*u(2,i,j,k)*dphi
90    continue
      opsi(j,k) = opsi(j,k-1) - dz(k)*ou(j,k)
80    continue
70 continue

open(10,file='../results/'//lout//'.opsi')
write(10,100)((opsi(j,k),j=0,jmax),k=0,kmax)
close(10)
c
c Pacific and Atlantic overturning streamfunctions
c
  ominp = 0
  omaxp = 0
  do j=jsf+1,jmax-1
    do k=1,kmax-1
      ou(j,k) = 0
      do i=ips(j),ipf(j)
        ou(j,k) = ou(j,k) + cv(j)*u(2,i,j,k)*dphi
      enddo
      opsip(j,k) = opsip(j,k-1) - dz(k)*ou(j,k)
      if(opsip(j,k).lt.ominp)ominp = opsip(j,k)
      if(opsip(j,k).gt.omaxp)omaxp = opsip(j,k)
    enddo
  enddo

open(10,file='../results/'//lout//'.opsip')
write(10,100)((opsip(j,k),j=0,jmax),k=0,kmax)
close(10)

  omina = 0
  omaxa = 0
  do j=jsf+1,jmax-1
    do k=1,kmax-1
      ou(j,k) = 0
      do i=ias(j),iaf(j)
        ou(j,k) = ou(j,k) + cv(j)*u(2,i,j,k)*dphi
      enddo
      opsia(j,k) = opsia(j,k-1) - dz(k)*ou(j,k)
      if(opsia(j,k).lt.omin)omina = opsia(j,k)
      if(opsia(j,k).gt.omaxa)omaxa = opsia(j,k)
    enddo
  enddo

open(10,file='../results/'//lout//'.opsia')
write(10,100)((opsia(j,k),j=0,jmax),k=0,kmax)
close(10)
c
c zonal overturning streamfunction
c
  do i=0,imax
    do k=0,kmax
      zpsi(i,k) = 0

```

```

        enddo
    enddo

do i=1,imax-1
    do k=1,kmax-1
        zu(i,k) = 0
        do j=1,jmax
            zu(i,k) = zu(i,k) + u(1,i,j,k)/c(j)*ds
        enddo
        zpsi(i,k) = zpsi(i,k-1) - dz(k)*zu(i,k)
    enddo
enddo

open(10,file='../results/'//lout//'.zpsi')
write(10,100)((zpsi(i,k),i=0,imax),k=0,kmax)
close(10)

100 format(e14.7)
110 format(11e14.6)

c write poleward heat flux in Atlantic and Pacific and total

pi=4*atan(1.0)
open(15,file='../results/'//lout//'.fofy')
write(15,'(10(a11,3x))')
$           ' latitude '
$           ', tot_tot ', ' Pac_tot '
$           ', Atl_tot ', ' tot_adv '
$           ', Pac_adv ', ' Atl_adv '
$           ', tot_dif ', ' Pac_dif '
$           ', Atl_dif '
phfmax = 0
do j=1,jmax-1
    do l=1,3
        hft(l) = 0
        hfp(l) = 0
        hfa(l) = 0
    enddo
    do i=1,imax
        if(k1(i,j).le.kmax.and.k1(i,j+1).le.kmax)then
            tv2 = 0
            tv3 = 0
            do k=k1(i,j),kmax
                tv2 = tv2 + 0.5*cv(j)*u(2,i,j,k)*(ts(1,i,j+1,k)
+
1                 ts(1,i,j,k))*dz(k)*dphi
                tv3 = tv3 - cv(j)*cv(j)*(ts(1,i,j+1,k) -
1                 ts(1,i,j,k))/ds*diff(1)*dz(k)*dphi
            enddo
            hft(1) = hft(1) + tv2 + tv3
            hft(2) = hft(2) + tv2
            hft(3) = hft(3) + tv3
            if(i.ge.ips(j).and.i.le.ipf(j))then
                hfp(1) = hfp(1) + tv2 + tv3
                hfp(2) = hfp(2) + tv2
                hfp(3) = hfp(3) + tv3
            elseif(i.ge.ias(j).and.i.le.iaf(j))then
                hfa(1) = hfa(1) + tv2 + tv3
            endif
        endif
    enddo
enddo

```



```

                hfa(2) = hfa(2) + tv2
                hfa(3) = hfa(3) + tv3
            endif
        endif
    enddo

write(15,110)180.0/pi*asin(s(j)),(hft(1),hfp(1),hfa(1),l=1,3)
    if(abs(hft(3)).gt.phfmax)phfmax = abs(hft(3))
enddo

    write(6,*)'max poleward heat flux ',phfmax

    close(15)
    stop
c write out potential vorticity or density

c    open(11,file='../results/'//lout//'.pv')
    open(11,file='../results/'//lout//'.rho')

c    print*,'input k for Sz plot'
    read (5,*)k
    do j=1,jmax
        do i=1,imax
            do k=1,kmax-1
                do k=1    ,kmax
                    if(k.ge.k1(i,j))then
c                        tmp = s(j)*(rho(i,j,k+1)-rho(i,j,k))/dza(k)
c                        tmp = (ts(2,i,j,k+1)-ts(2,i,j,k))/dza(k)
c                        write(11,*)tmp
c                        write(11,*)rho(i,j,k)
                    else
                        write(11,*)0.0
                    endif
                enddo
            enddo
        enddo
    enddo

    close(11)

c call routine to write terms in psi equation, gb is subsequently
wrong

c    call goose(lout)

c ropsi calculates overturning on steady density surfaces

c    call ropsi

c    open(11,file='../results/tmp.w')
c    do k=kmax,1,-1
c        tmp = 0
c        do i=1,imax
c            do j=1,jmax/2
c                tmp = u(3,5,8,k)
c            enddo
c        enddo
c        write(11,*)tmp
c    enddo

```

```

c      close(11)

c write average osc data

c      if(osc.and.icount.gt.0)then
c          open(10,file='../results/'//lout//'.av')
c          write(10,100)((((ats(l,i,j,k)/icount
c      1      ,l=1,lmax),k=1,kmax),i=1,imax),j=1,jmax)
c          close(10)
c          open(10,file='../results/'//lout//'.avu')
c          write(10,100)((((au(l,i,j,k)/icount,l=1,3)
c      1      ,k=1,kmax),i=1,imax),j=1,jmax)
c          close(10)
c          open(10,file='../results/'//lout//'.avf')
c          write(10,100)((((afn(l,i,j,k)/icount,k=1,kmax),i=1,imax)
c      1      ,j=1,jmax)
c          close(10)
c      endif
c
c for repeated runs
c
c      write(20,'(8e15.5)')0.01*iterun,ominp,omaxp,omina,omaxa
c      1      ,phfmax,avn,rms
c      write(6,'(a)')ominp,omaxp,omina,omaxa,avn,rms'
c      write(6,'(6e15.5)')ominp,omaxp,omina,omaxa,avn,rms
c      close(5)
c      enddo
c      close(20)

end

character*3 function conv(i)
character*1 a,b,c
if(i.lt.10)then
a=char(i+48)
conv=a//' '
else if(i.lt.100)then
i1=i/10
i2=i-i1*10
a=char(i1+48)
b=char(i2+48)
conv=a//b//' '
else
i1=i/100
itemp=i-100*i1
i2=itemp/10
i3=itemp-10*i2
a=char(i1+48)
b=char(i2+48)
c=char(i3+48)
conv=a//b//c
endif
end

```